



**HAL**  
open science

# Microfluidic flow of suspensions of deformable particles through constrictions

Lars Kool

► **To cite this version:**

Lars Kool. Microfluidic flow of suspensions of deformable particles through constrictions. Physics [physics]. Université Paris Cité, 2023. English. NNT : 2023UNIP7103 . tel-04579326

**HAL Id: tel-04579326**

**<https://theses.hal.science/tel-04579326>**

Submitted on 17 May 2024

**HAL** is a multi-disciplinary open access archive for the deposit and dissemination of scientific research documents, whether they are published or not. The documents may come from teaching and research institutions in France or abroad, or from public or private research centers.

L'archive ouverte pluridisciplinaire **HAL**, est destinée au dépôt et à la diffusion de documents scientifiques de niveau recherche, publiés ou non, émanant des établissements d'enseignement et de recherche français ou étrangers, des laboratoires publics ou privés.

École doctorale n° 564 : Physique en Île-de-France (EDPIF)

# Thèse de Doctorat

pour obtenir le grade de docteur délivré par

**Université Paris Cité**  
Spécialité doctorale “Physique”

*présentée et soutenue publiquement par*

**Lars KOOL**

le 15 juin 2023

## Microfluidic flow of suspensions of deformable particles through constrictions

Directrice de thèse : **Anke LINDNER**

### Jury

<b>M<sup>r</sup> Gioacchino VIGGIANI,</b>	Professeur, Université Grenoble Alpes	Rapporteur
<b>M<sup>me</sup> Emilie DRESSAIRE,</b>	Maîtresse de conférences, UCSB	Rapporteuse
<b>M<sup>r</sup> Paulo E. ARRATIA,</b>	Professeur, University of Pennsylvania	Examinateur
<b>M<sup>me</sup> Stéphanie DEBOEUF,</b>	Chargée de Recherche, CNRS	Examinatrice
<b>M<sup>r</sup> Elie WANDERSMAN,</b>	Maître de conférences, Sorbonne Université	Examinateur
<b>M<sup>r</sup> Ralf STANNARIUS,</b>	Professeur, Otto-von-Guericke-Universität	Examinateur
<b>M<sup>me</sup> Anke LINDNER,</b>	Professeure, Université Paris Cité	Directrice de thèse

**ESPCI**

**Laboratoire de Physique et Mécanique des Milieux Hétérogènes (PMMH)**  
CNRS UMR-7636, 7 Quai Saint-Bernard, 75005 Paris, France



# Abstract

Granular media are ubiquitous, from the soil we build our houses on to the beans we use to make our coffee. The behavior of granular materials depends on a wide variety of properties of the constituent particles, such as their size distribution, softness, coefficient of friction or roughness, to list a few. It is not fully clear yet how each of these particle properties separately influence the behavior of granular materials. Furthermore, experimentally testing the influence of these properties is challenging, as changing one property tends to change others as well. In this thesis, we describe a method to fabricate ensembles of particles with varying elastic properties, while keeping other properties mainly unaffected, inside a microfluidic channel by locally crosslinking a photosensitive solution. We studied the compaction of particles with different softnesses by compressing them against a membrane using oscillatory flow. We found that, regardless of the particle softness, the observed strain showed hysteretic behavior when represented as a function of the imposed stress. While this hysteresis could be attributed to the complex poro-elastic relaxation of the hydrogel particles, the hysteresis was found to be persistent even at vanishing driving frequency, pointing towards a time-independent origin. To delve into the possible microscopic origins of the hysteresis, we determined the interparticle forces from the deformations of the soft particles. We found that the microscopic descriptors, such as the coordination number and distribution of inter-particle forces followed the trends described in literature. Furthermore, we found that the bulk deformation scales linearly with the average deformation of the individual particles, and that the microscopic stress and bulk deformation did not show any hysteresis. Lastly, we developed a new microfluidic hopper to study the discharge of soft frictionless particles. We found that the discharge rate scaled linearly with the driving force, unlike for dry granular hoppers. Clogging was only obtained for very narrow orifice sizes, again in contrast to dry granular media. The experimental methods described in this thesis can easily be adapted to systematically study other particle properties. The precise control over the shape and size of the particles could be used to tune the roughness of the particles, as an analogue to interparticle friction.

**Keywords** : Granular, microfluidics, soft, hydrogel, suspension, hopper, compaction



# Résumé

Les milieux granulaires sont omniprésents, qu'il s'agisse du sol sur lequel nous construisons nos maisons ou des grains de café que nous utilisons. Le comportement des matériaux granulaires dépend d'une grande variété de propriétés des particules constitutives, telles que leur distribution de taille, leur rigidité, leur coefficient de frottement ou leur rugosité, pour n'en citer que quelques-unes. La manière dont chacune de ces propriétés influence séparément le comportement des matériaux granulaires n'est pas claire. De plus, tester expérimentalement l'influence de ces propriétés séparément est un défi, car la modification d'une propriété tend à modifier les autres également. Dans cette thèse, nous décrivons une méthode pour fabriquer des ensembles de particules avec des propriétés élastiques variables, sans affecter les autres propriétés, à l'intérieur d'un canal microfluidique en réticulant localement une solution photosensible. Nous avons étudié le compactage de particules ayant des propriétés élastiques différentes en les comprimant à l'aide d'un flux oscillant contre une membrane semi-perméable. Nous avons constaté que, quelle que soit la rigidité des particules, la déformation observée présentait un comportement hystérétique lorsqu'elle était représentée en fonction de la contrainte imposée. Alors que cette hystérésis pourrait être attribuée à la relaxation poro-élastique complexe des particules d'hydrogel, l'hystérésis s'est avérée persistante même lorsque la fréquence d'entraînement est nulle, ce qui indique une origine indépendante du temps. Pour approfondir les origines microscopiques possibles de l'hystérésis, nous avons déterminé les forces interparticulaires à partir des déformations des particules molles. Nous avons constaté que les quantités microscopiques, telles que le nombre de coordination et la distribution des forces interparticulaires, suivaient les tendances décrites dans la littérature. Nous avons découvert que la contrainte microscopique et la déformation globale ne présentaient pas d'hystérésis. En outre, nous avons constaté que la déformation globale s'échelonne linéairement avec la déformation moyenne des particules individuelles. Enfin, nous avons mis au point une nouvelle trémie microfluidique pour étudier la décharge de particules molles sans frottement. Nous avons constaté que le taux de décharge s'échelonnait linéairement avec la force motrice, contrairement aux trémies des granulaires secs. Le colmatage n'a été obtenu que pour des tailles d'orifice très étroites, là encore contrairement aux milieux granulaires secs. Les méthodes expérimentales décrites dans cette thèse peuvent facilement être adaptées pour étudier systématiquement d'autres propriétés des particules. Le contrôle précis de la forme et de la taille des particules pourrait être utilisé pour ajuster la rugosité des particules, en tant qu'analogie à la friction interparticulaire.

**Mots-clés** : Granulaire, microfluidique, rigidité, hydrogel, suspension, trémie, entonnoir, compactage



# Acknowledgements

Despite the fact that I'm the sole author of this PhD thesis and this thesis is used (at least in part) to judge my merits, the efforts described in this thesis would not have been possible without any help. As scientists, we are quick to acknowledge anyone who contributed scientifically, and rightfully so. However, in my opinion, a PhD is more than just about scientific advancement. It is also about personal development, learning about your strengths/weaknesses, learning about your preferences/dislikes, being aware of other cultures and adapt yourself in such a way to accommodate both your own and someone else's. I would, therefore, like to use this moment to acknowledge people that were invaluable to the completion of this thesis, not only on a scientific level, but also on a personal level.

First of all, I would like to thank my supervisor Anke Lindner. Her hands-off approach allowed me to not only to explore and find my scientific interests, but also develop myself personally as well as professionally. Furthermore, her keen eye in bringing structure to text and presentation really helped me hone my soft skills, both in scientific communication and outreach. I would also like to thank Olivia du Roure, who, despite not being involved with my project specifically, joined all the group meetings and always asked very insightful questions. I would also like to thank Philippe Bourrienne, who was of great help in the final stages of my thesis.

Furthermore, I would like to thank the past and current members of Anke's group: Jean, Lucas, Martyna, Noa, Francesca, Zhibo, Francesco, Peixin, Guillaume, Benjamin, Andrea, Marine, XiaoXiao, and Jules, for the wonderful time and great discussions we shared in the lab.

I would also like to thank Paulo Arratia. His enthusiasm upon discussing my first results started my curiosity in the connection between microstructure and macroscopic response. And, I would like to thank Ralf Stannarius, with whom I had the pleasure to discuss on hopper flow. Of course, I'm very grateful to the all jury members: Cino Viggiani, Emilie Dressaire, Elie Wandersman, Paulo Arratia, Stéphanie Deboeuf, and Ralf Stannarius for taking the time to read and judge my thesis, and for their questions and the insightful discussion.

My thesis was part of a European Innovative Training Network (ITN) Caliper. It was amazing to be part of a network with so many other PhD students: Chandan, Francisco, Michael, Nazanin, Gustavo, Tivadar, Ahmed, Ilija, Jing, Bo, Maheandar, Zorica, and Zohreh. We had some great moments in the limited amount of time we had together. I don't want to play favorites, however, I do want to thank the two with whom I spent more time explicitly. Chandan, I'm happy to call you my friend. Any journey with you turns into an adventure, like hiking in the soaking rain along the cliffs of Étretat. I would not have done any of this



without you, and I hope these adventures will not end after our PhD. Francisco, I was also delighted to host you here in Paris. It is always great to have a friend who's passionate about food and always willing to try new places. I will never forget the amazing dinner we had at Azabu. Since we'll both plan to stay in Paris for at least a little while, I'm sure we'll discover more of the culinary side of Paris.

I'm indebted to Joshua Dijkstra, who was the supervisor of my M.Sc. thesis and the coordinator of Caliper. He introduced me to Anke, and advised me to go to ESPCI to do my thesis. I would not have joined this project without his advice. Since we were both part of the European program, we met frequently. The meetings always ended with some new ideas (which were typically unfeasible, but always good to keep in mind). His seemingly never-ending knowledge of granular literature also resulted in the recommendation of a couple of very relevant papers during every meeting.

Another person who has shaped my academic career is Karen Daniels. Karen introduced me to granular materials. But she did much more than that. The start of my PhD was tough: new country, new language, new people, and worst of all being confined in a small apartment because of a lockdown. Her perception of my mental state and her ability to adapt her guidance accordingly, allowed me to stay mentally sane, and get more work done, both on our collaborative project, but also on my own project.

I also had the pleasure to work with the team of the "Plateforme Technologique d'IPGG", where I had many useful discussions with team of engineers: Bertrand, Audric, Kevin. Who I now have the great pleasure to join as an engineer, starting this August. I hope I can be as useful to others as they were to me.

A word of thanks goes out to the lab directors, Damien and Philippe. They were very perceptive to the impact of Covid-19 and the lockdown, not only from a scientific point-of-view, but also socially. They have gone to great lengths to keep the group as close as it was before. Most notably the now infamous "Les Houches" trip. Also, without the help of Frédérique and Claudette, I would still be stuck trying to figure out French administration.

This leads me to a very large group of people to thank: my coworkers, especially the non-permanents. I truly believe that the atmosphere people have created before us, and that we have maintained to the best of our ability, is special. Life doesn't end when you close the door to the lab, that's when the social life starts. The countless evenings at our favorite pub, "Les Arènes". The undisclosed amount of late nights or early mornings at an undisclosed location in the 10th arrondissement. The never-ending "pots-de-thèse". Les Houches, La Pépinière, Moulin d'Andé. The list goes on... It was an unforgettable experience.

I do want to mention some lab members who made my time here particularly memorable (please excuse my brevity, otherwise the length of the acknowledgements would far exceed the length of the rest of the thesis): Hector, who shared my love for fries like no one else. Saurabh, the philosopher and wordsmith, with whom I spent many evenings discussing anything on our mind. Magda, who's mere presence, managed to convert any conversation into English, for which I'm very grateful. Noa, with whom I had many interesting conversations about life and research. Manon, the free spirited, whose bliss I still have to master. Renaud, l'homme du match, the organizer of all things sport. Samantha, who always offered a listening ear to

who-ever needed it. Juan, who was always the first to let me know that overall productivity increases, if you decrease productivity once in a while. Chloë, who never failed to rally people for a social event.

I wanted to thank my office mates for the great balance between hard work, helping each other, and having fun. I, however, noticed I already mentioned everyone in the office, which (I think) says a lot about the amazing atmosphere in our office!

Last, but far from least, it rests me to thank my family. Papa, mama, ik ben bang dat deze alinea niet voldoende is om jullie te bedanken voor alles wat jullie voor mij hebben gedaan, zowel tijdens mijn promotieonderzoek als daarvoor. Mijn verblijf hier in Parijs is nooit makkelijk geweest, en zonder onze urenlange gesprekken had ik het nooit gered. Gijs, jij ook bedankt voor alles. De afgelopen paar jaar konden pappa en mamma mijn hulp prima gebruiken, maar ik zat hier in Parijs, en dus kwam er genoeg op jou bord terecht. Ook wil ik graag mijn opa's, Antoon en Wim, en oma's, Marian en Riet, graag bedanken voor hun jarenlange steun en liefde. Daarnaast waren zij ook de perfecte proefkonijnen om te leren om mijn onderzoek uit te leggen in simpele woorden. Mijn waardering voor hun enthousiasme en geduld valt amper in woorden uit te leggen.

— *Lars*



# Table of Contents

<b>Abstract</b>	<b>i</b>
<b>Résumé</b>	<b>iii</b>
<b>Acknowledgements</b>	<b>v</b>
<b>1 Introduction</b>	<b>1</b>
1.1 References . . . . .	8
<b>2 Materials and Methods</b>	<b>13</b>
2.1 Particle fabrication . . . . .	14
2.1.1 In-situ fabrication . . . . .	14
2.1.2 Chemistry of UV-photopolymerization . . . . .	14
2.2 Fabrication of PDMS microchannels . . . . .	16
2.2.1 Experimental setup . . . . .	17
2.2.2 Multi-particle systems . . . . .	20
2.3 Flow control . . . . .	23
2.4 Image acquisition and analysis . . . . .	27
2.4.1 Imaging particles . . . . .	27
2.4.2 Feature finding . . . . .	27
2.4.3 Feature linking . . . . .	29
2.4.4 Particle radius . . . . .	30
2.5 PIV . . . . .	31
2.6 References . . . . .	32
<b>3 Compaction of dense suspensions of soft particles: rheological perspective</b>	<b>35</b>
3.1 Introduction . . . . .	36
3.1.1 Hydrogel properties . . . . .	37
3.1.2 Kelvin-Voigt . . . . .	38
3.1.3 Generalized Kelvin-Voigt . . . . .	40
3.2 Materials and Methods . . . . .	40
3.2.1 Channel geometry . . . . .	40
3.2.2 Initialization . . . . .	41
3.3 Results and Discussion . . . . .	41
3.3.1 Average global strain . . . . .	41
3.3.2 Step stress . . . . .	43
3.3.3 Oscillatory compression . . . . .	48
3.3.4 Stepwise oscillation . . . . .	53

3.4	Conclusions . . . . .	54
3.5	References . . . . .	55
<b>4</b>	<b>Compaction of dense suspensions of soft particles: Micro-mechanical perspective</b>	<b>57</b>
4.1	Introduction . . . . .	58
4.1.1	Mechanics . . . . .	58
4.1.2	Microscopic stress . . . . .	59
4.1.3	Jamming . . . . .	62
4.1.4	Packing fraction . . . . .	62
4.1.5	Coordination number . . . . .	63
4.1.6	Force distributions . . . . .	64
4.2	Materials and Methods . . . . .	66
4.2.1	Particle radius . . . . .	66
4.3	Results . . . . .	68
4.3.1	Relation global and local strain . . . . .	68
4.3.2	Evolution of the microscopic pressure . . . . .	69
4.3.3	Coordination number . . . . .	70
4.3.4	Radial contact distribution . . . . .	71
4.3.5	Distribution of interparticle forces . . . . .	72
4.3.6	Reversible Plasticity . . . . .	73
4.4	Conclusion . . . . .	76
4.5	References . . . . .	76
<b>5</b>	<b>Discharge of soft particles through a microfluidic hopper</b>	<b>81</b>
5.1	Introduction . . . . .	82
5.1.1	Hopper discharge . . . . .	82
5.1.2	Hagen-Beverloo law . . . . .	84
5.1.3	Clogging . . . . .	86
5.1.4	Soft particles . . . . .	86
5.2	Materials and Methods . . . . .	87
5.2.1	Hopper channels . . . . .	87
5.2.2	Fabrication of Quake valves . . . . .	88
5.2.3	Initialization of microfluidic hoppers . . . . .	91
5.3	Results and Discussion . . . . .	92
5.3.1	Discharge rate . . . . .	92
5.3.2	Scaling laws of microfluidic hopper discharge . . . . .	98
5.3.3	Clogging of microfluidic hoppers . . . . .	102
5.4	Conclusions . . . . .	103
5.5	References . . . . .	104
<b>6</b>	<b>Conclusion and Perspectives</b>	<b>109</b>
6.1	Conclusions . . . . .	109
6.2	Perspectives . . . . .	111
6.2.1	Relaxation of single particles and particle packings . . . . .	111
6.2.2	Reversible plasticity . . . . .	112
6.2.3	Clogging of soft particles in microfluidic channels . . . . .	113
6.2.4	Visualize force chains . . . . .	114

---

6.2.5	Pillar fabrication . . . . .	115
6.3	References . . . . .	116
<b>7</b>	<b>Résumé substantiel</b>	<b>117</b>
7.1	Introduction . . . . .	117
7.2	Contenu . . . . .	118
7.3	Conclusion . . . . .	120
7.4	References . . . . .	120
<b>Appendix I: "Gardner-like crossover from variable to persistent force contacts in granular crystals"</b>		<b>125</b>
<b>Appendix II: Supporting Information for "Gardner-like crossover from variable to persistent force contacts in granular crystals"</b>		<b>132</b>



# Chapter 1

## Introduction

In this chapter, we will lay the foundation on which this thesis is build. First, we will give a brief overview of the tangible world and interesting phenomena involving granular media, and how environmental effects can change the behavior of granular media.

This is followed by a brief overview on the influence of certain particle properties, including particle softness, on the behavior of entire packings from a numerical and experimental point of view.

Next, we will introduce the method to fabricate particles with varying softnesses inside microfluidic channels, on which our experiments are based.

Lastly, we will give a chapter by chapter overview of the contents of the thesis. This starts with a chapter about the experimental setup, data collection and image analysis algorithms developed. This is followed by a chapter on the compaction of a 2D packing of granular materials from a rheological point-of-view, and a chapter on the compaction from a micro-mechanical point-of-view. The next chapter will be on the discharge of hydrogel particles of varying sizes and softness in a microfluidic hopper. Lastly, we will give an overview of the main conclusions, and interesting research opportunities for the future.



We're all familiar with sand, whether it reminds us of playing in the sandbox when we were kids, or the family trips to the beach in the summer. If you have a closer look around, granular materials (i.e. materials consisting of many small particles/grains) are everywhere. In industry, granular materials are also ubiquitous, as they are the second most handled material by weight, only surpassed by water [1].

In classical continuum mechanics, there are two main classes of materials: solids, which have a finite deformation upon an imposed load, and fluids, which have a finite deformation rate upon an imposed load. This distinction is, however, less clear for granular materials. Imagine walking on the beach, like the beach of Noordwijk aan Zee (Figure 1.1A). Stepping on the sandbed causes your foot to displace some sand, akin to how your foot would displace water when dipped in a pool. However, after displacing a small amount of sand (orders of magnitude less than predicted by Archimedes' principle of buoyancy), no more sand is displaced and the sandbed feels solid. Within one step, you experience both the fluid- and solid-like character of granular materials. Furthermore, as you keep walking towards the water, the sandbed suddenly becomes much darker, and the sandbed hardly deforms at all (Figure 1.1A). It turns out that the behavior of sand highly depends on its environment. Since the grains don't perfectly fill the space, and instead leave voids, a small amount of water is able to permeate into the sandbed. The water will form capillary bridges between the particles, causing them to "stick" together (Figure 1.1B) [2–4]. Walking closer to the water, the grains are completely encompassed by water, resulting in a suspension that flows like a liquid.

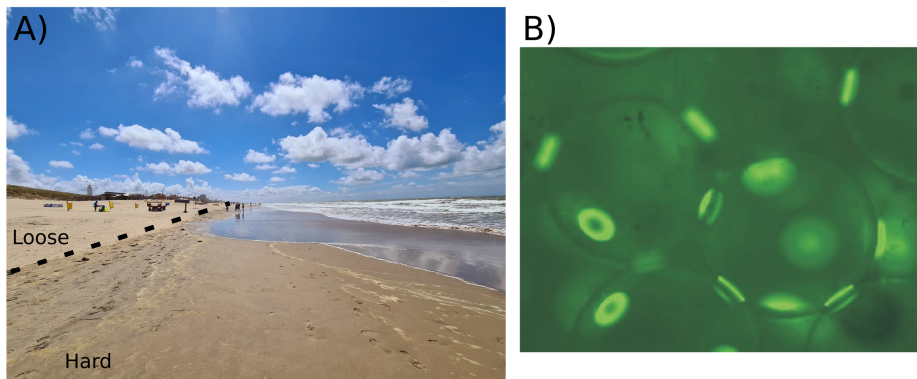


Figure 1.1: A) Picture of the beach of Noordwijk aan Zee in the Netherlands. On the left, one can see the loose (light) sand. Closer to the beach, marked by a clear transition in color, is the harder sandbed. Any copyright to this image belongs to Mandy Spitters. B) Glass spheres with an average diameter of  $375 \mu\text{m}$ , with the capillary bridges in fluorescently labelled. Figure taken from [4]

In their seminal paper, Liu and Nagel [5] proposed a unifying phase diagram for granular materials and thermally agitated particulate systems, called glasses, which are well described by statistical mechanics (Figure 1.2A) [6]. At high temperatures, glasses behave like liquids (upper part of the red plane in Figure 1.2A). The particles move in straight lines until they collide (ballistic regime), and slip past each other between these collisions (diffusive regime). However, when cooled to a critical temperature, the energy of the particles is no longer enough for the particles to diffuse and each particle is caged by its neighbors. This regime is called the glass regime. It is at this point that the system ceases to flow (like a liquid would) and can sustain a finite load (like a solid would).

Inspired by this transition from liquid to solid, Liu and Nagel [5] proposed that a granular material is just a glass at zero temperature. Therefore, to withstand a finite load, the grains

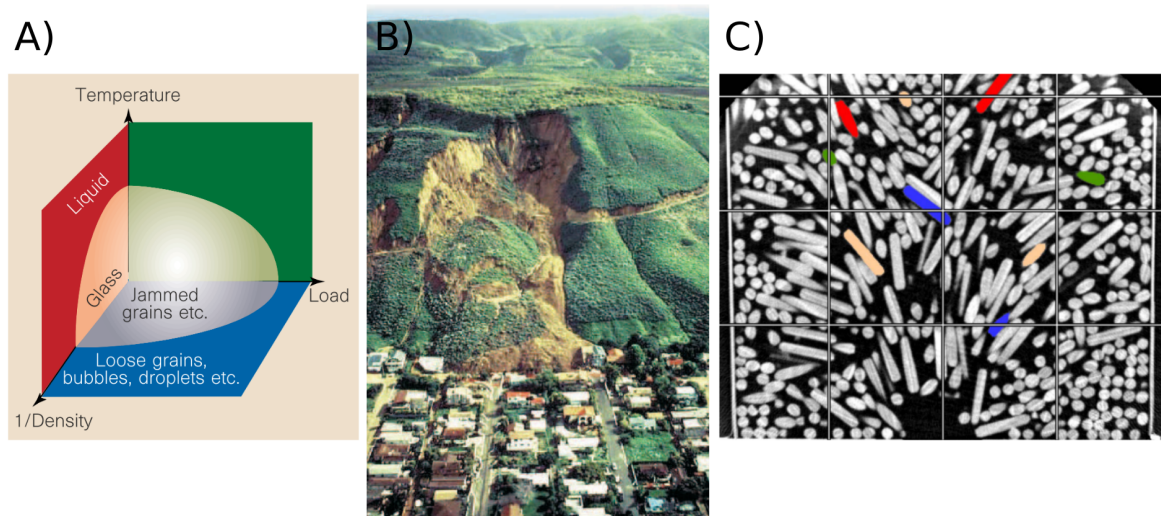


Figure 1.2: A) Phase diagram of jammed systems. Image taken from [5]. B) Landslide at La Conchita, California (1995). Image taken from [7] C) Alignment of elongated particles during the discharge from a hopper. Image taken from [8]

should be "jammed" together, hence the transition from liquid to solid is called the jamming transition. Where in glasses, thermal energy is driving the particles into the liquid regime, mechanical load was proposed as the mechanism behind the liquefaction of granular materials. If the (local) load is higher than a threshold, the yield stress, the particles will slip past each other and flow.

The last element to jamming is the density, particles can only sustain a load once they touch, otherwise they would just displace. At higher density, the system should be more jammed, hence the third axis scales as the inverse of the density.

Coming back to the beach example. At first, the sandbed is jammed, as it is able to sustain its own weight. Once the sandbed is stepped on, locally the load exceeds the yield stress and the sand starts to flow. Upon deformation, new particle contacts are made, spreading the load over more particles. At a certain point, the load is spread out over enough particles such that the local load no longer exceeds the yield stress, and the sandbed behaves like a solid again. Moving closer to the water, the attractive interactions caused by the capillary bridges increase the yield stress, which leads to less deformation. Moving into the water, the grains can be suspended in the water, breaking the particle contacts and effectively fluidizing the system.

Unlike ordinary solids, which spread out the load equally over the entire contact area, most of the load imposed on a granular material is carried by a small number of particles. The network of load bearing particles spanning the entire system is called a force network [9, 10]. Force networks turn out to be marginally stable, meaning that a small perturbation can cause a completely different force network to form [9]. This marginal stability might be linked to the tendency of granular media to fail in small bands, called shear bands [11–14]. These shear bands can be seen in natural events like avalanches and landslides, where there is a clear transition between undeformed, solid phase and the flowing liquid phase (Figure 1.2B).

So far, we have seen that the behavior of granular materials changes drastically under different external conditions, such as the applied load, surrounding medium, and presence of

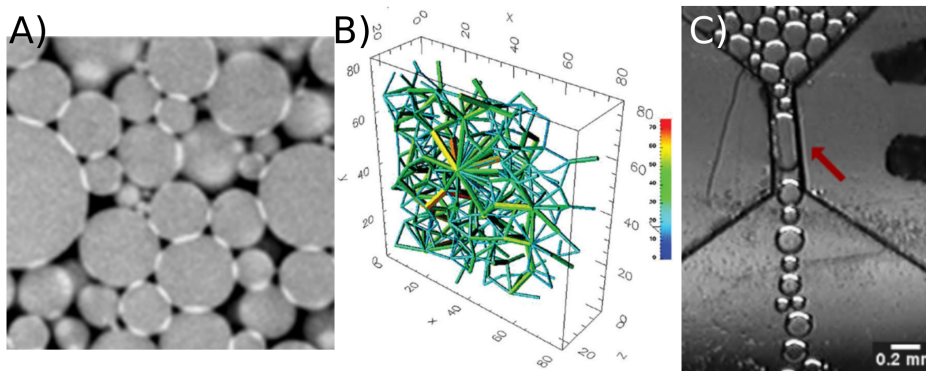


Figure 1.3: A) Confocal image of fluorescent droplets of silicone oil (gray regions) dispersed in an index matched mixture of glycerol and water (black regions). The interfaces between droplets appear to be brighter. Figure taken from [37]. B) Reconstructed 3D force network from the deformation of the droplets observed in A. Figure taken from [37]. C) Gravity driven discharge of polydisperse oil droplets in water through a microfluidic hopper. Oil droplet bigger than the orifice are able to be discharged due to their deformation (red arrow). Figure taken from [38]

capillary bridges. However, the properties of the grains constituting the granular medium also influences the behavior of granular media. During flow, elongated particles are known to align at a small angle compared to the shear direction, which reduces the effective viscosity [8, 15, 16]. Understanding the reorientation of elongated particles along the shear band could also prove vital in predicting the structural integrity and modes of failure in soils [17, 18].

Surface roughness also play a significant role in the behavior of granular media and suspensions. Roughness can lead to an effective friction between the grains [19, 20], and has been suggested as a key parameter determining the density at which the force network is determined in granular glasses [21, 22]. Furthermore, rough particles have been known to cause a very sharp increase in the viscosity of a suspension at low concentrations, if sheared fast enough [23, 24].

Another interesting particle property is the particle softness. The ground works on the influence of particle softness were laid with simulations, as simulations allow for the extraction of the macroscopic (system-level) response, as well as the microscopic (particle-level) response. It likely started with the development of the Discrete (or distinct) Element Method (DEM) to simulate granular media by Cundall and Strack [25]. Durian [26] developed a similar model to simulate the mechanics of foams. Both models work by assuming the particles are circles/spheres and the forces between the bubbles/particles depends linearly on the deformation of the particle, according to Hertzian contact mechanics [27–29].

These simulations were later improved by, for instance, modelling the particles as an elastic solid with Finite Element Method simulations, coupling this to the discrete particle-particle interactions [30], and allowing for a non-smooth transition between force laws with the Non-Smooth Contact Dynamics model [31–33].

Experimental efforts have long been focused on measuring sample averaged properties, such as the yield stress of emulsions and suspensions [34] using rheology, or relaxation timescales using scattering techniques like diffusive wave spectroscopy [35], as the strong scattering interfaces between the particles and the suspending fluid hindered the direct observation of microstructure [36].

Technological advances in confocal fluorescence microscopy and fabrication of channels

with microscopic features (microfluidics) were needed to observe the microstructure in more detail. Brujić et al. [37] were one of the first to reconstruct the 3D force-network of a jammed emulsion, and observe the distribution of interparticle forces (Figure 1.3AB). Typically, the softness (which depends on the surface tension between the dispersed phase and the continuous phase) was used to non-dimensionalize the applied pressure [39], suggesting that the softness only affected the magnitude of the deformations, but not any of the dynamics of the particles [40].

More recently, the flow of soft particles through a narrow gap has been studied, either by squeezing droplets between two parallel plates, or by confining swollen polymer networks (hydrogels) between two parallel plates [38, 41]. Ashour et al. [41] and Hong et al. [38] found that these soft, nearly frictionless particles have a reduced chance of clogging the orifice. Furthermore, they found that the formed clogs dissipated without the need of external perturbation (Figure 1.3C), which does not happen with hard frictional particles. [42, 43].

It turns out, however, that systematically investigating the effect of particle softness is challenging. The Young's modulus is inherently bound to a material. Changing the material, while maintaining compatibility with the experimental system, inevitably affects any of the other particle properties that influence the material response like friction coefficient and roughness. In many of the experimental investigations into the influence of particle softness on the behavior of granular materials, the dynamics and mechanics of hard (typically frictional) particles are compared against soft (typically frictionless) particles made of a completely different material. This makes it difficult to attribute the observed differences to just the particle softness or a combination of particle softness and any of the unintentionally changed parameters.

In this thesis, we will systematically investigate the effect of particle softness on the behavior of granular packings. To do so, we will adapt a microfabrication technique to produce 2D granular packings of disks inside microfluidic channels, which allows us to tune the particle softness without changing any of the other particle properties.

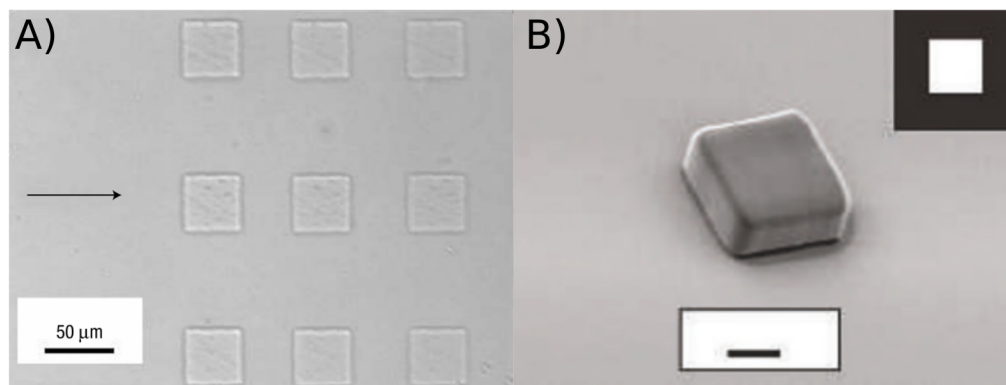


Figure 1.4: A) Array of square hydrogel particles fabricated by locally exposing the photo-sensitive solution to UV-light. Image taken from [44] B) Scanning Electron Microscopy image of a hydrogel particle. The inset shows the mask used to fabricate this particle. Image taken from [44]

The method was pioneered in the group of Patrick Doyle, who developed a technique to synthesize a hydrogel particle inside microfluidic channels by locally exposing a photo-sensitive solution to UV-light (Figure 1.4A) [44, 45]. They were able to change the shape and size of the particles by placing a mask in the path of the light, blocking most of the light and

forming a particle in the shape and size of the opening in the mask (Figure 1.4B). Duprat et al. [46] and Cappello et al. [47] found that it was possible to change the softness of these particles by either reducing the exposure to UV-light, or diluting the photo-sensitive solution. In this thesis, starting from the method to fabricate particles of varying softness developed by Cappello et al. [47], we will study the influence of particle softness on the behavior of granular packings.

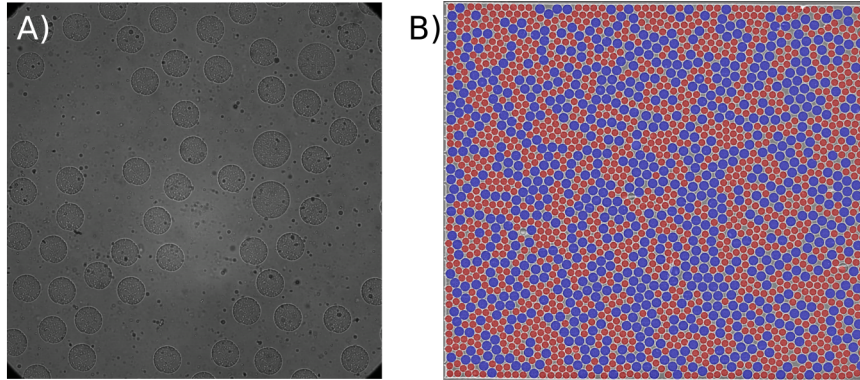


Figure 1.5: A) Image taken during the fabrication of the particles. All small particles are already fabricated, and the fabrication of the large particles is in progress. The big gaps between particles are yet to be filled with particles. B) Ensemble of  $\sim 2000$   $120 \mu\text{m}$  (red) and  $160 \mu\text{m}$  (blue) particles confined in a microfluidic channel. The channel is 5 mm wide (top to bottom).

We will investigate two different situations with this setup: first the step-wise and oscillatory compaction of a granular packing, both from a rheological (macroscopic) point-of-view and a microscopic point-of-view, and secondly the discharge of granular particles through a narrow orifice. In detail, the first chapter (this chapter) has given a short introduction to granular phenomena and parameters that influence these phenomena. The second chapter of this manuscript reviews the experimental methods used and developed, that are used throughout this thesis. First, we will explain the aforementioned technique to fabricate single particles of varying softness in more detail. Then, we present how we managed to expand the capabilities of this technique to fabricate ensembles of particles of different sizes in predefined locations inside the microfluidic channel (Figure 1.5A). This is followed by a description and a characterization of the flow of the carrier fluid inside the microfluidic channel, and how this exerts a force on the particles. Lastly, we will discuss how we extracted the locations of  $\sim 2000$  particles (with varying sizes) in the field of view with sub-pixel accuracy (Figure 1.5B).

The third chapter is dedicated to the compaction of packings of particles with varying softness inside a microfluidic channel, which we investigate from a rheological point-of-view. First, we develop a microfluidic channel that allows us to compress the particles against a membrane (far left edges of Figure 1.6AB). We then use this channel to perform step-stress experiments, to characterize the viscoelastic behavior of the particle packings, which we were able to capture with a generalized Kelvin-Voigt model for viscoelastic solids. Lastly, we show that the repeated compaction and decompaction of soft frictionless particles is non-trivial, and that a viscoelastic description of the particles is not enough to describe the hysteresis during the compaction in our system.

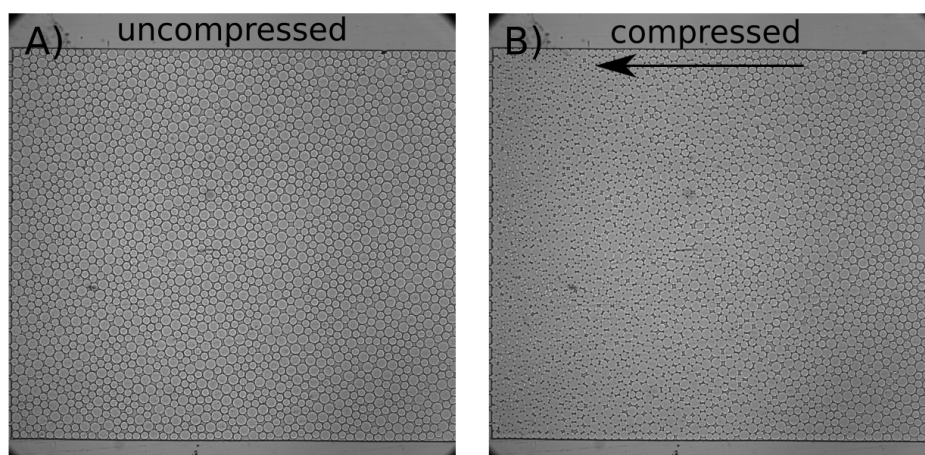


Figure 1.6: A) Image of an uncompressed packing. B) Image of a packing of soft particles compressed against a membrane (left-side). The compressive direction is indicated with the arrow. Both channels are 5 mm wide (top to bottom), containing particles of  $120\ \mu\text{m}$  and  $160\ \mu\text{m}$  in diameter.

The fourth chapter focuses on the same experiments as described in chapter 3, but now from a micro-mechanical point-of-view. We describe how we were able to get a near complete description of the microstructure of the packing during our experiments, as one would get from simulations. We then describe how microstructural parameters like the microscopic stress tensor, the average number of contacts of each particle and the distribution of forces change as function of the particle softness and applied pressure. Lastly, we will investigate the hysteresis during the compaction from the microscopic trajectories of the particles.

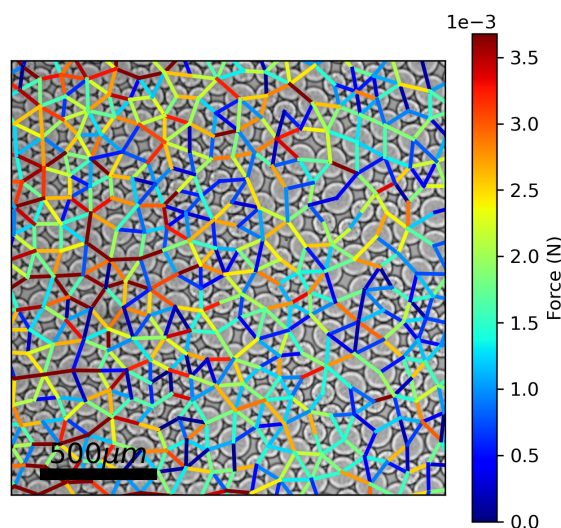


Figure 1.7: Zoom of a packing under compression. The inter-particle forces are indicated with the colored lines, where the color indicates the magnitude of the force between the particles.

In the fifth chapter, we study the discharge of soft particles in a microfluidic hopper. First, we describe the difficulty of obtaining a jammed suspension inside a microfluidic hopper, and how we integrated a valve inside our microfluidic channel to collect particles at the orifice.

We then study the discharge rate of particles of varying size for both pressure and flow-rate driven flows, and compare this to other viscous dominated hopper experiments (Figure 5.1). Lastly, we study the effect of particle softness on the discharge, and we find that particle softness not only has an effect on the discharge rate, but also the evolution of the discharge rate over time, and the clogging behavior.

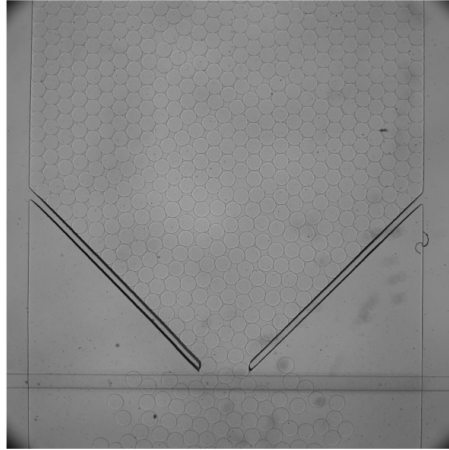


Figure 1.8: Image taken during the discharge of  $200\ \mu\text{m}$  particles through a  $600\ \mu\text{m}$  orifice.

The last chapter concludes this thesis. We will discuss new experiments that could provide a deeper understanding of the results presented here, as well as new fields of study that could emerge from the techniques described in this thesis.

The appendix contains the publication of a side-project I worked on during the start of my PhD in collaboration with Karen Daniels and Patrick Charbonneau. Briefly, the forces in a granular are distributed heterogeneously. The force network ensemble theory predicts that there are many equally likely configurations of the force network for each microscopic configuration of the particles, yet only one is observed at a time. In this paper, we answer the question "When is the force network determined?", by comparing force networks in 2D packings of photo-elastic particles before and after decompression.

## 1.1 References

- [1] P. G. de Gennes. Granular Matter: A Tentative View. *Reviews of Modern Physics*, 71 (2):629–643, 1999. 2
- [2] Arshad Kudrolli. Sticky sand. *Nature Materials*, 7(3):174–175, 2008. 2
- [3] Etienne Guyon, Jean-Yves Delenne, and Farhang Radjai. *Built on sand*. The MIT Press, Cambridge, 2020.
- [4] S. Herminghaus. Dynamics of wet granular matter. *Advances in Physics*, 54(3):221–261, 2005. 2
- [5] Andrea J. Liu and Sidney R. Nagel. Jamming is not just cool any more. *Nature*, 396 (6706):21–22, 1998. 2, 3

- 
- [6] L.D. Landau and E.M. Lifshitz. *Statistical physics*, volume 5. Pergamon Press Inc., Oxford, 1958. 2
- [7] Elliott C Spiker and Paula Gori. *National landslide hazards mitigation strategy, a framework for loss reduction*. Number 1244. US Geological Survey, 2003. 3
- [8] Tamás Börzsönyi, Ellák Somfai, Balázs Szabó, Sandra Wegner, Pascal Mier, Georg Rose, and Ralf Stannarius. Packing, alignment and flow of shape-anisotropic grains in a 3D silo experiment. *New Journal of Physics*, 18(9), 2016. 3, 4
- [9] M E Cates, J P Wittmer, J.-P Bouchaud, and P Claudin. Jamming, Force Chains, and Fragile Matter. *Physical Review Letters*, 81(9):1841–1844, 1998. 3
- [10] Aghil Abed Zadeh, Jonathan Barés, Theodore A. Brzinski, Karen E. Daniels, Joshua Dijkstra, Nicolas Docquier, Henry O. Everitt, Jonathan E. Kollmer, Olivier Lantsoght, Dong Wang, Marcel Workamp, Yiqiu Zhao, and Hu Zheng. Enlightening force chains: a review of photoelasticity in granular matter. *Granular Matter*, 21(4):1–12, 2019. 3
- [11] Osborne Reynolds. Experiments showing dilatancy, a property of granular material, possibly connected with gravitation. *Proc. R. Inst. GB*, 11(354363):12, 1886. 3
- [12] Ralph A. Bagnold. Experiments on a gravity-free dispersion of large solid spheres in a Newtonian fluid under shear. *Proceedings of the Royal Society of London. Series A. Mathematical and Physical Sciences*, 225(1160):49–63, 1954.
- [13] Ralph A. Bagnold. The shearing and dilatation of dry sand and the ‘singing’ mechanism. *Proceedings of the Royal Society of London. Series A. Mathematical and Physical Sciences*, 295(1442):219–232, 1966.
- [14] Michael L. Falk and J.S. Langer. Deformation and Failure of Amorphous, Solidlike Materials. *Annual Review of Condensed Matter Physics*, 2(1):353–373, 2011. 3
- [15] Tamás Börzsönyi, Balázs Szabó, Sandra Wegner, Kirsten Harth, János Török, Ellák Somfai, Tomasz Bien, and Ralf Stannarius. Shear-induced alignment and dynamics of elongated granular particles. *Physical Review E - Statistical, Nonlinear, and Soft Matter Physics*, 86(5):1–8, 2012. 4
- [16] Brisa Arenas-Gómez, Cristina Garza, Yun Liu, and Rolando Castillo. Alignment of worm-like micelles at intermediate and high shear rates. *Journal of Colloid and Interface Science*, 560:618–625, 2020. 4
- [17] Gustavo Pinzón, Edward Andò, Alessandro Tengattini, Gioacchino Viggiani, and Jacques Desrues. Contact evolution in granular materials with inherently anisotropic fabric. *EPJ Web of Conferences*, 249:06015, 2021. 4
- [18] Gustavo Pinzón, Edward Andò, Jacques Desrues, and Gioacchino Viggiani. Fabric evolution and strain localisation in inherently anisotropic specimens of anisometric particles (lentils) under triaxial compression. *Granular Matter*, 25(1):1–12, 2023. 4
- [19] Nicholas A. Pohlman, Benjamin L. Severson, Julio M. Ottino, and Richard M. Lueptow. Surface roughness effects in granular matter: Influence on angle of repose and the absence of segregation. *Physical Review E - Statistical, Nonlinear, and Soft Matter Physics*, 73(3):1–9, 2006. 4



- [20] Guilhem Mollon, Adriana Quacquarelli, Edward Andò, and Gioacchino Viggiani. Can friction replace roughness in the numerical simulation of granular materials? *Granular Matter*, 22(2):1–16, 2020. 4
- [21] Lars Kool, Patrick Charbonneau, and Karen E. Daniels. Gardner-like crossover from variable to persistent force contacts in granular crystals. *Physical Review E*, 106(5):1–6, 5 2022. 4
- [22] Patrick Charbonneau, Eric I. Corwin, Lin Fu, Georgios Tsekenis, and Michael Van Der Naald. Glassy, Gardner-like phenomenology in minimally polydisperse crystalline systems. *Physical Review E*, 99(2), 2 2019. 4
- [23] Philippe Bourrienne, Vincent Niggel, Gatien Polly, Thibaut Divoux, and Gareth H. McKinley. Tuning the shear thickening of suspensions through surface roughness and physico-chemical interactions. *Physical Review Research*, 4(3):33062, 2022. 4
- [24] Jeffrey F. Morris. Shear Thickening of Concentrated Suspensions: Recent Developments and Relation to Other Phenomena. *Annual Review of Fluid Mechanics*, 52:121–144, 2020. 4
- [25] P.A. Cundall and O.D.L. Strack. A discrete numerical model for granular. *Géotechnique*, 27(1):47–65, 1979. 4
- [26] D. J. Durian. Foam mechanics at the bubble scale. *Physical Review Letters*, 75(26):4780–4783, 1995. 4
- [27] H. Hertz. H. Hertz, Über die Berührung fester elastischer Körper, *Journal für die reine und angewandte Mathematik* 92, 156-171 (1881). *Journal für die reine und angewandte Mathematik*, 171:156–171, 1881. 4
- [28] A A Serrano and J M Rodriguez-Ortiz. A contribution to the mechanics of heterogeneous granular media Proc. Symp. Plasticity and Soil Mech, 1973.
- [29] H. M. Princen. Rheology of foams and highly concentrated emulsions. I. Elastic properties and yield stress of a cylindrical model system. *Journal of Colloid And Interface Science*, 91(1):160–175, 1983. 4
- [30] Göran Frenning. An efficient finite/discrete element procedure for simulating compression of 3D particle assemblies. *Computer Methods in Applied Mechanics and Engineering*, 197 (49-50):4266–4272, 2008. 4
- [31] Jean Jacques Moreau. Some numerical methods in multibody dynamics : application to granular materials. *European Journal of Mechanics*, 13(4):93–114, 1994. 4
- [32] M. Jean. The non-smooth contact dynamics method. *Computer Methods in Applied Mechanics and Engineering*, 177(3-4):235–257, 1999.
- [33] Manuel Cárdenas-Barrantes, David Cantor, Jonathan Barés, Mathieu Renouf, and Emilien Azéma. Compaction of mixtures of rigid and highly deformable particles: a micro-mechanical model. 5 2020. 4
- [34] Q. D. Nguyen and D. V. Boger. Measuring the flow properties of yield stress fluids. *Annual Review of Fluid Mechanics*, 24(1):47–88, 1992. 4

- [35] A.D. Gopal and Douglas J. Durian. Nonlinear Bubble Dynamics in a Slowly Driven Foam. *Physical Review Letters*, 75(13):2610–2613, 1995. 4
- [36] Douglas J Durian. Fast, nonevolutionary dynamics in foams. *Current Opinion in Colloid & Interface Science*, 2(6):615–621, 1997. 4
- [37] Jasna Brujić, Sam F. Edwards, Dmitri V. Grinev, Ian Hopkinson, Djordje Brujić, and Hernán A. Makse. 3D bulk measurements of the force distribution in a compressed emulsion system. *Faraday Discussions*, 123(1):207–220, 2003. 4, 5
- [38] Xia Hong, Meghan Kohne, Mia Morrell, Haoran Wang, and Eric R. Weeks. Clogging of soft particles in two-dimensional hoppers. *Physical Review E*, 96(6), 12 2017. 4, 5
- [39] H. P. Zhang and H. A. Makse. Jamming transition in emulsions and granular materials. *Physical Review E - Statistical, Nonlinear, and Soft Matter Physics*, 72(1):1–12, 2005. 5
- [40] Ivane Jorjadze, Lea Laetitia Pontani, and Jasna Brujic. Microscopic approach to the nonlinear elasticity of compressed emulsions. *Physical Review Letters*, 110(4):1–5, 2013. 5
- [41] Ahmed Ashour, Torsten Trittel, Tamás Börzsönyi, and Ralf Stannarius. Silo outflow of soft frictionless spheres. *Physical Review Fluids*, 2(12):1–9, 2017. 5
- [42] Ran Tao, Madelyn Wilson, and Eric R. Weeks. Soft particle clogging in two-dimensional hoppers. *Physical Review E*, 104(044909), 10 2021. 5
- [43] Kirsten Harth, Jing Wang, Tamás Börzsönyi, and Ralf Stannarius. Intermittent flow and transient congestions of soft spheres passing narrow orifices. *Soft Matter*, 16(34): 8013–8023, 9 2020. 5
- [44] Dhananjay Dendukuri, Daniel C. Pregibon, Jesse Collins, T. Alan Hatton, and Patrick S. Doyle. Continuous-flow lithography for high-throughput microparticle synthesis. *Nature Materials*, 5(5):365–369, 5 2006. 5
- [45] Dhananjay Dendukuri, Priyadarshi Panda, Ramin Haghgoeie, Ju Min Kim, T. Alan Hatton, and Patrick S. Doyle. Modeling of oxygen-inhibited free radical photopolymerization in a PDMS microfluidic device. *Macromolecules*, 41(22):8547–8556, 2008. 5
- [46] Camille Duprat, Hélène Berthet, Jason S. Wexler, Olivia Du Roure, and Anke Lindner. Microfluidic in situ mechanical testing of photopolymerized gels. *Lab on a Chip*, 15(1): 244–252, 1 2015. 6
- [47] Jean Cappello, Mathias Bechert, Camille Duprat, Olivia Du Roure, François Gallaire, and Anke Lindner. Transport of flexible fibers in confined microchannels. *Physical Review Fluids*, 4(3):1–22, 2019. 6



## Chapter 2

# Materials and Methods

In this work, we expand on a photo-lithographic technique developed in the lab of Patrick Doyle at MIT [1-3], which is already well-established in our lab [4-6]. This technique has been used to fabricate single hydrogel particles inside the microfluidic channels with excellent control over the shape, size, and softness. Subsequently, these particles can be used for further experiments in the same channel. In this chapter, we describe the concept and chemistry behind the *in-situ* fabricated particles, and how we can tune the shape, size and softness of the particles in detail. Then, we highlight how we expanded the capabilities of this technique to fabricate packings consisting of particles of different sizes, all placed in predefined locations. This is followed by a description and characterization of the flow used to externally drive the particles. Lastly, we describe the image analysis techniques developed to track the particles with sub-pixel accuracy.

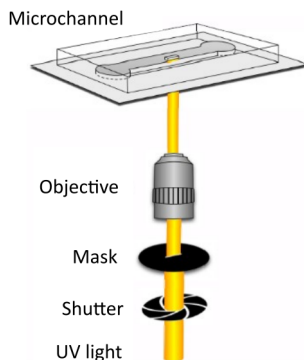


Figure 2.1: Schematic overview of the experimental setup to fabricate the PEGDA particles. The UV-light first passes through a shutter to be able to precisely control the exposure time. Then, the UV-light passes through a mask to control the shape and size of the beam of light. Next, the beam is focused on a small spot in the microfluidic channel by an objective, locally crosslinking the UV-sensitive solution, forming a hydrogel particle suspended in non-crosslinked solution. Figure taken from [7]

## 2.1 Particle fabrication

### 2.1.1 In-situ fabrication

We will first give an overview of the methods to fabricate hydrogel particles, and the microfluidic setup, followed by a more detailed look at each of the components. We fabricated the particles according to a photolithographic projection method described by Dendukuri et al. [1]. They discovered how a photo-sensitive mixture will form cross-linked polymer networks when exposed to UV-light. The UV-light is generated by a mercury-vapor lamp, and passes through a shutter to be able to precisely control the exposure time. The light then passes through a mask, which is a black sheet of plastic, with a transparent part in the center. The mask is in the field stop position, meaning that the beam of light will take the shape and size of the transparent part of the mask. After the mask, the light passes through the microscope objective, which focuses the beam of light onto a small spot in the channel. The light in this spot causes the UV-sensitive solution to locally react and form a cross-linked polymer network. The typical exposure time to fully cross-link a particle is  $\sim 600$  ms [4].

### 2.1.2 Chemistry of UV-photopolymerization

In this section, we will deepen our understanding of the crosslinking of the photosensitive solution. The solution consists mainly of two ingredients, a molecule that can cross-link (polymerize): polyethylene glycol diacrylate (PEGDA) and a molecule that can initiate the crosslinking (photo-initiator, PI): 2-hydroxy-2-methylpropiophenone (Figure 2.2, top). Upon exposure to UV-light, the PI will decompose into two radicals (molecules with a free unpaired electron, Figure 2.2, Initiation), which each can react with an acrylate moiety (reactive part of the PEGDA molecule). This reaction creates another radical, which can then in turn react with another acrylate moiety, which creates another radical etc. (Figure 4.10, Propagation). This radical polymerization is terminated when a radical reacts with another radical, with a dissolved oxygen molecule, or with a radical reaction inhibitor (4-methoxyphenol, MEHQ),

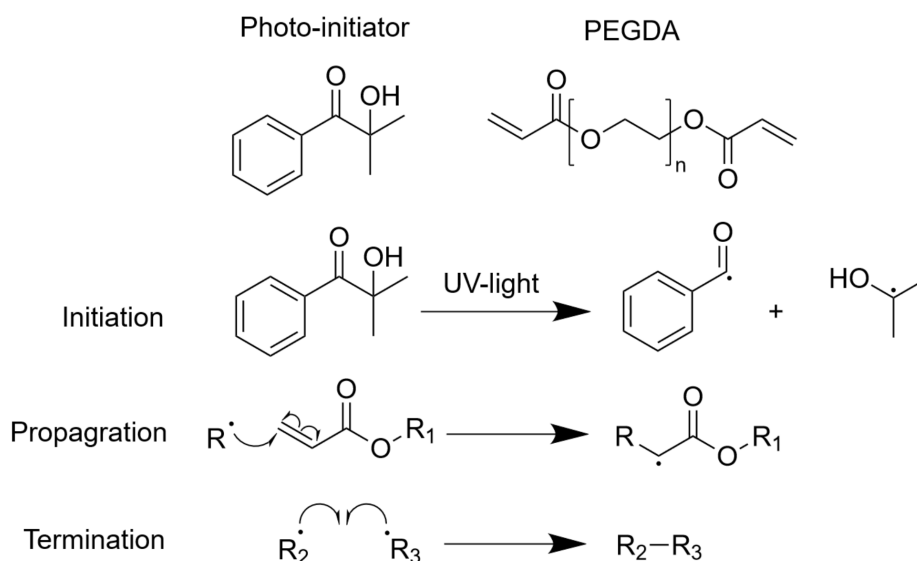


Figure 2.2: Schematic overview of the radical polymerization reaction. In this figure, the R (with potential subscript) indicates an arbitrary rest of the molecule which is not directly involved with the reaction.

of which a small amount (400-600 ppm) of is added to PEGDA during fabrication to prevent spontaneous polymerization during storage (Figure 2.2, Termination). PEGDA has two acrylate moieties, each of which can react with two radicals, resulting in a total of 4 possible connections between diacrylate molecules. Polymerization will therefore result in a highly cross-linked network.

Although the cross-linked particles are technically not hydrogels, as the interstitial liquid is not (mainly) composed of water. They are, however, porous networks with an interstitial liquid, just like hydrogels. Cross-linked polymers can have a wide variety of properties, from very hard (e.g., polystyrene), to very soft (e.g., PVA hydrogels). To give a more intuitive grasp on the nature of the particles, we will refer to the particles as hydrogels, even though the main component of the interstitial liquid is not water.

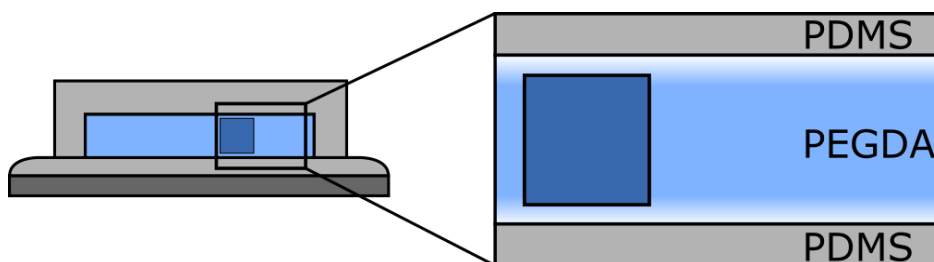


Figure 2.3: Schematic representation of the oxygen inhibition layer. The oxygen layer (white) is slightly doubled in size to make it stand out more.

### 2.1.A Spatial control

The combination of the two modes of termination (chain termination and inhibition) halt the reaction nearly instantly after the UV exposure is stopped. This allows us to tune the

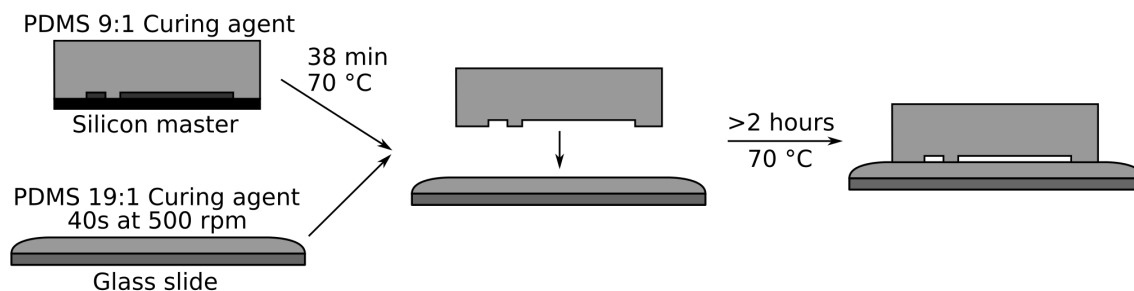


Figure 2.4: Schematic overview of the PDMS fabrication method.

reaction spatially by only exposing a small part of the channel to UV-light. This was achieved by placing a mask in the field-stop position, shaping the light beam according to the shape and size of the transparent part of the mask. Particles can be created with any shape and size by changing the shape and size of the transparent part of the mask. The only constraint is a constant profile along the direction of illumination, e.g. a circular mask will make cylinders, not spheres.

However, the hydrogel particles can also react with our microfluidic channel, which could cause the particles to stick to the channel, instead of moving freely. We have chosen to make our channels out of PDMS, which is quite porous to oxygen. Oxygen also inhibits radical reactions [8, 9]. Therefore, PDMS channels have an oxygen rich inhibition layer of  $\sim 5 \mu\text{m}$  next to the walls. The formed particle is therefore separated from the top and bottom walls, hence it can move freely (Figure 2.3) [1, 5].

## 2.2 Fabrication of PDMS microchannels

Typically, PDMS channels are sealed by activating the PDMS surface with oxygen plasma. Besides creating reactive hydroxyl (-OH) groups on the surface, the plasma treatment also vaporizes some methyl (-CH<sub>3</sub>) groups, leaving a thin, glass-like, layer behind. This glassy layer is much less porous to oxygen, causing the particles to stick to the surface [10, 11]. Therefore, the channels are fabricated as follows. First a SU-8 on silicon mold, called a master, is made using standard photo-lithographic techniques [12]. The protocol is described in detail by the manufacturer (Microchem, now Kayaku Advanced Materials, SU-8 2000 datasheet [13]). The master is then cast in a thick layer ( $\sim 5 \text{ mm}$ ) of degassed PDMS (Sylgard-184 and curing agent, mass ratio 9:1). Thick glass slides, which form the bottom of the channels, are spin-coated (40s at 500 rpm) with a thin layer ( $\sim 500 \mu\text{m}$ ) of PDMS (Sylgard-184 and curing agent, mass ratio 19:1). Note the different mass ratio for the spin-coated PDMS. It is very important that these ratios are respected, as they govern the rate of curing.

Both the glass slides and the PDMS cast master are then placed in an oven at 70 °C for 38-40 min. After 38 min, both the cast PDMS and the spin-coated PDMS are taken out of the oven. The cast PDMS should be fully cured, meaning that it is solid and does not stick to your gloves. The spin-coated PDMS should be semi-cured, i.e. it should be solid, but sticky enough to not detach from your gloves under its own weight. If it is not completely solid (i.e. it deforms plastically and leaves traces on your glove upon touching), the spin-coated PDMS is placed back in the oven for another minute, and checked again. If the spin-coated PDMS is fully-cured, i.e. it does not stick to your gloves anymore, new glass slides should be

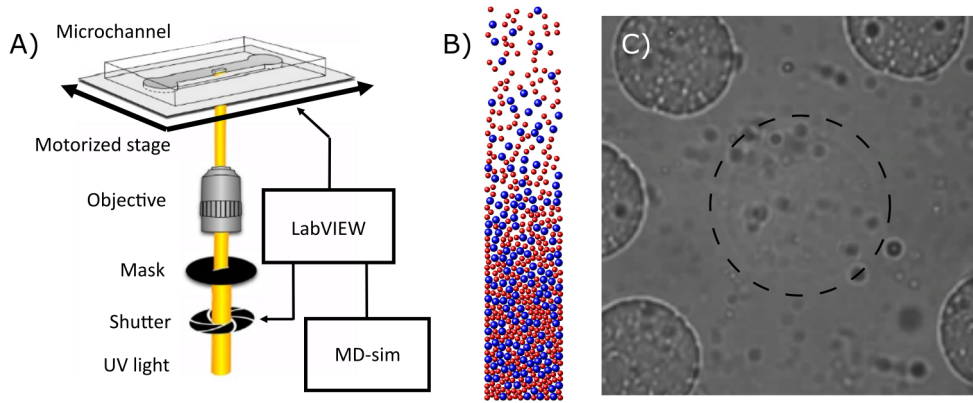


Figure 2.5: A) Schematic overview of the experimental setup to fabricate the PEGDA particles. Figure adapted from [7] B) The initial configuration was obtained by dropping a bidisperse mixture of particles in a box. Note: the number of particles in this example has been reduced by a factor 10 to increase the visibility of the particles. The big and small particles are colored blue and red, respectively. C) Snapshot during the particle fabrication process. The particle being fabricated is indicated with the dashed circle.

spin-coated and cured, as the channel seals will be prone to leakage at higher pressures ( $>10^4$  Pa).

Then, the cast PDMS is removed from the master, cut to size and holes for the inlet and outlet are punched. The microchannel is then assembled by placing the cast PDMS on top of the spin-coated PDMS, making sure not to trap any air bubbles. The assembled microchannel is then placed in the oven at  $70\text{ }^\circ\text{C}$  for at least two hours (usually overnight) for the two parts to fully bond. The entire PDMS fabrication process is schematically depicted in Figure 2.4.

### 2.2.1 Experimental setup

The particle fabrication and the subsequent experiments were performed on a Zeiss Axio Observer A1 inverted microscope placed on an optical breadboard (Newport SG breadboard) passively levelled by pneumatic vibration isolation feet (Newport CM-225). The microscope is equipped with a UV-light (Osram HBO 103W/2) filtered with a band-pass filter centered at  $\lambda = 365\text{ nm}$  and a bandwidth of  $10\text{ nm}$  (Chroma D365/10), which is reflected onto the channel by a reflector cube (Zeiss 424933). The filtered UV-light was modulated precisely by an electronic shutter (Uniblitz V25) with a mechanical response of  $10\text{ ms}$ , coupled to an external signal generator (Agilent A33220A). The channel was observed using a digital CMOS camera (Hamamatsu Orca-Fusion C14440), through either a Zeiss x10/0.2 Ultrafluar (great transparency to UV-light) during particle fabrication, or a Zeiss x2.5/0.12 Fluar (large field of view) during the following experiments. The channel is placed on a motorized stage (Märzhäuser Wetzlar Tango PCI-E), which can be controlled manually (by means of a joystick), as well as digitally using a LabView application we developed, based on the API provided by the manufacturer, hereafter named the Tango-application [14].



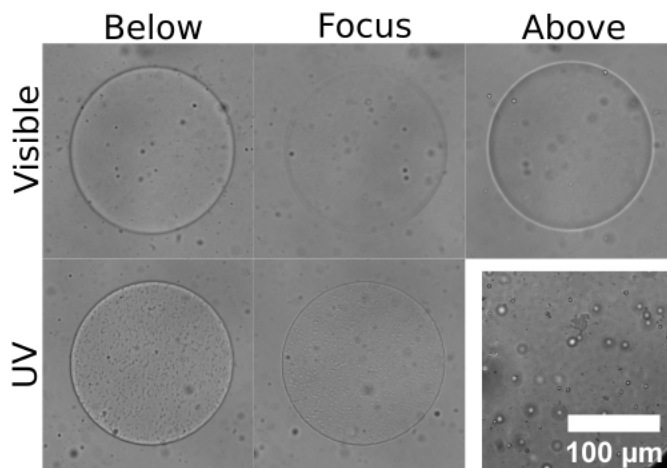


Figure 2.6: 5 Particles created with the exact same mask and photosensitive solution. They only differ in the place of the focal plane during the fabrication, and the place of the focal plane when the image was taken. The top row is fabricated when the visible light was in focus, whereas the bottom row was fabricated when the UV light was in focus. The columns indicate the place of the focal plane compared to the midplane of the channel when the image was taken. The images in the left column have been acquired when the focal plane was below the midplane, the images in the center when the focal plane was at the midplane, and the images in the right plane were taken when the focal plane was above the midplane. The image in the bottom right is the mask used. One can see 5-10  $\mu\text{m}$  sized white speckles embedded in the mask. These speckles give rise to the “texture” that can be seen in the particle when created with the UV-light in focus (bottom-left).

### 2.2.A Mask design

The masks were designed in Clewin or Adobe Illustrator. They were printed at FGN Éspace Numérique or Institute Pierre-Gilles de Gennes (IPGG). The masks consisted of a black circle with diameter 2.5 cm with the particle geometry as a transparent part in the center. Multiple masks were printed on a single sheet, and cut to size by hand.

### 2.2.B Optical focus

The focal point of a lens depends on the wavelength of the light that passes through it, so the focal point for the UV-light used to fabricate the particles is at a different distance than the focal point of visible light. This means that the channel will appear (slightly) out of focus when the UV-light is in focus. The focal point of the UV-light was determined by fabricating several test particles. The mask has microscopic speckles (Figure 2.6, bottom right), giving a slight “texture” to the surface of the particle when fabricated with the UV-light in focus (presence of speckles on the particles in the bottom row, and absence of them on the particles on the top row in Figure 2.6). Test particles were made with the focal plane in different positions until this “texture” was achieved.

### 2.2.C Controlling particle softness

The cross-linked particles have a Young’s modulus of approximately 10 MPa [1, 4, 5]. Although this is soft compared to silica particles ( $\sim 50$  GPa [15]) and polystyrene ( $\sim 3$  GPa [16]), it is very similar to that of PDMS ( $\sim 10$  MPa [17]). It is, however, possible to tune the softness of these

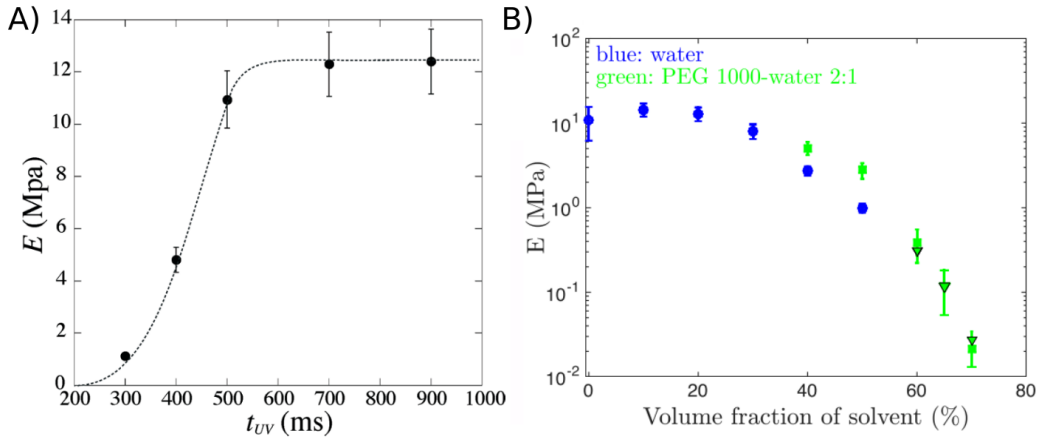


Figure 2.7: A) Young's modulus as function of the exposure time of the photosensitive solution. Measurement done by, and figure taken from Duprat et al. [4] B) Young's modulus as function of dilution with non cross-linkable solvent. Figure taken from Cappello et al. [5]

kinds of cross-linked networks, mainly by changing the average distance between the cross-links [18]. This can be achieved in three ways: 1) Reducing the exposure to UV-light. This will reduce the number of radicals produced, and therefore the number of cross-links formed (Figure 2.7A) [4]. 2) Adding mono-acrylates. Mono-acrylates will also react with PEGDA, but can only propagate the chain and not form cross-links between the chains, therefore spacing the cross-links. 3) Adding non-cross-linkable polymers, like polyethylene glycol (PEG). Since the radical reaction is terminated quickly, the radicals don't have much time to diffuse and find other radicals. Adding non-cross-linkable polymers will sterically hinder PEGDA finding other molecules to react with, and therefore limit the amount of crosslinking. This results in softer particles, which have been characterized by Cappello et al. [5] (Figure 2.7B)

We chose to dilute PEGDA with PEG to create softer particles, as adjusting the exposure is inconsistent for very soft particles, due to the mechanical response of 10 ms of the shutter. Using mono-acrylates to soften the particles would also be possible. However, commonly used short mono-acrylates (e.g. methyl acrylate) need to be handled in a fume hood, and could swell PDMS, and are thus not well suited for in-situ fabrication. PEG is an easy to handle viscous liquid that poses little to no health risks, with very similar properties to PEGDA. So, the photosensitive solutions used in this work were all composed of the following three component:

- the diacrylate: poly(ethylene glycol) diacrylate, with average molecular weight  $M_n = 575$  g/mol (PEGDA, Sigma Aldrich)
- the photo-initiator (PI): 2-hydroxy-2-methylpropiophenone, also known as Darocur 1173 (Sigma Aldrich)
- the solvent: polyethylene glycol, with average molecular weight  $M_n = 300$  (PEG, Sigma Aldrich)

In all photosensitive solutions, the amount of PI was kept constant at 10% v/v, to keep the inhibition layer at a constant thickness [19], which in our case is  $5.5 \pm 1.6 \mu\text{m}$  as determined by Cappello et al. [5]. The ratio between PEGDA and PEG was changed to achieve particles of different softness. The dilution dependent softness was determined previously by Cappello

et al. [5]. They showed that Young's moduli between  $\sim 12$  MPa (90% v/v PEGDA, 10% PI) and  $\sim 100$  kPa (30% v/v PEGDA, 60% PEG, 10% PI) can be achieved. They used a slightly different solvent, so we used the same microfluidic 3-point bending test to verify that these results are unchanged for our system. All particles were exposed for 600 ms, Duprat et al. [4] determined that longer exposure did not affect the Young's modulus (Figure 2.7A).

## 2.2.2 Multi-particle systems

### 2.2.A Continuous flow

To use this system as a model system for soft granular particles, we need to fabricate many particles, hundreds if not thousands and potentially with different sizes, for each experiment. Dendukuri et al. [1] produced many particles using continuous flow lithography. They had a continuous flow of the PEGDA/PI mixture, which they periodically exposed to UV-light. The created particle was then transported away by the flow of uncured PEGDA. For continuous flow, the ratio of the time spent in exposure over the time spent waiting for the particle to move out of the focal spot is roughly equal to the acceptable elongation of the particles due to them moving during the exposure. We found that in our case, for an exposure time of 600 ms as indicated by the onset of the plateau of the Young's modulus in Figure 2.7, it would take  $\sim 20$  minutes to fabricate 100 particles, assuming an acceptable elongation of 5%. This would be highly unpractical.

### 2.2.B Stop-flow

A faster method is so-called stop-flow lithography. Here, the flow is stopped just before the UV-exposure, and started again after the exposure. It turns out, however, that this method has its own drawbacks. For a flow-rate controlled setup, the fabrication rate is governed by the time needed for the flow to start and stop. Whereas for a pressure-driven setup, it is nearly impossible to get to a zero-flow state, due to gravity induced pressure difference between the reservoir and the waste container. Furthermore, the hydraulic resistance of the channel (and thus the fluid velocity at a given pressure) changes with the number of particles fabricated, making the system unreliable.

### 2.2.C No flow

Besides the speed and potential unreliability, the stop-flow lithography also doesn't allow for fabrication of a pre-mixed ensemble of particles, as only one particle type can be made at a time. We solved this by moving the channel, rather than the particles. First, the inlet and outlet were temporarily closed, to enforce a no-flow condition. Then the illuminated spot was moved to pre-determined locations in the channel. The microscope stage is able to move from one spot to the next in 100-500 ms, depending on the total amount of distance travelled. This makes it possible to fabricate a particle every 1.5-2 s, with an exposure time of 600 ms. To make multi-disperse suspensions, first, all particles of one type are fabricated. Then, the mask is changed, followed by the fabrication of the next type of particles. This is repeated for all types. This method assumes that particles don't drift over time, making the zero-flow state vital. The fabrication of  $\sim 2000$  particles takes approximately an hour. We found that the optimal spacing of the particles was  $\sim 20 \mu\text{m}$ , spacing them further will significantly reduce the number of particles that can be fabricated in the channel, whereas spacing them less would significantly increase the chance of fabricating overlapping particles.

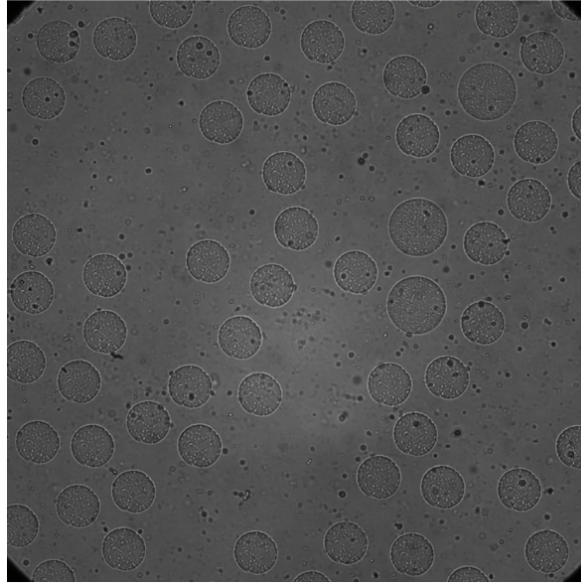


Figure 2.8: Snapshot taken during the fabrication of a bidisperse packing

Therefore, the drift of the particles should be less than  $10 \mu m$  per hour, or  $3 \text{ nm}$  per second! Even the smallest (temporary) pressure differences between the inlet and outlet could cause a drift of this magnitude, e.g. vibrations due to a metro passing under the building, inertia of the fluid inside the tubing, slight pressure difference due to the slide not being perfectly horizontal. This stresses the importance of placing the microscope on a vibration isolated platform, and closing of the inlet and outlet, making flow in the channel impossible. Figure 2.8 is a snapshot taken during the fabrication, all small particles are made 20–30 minutes before this picture was taken, and the fabrication of the large particles is in process. One can clearly see that all the particles are still well separated, even after 20–30 minutes. The visible gaps will be filled with big particles in the future.

#### 2.2.D Obtaining initial conditions

For multi-disperse systems, it is essential that initial configuration of the particles is randomized. If one were to first create all particles of one type, flow them towards the outlet, and then make a second type of particles. This would lead to two crystallized, mono-disperse phases. The athermal nature of granular materials causes the system to be trapped in this phase-separated state (as observed in e.g. [20, 21]), and the laminar nature of microfluidic flows makes mixing by flow nearly impossible.

There are several algorithms to obtain a well equilibrated initial condition, notably quenching and compressing a thermal glass until jamming, and swelling a thermal glass until jamming (Lubashevski-Stillinger algorithm [22], Monte-Carlo swapping algorithm [23]). However, both have as a constrained a fixed number of particles, and a flexible particle- or system size. Whereas in experiments, the number of particles can be adjusted, but the particle- and system size are fixed. Therefore, the initial conditions were obtained differently, by using a simple numerical simulation.

In LAMMPS [24], a molecular dynamics simulation code, a box identical in size to the experimental channel was simulated where athermal particles were dropped into the box under

gravity. The ratio between the small and large particles was taken to be  $\sim 1.4$ , to prevent crystallization, where both particles types contributed equally to the volume occupied by the particles. The simulated particles were quite soft (40 kPa), to be able to increase the timestep used in the simulation, as the timestep is governed by Nyquist-Shannon sampling theorem, where the frequency to be sampled must be higher than the harmonic frequency of a spring with spring constant equal to the particle softness [25]. To prevent interparticle overlap, the sample is relaxed by reducing gravity during the last phase of the simulation [26].

As we have seen before, the particles should be spaced apart to allow for a small amount of drift. The particles only interact sterically during the simulations, resulting in a packing where most neighboring particles are touching. Therefore, the radius of simulated particles was  $10 \mu\text{m}$  bigger than the particle to be fabricated, resulting in the required minimum spacing of  $20 \mu\text{m}$ .

Lastly, the output of the simulation was parsed, and the particle positions were separated by size. For each size, the particle order was optimized to reduce the total distance the stage needed to travel, using a simple heuristic algorithm. Starting from the bottom-left particle, the next particle was chosen to be the closest particle to the previous, excluding all already chosen particles.

For monodisperse systems, a much simpler approach was taken, and the particles were placed in a hexagonal lattice. The list of particles was linearized in a zigzag pattern, starting the first column of particles in the bottom left corner printing the column bottom to the top, then the next column top to bottom, the next column bottom to top etc.

### 2.2.E System alignment

To make the particle ensembles, it is paramount that the microchannel, camera, and stage are perfectly aligned. This was achieved by first aligning the camera and the stage by placing an object known to be aligned with the stage in the field of view, in our case the inner edge of the microscope stage, and physically rotating the camera until the edge was perfectly horizontal/vertical on the image. This ensures that the xy-coordinates of pixels of the camera are aligned with the xy-coordinates of the microscope stage. Next, the channel and the stage were aligned. The origin of the microscope stage coordinate system was placed at a reference point, typically the bottom left corner of the microchannel. The position of the reference point in the field of view of the camera was marked. The stage was then moved 20 mm to the left, and the channel manually adjusted until the marked point stayed within the inter-particle spacing,  $\sim 20 \mu\text{m}$ , of the bottom edge throughout the 20 mm travel. This ensures a maximum misalignment of  $20 \mu\text{m}$  over 20 mm, well within the margin of error of the fabrication procedure. The alignment between the channel and the stage was checked before every experiment.

### 2.2.F Mask offset

The circular masks used to control the particle shape and size were manually inserted into an analyzer slider and placed in the field stop position of the microscope. Since the masks were hand-cut, the transparent design will not be perfectly centered in the field of view. While this does not pose a problem when fabricating particles using a single mask, as all the particles will be offset by the same amount, it is problematic when fabricating particles using different masks, as the offset is not the same for all masks. The offset was determined by first zeroing the stage on an arbitrary location near the outlet of the channel and printing a single particle.

The stage was then moved until the fabricated particle was in the center of the field of view. The negative displacement of the stage as read out from the Tango application was taken as the offset. This was repeated every time the mask was changed.

### 2.2.G Fabrication

To fabricate (multidisperse) particle ensembles, first all the tubing was disconnected from the channel, and the inlet and outlet were sealed with metal plugs to limit potential sources of drift in the channel. One needs to take great care to not introduce any air bubbles into the channel while sealing the channel, as these are impossible to remove after the particle fabrication, rendering the channel inoperable. The microscope was also placed on a passively isolated optical table, to keep the microscope level, and isolate it from vibrations. Next, the sorted list of locations of one particle size was loaded into the Tango-application, and the corresponding mask was inserted into the field stop position. Then the offset for that mask was determined and applied, as described above. The stage was then zeroed on the bottom-left corner of the channel and all the particles of that type were fabricated. The Tango-application was programmed to incorporate a 700 ms buffer between the fabrication of two particles, to allow for the shutter to properly close, the stage to move to the new location, and the shutter to properly open again.

This process, besides the disconnecting of the tubing, was repeated for each particle type. Once all the particles were fabricated, the tubing was reconnected, again making sure to not introduce air bubbles into the channel.

## 2.3 Flow control

Since the fabricated particles are non-Brownian ( $D \gg 1 \mu\text{m}$ ), and naturally very close to density matched, as they are made of the same material as the suspending fluid, the particles are stationary unless externally perturbed. The external perturbation was achieved by imposing a flow of the suspending fluid, which transports the particles from the inlet towards the outlet by means of hydrodynamic drag. The Reynolds number,  $Re$ , is a dimensionless number comparing the inertial forces and viscous forces in a fluid flow. Considering a Newtonian fluid with density  $\rho$ , flow velocity  $u$ , characteristic length scale  $l$  and viscosity  $\mu$ , we can define the fluid Reynolds number as

$$Re = \frac{\textit{inertial forces}}{\textit{viscous forces}} = \frac{\rho ul}{\eta} \quad (2.1)$$

Taking typical values for our experiments,  $u = 10^{-5} - 10^{-4} \text{ m/s}$ ,  $\rho \approx 1000 \text{ kg/m}^{-3}$ ,  $\eta = 50 \text{ mPa} \cdot \text{s}$  and  $l = 0.1 \text{ mm}$ , we obtain  $Re \approx 10^{-5} - 10^{-4}$ , indicating that only viscous forces need to be considered.

Throughout this thesis, we will work with Hele-Shaw channels, which are channels whose length is larger than their width, and their width much larger than their height ( $L > W \gg H$ ). Flows in Hele-Shaw channels are well characterized. The velocity profile in the  $z$ -direction is parabolic (Poiseuille flow), and the flow velocity is independent of the  $x$  and  $y$  position, except very close to the side wall (plug flow, Figure 2.9A) [27]. The force on a particle in the channel consists of two parts, a force due to the decrease in pressure inside the channel over the length of the particle, and a hydrodynamic drag between fluid and the particle, the magnitude and direction of which depends on the relative velocity of the fluid and the particle (Figure 2.9B) [28]. For a single particle, this means that the hydrodynamic drag of the fluid

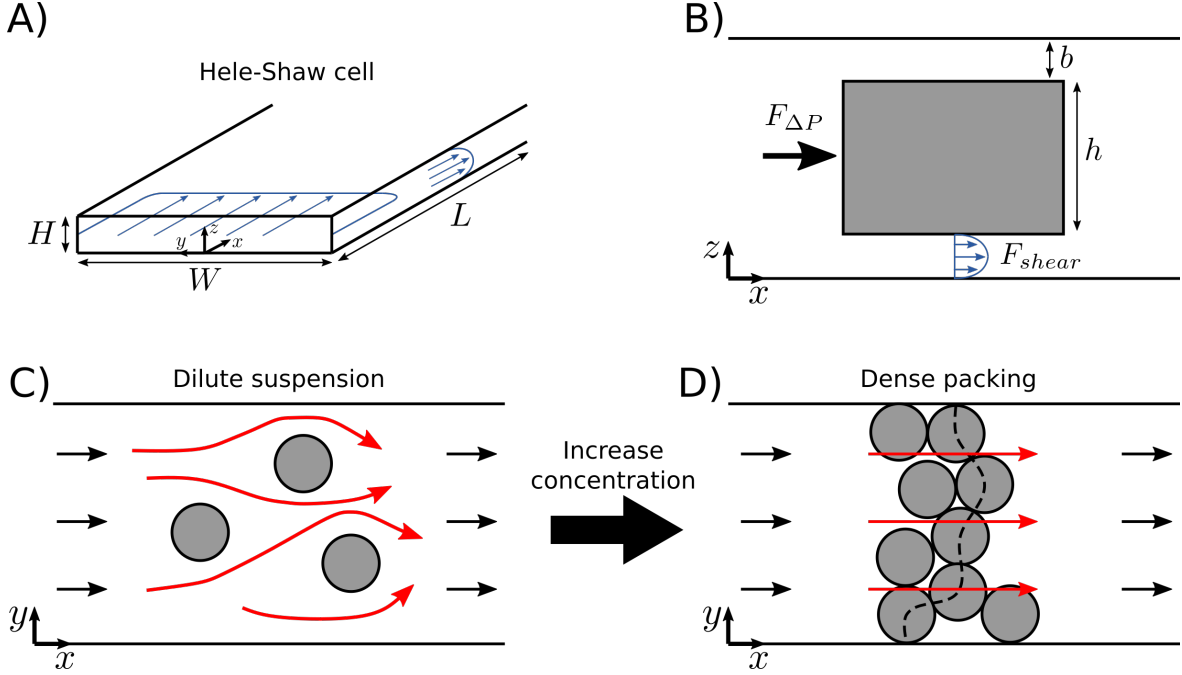


Figure 2.9: A) Schematic representation of fluid flow in a Hele-Shaw cell. B) Schematic representation of the side-view of the microchannel. The force on a particle transported in a microfluidic channel can be decomposed into two forces, a compressive force,  $F_{\Delta P}$ , due to a pressure gradient across the particle, and a shear force,  $F_{shear}$ , due to the hydrodynamic drag with the carrier fluid. C) Schematic representation of the flow around particles in a dilute suspension (top view). Before and after the particles, the fluid flow is homogeneous, whereas the fluid flow in the region with particles is complex. D) Schematic representation of the fluid flow in a channel with a jammed suspension (top view). The presence of percolating chains of particles (spanning from one side wall to the other, indicated with the dashed line), fluid flow between the particles is negligible. Instead, the fluid passes over the particles

with the side wall of the particle pushes the particle forward, and the interaction with the fluid above and below the particle will slow the particle down.

These interactions are well described for well separated particles in a flow, i.e. the perturbation of the flow field by a particle doesn't influence the flow field of around other particles [5, 28] (Figure 2.9C). This is, of course, not the case for a dense suspension, where most neighboring particles are touching. However, in 2D, a packing of cylinders is percolating, meaning that there are chains of particles spanning from one side of the channel to the other side (dashed line in Figure 2.9D). Since the particles are squeezed together, the flow between the particles is negligible. We can therefore consider the ensemble of particles as a single particle, and approximate the flow over/under the packing by the lubrication approximation. In the lubrication approximation, we know that pressure force can be approximated by  $F_{\Delta P} \approx wh\Delta P_p$ , with  $\Delta P_p$  the difference in pressure across the packing,  $w$  the width of the particle, and  $h$  the height of the particle [7, 28]. The shear force can be approximated by  $F_{shear} \approx bw\Delta P_p$ , with  $b$  the gap between the particle and the top/bottom of the channel, assuming Poiseuille flow in the gap. Assume that the difference in pressure across the packing is approximately equal to the pressure across the channel,  $\Delta P_p \approx \Delta P$  [7, 27]. We then obtain

$$F_{\Delta P} \approx Wh\Delta P \text{ and } F_{shear} \approx Wb\Delta P \quad (2.2)$$

This means that the relative importance of the confining force over the distributed shear force

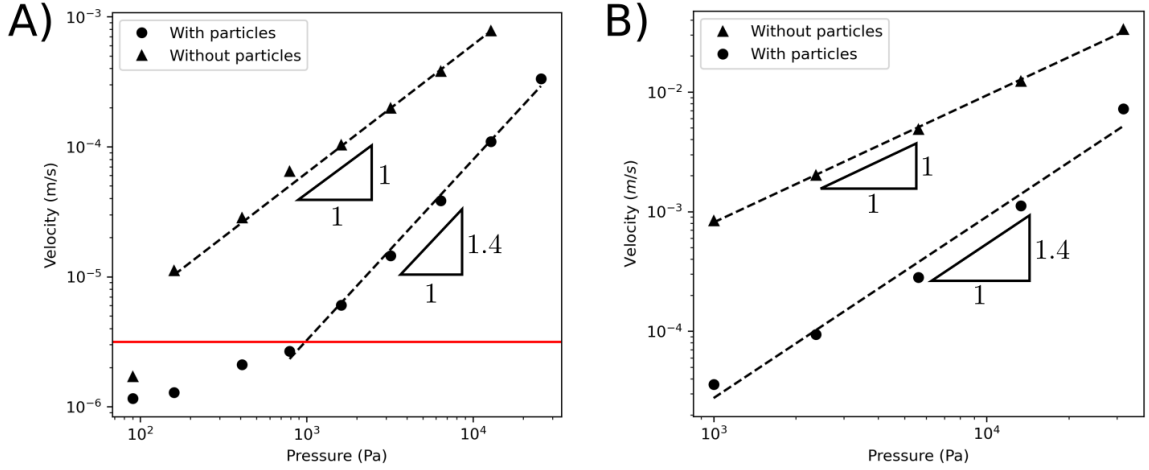


Figure 2.10: A) Fluid velocity, as measured by PIV, as function of the applied pressure drop over the channel for an empty channel and a channel filled with particles. The red line indicates the limit of detection of the PIV measurement. B) Calculated fluid velocity in a microfluidic channel according to eq. 2.4 for an empty channel of the same dimensions as the channel used for the PIV experiments in A, and a channel filled with particles.

is  $\frac{F_{\Delta P}}{F_{shear}} = \frac{h}{b}$ . In our case,  $h \approx 90$  and  $b \approx 5$ ,  $\frac{F_{\Delta P}}{F_{shear}} \approx 18$

Since PDMS is relatively soft and our channel is very wide compared to its height (Hele-Shaw cell), it is possible that the PDMS deforms due to the applied pressure. The height of the channel under pressure is given by [29]:

$$H(\Delta P) = \frac{2W\Delta P}{3E} + H_0 \quad (2.3)$$

with  $E$  the Young's modulus of PDMS. In our case  $W = 5 \text{ mm}$ ,  $E = 10 \text{ MPa}$  and  $H = 0.1 \text{ mm}$ . The maximum pressure applied is  $\sim 2 * 10^4 \text{ Pa}$ . Filling in these values gives  $H(2 * 10^4) = 1.06H_0$ , an increase of 6 % in channel height, in the worst-case scenario. In this case,  $\frac{F_{\Delta P}}{F_{shear}} \approx 11$ . Hence, between 5 and 10 % of the total applied pressure will be distributed over the packing as a gradient.

We have measured the deformation effect on the fluid velocity using Particle Image Velocimetry (PIV, more details on PIV in section 2.5). For an empty channel,  $u \propto \Delta P$ , as expected (Figure 2.10A). For a channel filled with particles, we found that  $u \propto \Delta P^{1.4}$ . This was quite surprising, as at such low  $Re$  ( $10^{-5}$ - $10^{-4}$ ), pressure and velocity are always expected to scale linearly. However, since the  $u \propto H^2$  [29], channel deformation could cause the deviation from linear scaling.

Gervais et al. [29] derived an analytical description of the volumetric flow rate ( $Q$ ) as function of the applied pressure:

$$Q = \frac{H_0^4 E}{48\alpha\mu L} \left[ \left( 1 + \alpha \frac{\Delta P W}{E H_0} \right)^4 - 1 \right] \quad (2.4)$$

with  $\alpha$  a material dependent fit parameter of order unity. At low pressures ( $\frac{\Delta P W}{E H_0} < 1$ ), this equation simplifies to  $Q \propto \Delta P$ . At high pressures, we obtain  $Q \propto \Delta P^4$ . Figure 2.10B shows the fluid velocity as obtained by substituting  $H_0 = 100 \text{ }\mu\text{m}$  for the channel without particles,



and  $H_0 = 10 \mu\text{m}$  for the channel with particles, and  $\alpha = 1$ ,  $E = 10 \text{ MPa}$ ,  $W = 5 \text{ mm}$  and  $L = 5 \text{ mm}$  for both channels. We find that the deformation of the empty channel is negligible, and thus recover the linear scaling  $u \propto \Delta P$ . The channel with particles, however, appears to be between the  $Q \propto \Delta P$  and  $Q \propto \Delta P^4$  regime. We made a linear approximation under the conditions used during the experiments, and we found the same  $u \propto \Delta P^{1.4}$  scaling as observed in the experiments, suggesting that our hypothesis of channel deformation was correct.

While we did observe the correct scaling, the correct magnitude was not obtained. This can be attributed to us underestimating  $\alpha$  (which we assumed to equal 1), and our assumption that the tubing and fittings don't contribute to the hydraulic resistance of the channel.

As the fluid flow is the driving force, controlling the flow is crucial. Flow rate driven systems, like with a syringe pump, allow for the direct control over the flow velocity, which is constant regardless of the number and location of the particles in the channel. However, a syringe pump tends to have a slow (10–25 seconds) build-up to a steady flow, making it unsuitable for experiments with changing flow velocities. Furthermore, the assumption that the flow velocity is constant over time does not hold at low flow velocities. A typical syringe pump pushes the fluid in small steps of constant volume (this is intrinsic to the mechanism behind the syringe pump). When enough steps occur each second (high flow rates), the flow velocity can be considered constant. At low flow rates, however, this can lead to pulsating flow, and therefore experimental artifacts [30].

An advantage of a pressure driven system is that it gives us an indication of the pressure in our system, which can only be estimated for a flow rate driven system. Furthermore, pressure controllers have a much faster ( $\sim 1$  second) response, making dynamical experiments possible. The drawback is that the fluid velocity, at constant pressure, depends on the hydraulic resistance of the channel, which depends on the number and location of the particles in the channel. Also, at zero *applied* pressure, there can still be flow due to a difference in gravitational potential between the inlet and outlet. Therefore, the input reservoir is placed lower than the output reservoir, such that a small pressure needs to be applied, in our case consistently 3 kPa, for the flow to cease. In all but a few experiments, the pressure controller is used. Only in experiments where we compare flow rate driven versus pressure driven experiments, a syringe pump is used. The fluid flow was mostly controlled using a pressure controller (Fluigent LineUp-series, 2000 mbar and 345 mbar maximum pressure), which was controlled either manually, or automatically using a LabView application we developed, based on the API provided by the manufacturer, hereafter named the Fluigent-application [31]. Besides the pressure controller, some experiments were performed using a syringe pump (Nemesys, Cetoni), with a 500  $\mu\text{L}$  gas-tight syringe with Luer Lock (Hamilton 1750 TLL).

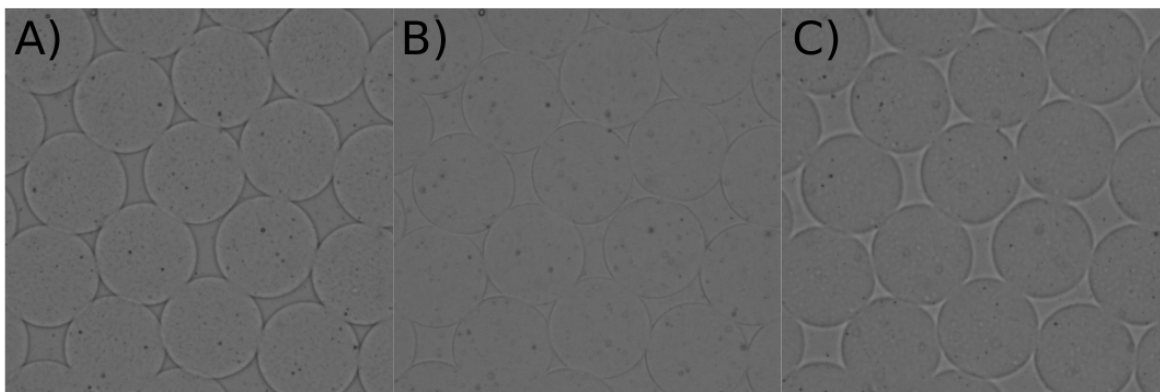


Figure 2.11: Exact same ensemble of particle observed with the focal plane in three different positions: A) below the midplane of the channel, B) at the midplane of the channel, and C) above the midplane of the channel.

## 2.4 Image acquisition and analysis

### 2.4.1 Imaging particles

The fabricated particles are made of cross-linked PEGDA suspended in liquid PEGDA. It is therefore not surprising that the refractive indexes are very close, making it nearly impossible to visualize the particles (Figure 2.11B). We, however, played a slight optical trick. Placing the focal plane slightly below the particles, the interface between the particle and uncured solution orthogonal to the observation plane will slightly bend the light causing a dark ring around the particle and a bright ring inside the particle, which we are able to observe (Figure 2.11A). Although placing the focal plane above the midplane works well to observe single particles (e.g. Figure 2.6, top right), placing the focal plane above the particles doesn't work well for ensembles, as the particles appear distorted when close to each other (Figure 2.11C).

The image acquisition was done with a digital CMOS camera (Hamamatsu Orca-Fusion C14440), which has a resolution of  $2304 \times 2304$  pixels, through a Zeiss x2.5/0.12 Fluar objective. The shutter time was put at 20 ms to reduce motion blur.

### 2.4.2 Feature finding

The particle locations are extracted from the images. Figure 2.12A shows a typical image taken during an experiment. One can observe that the illumination is not perfectly homogeneous, as the corners appear slightly darker. This is corrected by dividing the image with a version of itself to which a wide Gaussian filter ( $\sigma = 50$  pixels) was applied. The image was then inverted, such that the dark regions appears bright and vice versa. This highlights the dark rings around the particles, which were the easiest and most consistent to detect. Next, all pixel values below a threshold value, which changed from experiment to experiment, were set to zero. Then, all non-zero values were normalized, such that the minimum value after the threshold was set to zero, and the maximum value was set to 1. The result after these image processing steps is an image that has a homogeneous illumination, its background removed and the features to be tracked normalized. An example is shown in Figure 2.12B.

Now the image pretreatment is done, the particle locations were found with a convolutional algorithm. A convolution is a method to generate an image from two images, an image that

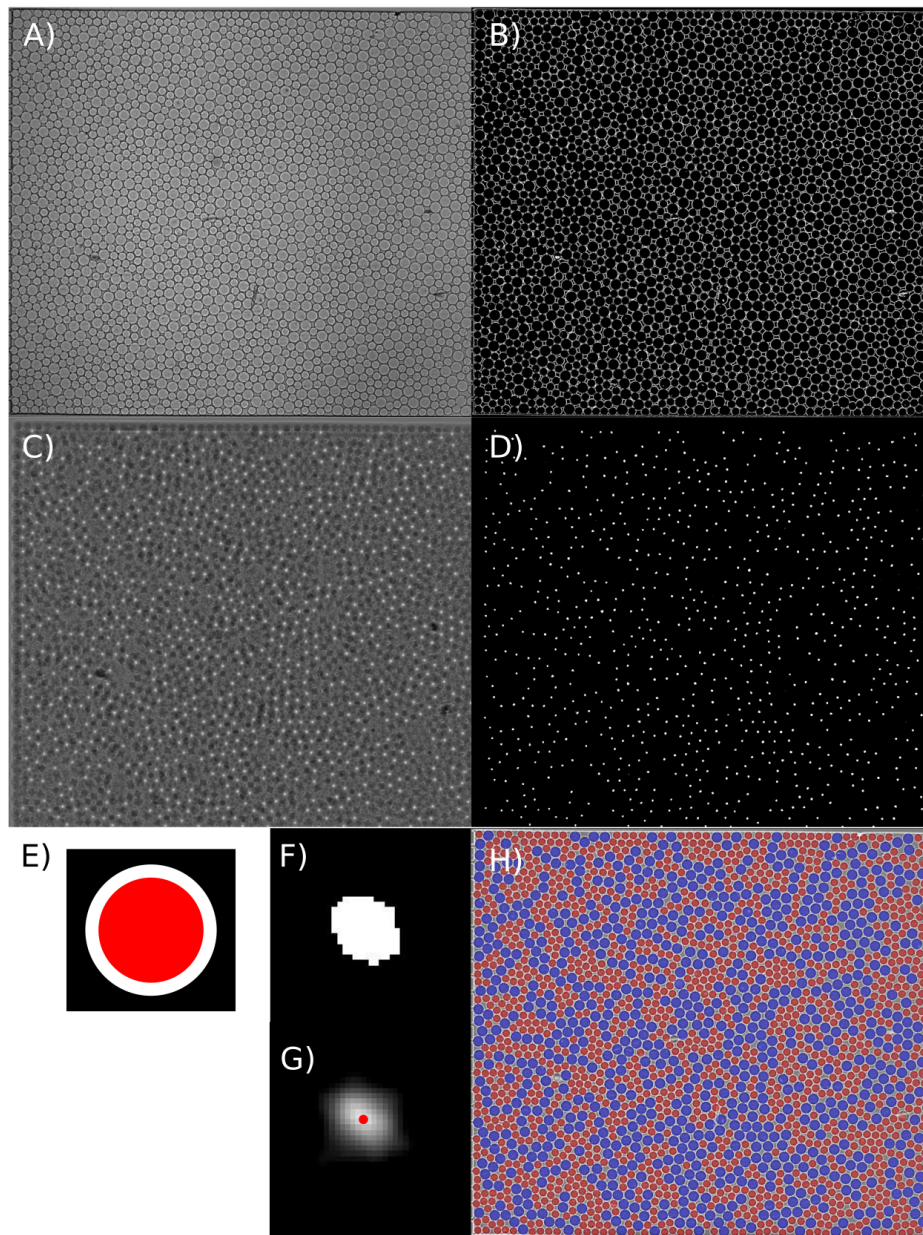


Figure 2.12: A) Typical image taken during an experiment. B) Image after gradient removal, inversion and background subtraction. C) Image after convolution. D) Convolved image after binarization E) Mask used for convolution, the black region is set to 0, the white region is set to 1, and the red region is set to -1. F) Zoom of one of the spots in D. G) Spot in F, where the pixel intensities are kept. H) Original image with all the found small and large particles indicated in red and blue, respectively.

contains features to be detected, and a template of such feature (called a mask). A schematic representation of the mask is shown in Figure 2.12E. The mask has the same size as the image, and has the feature to be detected centered around the origin.

The convoluted image is then built as follows. The value of pixel  $[x, y]$  becomes the sum of all pixel values after the element-wise multiplication of the image,  $I$  with the mask  $M$ , where the pixel values of  $M$  have been shifted by  $[x, y]$ , such that the feature is now centered

around  $[x, y]$ :

$$C(x, y) = \sum_i \sum_j I(i, j) \odot M(i + x, j + y) \quad (2.5)$$

In reality, performing a convolution as a double sum is unpractical, as the compute time scales with  $\mathcal{O}(N^2)$ , where  $N$  is the number of pixels in the image. In our case, each convolution would take  $\sim 75$  hours. Fortunately, a convolution is just an element-wise multiplication in Fourier-space  $C = \mathcal{F}^{-1}(\mathcal{F}(I) \odot \mathcal{F}(M))$ , for which the compute time scales with  $\mathcal{O}(N \log(N))$ . This results in a computation time of  $\sim 2$  seconds for each convolution.

Most pixels in the mask are set to zero, meaning that they don't contribute to the convolution. Since the feature we want to detect is a bright annulus, the mask contains an annulus of pixels that are set to 1. The pixel values in  $I$  corresponding to the pixels in the annulus are summed. Brighter pixels overlapping with the mask results in a higher convoluted value, and thus a higher chance that a particle is located there. Since we know there shouldn't be bright pixels in the center of the particle, we set the pixel values inside the annulus to -1. This means that finding bright pixels in the center of the annulus will reduce the likeliness that there is a particle centered at that location. This basically eliminates the chance of detecting a small particle as a large particle, and heavily reduces the chance of detecting a large particle as a small particle.

Figure 2.12C shows the convoluted image obtained after convoluting B) with E). At a first glance, this seems to have made things worse, as there is a noisy background with some bright peaks. However, the peaks and the background are well separated in intensity, as can be seen in Figure 2.12D, which is just a simple binarization of Figure 2.12C. All peaks are well separated in space, figure 2.12F shows an example peak. These peaks can be easily detected with commonly available Connected Component Labelling algorithms (e.g. as implemented in the function "label" of the Python library skimage) [32]. Determining the center of mass of the peaks typically results in an accuracy of 0.5-1 pixel accuracy, as the location is sensitive to the user-input in the form of a threshold value used for the binarization. However, we know that a higher value after convolution indicates a higher probability the particle is centered around that pixel. We can, therefore, use the pixel values after convolution as weights to determine the center of mass. Since pixels further away from the center of mass have lower value in the convoluted image, they contribute less to the location of the center of mass. This makes the analysis less dependent on user input, and thus increases accuracy. The typical accuracy of such convolutional particle finding algorithm is  $\sim 0.1$  px [33]. This process is repeated for each particle type. The algorithm takes about  $\sim 15$  seconds per image (for a  $\sim 4$  megapixel image containing  $\sim 2000$  particles of two different sizes), but is fully parallelized, and can be found on GitHub [34].

### 2.4.3 Feature linking

The found particles are linked into tracks using the free and open-source python package Trackpy [35]. Since the particles move less than one particle radius between frames, the simple nearest-neighbor algorithm was used, which is based on the Crocker-Grier algorithm [36]. During image analysis, it is likely that a few spurious particles will be found, or sporadically a real particle is missed. To combat this as best as possible, tracks shorter than 95% of the expected length, as well as tracks where a particle was missing for 5 or more consecutive images were removed, and the locations of missing particles (less than 5 consecutive frames, and not more than 5 % unidentified particles in an entire track) were linearly interpolated

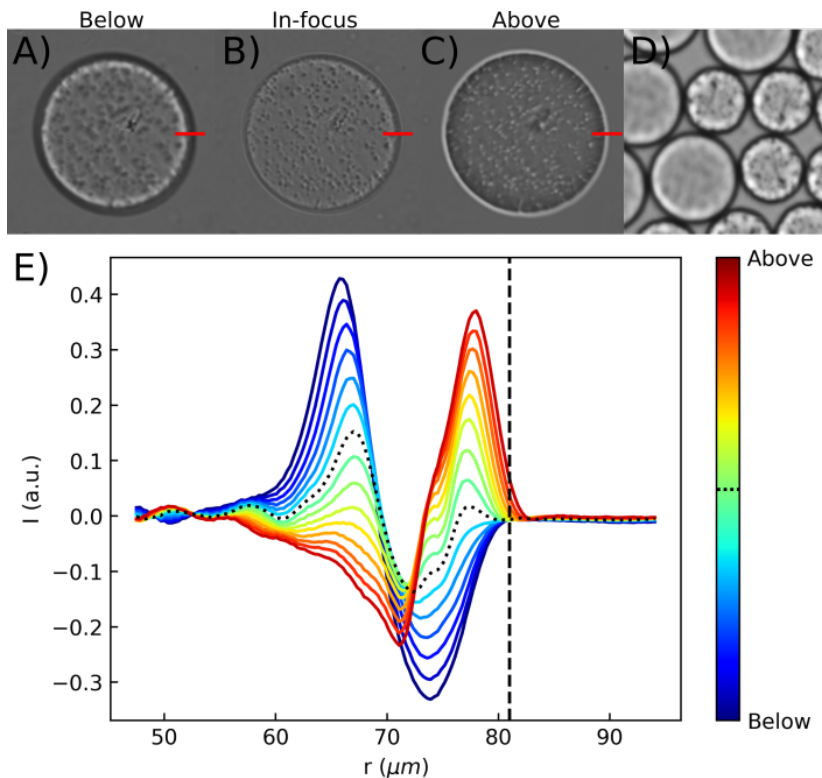


Figure 2.13: A-C) Snapshots of the same particle, taken with the focal plane at different positions (below, at the mid-plane, and above the particle). D) Crop of a particle packing under very light compression. E) Radially averaged intensity profile (normalized by the background intensity) of the same particle, taken with the focal plane in different positions (indicated by the line color). The mid-plane (position where the particle is in focus) is highlighted with the dotted line. The part of the intensity profile shown is indicated by the red line in A-C.

from the positions before and after the small gap. After this process,  $>95\%$  of the particles are found. This algorithm can also be found on GitHub [34].

#### 2.4.4 Particle radius

While defining the center of the particle could be done very accurately ( $\sim 0.1$  px), defining its radius proved to be much more tricky. In Figure 2.13E, the radially averaged intensity profile of the particle normalized by the background intensity is shown for different focal points, where a negative intensity  $I(r)$  indicates pixels at a distance  $r$  from the center are darker than the background, and a positive intensity means pixels  $r$  away from the center of the particle are brighter than the background. Since the fringes around the particle are due to the scattering interface between the particle and the suspending fluid, we can expect that the fringes shift upon changing the focal point of the objective (Figure 2.13A-C, E). Indeed, we observed that when the focal point is below the midplane of the particle, the intensity profile resembles a wavelet where there is a dark ring outside the particle and a light ring inside the particle. Whereas the rings are inverted, when the focal point is above the midplane. At a first glance, it is not directly evident how the radius should be defined, as all peaks and the pass through zero depend on the focal point. Looking at a packing under very small confining pressure, as

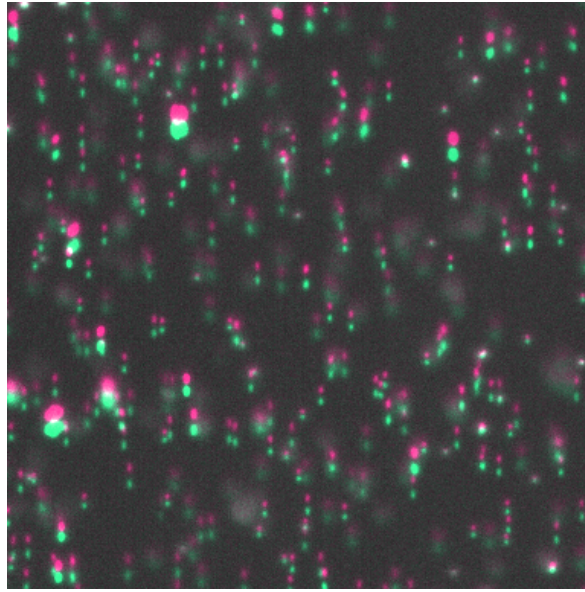


Figure 2.14: Overlay of two images of the same sub-region, taken 20 ms apart. The tracers in the first image are indicated in red, and the tracers in the second region are in green.

to push the particles together but not deform them significantly, it becomes apparent that the physical radius of the particles is at the edge of the dark ring when the focal point is below the midplane. This point does not seem to be affected much by the focal point, as long as the focal point is below the mid-point. We therefore defined the radius of these particles as  $81 \mu\text{m}$ , as indicated by the dashed vertical line. This process was repeated for differently sized particles.

## 2.5 PIV

Since the forces exerted on the particles depends on the velocity of the carrier fluid. It is important to measure the velocity of the fluid. This is typically done with Particle Image Velocimetry (PIV). The fluid flow was visualized by incorporating a small amount of fluorescent tracers, 1 droplet  $\sim 50 \mu\text{L}$ , of Thermo Fisher Scientific Fluoro-Max red fluorescent polystyrene beads in aqueous solution,  $1.1 \mu\text{m}$  1 % concentration, in 2 mL of the photo-sensitive mixture. Tracking each particle in space and time can be quite slow. Therefore, PIV doesn't rely on tracking the particles themselves. Instead, it assumes that the particles in a small sub-region of the image don't move relative to each other. One can then use that sub-region as a mask for a convolution, and apply it to the image taken a fraction of a second later (Figure 2.14). The convolution will then yield a sub-pixel ( $\sim 0.1 \text{ px}$ , like the convolutional particle detection) displacement of that sub-region. Given the conversion factor between pixels and micrometers and the time between the two images, allows you to calculate the velocity of the fluid in that sub-region. This can then be done for different sub-regions in the image, to obtain a flow field for the entire image. We divide the image into an  $8 \times 8$  grid of sub-regions, for each of which a flow velocity is calculated. For each data point, 10 images are taken in 10 ms intervals. Since we expect a homogeneous flow field along the length and width of the channel, the values of each of the sub-regions, in each of the 9 pairs of images, is averaged to provide a single value for the flow velocity at that moment in time. The values in each sub-region fluctuate, because

the images not taken with a confocal microscope. This means that the observed particles are in different planes along the height of the channel, which have a different flow velocity, since Poiseuille velocity profile is in this direction. These fluctuations are averaged out over all the sub-regions and multiple image pairs.

## 2.6 References

- [1] Dhananjay Dendukuri, Daniel C. Pregibon, Jesse Collins, T. Alan Hatton, and Patrick S. Doyle. Continuous-flow lithography for high-throughput microparticle synthesis. *Nature Materials*, 5(5):365–369, 5 2006. 13, 14, 16, 18, 20
- [2] Dhananjay Dendukuri, Kim Tsoi, T. Alan Hatton, and Patrick S. Doyle. Controlled synthesis of nonspherical microparticles using microfluidics. *Langmuir*, 21(6):2113–2116, 3 2005.
- [3] Dhananjay Dendukuri and Patrick S. Doyle. The synthesis and assembly of polymeric microparticles using microfluidics. *Advanced Materials*, 21(41):4071–4086, 11 2009. 13
- [4] Camille Duprat, H el ene Berthet, Jason S. Wexler, Olivia Du Roure, and Anke Lindner. Microfluidic in situ mechanical testing of photopolymerized gels. *Lab on a Chip*, 15(1):244–252, 1 2015. 13, 14, 18, 19, 20
- [5] Jean Cappello, Mathias Bechert, Camille Duprat, Olivia Du Roure, Fran ois Gallaire, and Anke Lindner. Transport of flexible fibers in confined microchannels. *Physical Review Fluids*, 4(3):1–22, 2019. 16, 18, 19, 20, 24
- [6] Jean Cappello, Vincent Herbemont, Anke Lindner, and Olivia Roure. Microfluidic In Situ Measurement of Poisson ’ s Ratios of Hydrogels. pages 1–12, 2020. 13
- [7] Jean Cappello. *Dynamics of freely transported fibers in confined viscous flows : Role of shape and flexibility*. PhD thesis, Universit e de Paris Cit e, 2020. 14, 17, 24
- [8] Rok Simi c, Joydeb Mandal, Kaihuan Zhang, and Nicholas D. Spencer. Oxygen inhibition of free-radical polymerization is the dominant mechanism behind the “mold effect” on hydrogels. *Soft Matter*, 17(26):6394–6403, 7 2021. 16
- [9] Christian Decker and Aubrey D Jenkins. Kinetic Approach of O<sub>2</sub> Inhibition in Ultraviolet- and Laser-Induced Polymerizations. Technical report, 1985. 16
- [10] Jennifer L. Fritz and Michael J. Owen. Hydrophobic recovery of plasma-treated polydimethylsiloxane. *The Journal of Adhesion*, 54(1-4):33–45, 1995. 16
- [11] Dmitry A. Markov, Elizabeth M. Lillie, Shawn P. Garbett, and Lisa J. McCawley. Variation in diffusion of gases through PDMS due to plasma surface treatment and storage conditions. *Biomedical Microdevices*, 16(1):91–96, 2014. 16
- [12] P Rai-Choudhury. *Handbook of Microlithography, Micromachining, and Microfabrication: Micromachining and Microfabrication*, volume 2. IET, 1997. 16
- [13] Kayaku Advanced Materials. Su-8 2000 data sheet. 16
- [14] M arzh auser Wetzlar. Tango api. 17

- [15] M. Karabulut, E. Melnik, R. Stefan, G. K. Marasinghe, C. S. Ray, C. R. Kurkjian, and D. E. Day. Mechanical and structural properties of phosphate glasses. *Journal of Non-Crystalline Solids*, 288(1-3):8–17, 2001. 18
- [16] Imran Oral, Hatice Guzel, and Gulnare Ahmetli. Measuring the Young’s modulus of polystyrene-based composites by tensile test and pulse-echo method. *Polymer Bulletin*, 67(9):1893–1906, 2011. 18
- [17] R. Moučka, M. Sedlačík, J. Osička, and V. Pata. Mechanical properties of bulk Sylgard 184 and its extension with silicone oil. *Scientific Reports*, 11(1):1–9, 2021. 18
- [18] Michael Rubinstein and Ralph H. Colby. *Polymer Physics*. Oxford University Press, 2003. 19
- [19] Dhananjay Dendukuri, Priyadarshi Panda, Ramin Haghgooei, Ju Min Kim, T. Alan Hatton, and Patrick S. Doyle. Modeling of oxygen-inhibited free radical photopolymerization in a PDMS microfluidic device. *Macromolecules*, 41(22):8547–8556, 2008. 19
- [20] Manuel Cárdenas-Barrantes, David Cantor, Jonathan Barés, Mathieu Renouf, and Emilien Azéma. Compaction of mixtures of rigid and highly deformable particles: a micro-mechanical model. 5 2020. 21
- [21] Emilien Azéma, Itthichai Preechawuttipong, and Farhang Radjai. Binary mixtures of disks and elongated particles: Texture and mechanical properties. *Physical Review E*, 94(4):1–12, 2016. 21
- [22] Boris D Lubachevsky and Frank H Stillinger. Geometric Properties of Random Disk Packings. Technical Report 5, 1990. 21
- [23] Ludovic Berthier, Daniele Coslovich, Andrea Ninarello, and Misaki Ozawa. Equilibrium Sampling of Hard Spheres up to the Jamming Density and beyond. *Physical Review Letters*, 116(23):1–5, 2016. 21
- [24] Aidan P. Thompson, H. Metin Aktulga, Richard Berger, Dan S. Bolintineanu, W. Michael Brown, Paul S. Crozier, Pieter J. in ’t Veld, Axel Kohlmeyer, Stan G. Moore, Trung Dac Nguyen, Ray Shan, Mark J. Stevens, Julien Tranchida, Christian Trott, and Steven J. Plimpton. LAMMPS - a flexible simulation tool for particle-based materials modeling at the atomic, meso, and continuum scales. *Computer Physics Communications*, 271:108171, 2022. 21
- [25] Claude E. Shannon. Communication theory in the presence of noise. *Proceedings of the IRE*, 37(1):10–21, 1949. 22
- [26] Farhang Radjai and Frédéric Dubois. *Discrete-element modeling of granular materials*. Wiley-Iste, 2011. 22
- [27] Etienne Guyon, Jean-Pierre Hulin, Luc Petit, and Pierre Gilles de Gennes. *Physical Hydrodynamics*. EDP sciences Les Ulis, 2001. 23, 24
- [28] Helene Berthet, Marc Fermigier, and Anke Lindner. Single fiber transport in a confined channel: Microfluidic experiments and numerical study. *Physics of Fluids*, 25(10), 2013. 23, 24



- 
- [29] Thomas Gervais, Jamil El-Ali, Axel Günther, and Klavs F. Jensen. Flow-induced deformation of shallow microfluidic channels. *Lab on a Chip*, 6(4):500–507, 2006. 25
- [30] Zida Li, Sze Yi Mak, Alban Sauret, and Ho Cheung Shum. Syringe-pump-induced fluctuation in all-aqueous microfluidic system implications for flow rate accuracy. *Lab on a Chip*, 14(4):744–749, 2014. 26
- [31] Fluigent. Fluigent software development kit. 26
- [32] Christophe Fiorio and Jens Gustedt, ' '. Two linear time Union-Find strategies for image processing. Technical report, 1996. 29
- [33] Scott V Franklin and Mark D Shattuck. *Handbook of granular materials*. CRC Press, 2016. 29
- [34] Lars Kool. Feature finding and tracking for dense suspensions. 29, 30
- [35] Daniel B. Allan, Thomas Caswell, Nathan C. Keim, Casper M. van der Wel, and Ruben W. Verweij. `soft-matter/trackpy`: v0.6.1, February 2023. 29
- [36] John C Crocker and David G Grier. *Methods of Digital Video Microscopy for Colloidal Studies*. Technical report, 1996. 29

## Chapter 3

# Compaction of dense suspensions of soft particles: rheological perspective

In the previous chapter, we presented an experimental technique to fabricate ensembles of hydrogel cylinders in a microfluidic channel, and we presented a method to exert an external force on these particles. In this chapter, we will use these techniques to study the response of an ensemble of hydrogel particles to an imposed pressure. We will do this from a rheological point-of-view, and look at the time-dependent deformation of the entire packing upon an imposed pressure.

First, we will introduce the general response of solids and fluids to an imposed stress. Then, we will discuss the complex nature of hydrogels, and why their behavior cannot be described as purely elastic, nor purely viscous. This is followed by an introduction of the Kelvin-Voigt model, a common model to describe solids with an intrinsic relaxation timescale, and derive the response of a Kelvin-Voigt element to a sudden increase in pressure. This model is then generalized to accommodate for solids with multiple relaxation timescales.

Next, we introduce the microfluidic channel we developed that allows us to compact the particles against a membrane by flowing fluid over and under the packing. This is followed by the protocol used to create reproducible initial conditions.

Then, we discuss the observed strain at a constant imposed stress as function of the position in the channel. After which, we study the time-dependent strain response to a sudden increase or decrease in stress. We try to link the relaxation time observed for the packing to the relaxation time of the single hydrogel particles.

Furthermore, we study the strain response to a continuously oscillating pressure, and link the observed deformation to the expected response from a Kelvin-Voigt material, as characterized by the step-stress experiments. We then systematically investigate the influence of the particle softness as well as the oscillation period on the phase lag between the imposed pressure and the observed strain.

Lastly, we perform a step-wise oscillation, where each step is described by the generalized Kelvin-Voigt model, allowing us to approximate the strain response in the fully relaxed limit. Studying the extrapolated strain response as function of the applied pressure in both compression and decompression can be considered analogous to a dynamic oscillation with infinitely long oscillation period.

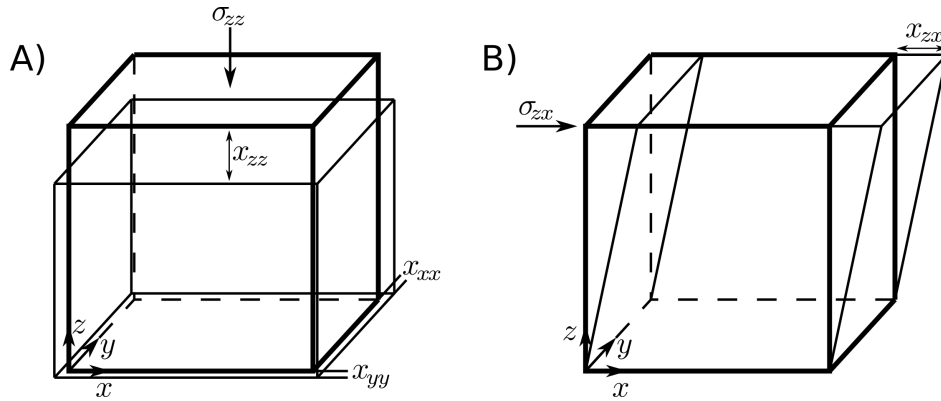


Figure 3.1: A) Schematic representation of the deformation of a solid under uniaxial compression. B) Schematic representation of the deformation of a solid under shear.

### 3.1 Introduction

The response of granular materials to an applied load is of vital importance, as we rely on the stability of granular materials to build houses and infrastructure. In this chapter, we study the deformation of an ensemble of soft frictionless particles with varying softness on repeatedly applied loads. In continuum mechanics, there are two main classes of materials, solids, and fluids. The stresses in both solids and fluids are represented by a second order tensor  $\boldsymbol{\sigma}$ , which is called the Cauchy stress tensor for solids, and the viscous stress tensor for fluids, where  $\sigma_{\alpha\beta}$  is the stress acting on the plane perpendicular to the direction vector  $\alpha$  in the direction of the direction vector  $\beta$ .

Upon imposing an uniaxial stress (a stress perpendicular to one of the surfaces where the other surfaces are unconstrained, e.g.  $\sigma_{zz}$  Figure 3.1A), an isotropic and linearly elastic solid has a finite deformation according to,

$$\sigma_{zz} = E\varepsilon_{zz}, \text{ with } \varepsilon_{zz} = \ln \left( 1 + \frac{x_{zz}(\sigma_{zz})}{x_z} \right) \quad (3.1)$$

with  $x_z$  the length of the unstressed solid along the z-direction,  $x_{zz}(\sigma_{zz})$  the displacement of the z-surface of the solid along the z-axis under a stress  $\sigma_{zz}$ ,  $\varepsilon_{zz}$  the strain, and  $E$  the Young's modulus, a proportionality constant relating stress and strain.

Typically, solid materials expand in the directions perpendicular to the compressional direction to conserve (most of the) volume. The amount of volume conservation (compressibility) is given by the Poisson's ratio,  $\nu$ , which is the ratio between the strain perpendicular to the axis of compression over the strain parallel to the axis of compression. For the example of an uniaxial compression along the z-axis, this would be

$$\nu = -\frac{\varepsilon_{xx}}{\varepsilon_{zz}} = -\frac{\varepsilon_{yy}}{\varepsilon_{zz}} \quad (3.2)$$

An incompressible material (all volume is conserved during compression) has a Poisson's ratio of 0.5, whereas a completely compressible has a Poisson's ratio of 0. (material width remains constant during compression) All natural materials have a Poisson's ratio between 0 and 0.5.

One can also apply a stress parallel to one of the surfaces, a shear stress e.g.  $\sigma_{zx}$ , resulting in a shear deformation for solids (Figure 3.1B):

$$\sigma_{zx} = G\varepsilon_{zx}, \text{ with } \varepsilon_{zx} = -\ln\left(1 + \frac{x_{zx}(\sigma_{zx})}{x_z}\right) \text{ and } G = \frac{E}{2(1+\nu)} \quad (3.3)$$

with  $x_z$  the length of the unstressed solid along the z-direction,  $x_{zx}(\sigma_{zx})$  the displacement of the z-surface of the solid along the x-direction under a stress  $\sigma_{zx}$ ,  $\varepsilon_{zx}$  the strain, and  $G$  the shear modulus, a proportionality constant relating stress and strain, which relates to the Young's modulus and Poisson's.

Where solids have a finite deformation upon an applied stress, fluids have a finite deformation *rate*. Applying a shear stress  $\sigma_{zx}$  does not result in an immediate deformation, but instead in a deformation rate  $\dot{\varepsilon}_{zx}$

$$\sigma_{zx} = \eta\dot{\varepsilon}_{zx} \quad (3.4)$$

with  $\eta$  the viscosity, a proportionality constant relating the deformation rate and the applied stress.

When a solid is deformed, the energy required for the deformation is stored elastically, and released upon the removal of the load. The load exerted on a fluid is dissipated by the friction between the moving fluid molecules, and none of the energy is recovered upon the removal of the load. There are, however, many materials that share both properties, meaning they store a part of the load, and dissipate the rest. This is called viscoelasticity. In this chapter, we will investigate to what extent a 2D packing of hydrogel particles can be described as an "effective" viscoelastic material.

### 3.1.1 Hydrogel properties

The response of hydrogels to an applied deformation or stress is very complex. Hydrogels consist of a polymer network filled with a solvent, typically water. The polymer network can consist of two types of bonds, covalent bonds (atoms sharing electrons), and non-covalent bonds (electrostatic and/or van der Waals interactions, hydrogen bonding etc.). Covalent bonds are strong, and can therefore store a large amount of energy. However, when loaded too much, the bond will break permanently, dissipating the stored energy in the process. Non-covalent bonds are weaker, and can therefore store less energy before breaking, but will reform over time. Polymer networks can thus store energy in both covalent and non-covalent bonds, and dissipate energy with the non-covalent bonds without permanently changing the material properties. The ratio of the storage and dissipation depends on the ratio between, and the strength of, the covalent and non-covalent bonds. The rate of dissipation defines a typical relaxation time of the polymer network. Furthermore, a polymer network can also dissipate energy due to friction between polymer chains. When a polymer network is deformed, the polymer chains slide past each other, dissipating energy in the form of friction in the process.

The interaction and breakage of polymer chains is, however, not the only way hydrogels can dissipate energy. The polymer network is filled with a liquid. Since liquids are incompressible, the liquid has to be squeezed out before the network can deform, dissipating energy in the process due to viscous friction. This process is called poro-elasticity [1, 2]. The timescale involved with poro-elasticity ( $\tau_{poro}$ ) corresponds to a diffusion distance comparable with length of the deformed region ( $a$ ) of the poro-elastic material [3, 4]

$$\tau_{poro} = \frac{a^2}{D} \quad (3.5)$$

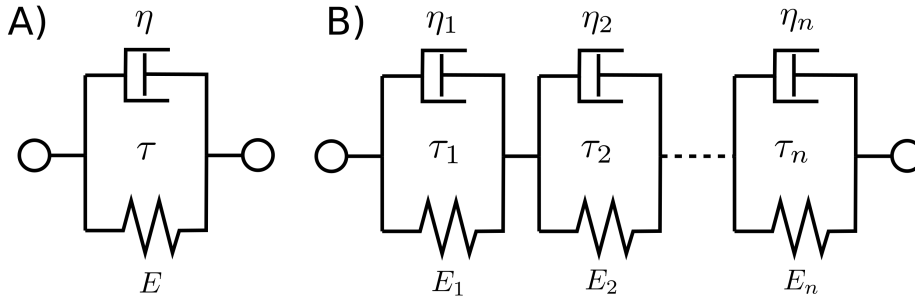


Figure 3.2: A) Schematic representation of a Kelvin-Voigt model with a spring element of strength  $E$ , a dashpot with viscosity  $\eta$ , and a resulting relaxation timescale  $\tau$ . B) Representation of a generalized Kelvin-Voigt model with  $n$  elements. Each element  $i$  has a spring of strength  $E_i$ , a dashpot with viscosity  $\eta_i$  and relaxation timescale  $\tau_i$ .

with  $a^2$  the area of the contact patch and  $D$  the diffusion coefficient of the solvent through the pores. This means that the relaxation time scales with the square of the particle size [5]. Therefore, the poro-elastic relaxation is best to be investigated *in-situ*.

The relaxation of the polymer network and poro-elastic relaxation are coupled, meaning that the overall relaxation is governed by the slowest relaxation timescale. If the poro-elastic timescale is slower than the network relaxation, the network can only deform once the liquid has diffused out of the pores. Likewise, the liquid will only be forced out of the pores once the network starts deforming. We can compare the two timescales. Typical reported relaxation times of the polymer networks are in the order of  $\sim 0.1$  seconds [6, 7]. It is difficult to find an estimation of the poro-elastic timescale for our system, since it depends on the size of the particles and diffusion coefficient of molecules through the network mesh. Extrapolating the data from the experiments done by [5] and correcting for the difference in the viscosity of the solvent yields a poro-elastic timescale of  $\sim 10$ – $100$  seconds. We can therefore ignore the relaxation time of the network, and consider the poro-elastic timescale as the only relaxation timescale of the particles themselves.

### 3.1.2 Kelvin-Voigt

The response of a viscoelastic material to an imposed stress can be modelled by decomposing the response into parts (elements) with a well-described response. The elastic part can be well described by a linear spring with spring constant  $E$  (the Young's modulus of the elastic network),  $\sigma_s = E\varepsilon$ . The viscous dissipation can be modelled by a dashpot, which dissipates energy depending on the strain rate  $\dot{\varepsilon}$  and a viscosity  $\eta$ ,  $\sigma_d = \eta\dot{\varepsilon}$ .

Viscoelastic solids are typically well described by a Kelvin-Voigt model, which consists of a spring and a dashpot in parallel, thus assuming the strain is identical for both elements, and the stresses of the elements add up to the total stress (Figure 3.2A).

$$\sigma = \sigma_s + \sigma_d \text{ and } \varepsilon = \varepsilon_s = \varepsilon_d \quad (3.6)$$

Substituting the models for the stresses of the spring and dashpot elements yields the governing equation:

$$\sigma = E\varepsilon + \eta\dot{\varepsilon} \quad (3.7)$$

We can solve this governing equation for a well described experiment, creep relaxation upon a stepwise increase in stress ( $t = 0; \sigma = \sigma_0, \varepsilon = 0$ ). Substituting these initial conditions

in eq. 3.7 gives the inhomogeneous differential equation:

$$\dot{\varepsilon} + \frac{E}{\eta}\varepsilon = \frac{\sigma_0}{\eta} \quad (3.8)$$

Solving the homogeneous part first gives

$$\frac{d\varepsilon}{dt} + \frac{E}{\eta}\varepsilon = 0 \quad (3.9)$$

$$\frac{d\varepsilon}{\varepsilon} = \frac{-E}{\eta}dt \quad (3.10)$$

$$\int \frac{d\varepsilon}{\varepsilon} = \int \frac{-E}{\eta}dt \quad (3.11)$$

$$\ln(\varepsilon(t)) = \frac{-E}{\eta}t + C \quad (3.12)$$

$$\varepsilon(t) = Ce^{-t/\tau} \text{ with } \tau = \frac{\eta}{E} \quad (3.13)$$

To find the particular solution, we first have to make a guess on the potential solution. In such creep experiment, a constant stress is exerted, part of which is dissipated viscously and part of it is stored elastically. In the limit of  $t \rightarrow \infty$ , it is intuitive to say that the stored stress equals the imposed stress, resulting in a constant strain  $\varepsilon_\infty$ . This would mean that eq. 3.8 becomes:

$$\frac{E}{\eta}\varepsilon_\infty = \frac{\sigma_0}{\eta} \quad (3.14)$$

The complete solution then becomes the sum of the homogeneous solution (eq. 3.13) and the particular solution (eq. 3.14)

$$\varepsilon(t) = Ce^{-t/\tau} + \frac{\sigma_0}{E} \quad (3.15)$$

Filling in the initial conditions ( $t = 0 : \sigma = \sigma_0, \varepsilon = 0$ ) gives:

$$\varepsilon(0) = Ce^{-0/\tau} + \frac{\sigma_0}{E} = 0 \quad (3.16)$$

$$C = -\frac{\sigma_0}{E} \quad (3.17)$$

This leads to the final solution for creep:

$$\varepsilon(t) = -\frac{\sigma_0}{E}e^{-t/\tau} + \frac{\sigma_0}{E} = \frac{\sigma_0}{E}(1 - e^{-t/\tau}) \quad (3.18)$$

This is also often given in form of creep compliance,  $J$ :

$$J(t) = \frac{\varepsilon(t)}{\sigma_0} = \frac{1}{E}(1 - e^{-t/\tau}) \quad (3.19)$$

For the strain relaxation at a step-wise decrease in stress ( $t = 0 : \sigma = 0, \varepsilon = \varepsilon_0$ ), the differential equation is already homogeneous, as  $\frac{\sigma_0}{\eta} = 0$  (eq. 3.8). We can therefore immediately fill in the initial conditions

$$\varepsilon(0) = Ce^{-0/\tau} = \varepsilon_0 \rightarrow C = \varepsilon_0 \quad (3.20)$$

$$\varepsilon(t) = \varepsilon_0 e^{-t/\tau} \text{ with } \varepsilon_0 = \frac{\sigma_0}{E} \quad (3.21)$$

### 3.1.3 Generalized Kelvin-Voigt

It can be that one timescale is not enough to describe the relaxation of a viscoelastic material. We can generalize the Kelvin-Voigt model by assuming the viscoelastic relaxations are independent, and can each be modelled by a Kelvin-Voigt element. Assuming that the stress experienced by each of the Kelvin-Voigt elements is equal, and the strain responses are additive, one obtains the generalized Kelvin-Voigt model for  $n$  elements (Figure 3.2B).

$$\sigma = \sigma_{KV1} = \sigma_{KV2} = \sigma_{KVn} \text{ and } \varepsilon = \varepsilon_{KV1} + \varepsilon_{KV2} + \dots + \varepsilon_{KVn} \quad (3.22)$$

It can be shown that the solution to the generalized Kelvin-Voigt model with  $n$  elements is just the sum of the individual components

$$\varepsilon(t) = \sum_i^n \varepsilon_i (1 - e^{-t/\tau_i}) \quad (3.23)$$

with  $\varepsilon_i$  and  $\tau_i$  the strain contribution and characteristic timescale of element  $i$ , respectively. Resulting in eq. 3.24 and eq. 3.25 for the creep and relaxation, respectively

$$\varepsilon(t) = \varepsilon_1 (1 - e^{-t/\tau_{1,c}}) + \varepsilon_2 (1 - e^{-t/\tau_{2,c}}) \quad (3.24)$$

with  $\varepsilon_0$  the strain contribution of the spring, and  $\varepsilon_i$  the strain contribution of Kelvin-Voigt element  $i$  with characteristic creep timescale  $\tau_{i,c}$ , where we define  $\tau_1 < \tau_2$

$$\varepsilon(t) = \varepsilon_1 e^{-t/\tau_{1,r}} + \varepsilon_2 e^{-t/\tau_{2,r}} \quad (3.25)$$

with  $\varepsilon_i$  the strain contribution of Kelvin-Voigt element  $i$  with characteristic relaxation timescale  $\tau_{i,r}$ , where again  $\tau_1 < \tau_2$ .

## 3.2 Materials and Methods

To study the compaction of dense soft particle suspensions, we used a system consisting of  $\sim 2000$  bidisperse particles, with diameters of  $120 \mu\text{m}$  and  $160 \mu\text{m}$ , both contributing equally to the volume occupied by particles, and fabricated according to the methods mentioned in sections 2.2.1 and 2.2.2. We used several particle softnesses, ranging between 10 MPa and 400 kPa, which are obtained by crosslinking solutions of 90% PEGDA + 10% PI up to 30% PEGDA + 60% PEG and 10% PI, respectively (see Table 3.1) The fill level of the channel is indicated by the red dashed line in Figure 3.3. A typical bidisperse packing before compression is provided on the right side of the same figure.

### 3.2.1 Channel geometry

Given the conditions of our microfluidic setup, athermal particles and no movable boundaries, particles only move when they are externally perturbed. This was achieved by imposing a pressure different between the inlet and outlet, as described in section 2.3. The hydrodynamic drag on the particles by the suspending fluid causes the particles to be transported towards the outlet. A solid object needs to be placed in the channel to keep the particles in the channel, and provide a surface to compress the particles against. It is, however, not as simple as pushing them against a solid barrier, as this would also block the fluid, and thus remove the driving force from our system. Figure 3.3 shows a schematic overview of the channel we designed. We chose to place a membrane, consisting of  $150$  by  $200 \mu\text{m}$  blocks of PDMS, spaced  $50 \mu\text{m}$  apart, near the outlet of the channel (Figure 3.3, left). The gaps are big enough to let the fluid flow through, whereas they are small enough to hold the particles back.

PEGDA (v/v%)	PEG (v/v%)	PI (v/v%)	E (MPa)
90	0	10	12.0
70	20	10	8.7
60	30	10	6.8
50	40	10	4.9
40	50	10	4.6
30	60	10	0.4

Table 3.1: Table of PEGDA-PEG mixtures used and the associated Young’s modulus

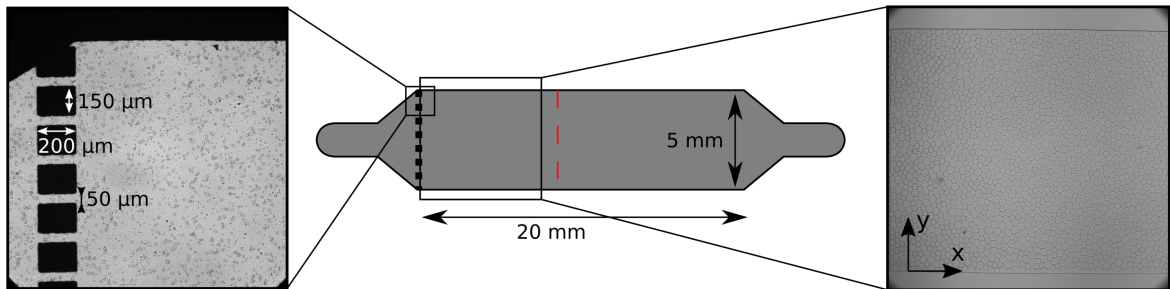


Figure 3.3: Schematic overview of the compression channel. The red dashed line indicates the fill level of the channel when the particles are uncompressed. Left: zoom on the geometry of the PDMS blocks that block the particles, but let the fluid pass. Right: Image of the compression channel filled with particles.

### 3.2.2 Initialization

After printing the particles at low density (roughly 40% v/v, see section 2.1), the particles were slowly settled on the membrane by applying a small pressure drop ( $\Delta P$ ), typically 3 kPa. After all the particles have settled,  $\Delta P$  was reduced to 0.2 kPa to ensure the pressure drop will always be positive, as even small negative pressure drops would cause the particles to drift away from the membrane. This small “over-pressure”,  $\delta P$ , was therefore maintained throughout all experiments.

Furthermore, there is no guarantee that the settled packing is the densest configuration, as the system might be trapped in a looser configuration. Compressing the sample could result in a rearrangement of the particles into a more dense configuration. These rearrangements would lead to an observed “plastic” strain, even at vanishing stress. The effect of compaction was limited by compressing the packing 10–20 times over the course of an hour, before starting the experiments.

## 3.3 Results and Discussion

### 3.3.1 Average global strain

For  $\Delta P > \delta P$ , the particles were compressed against the membrane. The centers of all particles were found using a convolutional algorithm (for more details see section 2.4.2), and the displacements of particles were tracked by linking the centers found over the images taken, as described in section 2.4.3. Knowing the displacements of the particles, we can define the mesoscopic strain response of each particle as its distance to the membrane compared to the



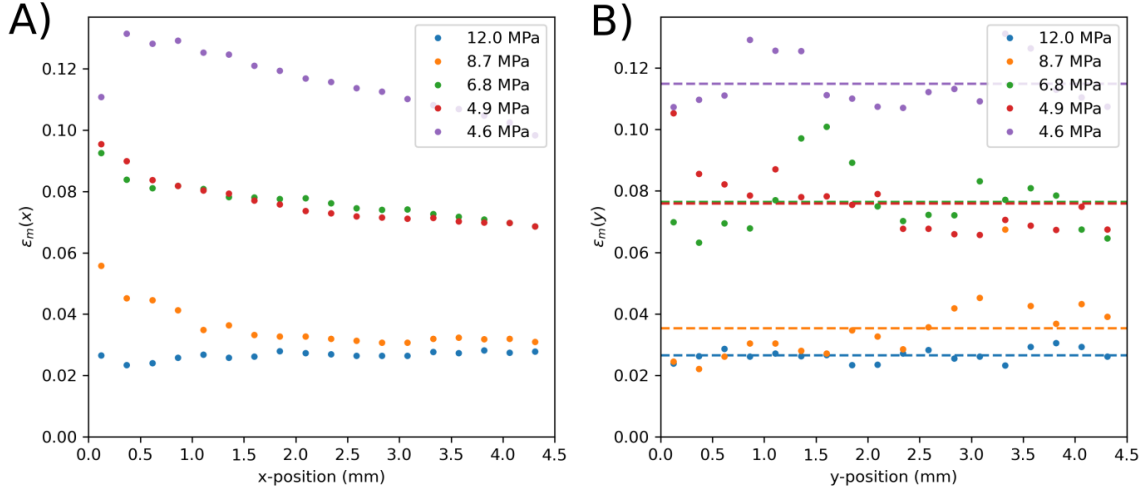


Figure 3.4: A) Mesoscopic strain averaged over the y-direction, as function of the position along the x (compressive) direction in the channel, where zero indicates the membrane position. B) Mesoscopic strain averaged over the x-position, as function of the position along the y (non-compressive) direction.

distance to the membrane at rest:

$$\epsilon_{m,i}(t) = -\ln\left(\frac{x_i(t)}{x_i(0)}\right) \quad (3.26)$$

with  $\epsilon_{m,i}(t)$  the mesoscopic strain on particle  $i$  at time  $t$ ,  $x(t)$  the position of particle  $i$  at time  $t$  along the compressive (x) axis of the system. Throughout this thesis, compressive strains are defined to be positive.  $t = 0$  is defined as the first image in an experiment. Between the repeated cyclic compression to induce compaction and the start of the experiment, the system is kept at  $\Delta P = \delta P$  for 5-10 min, to ensure a reproducible non-compressed initial condition.

We expect a slight gradient in the mesoscopic strain along the compressive direction, due to the shear component of the applied force being distributed over the entire packing (see section 2.3). Figure 3.4A shows the mesoscopic strain (averaged over the y-direction) as function of the position along the compressive (x) direction at the highest applied pressure (20 kPa) for ensembles consisting of particles with different Young's moduli (indicated in the legend). We indeed observe a difference of 10-15 % between the mesoscopic strain near the membrane compared to the mesoscopic strain at the other end of the packing, as was predicted in section 2.3. The gradient is not always constant, but seems to be stronger near the membrane for the most soft particles. Figure 3.4B shows the average mesoscopic strain as function of the position along the *non*-compressive (y) direction for different Young's moduli at  $\Delta P = 20$  kPa. Although the values fluctuate, there does not seem to be a gradient, as expected. The average (indicated with the colored dashed lines) shows that the strain at identical pressure is different for different Young's moduli, indicating variability during the fabrication process.

Since this gradient is relatively small, we can define a global average strain,  $\epsilon_g$  as:

$$\epsilon_g(t) = \frac{1}{N_p} \sum_i^{N_p} \epsilon_{m,i}(t) \quad (3.27)$$

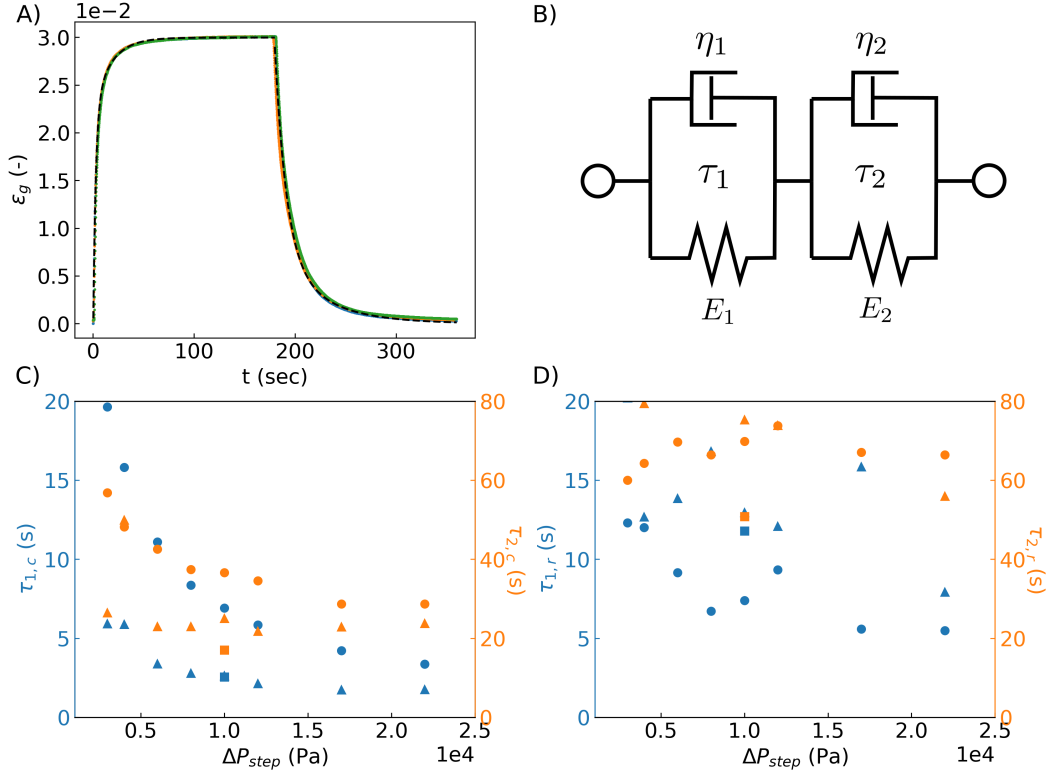


Figure 3.5: A) Creep (step increase in  $\Delta P$ ) followed by a relaxation (step decrease in  $\Delta P$ ) for an ensemble of particles with  $E=12$  MPa and  $\Delta P_{step} = 10$  kPa, fitted with a generalized Kelvin-Voigt model of order 2. B) Schematic representation of the generalized Kelvin-Voigt model used to fit all creep and relaxation data. C) Fast and slow characteristic creep times (blue and orange, respectively) for different pressures, and different Young's moduli (0.4 MPa  $\bullet$ , 4.9 MPa  $\blacktriangle$ , and 12 MPa  $\blacksquare$ ). D) Fast and slow characteristic relaxation times (blue and orange, respectively) for different pressures, and different Young's moduli (0.4 MPa  $\bullet$ , 4.9 MPa  $\blacktriangle$ , and 12 MPa  $\blacksquare$ ).

This, will then allow us to follow the strain response of the entire packing over time as a function of the applied pressure drop.

### 3.3.2 Step stress

#### 3.3.A Relaxation times

We investigated the relaxation times of ensembles of viscoelastic particles by observing the strain relaxation upon a step change in stress. The step stress experiments consist of two parts: a creep test, an increase in strain over time upon a step *increase* in stress; and a relaxation test, a decrease in strain over time upon a step *decrease* in stress. The step stress experiments started with a fully equilibrated sample at rest ( $t < 0$ ;  $\Delta P = \delta P$ ), after which a nearly instantaneous increase in  $\Delta P$  was imposed at  $t = 0$ ,

$$\Delta P(t) = \Delta P_{step} \mathcal{H}(t) + \delta P \quad (3.28)$$

with  $\mathcal{H}(t)$  the Heaviside step function, and  $\Delta P_{step}$  the step increase in pressure applied. We then recorded the  $\varepsilon_g$  response over time. After 180 seconds, which was enough for the ensemble to reach equilibrium, we decreased the pressure ( $\Delta P(t) = \Delta P_{step} - \Delta P_{step} \mathcal{H}(t) + \delta P$ ) and

again recorded the  $\varepsilon_g$  response over time. Figure 3.5A shows 3 typical creep experiments upon a step-increase in stress followed by a relaxation experiment upon a step-decrease in stress of 12 MPa particles done consecutively on the same sample. This experiment nicely shows that the pre-equilibration works well, as the three responses were virtually identical, and after full relaxation  $\varepsilon_g \approx 0$ , indicating that no unrecoverable (plastic) strain accumulated during the creep-relaxation cycle.

Fitting the data with a generalized Kelvin-Voigt model with two timescales (Figure 3.5B) gives a very good agreement both during creep and relaxation (Figure 3.5A dashed lines). We've investigated the timescales of multiple Young's moduli (12 MPa, 4.9 MPa and 0.4 MPa) for a range of  $\Delta P_{step}$  (Figure 3.5CD). We find that the slow creep timescales (blue data points) depend on the pressure applied, where higher pressures lead to faster relaxation.

In the case of the slow relaxation, it is much less clear. For the 0.4 MPa particles (orange circles), the relaxation time also seems to decrease with increasing  $\Delta P_{step}$ , whereas for the 4.9 MPa particles (orange triangles) appears to be independent of  $\Delta P_{step}$ . We also found that harder particles seem to relax faster. Unlike the creep timescales, the relaxation timescales appear to be independent of both steps in pressure, and the Young's modulus of the particles.

### 3.3.B Link to hydrogel-rheology

Now we have a complete macroscopic description of the creep and relaxation response of the ensemble of soft particles, we can try to find the origins of these two timescales. Since the long relaxation timescale is in the order of the poro-elastic timescale (section 3.1.1, we will first try to find a link between the relaxation to the rheology of a single particle, and the relaxations observed for packings.

**Macroscopic rheology** Studying particle relaxation is more complicated than one might expect. A common tool to study the response of (hydro)gel particles is oscillatory rheology. Here, the sample is sheared between two plates in an oscillatory fashion, and the stress (strain) response on an imposed strain (stress) is recorded, where the time lag between the imposed strain and the measured stress is a measure for the viscous response of the system. A big disadvantage is that the samples need to be macroscopic, i.e. in the order of  $\sim 20$  mm in diameter, which is  $\sim 100x$  larger than the particles inside the microfluidic channels. Also, the hydrogel cannot be submerged during macroscopic rheological experiments. This makes it hard to compare the microfluidic and the rheological relaxation timescales.

Furthermore, for these experiments a no-slip boundary condition needs to be enforced, as slip and viscous relaxation are difficult to distinguish. There are two main ways to enforce the no-slip boundary condition. The most simple approach is friction. As long as the imposed shear force doesn't surpass the Coulomb-friction ( $F_{max} = \mu F_N$ , with  $F_{max}$  the shear force threshold,  $\mu$  the friction coefficient, and  $F_N$  the normal force), the gel will not slip. However, hydrogels have a notoriously low friction coefficient, typically in the order of 0.001. This can be compensated by applying a higher normal force. However, compressing the gel applies a pure shear (compression in one direction, extension in orthogonal directions) to the gel network, effectively pre-tensioning the network. As it turns out, gel networks tend to be strain stiffening [8], meaning that the measured (time-dependent) response also depends on the confining force. Furthermore, since the hydrogel is expected to be viscoelastic, one expects the normal force (and thus the shear-stress threshold) to decrease over time for experiments done at constant normal strain. Experiments done at constant normal force would have a

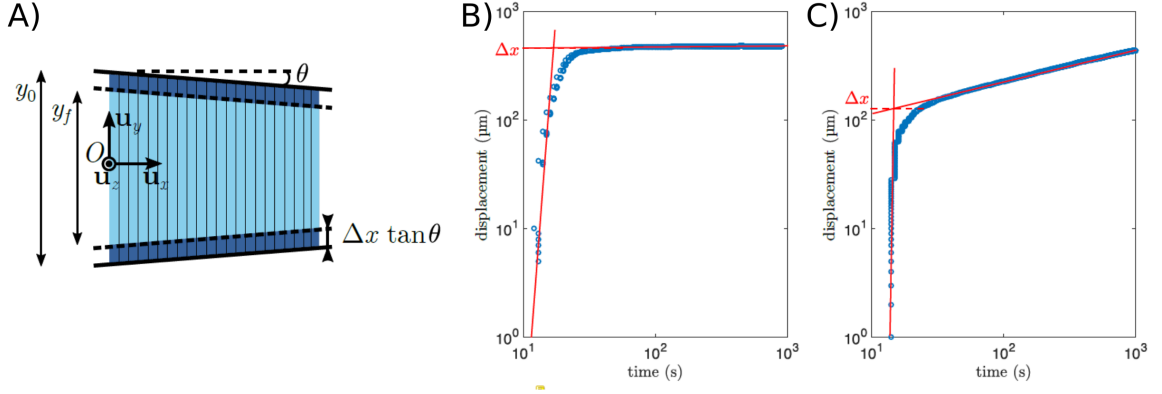


Figure 3.6: A) Schematic overview of the microfluidic compression of a trapezoidal particle in a constriction of angle  $\theta$ . B) Displacement of the trapezoidal particle over time upon a step increase in stress, where the particle approaches a constant deformation state. C) Displacement of the trapezoidal particle over time upon a step increase in stress, where the particle approaches a constant deformation rate. Figures are taken from [9]

constant shear stress threshold, but would continue to tension the network to keep the normal force constant, leading to an increase in apparent stiffness of the hydrogel.

In collaboration with Guyline Ducouret, we tried etched/sanded and even serrated geometries to increase the surface area, and therefore higher friction force. However, the etched geometry had no effect, we still observed slip at during the oscillatory shear experiments. The serrated plates even worked adversely, lowering the threshold for slip. Even for the softest gels, with a Young's modulus of 100 kPa, the penetration depth would be  $\delta = \frac{HF}{2EA} \approx \frac{2 \cdot 10^{-3} \cdot 1}{2 \cdot 1 \cdot 10^5 \cdot \pi \cdot (1.25 \cdot 10^{-3})^2} \approx 20 \mu\text{m}$ , with H the height of the disk, F the normal force applied, E the Young's modulus and A the area of the disk. This effectively reduces the contact area, if the gel is not fabricated in-situ. Furthermore, this does not even take into account that a normal force is still required.

Briefly summarizing, macroscopic rheology experiments were not suitable to determine the timescales for two main reasons: firstly, the presence of slip makes it difficult to measure a meaningful timescale; secondly, applying a normal force pre-tensions the network, changing the relaxation behavior, which complicates the interpretation of the measured values.

A second approach, which we didn't try, would be to chemically bond the hydrogel to the plates. Although hydrogels don't bond to metal (we used metal molds to fabricate gels to put in the rheometer), it is possible to chemically modify the surface of the rheometer plates with acrylate groups. Upon curing the PEGDA solution in-situ, the hydrogel would link to the Al-acrylate surface, providing a no-slip condition without exerting normal forces. However, metal surface chemistry is complicated, and the strength of the bonds remains to be seen. Moreover, the polymerization is initiated by UV and since illumination is only possible from the side, ensuring homogeneous curing in a narrow gap would be a challenge as well.

**Microfluidic rheology** Previously, attempts have been made at quantifying the mechanical response of the PEGDA particles [9], by squeezing a trapezoidal particle through a constriction at constant pressure, where the angle of the trapezoidal particle matches the angle of the constriction (Figure 3.6A). This allows for the decomposition of the trapezium into uni-axially compressed columns of varying length. A displacement  $\Delta x$  in  $x$  would then constitute a

compression of  $\Delta y = \tan(\theta)\Delta x$  [9]. In these experiments, we expect that the relaxation is influenced by the friction with the side-walls of the microfluidic channel, making it not straightforward to extract a viscoelastic timescale using this experiment. Furthermore, they also saw that at times, the particle approached a constant deformation *rate*, resembling a viscoelastic fluid, rather than a viscoelastic solid. This makes this method unsuitable to determine the relaxation accurately. However, by looking at the intersection of the extrapolated two regimes (red lines in Figure 3.6BC), we can get an estimation of the relaxation time of  $\sim 20$  seconds, which is of the same order of magnitude as the long relaxation timescale we observed in the step-stress experiments.

**Indentation** Another possibility to test the rheological properties of the gels by indentation. Since the relaxation timescale of hydrogels is governed by the time the interstitial liquid takes to flow out of the particle, which depends on the particle size [3–5], the particles used for indentation need to be of similar size to the particles used in the microfluidic experiments. Furthermore, for indentation, the probe needs to be much smaller than the thickness of the sample. This means that one cannot use standard indentation techniques (load cell connected to spherical probe), and has to use cantilever deflection based nano-indentors or Atomic Force Microscopes (AFM). In collaboration with Mathieu Hautefeuille and Jonathan Fouchard, we have tried some first tests on an Optics11 Piuma nano-indentor, but we were not able to collect any data. After discussing with the manufacturer, we believe that the PEG/PEGDA solvent is incompatible with their nano-indentors, as it interferes with the light used to measure the force exerted on the material. We believe that this approach is the most promising method to determine the relevant relaxation time of the individual particles. We are currently investigating the use of other brands of AFM or nano-indentors to check whether they are compatible with our particles and the solvent.

### 3.3.C Other possible effects

**Viscous timescale of solvent** Unable to link one of the relaxation timescales to the relaxation timescale of a single particle, we should investigate other causes of relaxation. Another possibility is the inherent timescale involved with the flow of the solvent. We can compare the viscosity of the solvent ( $\eta$ ) to the Young’s modulus to give us an estimation of the timescale involved with compressing the particle with a viscous fluid

$$\tau_{fluid} = \frac{\eta}{E} \quad (3.29)$$

The viscosity of the carrier fluid is approximately 50 mPa·s for all experiments. This indicates that the viscous timescale would scale inversely with the Young’s modulus of the particles. The longest possible timescale would be obtained for the softest particles ( $E = 0.4$  MPa), such that  $\tau_{fluid} = \frac{5 \cdot 10^{-2}}{4 \cdot 10^5} \approx 10^{-7}$  s. A relaxation time in the order of 100 nanoseconds is orders of magnitude faster than we could possibly measure with this setup, hence we can conclude that this effect is not the origin of one of the timescales.

**Pressure controller delay** There is, however, another setup related timescale. There is the time needed for the fluid to reach a steady state. There are several factors contributing to this: the compliance of the tubing and channel, and the internal feedback loop of the electronics of the pressure controller [10]. We tested the sum of all these effects by applying a

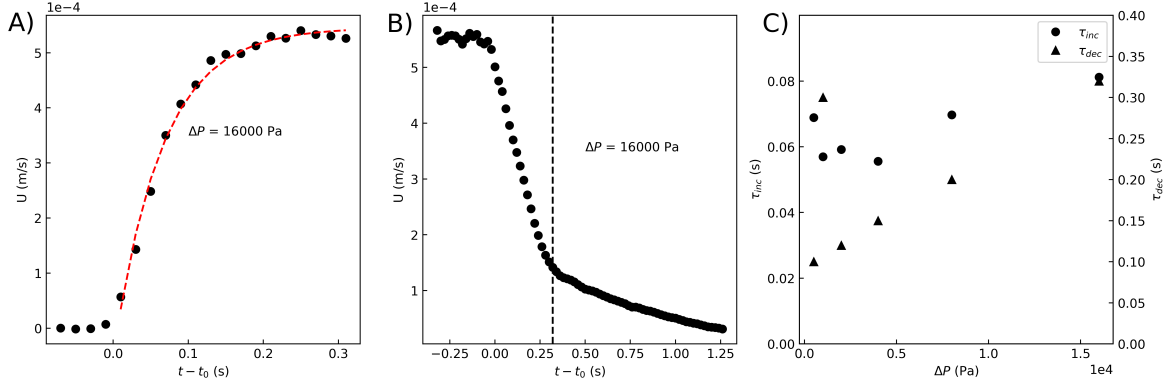


Figure 3.7: A) Fluid velocity, measured by PIV, as function of time after an imposed step-increase in  $\Delta P$  over the channel. The response was fitted with  $U = U_{max}(1 - e^{-t/\tau_{inc}})$  (red dashed line), yielding a characteristic timescale  $\tau_{inc}$ . B) Fluid velocity, measured by PIV, as function of time after an imposed step-decrease in  $\Delta P$  over the channel. The end of the initial linear decrease, indicated by the black dashed line, was taken as the characteristic timescale for the decrease in  $\Delta P$ ,  $\tau_{dec}$ . C) Pressure dependence of the characteristic timescales for the step-increase ( $\tau_{inc}$ ) and step-decrease ( $\tau_{dec}$ ), on the left and right axis, respectively.

step in pressure and recording the fluid velocity by means of PIV, as is shown in Figure 3.7A-B. We found that the change in fluid velocity upon a step increase in  $\Delta P$  was not immediate, and was actually well captured by a Kelvin-Voigt-like timescale  $U(t) = U_{max}(1 - e^{-t/\tau_{inc}})$ , with  $\tau_{inc}$  the response time of the pressure controller. We found that the response time was roughly 60 ms, and was independent of the  $\Delta P$  applied (Figure 3.7C, left axis and circles). Slightly longer response times have been reported by others using different equipment [11, 12].

The same approach, however, did not work for the step-decrease. Initially, the velocity decreased linearly with time, the rate of which did not depend on the magnitude of the step-decrease. After the velocity is close to zero, the response enters a second (slower) phase, the origin of which we do not fully understand. We defined the time spend in the linear regime as the response time of the pressure controller (indicated by the dashed line in Figure 3.7B). This timescale is larger than the time required for the flow to increase, it also seems to depend linearly on the size of the pressure step applied, with a delay of  $\sim 0.1$  seconds for very small steps. Gao et al. [13] saw a similar slower pressure-dependent decrease in the open-source pressure controller they developed.

However, both timescales are still an order of magnitude faster than the relaxation times observed during the step-stress experiments. Hence, we can conclude that the pressure controller is not the cause of one of the relaxation timescales.

To summarize, the long relaxation timescale observed during the step compression and decompression of a packing of hydrogels seems to correspond to the poro-elastic relaxation time of the hydrogel particles. However, the complex conditions under which the relaxation timescale(s) of the individual particles needs to be measured did not allow for an accurate measurement, and further investigations should focus on finding such particle relaxation timescale. We have not, yet, found an explanation for the second timescale. We ruled out the viscous timescale of the solvent, and the time needed for the pressure controller to reach the desired pressure. Other origins of relaxation timescales could include microstructural rearrangements. However, the influence of rearranges on the relaxation is unclear, especially in the absence of an accurate description of the relaxation of individual particles.

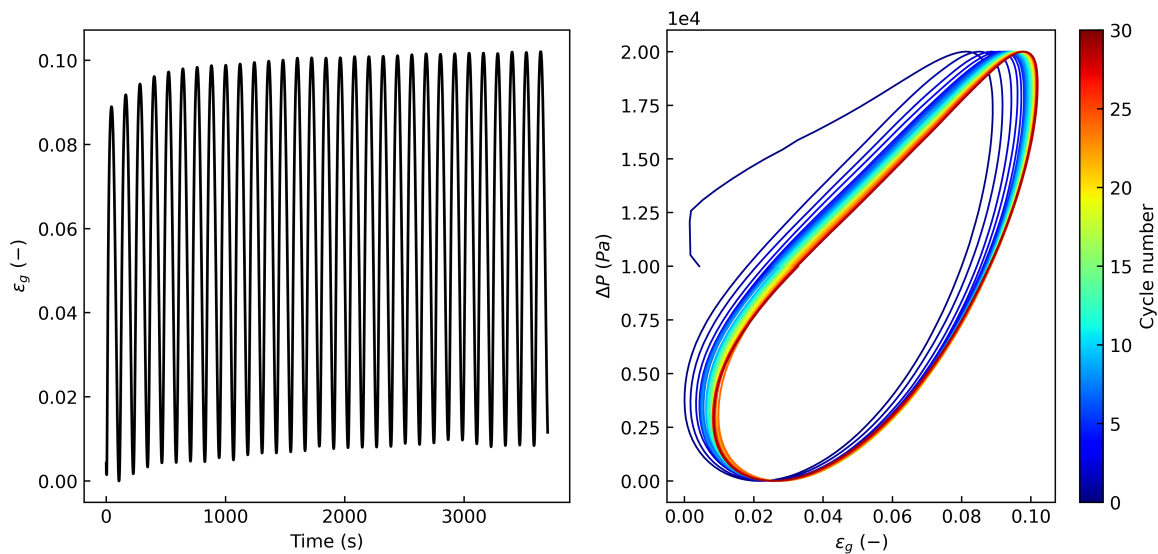


Figure 3.8: Oscillatory compaction and decompaction of an ensemble of particles with a Young’s modulus of 4.6 MPa and an oscillation period,  $T$ , of 120 seconds. A) Evolution of the global strain,  $\varepsilon_g$  over time. B) Imposed pressure versus observed global strain for the same compaction, where the color of the line indicates the cycle number, from blue at the start of the experiment, to red at the end of the experiment.

### 3.3.3 Oscillatory compression

#### 3.3.A Observations

We further investigated the response of the packing under external solicitation by varying  $\Delta P$  continuously according to:

$$\Delta P(t) = P_{mean} \left( -\cos \left( 2\pi \frac{t}{T} \right) + 1 \right) + \delta P \quad (3.30)$$

with  $P_{amp}$  the amplitude of the oscillation,  $T$  the oscillation period, and  $\delta P$  the over-pressure. Snapshots of the particles were taken 120 times per cycle to accurately capture the displacements during the oscillations. Figure 3.8A shows evolution of the global strain over time during the pre-oscillation. We can see that the sample evolves over the first 10 to 15 compression cycles, as the particles rearrange slightly to find a more dense configuration. Once this configuration is reached, the system is in a limit cycle and the response doesn’t change from cycle to cycle. Therefore, all other experiments were pre-oscillated by at least 10–15 cycles (as explained above).

Since we know the imposed pressure at any point in time, as well as the time at which the snapshot was taken, we can plot the imposed  $\Delta P$  versus the observed strain, as shown in Figure 3.8B. Interestingly, the imposed pressure and the observed strain seem to be out of phase. The maximum global strain is observed when the applied pressure is already decreasing, and the minimum observed strain does not occur at  $\Delta P = 0$ , but shortly after. This is despite the oscillation period being 2-3 times slower than the slow relaxation time, as determined from the step-stress experiments. There are various reasons a system can exhibit such history-dependent (hysteretic) response.

### 3.3.B Link with Kelvin-Voigt model

**Software/synchronization delays** Firstly, let us exclude artifacts caused by the experimental setup. Since the imposed pressure cannot be directly observed alongside the strain, the pressure controller and camera need to be synchronized. Our camera can be synchronized using an external start trigger, which can conveniently be provided by the pressure controller. Forcing events to be executed simultaneously in LabView is complicated, due to the way LabView handles events. However, even the worst case scenario of the events being executed in series, would cause a delay in the order of milliseconds, which is negligible compared to the oscillation period of in this case 120 seconds. Next, there could be a time delay between receiving the trigger pulse and actually capturing the first frame. The camera allows us to set the trigger delay between 0–10 seconds (in 1  $\mu$ s increments), which we set to zero seconds. We were, however, unable to get an accurate measurement whether the claimed delay was accurate. But since time delay is in the order of 10–20 seconds, we deem the potential deviation insignificant.

Like step-stress experiments, a phase-shift can also be caused by the delay between imposing the pressure, and the pressure arriving at the imposed level. However, as determined before, the delay is well below a second, and therefore we also deem any delay by the pressure controller insignificant.

**Viscoelasticity** Let us now analyze to what extent the observed time shift agrees with the viscoelastic relaxation as measured by the step-stress experiments. The oscillation period is in the order of the slowest relaxation time. We can determine the phase shift caused by the relaxation time as follows. For a stress  $\sigma$ , the rate of change of the stress  $\dot{\sigma}$  in the system is given by

$$\sigma = \sigma_0(\cos \omega t + 1) \text{ and } \dot{\sigma} = -\sigma_0 \sin \omega t \quad (3.31)$$

with  $\sigma_0$  the amplitude of the oscillation, and  $\omega = \frac{2\pi}{T}$  the oscillation frequency. According to Bae et al. [14], we can write the strain response as

$$\varepsilon(t) = J'(\omega)\sigma_0 \cos \omega t + J''(\omega)\sigma_0 \sin \omega t \quad (3.32)$$

$$J'(\omega) = \frac{E'(\omega)}{\|E^*(\omega)\|^2} \text{ and } J''(\omega) = \frac{E''(\omega)}{\|E^*(\omega)\|^2} \quad (3.33)$$

with  $E'$  the storage modulus,  $E''$  the loss modulus, and  $E^*$  the complex modulus.

For a Kelvin-Voigt element, it is known that [15]

$$E' = E \text{ and } E'' = \omega\eta = \omega\tau E \quad (3.34)$$

substituting the viscosity for the relaxation timescale obtained from the step-stress experiments using  $\tau = \frac{\eta}{E}$ , as defined in eq. 3.13. This allows us to write the loss tangent  $\tan \delta$  as:

$$\tan \delta = \frac{J''}{J'} = \frac{E''(\omega)}{\|E^*(\omega)\|^2} \frac{\|E^*(\omega)\|^2}{E'(\omega)} = \frac{\omega\tau E}{E} = \frac{2\pi\tau}{T} \quad (3.35)$$

where  $\delta$  is the phase shift in radians.

Equation 3.35 suggests that the phase shift would depend on the softness of the particles, as for a Kelvin-Voigt model  $\tau = \frac{\eta}{E}$ . However, we have seen before that the relaxation time only weakly depends on the particle softness (Figure 3.5CD). This model predicts that the lag time depends inversely on the oscillation period, where we would expect the lag time to approach zero for longer oscillation periods,  $\lim_{T \rightarrow \infty} \tan \delta(T) = 0$ . In the next sections, we will systematically investigate both dependencies.



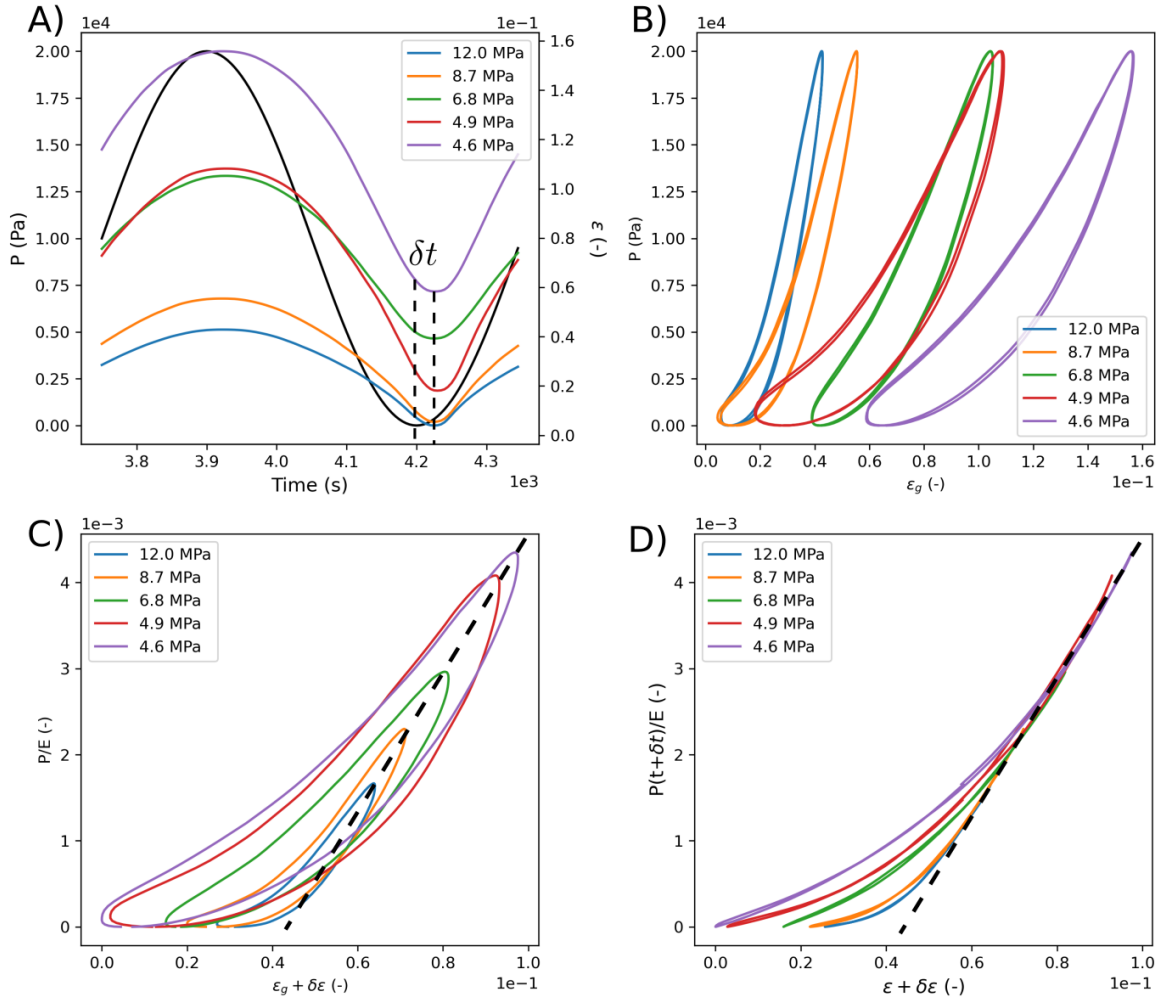


Figure 3.9: A) Imposed pressure (left y-axis, black line) and observed strain (right y-axis, colored lines) over time for one oscillation, for packings of particles with different Young's moduli (indicated in the legend). B) Imposed pressure as function of the observed strain for the last two compression cycles in a series of 10, for different particle softnesses. C) Imposed pressure, non-dimensionalized by the Young's moduli of the particles, as function of the observed strain. A small offset ( $\delta\epsilon$ ) was applied to the strain to align the linear regimes during the compression. D) Phase shift corrected, non-dimensionalized pressure as function of the observed strain. Again, an offset was applied to the observed strains to align the linear regimes.

### 3.3.C Systematic investigation of particle softness

We performed the oscillatory compression for several particle softnesses, all at an oscillation period of 600 seconds. Figure 3.9A shows both the imposed pressure ( $P$ , black line, left y-axis) and the observed global strain ( $\epsilon$ , colored lines, right y-axis) over time. The observed strains all appear shifted  $\delta t \approx 25$  s for a 600 s cycle (or a phase-shift  $\delta \approx 0.26rad$ ), irrespective of the particle softness, despite the weak dependency of  $\tau$  on  $E$ . If we assume the longest relaxation time is the major contributor to the lag time, and fill in the relaxation time obtained from the step-stress experiments,  $\tau_2 \approx 25s$ , we find that the  $\delta = \tan^{-1}(2\pi 25/600) \approx 0.26$ .

Figure 3.9C shows the non-dimensionalized pressure ( $P/E$ ) as function of the observed

global strain. Here, we can see that all compressions appear to reach a linear stress-strain relationship with the same slope (indicated by the dashed line), albeit a bit obfuscated by the hysteresis. However, not all experiments reach this linear regime at the same strain. There appears to be a soft onset of the compaction, the magnitude of which depends on the particle softness. Hence, a collapse was only observed when an offset ( $\delta\varepsilon_g$ ) was applied to align the linear regimes.

This linear region becomes much more apparent in Figure 3.9D, which shows the phase-shift corrected pressure ( $P(t + \delta t)/E$ ) non-dimensionalized by the Young's modulus of the particles. A clear linear scaling at higher strains can be observed that is independent of particle softness. At lower strains, there is a difference between the different softnesses. We suspect that this difference is caused by rearrangements. The confining pressure at equal strain is lower for softer particles, which would make rearrangements easier. The potential presence of reversible rearrangements will be touched upon in the next chapter (4).

### 3.3.D Systematic investigation of oscillation period

Where the loss tangent didn't depend on the particle softness, eq. 3.35 indicates that the loss tangent scales inversely with the oscillation period. Figure 3.10 shows the observed  $\varepsilon_g$  for cyclically imposed  $\Delta P$  (two cycles) for different oscillation periods  $T$ , for two different particle softnesses (12 MPa and 0.4 MPa, Figure 3.10AB and CD, respectively).

We see that for fast oscillations (Figure 3.10AC, dark blue,  $T = 30\text{-}60$  s), it takes more than two cycles for the system to reach a steady state (no overlap between the first and second cycle). This indicates that the oscillation period is close to (one of) the relaxation time(s). Furthermore, the imposed  $\Delta P$  and observed  $\varepsilon_g$  response seem almost completely out of phase, the strain is minimum/maximum close to where  $\frac{d\Delta P}{dt}$  is maximum ( $\Delta P = 10^4 Pa$ ), whereas we would expect the elastic response to be in phase, further indicating that these experiments are dominated by viscous relaxation.

On the other side of the spectrum is the quasi-static approach, where the oscillation period is much longer than the relaxation timescale. We observed that at longer  $T$ , the system enters the limit cycle almost immediately, as the first and second cycle overlap almost entirely, as expected. We also observed that the hysteresis (enclosed area) decreases with increasing  $T$ , but doesn't fully disappear even at an oscillation period nearly 2 orders of magnitude larger than the relaxation time (Figure 3.10BD).

We can determine the experimental phase-shift like in Figure 3.9 for different oscillation periods. Figure 3.10E shows the loss tangent as function of the oscillation period. We can observe two main features. Firstly, the loss tangent is independent of particle softness. All data corresponding to 12 MPa particles and 0.4 MPa particles perfectly overlap. This further strengthens our previous experiments, which also indicated that the phase-shift does not depend on the particle softness.

Secondly, we observe that the loss tangent scales inversely with the oscillation period, as predicted by the model (eq. 3.35). However, where the model predicts that the loss tangent approaches zero for increasing oscillation periods, the data approaches a non-zero value at long oscillation periods. This is very counter-intuitive, as this implicates that, even under quasi-static conditions, stress and strain would be out of phase. This cannot be explained by any viscoelastic model.

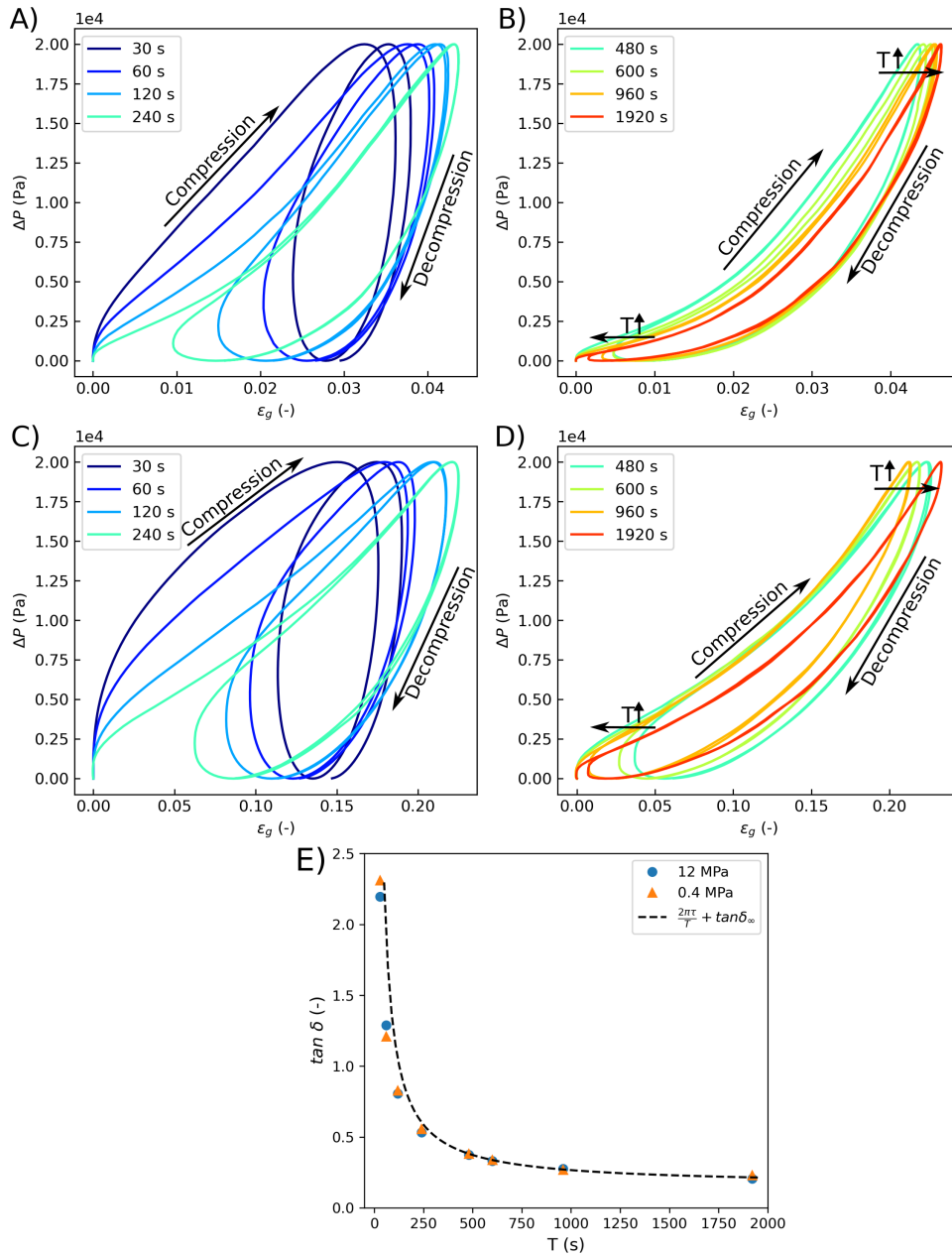


Figure 3.10: A) Global strain response of an ensemble of hard particles ( $E = 12$  MPa) on oscillatory imposed pressure for different short oscillation periods. B) Global strain response of an ensemble of hard particles ( $E = 12$  MPa) on oscillatory imposed pressure for different long oscillation periods. The arrows indicate the trend of the minima and maxima with increasing  $T$ . C) Global strain response of an ensemble of soft particles ( $E = 0.4$  MPa) on oscillatory imposed pressure for different short oscillation periods. D) Global strain response of an ensemble of soft particles ( $E = 0.4$  MPa) on oscillatory imposed pressure for different long oscillation periods. The arrows indicate the trend of the minima and maxima with increasing  $T$ . E) Loss tangent as function of oscillation period for two different Young's moduli. The dashed line indicates the fit with eq. 3.35 with an offset for a period independent phase shift.

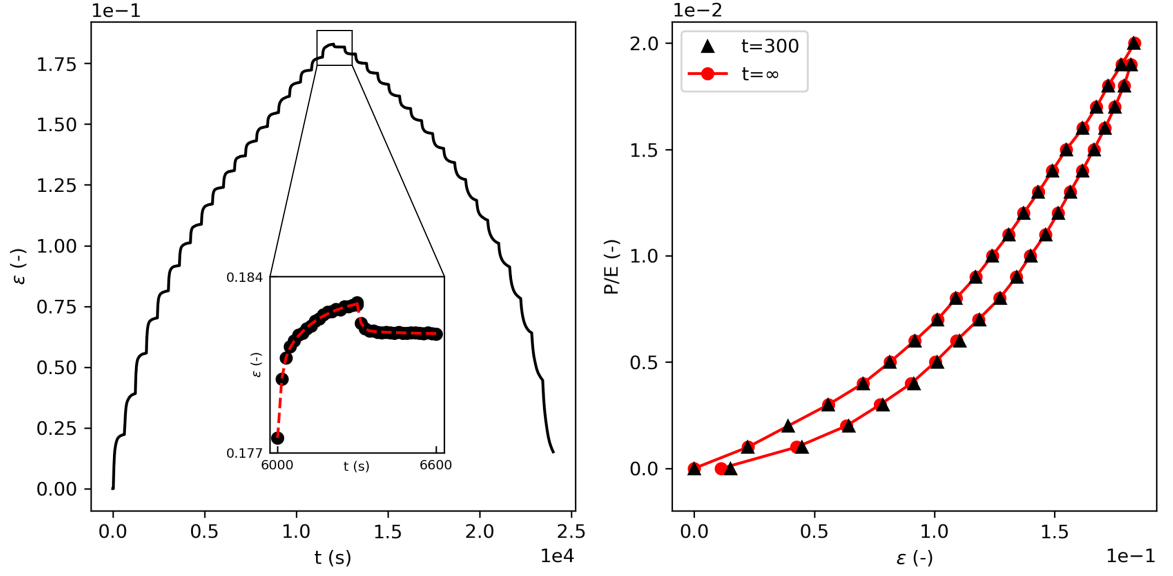


Figure 3.11: A) Oscillation of an ensemble of 0.4 MPa particles in discrete steps of 1 kPa of additional applied pressure, where the strain was monitored over time. Insert: strain over time for the last compression step and first decompression step.  $\Delta P$  at the start of the last compression and the end of the first decompression is identical. Red dashed line indicates the fit with the models eq. 3.24 and 3.25. B) Non-dimensionalized pressure as function of observed strain for the step-wise oscillatory compression. The black triangles ( $\blacktriangle$ ) indicate the strain observed at 300s after the step-increase in pressure. The red circles, connected by a solid red line to guide the eye, indicate the limit strain as  $t \rightarrow \infty$ .

### 3.3.4 Stepwise oscillation

Intrigued by the hysteresis that persists at long time-scales, we performed an oscillation in discrete steps, rather than continuously, and followed the strain response over time. For each of the steps, we fitted the response using the generalized Kelvin-Voigt model. While experimentally it might not be feasible to reach the equilibrium state, we can approximate the equilibrium state by fitting  $\varepsilon(t)$  with the generalized Kelvin-Voigt model and taking  $\lim_{t \rightarrow \infty} \varepsilon_{GKV}(t)$ .

Figure 3.11A shows such stepwise oscillation. Each of the steps were well-fitted with the previously mentioned model (example fit given in the insert of Figure 3.11A). It's worth mentioning the level of detail and accuracy (both spatial and temporal) our experiments provide. During the first decompression step, the strain decreases from 0.1830 to 0.1817, which we are easily able to detect. Moreover, we can follow how the packing approaches this plateau. The standard deviation in the plateau (15 data points) is  $2.3 \cdot 10^{-5}$ . We're not aware of any experimental setup that can provide this level of detail. Furthermore, we currently limited the experiment to 1 image per 30 seconds, as this already gathers  $\sim 10$  Gb of data over the course of the experiment. Without having to change anything in the setup, we could increase the sampling frequency to 10 Hz without having to change anything in the setup, giving also an incredibly high temporal accuracy.

Taking the spatial and temporal accuracy into account, it becomes obvious that the difference between the last data point collected (indicated with  $\blacktriangle$  in Figure 3.11B, taken 300 s after the step in pressure) and the extrapolated limit (indicated with  $\bullet$ ) is insignificant for all but

the last data-point during decompression, which will go to  $\varepsilon_g = 0$ , if given enough time. This indicates that at each step, the system is able to reach equilibrium. Yet, the compression and decompression curves don't overlap, meaning that there is a time-independent, but history dependent, component that causes the hysteresis.

The time-independence part of the hysteresis becomes very apparent when comparing the last compression step and the first decompression step (Figure 3.11A insert). The pressure at  $t=6000$  s (just before the last compression step is started) is equal to the pressure during the first decompression step ( $t=6300-6600$  s), one would therefore expect that the strain at the start of the last compression step and the end of the first decompression step would be identical,  $\varepsilon_g(t = 6000) = \varepsilon_g(t = 6600)$ . However, this is far from the case, as during the decompression only  $\sim 25\%$  of the strain is recovered. Yet, after a full cycle, the strain is recovered.

One explanation could be that there are microscopic rearrangements that seem irreversible *within* one cycle (meaning the position of an arbitrary particle  $i$  in cycle  $n$ ,  $\mathbf{x}_i$  in, depends on whether the pressure,  $P$ , is approach by increasing  $P$  or decreasing  $P$ )  $\mathbf{x}_i(P^\uparrow(n)) \neq \mathbf{x}_i(P^\downarrow(n))$ , whereas the rearrangements are reversible over a whole cycle  $\mathbf{x}_i(P^\uparrow(n)) = \mathbf{x}_i(P^\uparrow(n+1))$ . This phenomenon has been reported in both experiments and simulations, but only under oscillatory shear conditions [16–21]. This will be briefly touched upon in the next chapter (section 4.3.6).

### 3.4 Conclusions

In this chapter, we have shown a new method to fabricated ensembles of particles inside a microfluidic channel using an in-situ photolithographic technique. We compressed these particles against a membrane by means of hydrodynamic friction with the uncured solution surrounding the particles. We found that, upon imposing a step increase or decrease, the strain approached the new stable value exponentially, which was very well described by a generalized Kelvin-Voigt model with 2 relaxation timescales. We attempted to attribute one of the relaxation timescales to the poro-elastic relaxation of the particles. However, obtaining accurate relaxation timescales on small particles has proven to be difficult.

The full characterization of the viscoelastic behavior of the particle packings by the step stress experiments allowed us to describe the time lag observed during the continuous oscillatory compressions of the packing, which was shown to be independent of the particle softness, and scales as  $\tan \delta \propto 1/T$  with  $T$  the oscillation period. The loss tangent did, however, not decay to zero in the quasi-static limit, as one would expect for a viscoelastic material. Instead, it approached a loss tangent of  $\sim 0.25$ .

We further confirmed the presence of this time-independent loss tangent by performing step-wise oscillatory compressions. The time-evolution of the strain during each compression step was fitted with the generalized Kelvin-Voigt model, which confirmed that the packing reached equilibrium during each of the compression steps, and that any hysteresis was therefore independent of the driving frequency. This could potentially be due to microscopic rearrangements, however, the role and timescale of particle-scale rearrangements on the relaxation are not clear yet.

### 3.5 References

- [1] Maurice A Biot. General theory of three dimensional consolidation. *J. Appl. Phys.*, 12 (155):155–164, 1941. 37
- [2] Alexander H.D. Cheng. *Poroelasticity*, volume 27. Springer Berlin Heidelberg, 2016. 37
- [3] Yu Yun Lin and Bao Wun Hu. Load relaxation of a flat rigid circular indenter on a gel half space. *Journal of Non-Crystalline Solids*, 352(38-39):4034–4040, 10 2006. 37, 46
- [4] Wei Chun Lin, Kenneth R. Shull, Chung Yuen Hui, and Yu Yun Lin. Contact measurement of internal fluid flow within poly(n- isopropylacrylamide) gels. *Journal of Chemical Physics*, 127(9), 2007. 37
- [5] Jean François Louf and Sujit S. Datta. Poroelastic shape relaxation of hydrogel particles. *Soft Matter*, 17(14):3840–3847, 2021. 38, 46
- [6] Edwin P. Chan, Yuhang Hu, Peter M. Johnson, Zhigang Suo, and Christopher M. Stafford. Spherical indentation testing of poroelastic relaxations in thin hydrogel layers. *Soft Matter*, 8(5):1492–1498, 2 2012. 38
- [7] Michael Rubinstein and Ralph H. Colby. *Polymer Physics*. Oxford University Press, 2003. 38
- [8] Giuseppe Ciccone, Oana Dobre, Graham M. Gibson, Jose Manuel Rey, Cristina Gonzalez–Garcia, Massimo Vassalli, Manuel Salmeron–Sanchez, and Manlio Tassieri. What Caging Force Cells Feel in 3D Hydrogels: A Rheological Perspective. *Advanced Healthcare Materials*, 9(17), 9 2020. 44
- [9] Jean Cappello. *Dynamics of freely transported fibers in confined viscous flows : Role of shape and flexibility*. PhD thesis, Université de Paris Cité, 2020. 45, 46
- [10] Fluigent. Microfluidic instrument responsiveness. 46
- [11] Nicholas Mavrogiannis, Markela Ibo, Xiaotong Fu, Francesca Crivellari, and Zachary Gagnon. Microfluidics made easy: A robust low-cost constant pressure flow controller for engineers and cell biologists. *Biomicrofluidics*, 10(3), 2016. 47
- [12] Run Ze Gao, Marie Hébert, Jan Huissoon, and Carolyn L. Ren.  $\mu$ Pump: An open-source pressure pump for precision fluid handling in microfluidics. *HardwareX*, 7, 2020. 47
- [13] Yandong Gao, Jiashu Sun, Wan Hsin Lin, Donna J. Webb, and Deyu Li. A compact microfluidic gradient generator using passive pumping. *Microfluidics and Nanofluidics*, 12(6):887–895, 2012. 47
- [14] Jung Eun Bae, Mirin Lee, Kwang Soo Cho, Kwan Ho Seo, and Dong Gug Kang. Comparison of stress-controlled and strain-controlled rheometers for large amplitude oscillatory shear. *Rheologica Acta*, 52(10-12):841–857, 11 2013. 49
- [15] Patrick Oswald. *Rheophysics: The Deformation and Flow of Matter*. Cambridge University Press, 1 edition, 2009. 49

- 
- [16] Nathan C. Keim and Paulo E. Arratia. Yielding and microstructure in a 2D jammed material under shear deformation. *Soft Matter*, 9(27):6222–6225, 7 2013. 54
- [17] Nathan C. Keim and Paulo E. Arratia. Mechanical and Microscopic Properties of the Reversible Plastic Regime in a 2D Jammed Material. *Physical Review Letters*, 112(2): 1–5, 2014.
- [18] K. Lawrence Galloway, Douglas J. Jerolmack, and Paulo E. Arratia. Quantification of plasticity: Via particle dynamics above and below yield in a 2D jammed suspension. *Soft Matter*, 16(18):4373–4382, 2020.
- [19] Nathan C. Keim and Paulo E. Arratia. Role of disorder in finite-amplitude shear of a 2D jammed material. *Soft Matter*, 11(8):1539–1546, 2 2015.
- [20] Nikolai V. Priezjev. Reversible plastic events during oscillatory deformation of amorphous solids. *Physical Review E*, 93(1), 1 2016.
- [21] Micah Lundberg, Kapilanjani Krishan, Ning Xu, Corey S. O’Hern, and Michael Dennin. Reversible plastic events in amorphous materials. *Physical Review E - Statistical, Nonlinear, and Soft Matter Physics*, 77(4), 4 2008. 54

## Chapter 4

# Compaction of dense suspensions of soft particles: Micro-mechanical perspective

So far, we've approached the experiments from a continuum mechanical point-of-view by considering the ensembles of particles to be a complex viscoelastic solid, and disregarding all extra insights the microscopic data can provide. Together with Larry Galloway and Paulo Arratia, we switched point-of-view, and analyzed the exact same experiments from a micro-mechanical point-of-view.

This chapter starts with a description of the interaction between the particles. Next, we describe the microscopic pressure, calculated from particle-particle interactions. From this microscopic pressure, we derive a constitutive equation for the pressure as function of the deformation of the entire packing. Then, we explain the origin of microscopic quantities, their distributions and how they change during compaction. This is followed by a discussion on the determination of the particle radii.

Next, we study the evolution of the microscopic quantities, such as the average overlap between particles, microscopic pressure, average number of contacts per particle, the contact orientation, as well as the distribution of forces as function of the global strain. Lastly, we perform a preliminary investigation on the trajectories of the particles during compression, to find a possible origin of the soft onset of the compaction.



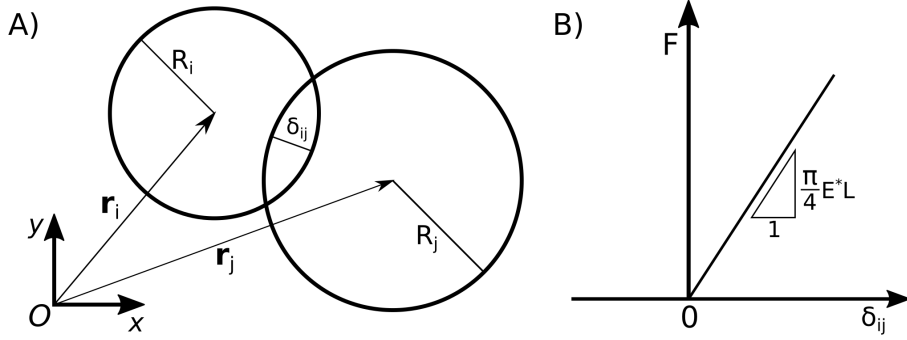


Figure 4.1: A) Schematic overview of two interacting particles,  $i$  and  $j$ , with radii  $R_i$  and  $R_j$ , and positions  $\mathbf{r}_i$  and  $\mathbf{r}_j$ , respectively. B) Interaction force  $F$  as function of the overlap between the particles. The slope is given by the Hertzian contact mechanics for cylinders with parallel axes, where  $E^*$  is the corrected Young's modulus and  $L$  the length of the cylinder.

## 4.1 Introduction

### 4.1.1 Mechanics

Two neighboring particles,  $i$  and  $j$ , are assumed to interact upon contact. This interaction can be decomposed in two forces, a normal force perpendicular to the contact ( $\mathbf{F}_{ij,\perp}$ ), and a frictional force tangential to the contact ( $\mathbf{F}_{ij,\parallel}$ ). The normal force exerted by particle  $i$  on  $j$  ( $F_{ij}$ ) can be described as a function of the magnitude and direction of their deformation ( $\delta_{ij}$  and  $\hat{\mathbf{r}}_{ij}$ , respectively), which is a function of their centers ( $\mathbf{r}_i$  and  $\mathbf{r}_j$ ), and their radii ( $R_i$  and  $R_j$ ) (Figure 4.1A):

$$\delta_{ij} = \|\mathbf{r}_j - \mathbf{r}_i\| - R_i - R_j \text{ and } \hat{\mathbf{r}}_{ij} = \frac{\mathbf{r}_j - \mathbf{r}_i}{\|\mathbf{r}_j - \mathbf{r}_i\|} \quad (4.1)$$

$$\mathbf{F}_{ij} = F(\delta_{ij})\mathcal{H}(\delta_{ij})\hat{\mathbf{r}}_{ij} \quad (4.2)$$

Where  $F(\delta_{ij})$  is some function describing the magnitude of the force given some overlap  $\delta_{ij}$ ,  $\mathcal{H}(\delta_{ij})$  the Heaviside step function, such that particles only exert a force when they are in physical contact:

$$\mathcal{H}(\delta_{ij}) = \begin{cases} 0 & \text{if } \delta_{ij} \leq 0 \\ 1 & \text{if } \delta_{ij} > 0 \end{cases} \quad (4.3)$$

The magnitude of the interaction between two particles  $i$  and  $j$  (cylinders with parallel axes) can be approximated by a Hookean spring with spring constant  $k = \frac{\pi}{4}E^*L$ , according to Hertzian contact mechanics for cylinders with parallel axes [1]:

$$F_{ij}(\delta_{ij}) = \frac{\pi}{4}E_{ij}^*L\delta_{ij} \quad (4.4)$$

with  $F_{ij}$  the repulsive force between particles  $i$  and  $j$ ,  $L$  the length of the cylinder,  $\delta_{ij}$  the overlap between particles  $i$  and  $j$ , and

$$\frac{1}{E_{ij}^*} = \frac{1 - \nu_i^2}{E_i} + \frac{1 - \nu_j^2}{E_j} \quad (4.5)$$

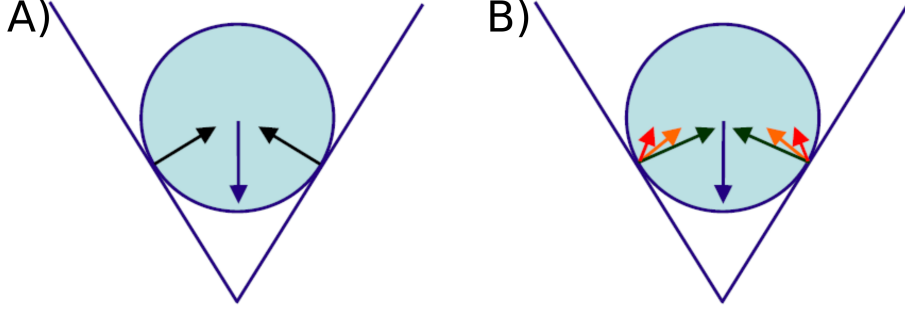


Figure 4.2: A) Schematic illustration of a frictionless 2D disk (light blue circle) settled in a groove (blue lines), with the arrows indicating the magnitude and direction of the contact forces that balance all forces B) Schematic illustration of a 2D disk with friction (light blue circle) settled in a groove (blue lines), with the arrows indicating the magnitude and direction of some of the infinitely many possible contact forces that satisfy the balance of forces. Figure adapted from [2]

with  $E_i$  the Young's modulus of particle  $i$ ,  $\nu_i$  the Poisson's ratio of particle  $i$ . Since in all our experiments, particles  $i$  and  $j$  are made of the same material,  $E_i = E_j$  and  $\nu_i = \nu_j$ . Simplifying eq. 4.5 to

$$E^* = \frac{E}{2(1 - \nu)} \quad (4.6)$$

The contact force as function of the overlap is schematically represented in Figure 4.1B.

The tangential force,  $F_{ij,\parallel}$ , follows Amontons-Coulomb's law

$$F_{ij,\parallel} \leq \mu F_{ij,\perp} \quad (4.7)$$

with  $\mu$  the friction coefficient. This inequality is, however, problematic in experiments, as it leads to an indeterminacy of the forces. When a frictionless (2D) disk settles in a groove under gravity, there are two degrees of freedom (normal forces with both sides) and two balance equations (total force in x and y direction), leading to a unique isostatic solution (Figure 4.2. When particles are frictional, the disk has 4 degrees of freedom (two normal forces and two tangential forces) and only 3 equations to balance. (net force in x and y, and net torque). This leads to an infinite set of solutions, where the actual solution depends on the history of contact, which is hard (if not impossible) to access experimentally.

Fortunately, hydrogels are known for their low coefficient of friction. Although we were not able to get an accurate measure of the friction coefficient of our particles, nor able to find reported values for the exact same material and composition as ours, reported values of similar hydrogels range from 0.03 down to  $\sim 10^{-4}$  [3-5]. We believe it is therefore justified to assume  $F_{ij,\parallel} = 0$ . This eliminates the inequality, and allows us to extract a single solution of the interparticle forces from the particle overlaps.

#### 4.1.2 Microscopic stress

In their seminal work Irving and Kirkwood [6] formulated a stress tensor,  $\boldsymbol{\sigma}$ , based on microscopic quantities. They described  $\boldsymbol{\sigma}$  to be the sum of a kinetic component and a contact component,  $\boldsymbol{\sigma} = \boldsymbol{\sigma}^K + \boldsymbol{\sigma}^C$ , with

$$\sigma_{\alpha\beta}^C = \frac{1}{\Omega_t} \sum_{i < j} F_{ij}^{\alpha} r_{ij}^{\beta} \quad (4.8)$$

where  $\Omega_t$  is the total volume of the system, the sum is over all contact pairs  $ij$ ,  $F_{ij}^\alpha$  the component of the contact force between particles  $i$  and  $j$  along the coordinate axis  $\alpha$ , and  $r_{ij}^\beta$  the vector component of  $\mathbf{r}_j - \mathbf{r}_i$  along the  $\beta$  coordinate axis.

The kinetic part of the stress tensor was determined to be:

$$\sigma_{\alpha\beta}^K = \frac{1}{\Omega_t} \sum_i m_i u_i'^\alpha u_i'^\beta \quad (4.9)$$

where the sum is over all particles,  $m_i$  is the mass of particle  $i$  and  $u_i'^\alpha$  is the velocity fluctuation component of particle  $i$  along coordinate axis  $\alpha$  with

$$u_i'(t) = u_i(t) - U(\mathbf{r}_i, t) \quad (4.10)$$

with  $u_i(t)$  the velocity of particle  $i$  at time  $t$  and  $U(\mathbf{r}_i, t)$  the average particle velocity at the position of particle  $i$  ( $\mathbf{r}_i$ ) at time  $t$ .

$\sigma^C$  can be seen as the force the particles are exerting on each other and the confining box because they are squeezed into a (slightly) too small box. Whereas  $\sigma^K$  can be seen as the pressure caused particles bumping into the confining box, akin to how gas atoms exert pressure on the vessel they are contained in. For gases in a closed isochoric system, the kinetic energy depends on the temperature. Hence,  $u_i'$  is often referred to as the ‘‘granular temperature’’ [7–9]

For jammed packings ( $\sigma^C > 0$ ) under quasi-static conditions ( $U(\mathbf{r}_i) \approx 0$  and  $v_i' \approx 0$ ), the stress is dominated by the contact forces ( $\sigma^C > \sigma^K$ ). Therefore, the total stress is approximately equal to the contact stress:

$$\sigma_{\alpha\beta} \approx \sigma_{\alpha\beta}^C = \frac{1}{\Omega_t} \sum_{i<j} F_{ij}^\alpha r_{ij}^\beta \quad (4.11)$$

This is commonly referred to as the Kirkwood-Irving stress or Kirkwood-Irving equation [6].

From this equation, it is possible to derive a macroscopic stress-strain scaling. First, we can rewrite eq. 4.11 as

$$\sigma_{\alpha\beta} = \frac{N_c}{\Omega_t} \langle F_{ij}^\alpha r_{ij}^\beta \rangle \quad (4.12)$$

where  $\langle \cdot \rangle$  indicates the average over all contacts with  $i < j$  and  $N_c$  is the total number of contacts. We can then define the coordination number  $Z$  (the average number of contacts of each particle), and the packing fraction  $\phi$  (fraction of the total volume occupied with particles), assuming a pseudo 2D system of co-axial cylindrical particles of length  $L$  that span the entire system height.

$$Z = \frac{2N_c}{N_p} \quad (4.13)$$

$$\phi = \frac{\Omega_p}{\Omega_t} = \frac{\pi \langle D^2 \rangle L N_p}{4\Omega_t} \quad (4.14)$$

with  $N_p$  the number of particles,  $\Omega_p$  the volume occupied by the particles and  $\langle \cdot \rangle$  the average taken over all particle diameters,  $D$ . The prefactor 2 comes from the fact that each contact is counted for both particles involved in the contact. Now using the definition of the microscopic pressure (for a 2D-system)

$$P_m = \text{tr}(\boldsymbol{\sigma})/2 \quad (4.15)$$

and the fact that the inter-particle forces are not correlated with the particle size [10], as well as the assumption that the forces are randomly oriented (which we will later verify), we can write the microscopic pressure as:

$$P_m = \frac{Z\phi}{\pi L \langle D^2 \rangle} \langle |F_{ij}| \rangle \langle |r_{ij}| \rangle \quad (4.16)$$

Under small deformation of circular particles the magnitude of the branch vector (vector connecting the two particle centers) is equal to the sum of the radii of the particles,  $|r_{ij}| = R_i + R_j$ . Then, assuming the neighbors of a particle are random (e.g. no polycrystalline domains), the average of the branch vector magnitudes is equal to the average particle diameter  $\langle |r_{ij}| \rangle = \langle D \rangle$ . And, assuming that polydispersity is minor, such that  $\langle D^2 \rangle \approx \langle D \rangle^2$ , the microscopic pressure becomes:

$$P_m = \frac{Z\phi}{\pi L \langle D \rangle} \langle F \rangle \quad (4.17)$$

Given the Hertzian contact mechanics of 2 parallel cylinders with an overlap  $\delta$  (eq. 4.4 [1]), we can approximate the average inter-particle force as

$$\langle F \rangle = \frac{\pi}{4} E^* L \langle \delta \rangle \quad (4.18)$$

writing the average overlap  $\langle \delta \rangle$  as the average particle size deformed by an average local strain  $\langle D \rangle \langle \varepsilon_l \rangle$ , and substituting this into eq. 4.18 yields

$$\langle F \rangle = \frac{\pi}{4} E^* L \langle D \rangle \langle \varepsilon_l \rangle \quad (4.19)$$

We can substitute eq. 4.19 into eq. 4.17 to obtain a description of the microscopic pressure, as function of the local strain:

$$P_m = \frac{Z\phi}{4} E^* \langle \varepsilon_l \rangle \quad (4.20)$$

There are now two descriptions of the strain of a single sample: a global strain derived from the global deformation of the packing, and a local strain derived from the deformation of the constituent particles. Finding a relation between them, would yield a macroscopic description of compaction, purely from microscopic parameters. We should note that despite both strains being non-dimensional, they describe a different quantity. The global strain is a 2D strain (decrease in area), whereas the local strain is a 1D strain (decrease in distance). It is therefore not obvious if they are identical, or even scale linearly.

Cantor et al. [12] found that  $\varepsilon_g$  and  $\varepsilon_l$  are proportional for all their simulations, with proportionality constant  $\alpha = 4$ . The same group found a similar scaling for a 3D packing and for a 2D packing of pentagons [13, 14]. Substituting  $\varepsilon_l$  for  $\varepsilon_g$  in eq. 4.20 yields the macroscopic description of compaction obtained from microscopic parameters

$$P_m = \frac{Z\phi}{4\alpha} E^* \varepsilon_g \quad (4.21)$$

Slight variations on this model for the macroscopic stress-strain relationship exist, Agnolin and Roux provide an model for a 3D system of spheres while not specifying a contact model [15–17], Nezamabadi et al. [11] assume that  $\varepsilon_g = \varepsilon_l$ , and Cantor et al. [12] assume the contact forces are linear springs, and therefore don't include the geometrical prefactor,  $\frac{\pi}{4}$ , obtained from the Hertzian approximation of the contact forces.

This model is only valid for small deformations, several assumptions fail at larger deformations, as can be concluded from the deviation from the linear regime in Figure 4.3A, and the pink dashed line in Figure 4.3B. Efforts have been made to extend this model into the large deformation regime, which will not be discussed here [12, 18, 19].

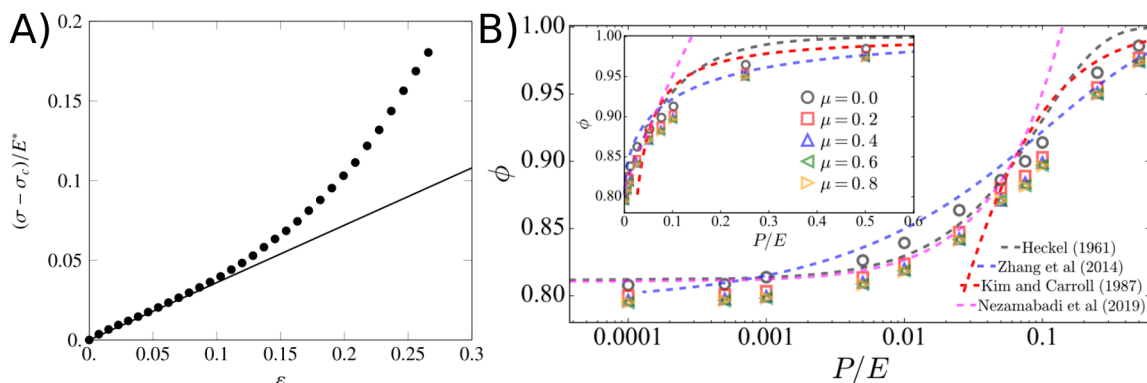


Figure 4.3: A) Non-dimensionalized microscopic pressure versus global strain for simulations of neo-Hookean particles. Figure taken from [11] B) Non-dimensionalized microscopic pressure as function of packing fraction for a simulation of a coupled discrete and finite element method. Inset: same data on lin-lin axis. Figure taken from [12]. The model described here is indicated with the pink dashed line. In both cases, the model captures the initial linear regime well, but fails to capture the non-linear regime at higher compressions.

### 4.1.3 Jamming

To calculate the global strain (as function of time), the volume of the system in a stressed state is compared to the volume of the system in an unstressed state. However, the requirement  $P_m = 0$  alone is not enough to define a unique reference configuration. If none of the particles are touching, and thus  $P_m(\Omega_t) = 0$ ,  $P_m(2\Omega_t) = 0$  also holds. We, therefore, define the reference volume as the volume when  $P_m$  approaches zero:

$$\Omega_{t,0} = \lim_{P_m \rightarrow 0^+} \Omega_t(P_m) \quad (4.22)$$

This is the point at which the particles just start to touch, and is commonly referred to as the jamming point (or jamming transition). At jamming, the packing becomes marginally stable, meaning that the loss of a single contact would cause the packing to become unstable. This means that the number of degrees of freedom is perfectly balanced by the number of constraints, which is called isostaticity. For a packing of  $N_p$  frictionless spheres in  $d$  dimensions, using the definition of the coordination number  $Z = \frac{2N_c}{N_p}$  (eq. 4.13) the total number of contacts is  $N_c = \frac{ZN_p}{2}$ , which needs to balance  $Nd$  degrees of freedom, where  $d$  is the dimensionality of the system. Hence, the coordination number at isostaticity for a 2D system is  $Z_0 = 2d = 4$ . For frictional spheres, also torque components need to be taken into account. This leads to  $\frac{ZN_d}{2}$  force components and  $Nd$  translation degrees of freedom and  $\frac{d(d-1)N}{2}$  rotational degrees of freedom. So, at isostaticity  $Z_0 = d + 1 = 3$  [2, 20]. In reality,  $Z_0$  will be somewhere between the two, where  $Z_0$  will be close to 4 for nearly frictionless particles, and get closer to 3 when the coefficient of friction increases [21–23].

### 4.1.4 Packing fraction

As the system is compressed, naturally the volume occupied by the particles relative to the total volume of the system increases. Assuming incompressible particles ( $\nu = 0.5$ ), a simple relation between  $\varepsilon_g$  and  $\phi$  can be derived, as the total volume occupied by the particles is

constant.

$$\phi = \frac{\Omega_p}{\Omega_t} \text{ and } \varepsilon_g = -\ln\left(\frac{\Omega_t}{\Omega_{t,0}}\right) \quad (4.23)$$

$$\phi = \frac{\Omega_p}{\Omega_{t,0}} e^{\varepsilon_g} = \phi_0 e^{\varepsilon_g} \quad (4.24)$$

with  $\Omega_p$  the volume occupied by the particles,  $\Omega_t$  the total volume under compression,  $\Omega_{t,0}$  the volume of the uncompressed system (at jamming), and  $\phi_0$  the packing fraction of the uncompressed system. This relation approximates  $\phi$  well at low strains, but will overestimate the packing fraction at high strains, especially for compressible materials ( $\nu < 0.5$ ).

#### 4.1.5 Coordination number

Previously, we have defined the coordination number (the average number of contacts of each particle) as the number of contacts over the number of particles  $Z = \frac{2N_c}{N_p}$  (eq. 4.13). We considered no new contacts to be formed in the small deformation limit. This is, however, not entirely true. We can approximate the number of newly formed contacts by taking a closer look at the microstructure.

One common way to characterize the microstructure is with the pair correlation function,  $g(r)$ , which is the number of particles in a shell from  $r$  to  $r + dr$  (green particles in Figure 4.4A) around a reference particle (gray particle in Figure 4.4A), normalized by the expected number of particles based on the area of the shell and the average number density in the system. The pair correlation function has a typical form for disordered materials of monodisperse particles (Figure 4.4C). To make  $g(r)$  independent of the particle size,  $r$  is normalized by the particle diameter. For  $r \ll 1$ ,  $g(r) \approx 0$ , as the inter-particle forces are not sufficient to reach such overlaps. For  $r \approx 1$ ,  $g(r)$  spikes, as it is likely to find particles that are slightly deforming each other or almost touching. Lower and broader correlations are found at other small gaps (Figure 4.4BC). For  $r \gg 1$ , the probability of finding a particle is equal to the number density of the material ( $g(r) = 1$ ) as there is no long-range correlation between particle positions (unlike in ordered materials).

Taking a closer look at the first peak, we can interpret  $g(r + dr)$  as the probability of finding two particles  $dr$  apart. For small strains,  $\varepsilon_l \approx dr$ . Hence, applying a local strain,  $\varepsilon_l$  will bring all particles with a spacing less than  $dr$  in contact. In their seminal work [24] showed in simulations of monodisperse, soft, spheres that for  $r > 1$ ,  $g(r) \propto (r - 1)^{-0.5}$ . Integrating  $g(r)$  from  $r = 1$  to  $r = 1 + dr$  is then a good measure of the amount of newly formed contacts upon an applied strain, and yields

$$Z - Z_0 \propto \sqrt{\phi - \phi_0} \quad (4.25)$$

with  $Z_0$  the coordination number at jamming ( $P \approx 0$ ),  $\phi$  the packing fraction, and  $\phi_0$  the packing fraction at jamming. This was in good agreement with their data, as well as previous studies [20, 26, 27, 27].

While this numerical and experimental scaling has already been observed ubiquitously, the origin of this scaling was not obvious. Only recently, theoretical efforts in the field of hard-sphere (thermal) glasses have shown a very similar scaling derived from first-principles. The full replica symmetry breaking (fullRSB) theory predicts the probability of small gaps  $\delta r$  to scale as  $g(\delta r) \propto (\delta r)^{-0.412\dots}$ , and therefore  $Z - Z_0 \propto (\phi - \phi_0)^{0.588\dots}$  [28, 29], and saw recent experimental verification [30].

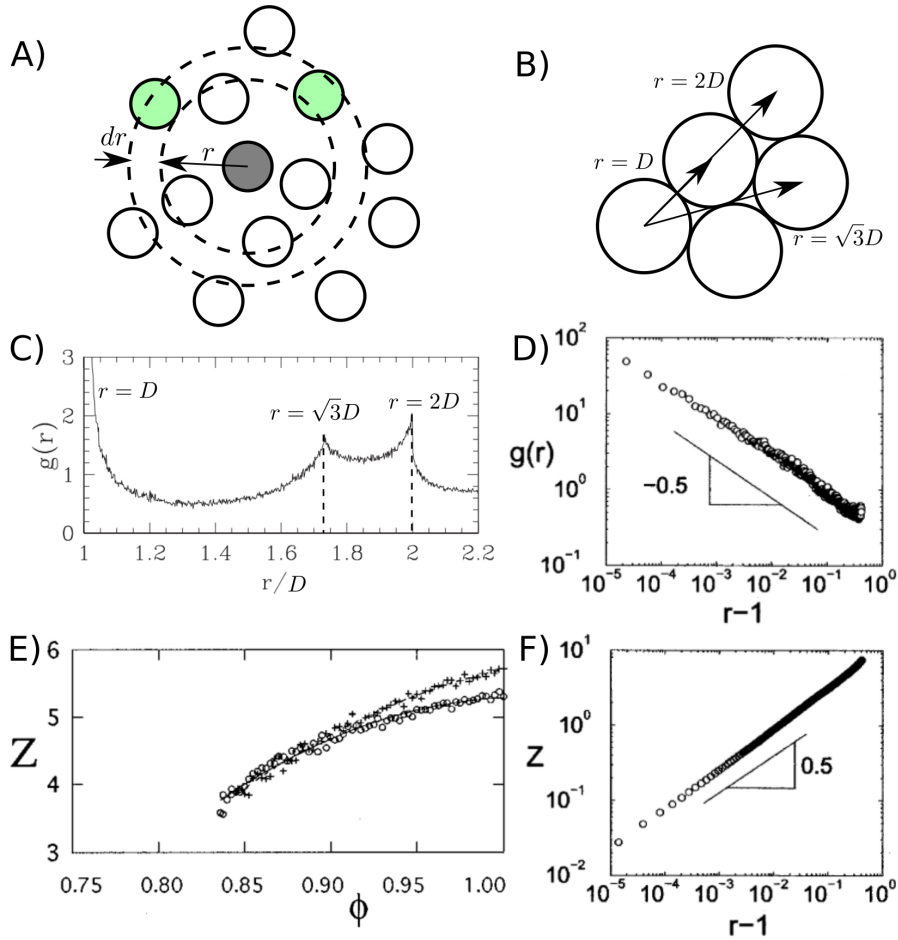


Figure 4.4: A) Schematic representation of the probability of finding a particle in a shell of width  $dr$  (green) around a central particle (gray). B) Common center to center distances for monodisperse particles. C) Typical  $g(r)$  for a disordered packing of monodisperse particles. Figure adapted from [15] D) Zoom of  $g(r)$  as function of  $r-1$  around the first peak in  $g(r)$ . Figure taken from [24] E) Coordination number as function of packing fraction obtained from a simulation of the compression of a bubble raft. Figure taken from [25]. F)  $Z$  as function of  $r-1$ .  $Z$  was obtained by numerically integrating  $g(r)$  from 1 to  $r-1$ . Figure taken from [24].

For multidisperse or polydisperse systems, the non-dimensionalization of  $r$  is less trivial than the non-dimensionalization of monodisperse systems. Non-dimensionalization by the average particle diameter will lead to distinct peaks, each corresponding to a different combination of particles interacting (small-small, small-large, large-large). Since all these interactions are binary (two particles touching), intuitively the non-dimensionalization should collapse these peaks. This can be achieved by non-dimensionalizing the distance between particles  $i$  and  $j$  by the sum of their radii ( $R_i + R_j$ ). This however has the disadvantage that overlaps and separations no longer represent a distance, but rather a strain [30].

#### 4.1.6 Force distributions

Besides information of the small gaps between particles,  $g(r)$  also provides information on the (small) overlaps between particles. Unlike in an elastic solid, which homogeneously carries

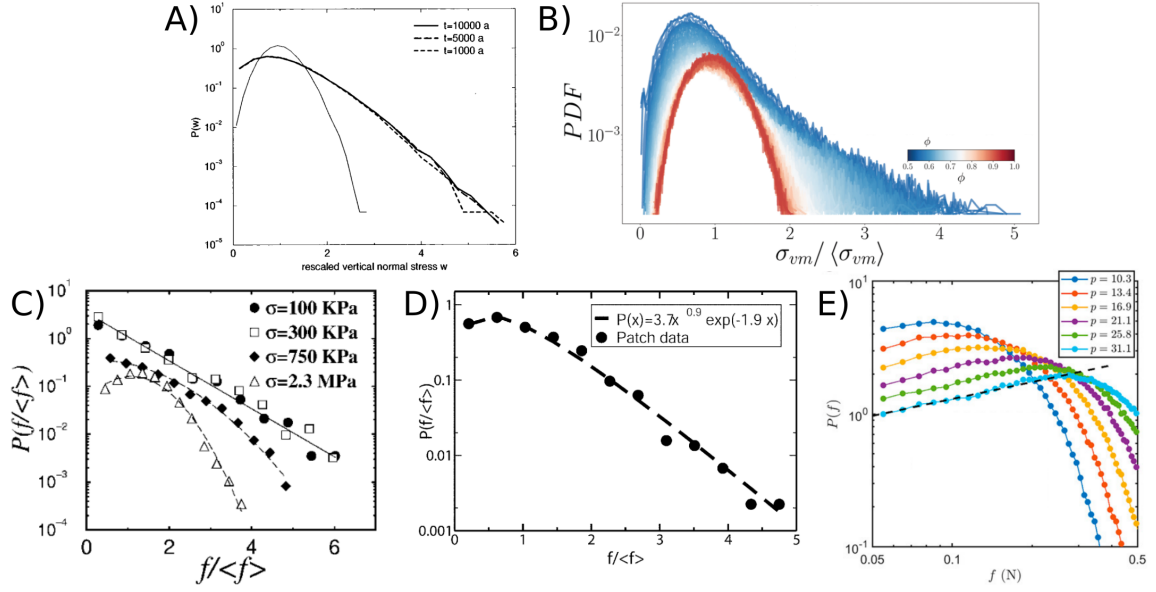


Figure 4.5: A) Force distribution as calculated from the statistical three-legged model. At high noise levels, an exponential decay is found (three lines are three different system sizes), whereas for a small amount of noise, a Gaussian-distribution was obtained. Figure is taken from [31]. B) Force distributions obtained from Non-Smooth Contact Dynamic Method simulations. As the packing fraction (and thus the confining pressure) increases, the force distribution goes from exponential (blue) to Gaussian (red). Figure adapted from [13] C) Force distributions obtained from a 3D packing of glass beads under different confining pressures. The forces are obtained by lining the wall of the container with carbon-paper, and calibrating the size of the black spot left by pressing a sphere on the carbon paper with a certain force. Again, an exponential to Gaussian transition is observed. Figure taken from [32] D) Experimental force distribution of a jammed emulsion (3D). The forces are calculated from the center-to-center distance of the droplets. Figure taken from [33] E) Distribution of the small forces as determined from experiments with photoelastic particles. The dashed line indicates the theoretical prediction for the small forces [28]. Figure is taken from [30].

the applied load across the contact area, the load in a granular material is carrier by a sparse network of particles, called a force network [34–36]. For each configuration of particles there are many (equally likely) microscopic configurations of the forces that satisfy force balance and boundary conditions [37, 38], the exact configuration is determined at jamming for athermal systems (but slightly before jamming for thermal systems [39, 40]). Hence, if a system ever unjams, it will form a different force network [40, 41]

While there are many different force-networks given a microscopic configuration, it turns out that these force-networks share the probability distribution of the magnitude of the forces. It was found that interparticle forces less than the average,  $F < \langle F \rangle$  (where the average  $\langle \cdot \rangle$  is over all particle contacts), follow a power-law distribution  $P(F/\langle F \rangle) \propto (F/\langle F \rangle)^\alpha$ , where Thornton [42] found  $\alpha = 0.16$ , whereas Radjai et al. [43] found  $\alpha = 0.3$ . Both are comparable to the recent prediction from the fullRSB theory,  $\alpha \approx 0.423$  [28–30].

For the distribution of forces larger than the average force, an exponential distribution has been found in both experiments and simulations  $P(F/\langle F \rangle) \propto e^{-\beta P(F/\langle F \rangle)}$ , where  $\beta$  depends on a wide variety of parameters, including the pressure applied (Figure 4.5A–D) [31, 43–45]. It was also found that, as the strain (or similarly the packing fraction) is increased, the



distribution gradually transforms to a Gaussian-like distribution  $P(F/\langle F \rangle) \propto e^{-\beta(F/\langle F \rangle)^2}$ , which was explained by the observation that at high strains more contacts are formed, allowing for a more homogeneous distribution of the forces [13].

## 4.2 Materials and Methods

The microscopic analysis was performed on the same datasets as described in chapter 3. All experiments comprised of an ensemble of  $\sim 2000$  bidisperse particles, with diameters of  $120 \mu\text{m}$  and  $160 \mu\text{m}$ , both contributing equally to the volume occupied by particles. The ensembles were first preconditioned by compressing them cyclically for 10–15 cycles over the course of 1–2 hours. The ensembles were then compressed for 10 cycles with an oscillation period of 600 s, and the strain was observed 120 times per compression cycle. Particles of different softness were used, and are listed in table 4.1.

### 4.2.1 Particle radius

In section 2.4.4, we defined a method to determine the particle radius with an accuracy of  $\sim 1$  pixel ( $\sim 2.5 \mu\text{m}$ ). This is, as it turns out, not accurate enough, as quantities like the coordination number and the microscopic pressure depend very strongly on the nominal radius of the particles. Figure 4.6A shows the calculated coordination number as function of strain during a cyclic compression ( $T = 600$  seconds) of particles with a Young's modulus of 12 MPa. All curves originate from the same dataset, where the only difference is the nominal particle radius. The legend shows the ratio between the nominal particle radius ( $R_n$ ) and the original particle radius ( $R_o$ , as determined in section 2.4.4),  $R_n/R_o$ . From isostaticity arguments we would expect  $Z_0 \approx 4$ , however, when the nominal particle radii are kept close to the original particle radius ( $0.98 \leq R_n/R_o \leq 1.02$ ), the  $Z_0$  is well below 4. Increasing the  $R_n/R_o$  further, we see that the  $Z_0 \approx 4$ . Furthermore, Figure 4.6B shows the average number of newly formed contacts per particle during compression ( $Z - Z_0$ ) as function of the packing fraction past jamming ( $\phi - \phi_0$ ). As discussed in section 4.1.5, we expect  $Z - Z_0 \propto \sqrt{\phi - \phi_0}$ . The best fit for each  $R_n/R_o$  is indicated with a line of the same color. We found that the square-root scaling for all  $\phi$  is only obtained for  $R_n/R_o > 1.04$ .  $R_n/R_o$  also slightly changes  $\phi$  and  $\phi_0$ . However, this will result in a slightly different proportionality constant, and does not affect the scaling at all. Therefore,  $\phi_0$  was taken to be constant for all experiments.

Since the nominal radius does not only influence the moment when particles are assumed to be in contact, but also the magnitude of the deformation, we expect it to influence the microscopic pressure ( $P_m$ ) as well. Figure 4.6C shows the increase in pressure ( $P_m = \text{tr}(\boldsymbol{\sigma})/2$ , as defined in section 4.1) as function of global strain. We see that for  $R_n/R_o < 1.02$ ,  $P \approx 0$  further confirming that contacts are under-detected. For  $R_n/R_o \geq 1.02$ , we see that the microscopic pressure at maximum strain ( $\sim 4\%$ ) increases rapidly with increasing  $R_n/R_o$ . The  $\Delta P$  imposed at maximum strain was 20 kPa, and the microscopic stress can reasonably not be higher than the imposed stress. Yet, for all  $R_n/R_o \geq 1.04$  we find that  $P_m > \Delta P$ . The closest reasonable scaling is obtained for  $R_n/R_o = 1.04$ , where  $P_{m,max} \approx 2\Delta P_{max}$ .

The expected contact number scaling for this example dataset is obtained for  $R_n/R_o \geq 1.04$ , and  $R_n/R_o$  should be as small as possible to minimize the error in the microscopic pressure. We, therefore, chose  $R_n/R_o = 1.04$  for this dataset. Although all particles were made with the same mask, and should therefore have the same size, this analysis was repeated for each experiment.  $R_n/R_o$  appeared to depend slightly on the particle softness, where

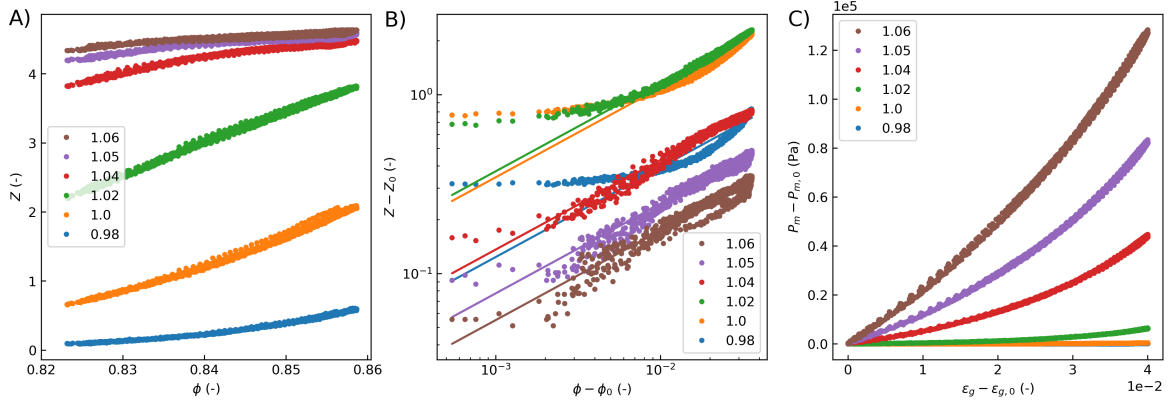


Figure 4.6: Investigation of quantities that depend on the nominal particle radius on an oscillatory compression ( $T=600$  s) of a packing of 12 MPa particles. The legend indicates the ratio between the nominal radius and the radius as determined according to section 2.4.4,  $R_n/R_o$ . A) Coordination number as function of packing fraction for different  $R_n/R_o$ . B) Excess coordination number versus packing fraction past jamming for different  $R_n/R_o$ . C) Microscopic pressure as function of global strain for different  $R_n/R_o$ .

PEGDA (v/v%)	PEG (v/v%)	PI (v/v%)	E (MPa)	$R_n/R_o$
90	0	10	12.0	1.04
70	20	10	8.7	1.02
60	30	10	6.8	1.00
50	40	10	4.9	1.00
40	50	10	4.6	1.00

Table 4.1: Table of PEGDA-PEG mixtures used, their associated Young’s moduli and the correction factor used for the particle radius

$R_n/R_o \approx 1.04$  for the 12 MPa particles and  $R_n/R_o \approx 1.00$  for the 0.4 MPa particles. These deviations, however, are rather small and given in Table 4.1. The biggest particles are  $\sim 28$  pixels, meaning that most deviations in size are sub-pixel and thus completely indiscernible by eye.

One could imagine that for the solution that makes the 12 MPa particles, which has the highest concentration of reactive molecules (90% v/v PEGDA and 10% v/v PI), there are reactive molecules everywhere, allowing the reaction to “diffuse” slightly ( $\sim 500$  nm) outside the area indicated by the mask before being quenched. Whereas for the solution that makes the 4.6 MPa particles, which consists of 50% v/v inert polymers, the reaction-diffusion is limited due to local starvation of reactive species. Hence, the softer particles are slightly smaller. However, a more thorough investigation is required to verify this hypothesis.

In the following, we will use this scaling, but one should always keep in mind that the uncertainty in their determination leads to a non-negligible error in the presented analysis.

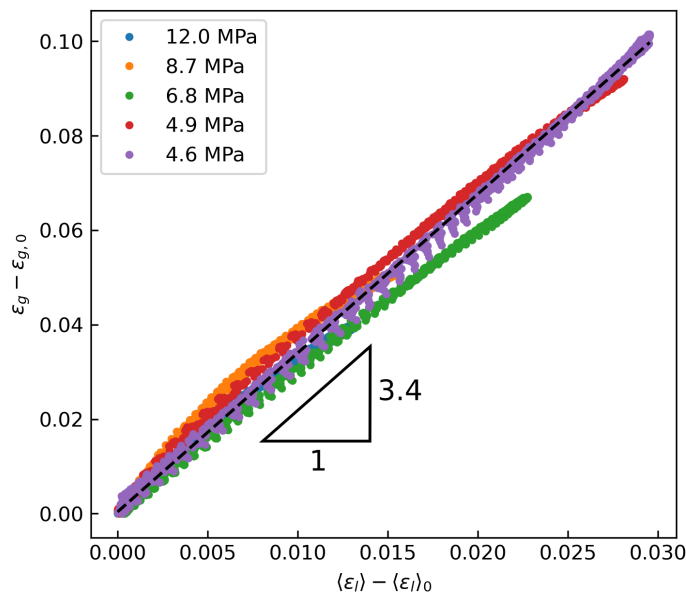


Figure 4.7: The average global strain as function of the average particle deformation for different particle softnesses (see legend) for 7 consecutive compression cycles with  $T=600$ s. Both the global and local strain observed at  $\Delta P = \delta P$  were subtracted.

## 4.3 Results

### 4.3.1 Relation global and local strain

Having established a more accurate radius for the particles, we investigated the relation between the global deformation,  $\varepsilon_g$ , of the packing and the average deformation of the individual particles  $\varepsilon_l$  during compression with  $T=600$  s for various particle softnesses. We have seen in the previous chapter that the packing does not fully relax during an oscillation (Figure 3.9B), where the strain at the lowest applied pressure depends on the particle softness (Figure 3.9B). Also, we have seen in Figure 3.10 that the response during can be transient, despite the system being pre-compacted, and will reach a limit cycle after 1-2 compression cycles. Figure 4.7 shows the increase in local and global deformation past the deformation at  $\Delta P = \delta P$ ,  $\langle \varepsilon_l \rangle_0$  and  $\varepsilon_{g,0}$ , respectively, for the last 7 cycles out of a series of 10. We found that, independent of particle softness,  $\varepsilon_g \approx 3.4\varepsilon_l$ , which agrees reasonably well with previously reported numerical values  $\sim 4$  [13, 14].

While this proportionality constant between the local and global deformation has been reported for several systems, [13, 14] including this work, a clear origin of this scaling factor is still missing. We managed to show it is independent of particle softness. A further investigation, involving parameters such as polydispersity and particle shape, which can both change the packing fraction at jamming, might shed more light on the origin of this scaling. This would bring us closer to description of the compaction of porous media free of fitting parameters.

Furthermore, unlike all the imposed pressure versus global strain curves encountered in the previous chapter, no hysteresis is observed when comparing the local strain to the global strain. This is most likely because they are both calculated from the particle positions, and are thus always in-phase.

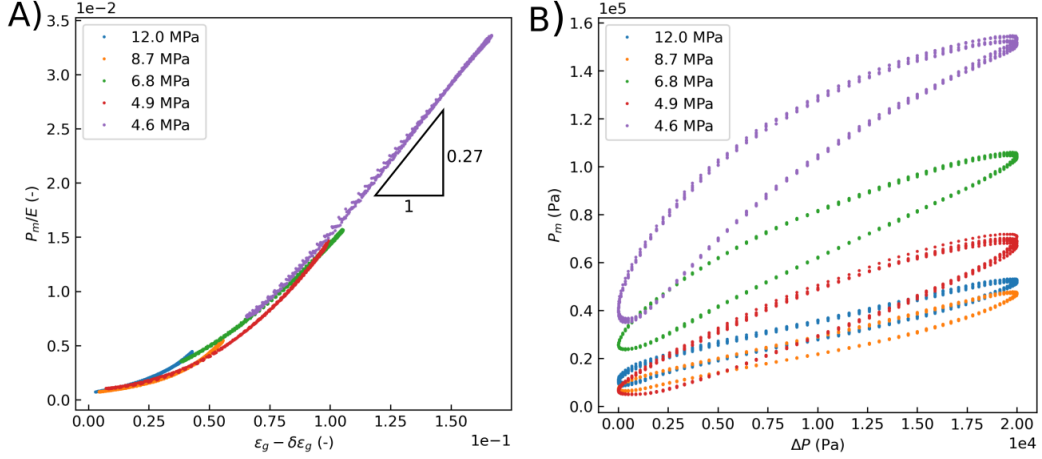


Figure 4.8: A) The microscopic pressure as function of global strain for particles with different Young’s moduli for 7 compression cycles. B) The microscopic pressure as function of the applied pressure for 7 compression cycles.

### 4.3.2 Evolution of the microscopic pressure

Knowing the relationship between the global and local strain, we can now calculate the microscopic pressure (non-dimensionalized by the Young’s modulus of the particles) from the interparticle forces (eq. 4.12 and 4.15) for different global strains and Young’s moduli, which can be seen in Figure 4.8A. Each dataset shows the  $P_m$  and  $\varepsilon_g$  collected throughout 7 consecutive cycles obtained with an oscillation period of 600 seconds. Similar to the local and global deformation, there is no hysteresis, each  $P_m/E$  is uniquely defined by a  $\varepsilon_g$ .

In addition, all experiments performed with different particle softnesses collapse onto a single curve. To obtain this collapse, however, the  $\varepsilon_g$  of the 4.9 MPa and 4.6 MPa had to be shifted by a small amount  $\delta\varepsilon_g \approx 0.01$ . This is most likely due to insufficient equilibration before the start of the experiments. This allowed the packing to slightly compact during the first cycles, leading to a small amount of irreversible strain, which doesn’t contribute to  $P_m$ .

At higher strains, we obtained a linear relationship between  $P_m/E$  and  $\varepsilon_g$ . Eq. 4.21 gives the theoretical approximation,  $P_m/E = \frac{Z\phi}{4\alpha}\varepsilon_g$ . For a 2D packing of frictionless particles at jamming,  $Z \approx 4$ ,  $\phi \approx 0.8$ , and  $\alpha = 3.4$  yielding  $P_m/E \approx 0.24\varepsilon_g$ , which agrees well with the  $P_m/E = 0.27\varepsilon_g$  we found experimentally.

Interestingly, this linear scaling doesn’t hold at low strains. There appears to be a soft onset to the compaction. One hypothesis is that this is due to the reversible plasticity of the system. At low strains, the nearly frictionless, fully lubricated hydrogel packings can undergo slight rearrangements to find a more dense configuration only accessible at higher pressure. These rearrangements contribute to  $\varepsilon_g$ , but hardly affect  $P_m/E$ . As soon as this configuration is reached, the expected linear scaling is obtained. Furthermore, the resemblance of Figure 4.8A and Figure 3.9D (the phase corrected pressure as function of the observed global strain) is uncanny, further strengthening the evidence for a soft onset of the compression. We are not aware of any literature mentioning a similar soft onset of the compaction. This could be because interparticle friction and particle roughness prevent these rearrangements from happening. There are several ways one can suppress rearrangements to test this hypothesis. Similar oscillatory compression experiments could be performed on monodisperse disks, which crystallize immediately. Since the packing is already in the densest possible state, rearrange-

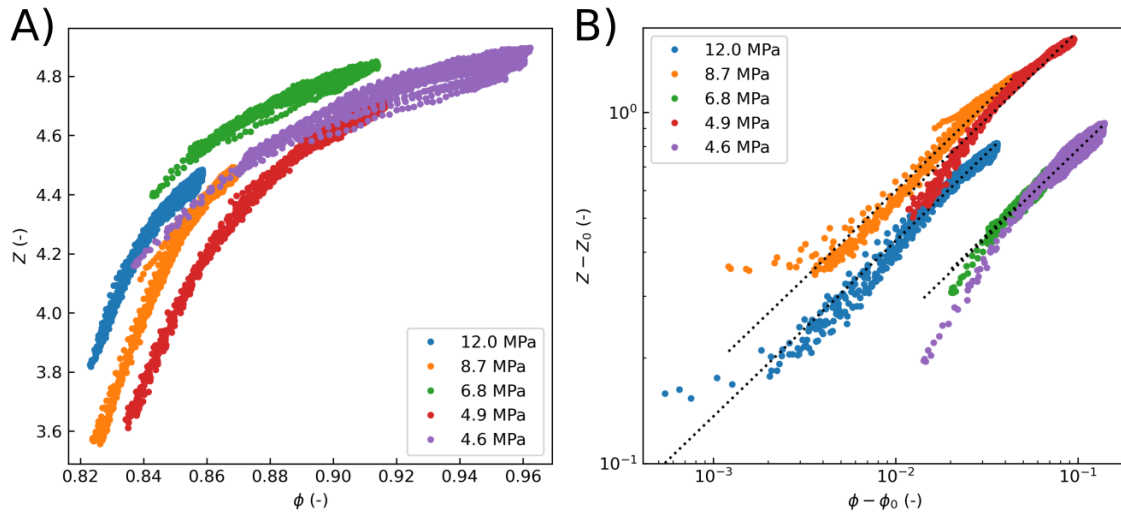


Figure 4.9: A) The coordination number as function of packing fraction for particles with several Young's moduli B) The reduced coordination number as function of the density past jamming. Dotted lines are fits with  $Z - Z_0 = k\sqrt{\phi - \phi_0}$ .

ments are suppressed and a completely linear pressure-strain scaling should be observed. One could also use very rough particles. Rough particles can mechanically interlock, which suppresses rearrangements. I believe a further investigation under the aforementioned conditions will provide more inside in the origin of the soft onset, and potentially the hysteresis.

Figure 4.8B shows the observed microscopic pressure  $P_m$  for different imposed pressure drops over the channel  $\Delta P$ , for different particle softnesses. The calculated microscopic pressures exceeded the imposed pressures, which is not physical.  $P_m$  is, however, very susceptible to changes in the actual radius (as discussed in section 4.2.1). Higher resolution images, and a more accurate (externally calibrated) particle radius might resolve this conflict. Another key thing to note is that a hysteresis can be observed, as soon as a microscopic quantity is compared with the externally imposed pressure. This would hint at the camera and the pressure controller being out of phase. However, as determined in chapter 4, this is not the case.

### 4.3.3 Coordination number

We also followed the number of contacts of each particle during compaction. Figure 4.9 shows the coordination number as function of packing fraction, where the dashed line shows the  $Z - Z_0 = k\sqrt{\phi - \phi_0}$  scaling, as discussed in section 4.1.5. Unsurprisingly, we recover this scaling, as this was one of the selection criteria to determine the actual size of the particles. While the square-root scaling was not sensitive to the nominal particle radius, as long as the nominal radius was over a critical radius, the coordination number at jamming ( $Z_0$ ) and the proportionality constant ( $k$ ) were sensitive to the chosen nominal radius. Although we expect  $Z_0$  to be independent of particle softness, as the deformation at  $\Delta P \approx 0$  is negligible, we were not able to confirm this, due to the dependency of  $Z_0$  on user input. Furthermore, isostaticity states it only depends on the friction coefficient and dimensionality of the system (see section 4.1.5). Whether  $k$  is expected to be (weakly) affected by particle softness is not as clear, as it seems also to be affected weakly by polydispersity of the particles [20]. However, given the

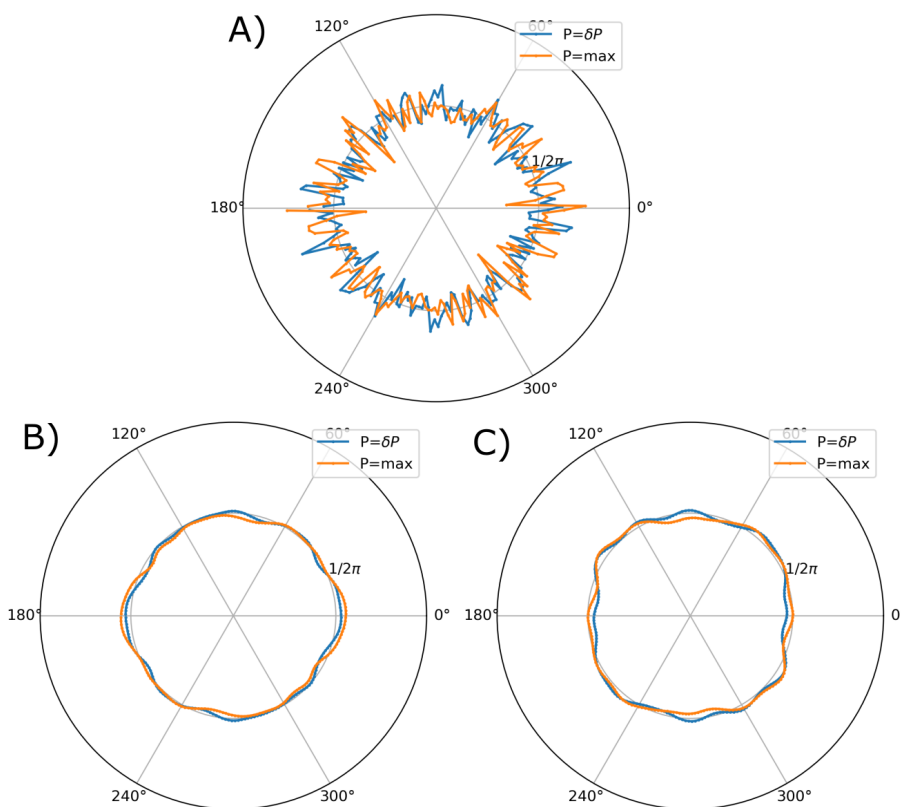


Figure 4.10: PDF of contact orientations of a cyclically compressed packing, where  $180^\circ$  was the compressive direction. A) PDF of the contact angle orientation for 12 MPa particles at two different applied pressures. The gray line indicates probability of a random contact direction ( $1/2\pi$ ). Each of the 200 bins has approximately 350 contacts. B) Data from A), where all the high frequency changes in contact orientation are removed using a Gaussian filter with  $\sigma = \pi/50$  C) PDF of the contact angle orientation for 4.6 MPa particles at two different applied pressures.

sensitivity to the nominal radius, and a lack of external calibration/verification of the particle radius, it is not possible to draw clear conclusions on  $k$  from the current data.

#### 4.3.4 Radial contact distribution

Besides investigating the number of newly formed contacts, we can also look at how they are oriented. Figure 4.10A shows the contact orientation of a packing of 12 MPa particles under two different imposed pressures, the lowest attainable pressure ( $P = \delta P \approx 0.2 \text{ kPa}$ ) and maximum pressure achieved ( $P = 20 \text{ kPa}$ ). In the experiment, the packing was compressed cyclically with  $T=600$  s. The contact orientations were binned in 200 equally sized bins of size  $1/100\pi$ , where each containing approximately 50 contacts. The contact orientations at identical  $\Delta P$  of the last 7 cycles (similar to the analysis in section 4.3.2) were pooled. Pooling did not reduce the high frequency changes in contact angle, the PDF of a single configuration is nearly identical to the average of 7 cycles. This is most likely because the microscopic configurations aren't statistically independent for such pre-oscillated systems under cyclic compression.

To suppress the high frequency changes, the PDF in Figure 4.10A was filtered with a

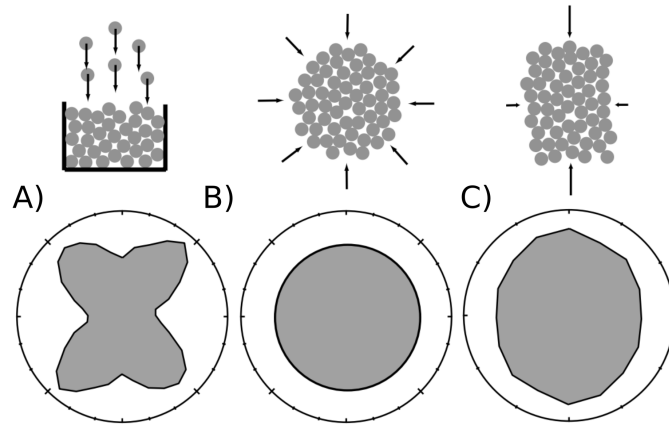


Figure 4.11: A) Contact orientation after deposition under gravity, data originally from [46]. B) Contact orientation of a packing under isotropic compression. C) Contact orientation of a packing under axial load. Data originally from [35]. Figures A, B and C have been taken from [47]

Gaussian filter with  $\sigma = 1/50\pi$ . The filtered PDF for the 12 MPa and 4.6 MPa particles is shown in Figure 4.10 B and C, respectively. Let us quickly review what is known about the contact orientation in literature. Particles settled under gravity tend to preferentially form contacts in the directions oblique to the direction of compression [46, 47] (Figure 4.11A), as a single contact in the gravitational direction is marginally stable. Hence, contacts on either side are needed to provide stability, resulting in two contacts oblique and one contact parallel to the direction of gravity. A particle supported by just two particles only has oblique contacts. Hardly any contacts are made orthogonal to the gravitational direction, as these contacts can only bear load by frictional forces.

Under axial load, the contact distribution shifts. The contacts are formed preferentially in the direction of compression (Figure 4.11C), whereas under isotropic compression the contacts are uniformly distributed in all directions (Figure 4.11B). The contacts in our experiments appear quite uniform (besides a slight preference for the direction of compression for the hardest particles) like one would expect for an isotropic compression [35, 47]. This is most likely due to the frictionless nature of the particles and the extensive equilibration before collecting data. More experiments with rough particles of varying roughness, without equilibration need to be performed to confirm this hypothesis.

### 4.3.5 Distribution of interparticle forces

As discussed in section 4.1.6, granular materials bear most of their load on a sparse network of particles (Figure 4.12). We've calculated the interparticle forces for the oscillatory compression ( $T=600$  s) of particles of different softness over 7 cycles (again, the initial transient cycles are not included here). Figure 4.13A shows the PDF of the interparticle forces, non-dimensionalized by the average interparticle force, of 12 MPa particles at  $\Delta P = 20kPa$  for each of the 7 cycles. While each of the individual PDF's is relatively noisy, they all follow the same trend. Even though the microscopic configurations are not statistically independent (as they stem from the same initial packing), the Force Network Ensemble theory predicts that there are many equally likely force-networks for each microscopic configuration [38]. Recently, we've shown that indeed the force-network is only marginally stable and completely different force-networks can be achieved without the need for rearrangements [40]. Hence, pooling

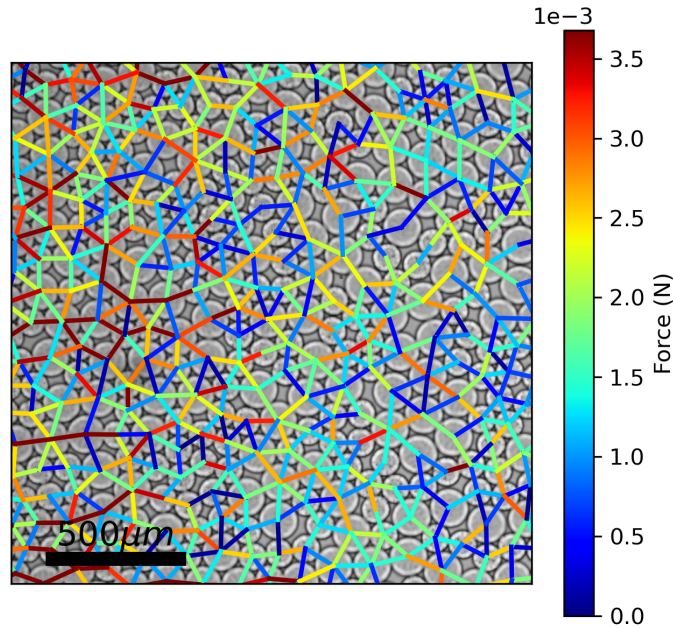


Figure 4.12: Zoom of a packing of 4.6 MPa particles under compression. The inter-particle forces are represented by lines, where the color of the line indicates the magnitude of the force.

data collected at the same pressure works well to reduce the noise, which we did for the other figures.

Figure 4.13B shows the PDF for particles with a Young's modulus of 8.7 MPa at  $\Delta P = \delta P$  (blue dots, strain given in legend), and  $\Delta P = 20kPa$  (orange dots), averaged over the 7 configurations. We found that the distributions were well-fitted by a Gaussian distribution, where the width depends on the pressure. While this was expected at high pressures, as a higher pressure causes a more homogeneous force-network and therefore a narrower distribution around the mean, as has been seen before in simulations [13], it was surprising that the deformations at  $\Delta P = \delta P$  still followed a Gaussian distribution.

Figure 4.13C shows the PDF of the interparticle forces (on a log-log scale) at low pressure ( $\Delta P = \delta P$ ). Theory predicts that the weak forces ( $F/\langle F \rangle < 1$ )  $PDF(F/\langle F \rangle) \propto f^{0.432\dots}$  [29, 48]. However, such power-law scaling is not obtained. This is most likely due to the lack of accuracy for the small overlaps (and thus small forces). Photoelastic techniques provide much better accuracy for small forces, and show more potential to study weak forces [30, 49].

The PDF's of interparticle forces, non-dimensionalized by the average interparticle force, for different particle softnesses at  $\Delta P = 20kPa$  are shown in Figure 4.13. We see that the distributions of the forces around the mean are very similar, showing the formation of a homogeneous force network at higher pressures.

### 4.3.6 Reversible Plasticity

Besides viscoelastic dissipation by the particles themselves, as discussed in Chapter 3, granular materials can also dissipate energy via their microstructure. Typically, we assume that the deformation of disordered media is elastic if the deformation is below a certain threshold, the yield strain or yield stress. Meaning that, when the system is relaxed after a deformation below the yield strain, all particles come back to their initial position. Furthermore, particles would



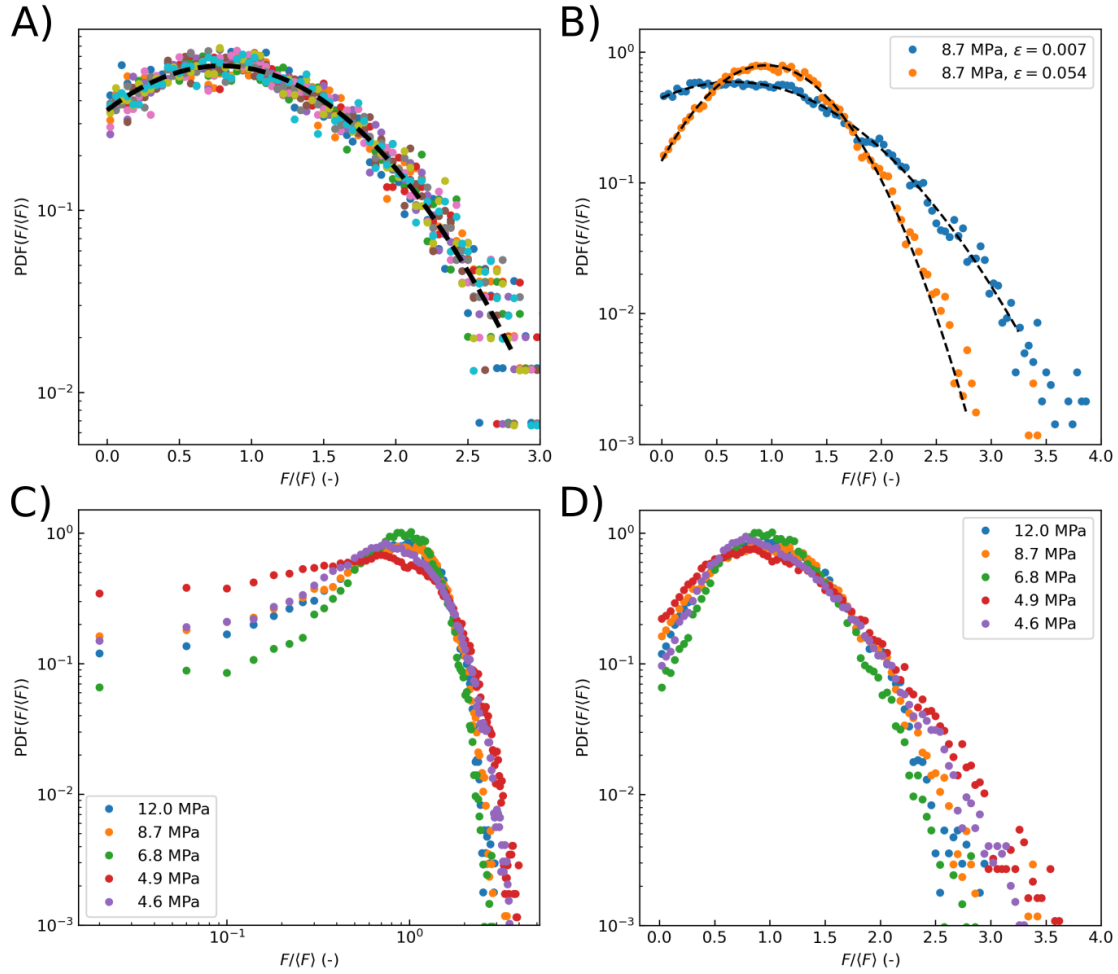


Figure 4.13: A) PDF of 7 instances of the interparticle forces of 12 MPa at identical pressure ( $\Delta P = 20kPa$ ), dashed black line, is a fit with a Gaussian distribution. B) PDF of interparticle forces of 8.7 MPa particles at two different strains, black dashed lines are fits with a Gaussian distribution. C) Log-log plot of the PDF of the interparticle forces at minimal strain. D) PDF of the interparticle forces for particles with different Young's moduli all taken at  $\Delta P = 20kPa$

trace the same path during relaxation as they followed during compression, whereas during deformations above the yield strain, rearrangements would change the microstructure causing the particles to not return to their original position. This gives rise to interesting phenomena, such as the ability to “encode” a certain strain into the microstructure by repeatedly straining the sample to the strain to be encoded [50–52].

Recently Galloway et al. [53] showed there is also a subsection of particles that don't follow the same path during increasing strain and decreasing strain (plasticity), but do come back to their original position (reversible). Hence, they coined this reversible plasticity. Brujić et al. [54] showed relaxation in frictional granular media (both exp and simulations), which they attributed to sliding, which can happen relatively easily for frictionless particles, like in our experiments.

It could be that the soft onset of compression, as can be observed in Figure 4.8A, are due to reversible plastic events. These small rearrangements could contribute to the global

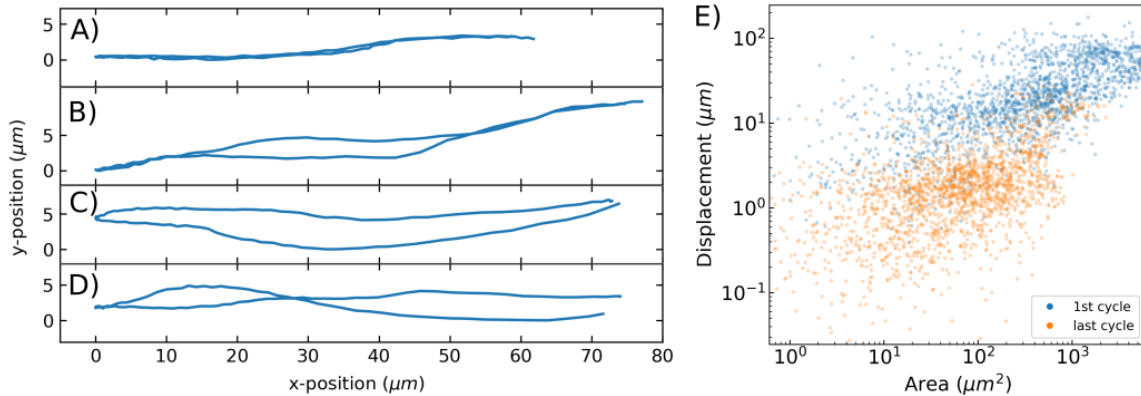


Figure 4.14: Trajectories of single particles, all taken during a single compression cycle. A) Reversibly elastic trajectory. B) Mostly reversibly elastic, with a reversible plastic regime. C) Reversibly plastic trajectory. D) Irreversibly plastic trajectory. E) Area enclosed by the trajectory as function of the displacement of a particle after an entire cycle. The two point-clouds are from two different compression cycles, the first and the last cycle in a sequence of compressions.

strain, yet don't cause any deformation of the particles. We're not aware of any literature on reversible plasticity during compaction of granular materials. It could be that these reversible events are typically not observed because frictional dissipation prevents the particles from returning to their original position.

To investigate this possibility, we investigated the paths particles trace during compaction. Figure 4.14A-D show typical paths observed. All example paths are taken from a similar section of the last cycle of a sequence of 10 cycles with a period of 600 s, such that all paths are of similar length. Figure 4.14A is a good example of a perfectly elastic trajectory, during decompression the particle nearly perfectly traces its path back to its original position. Whereas, 4.14B and C are examples of reversibly plastic trajectories. Figure 4.14B appears elastic throughout most of the cycle, but the path is hysteretic in a certain section. Figure 4.14C shows a hysteresis throughout the entire cycle. A small number of particles doesn't come back to their original position, like Figure 4.14D, and could therefore be labelled as irreversibly plastic.

Figure 4.14E shows the area encompassed by the traced path, as determined by the Surveyor's algorithm (also called shoelace algorithm) [55], as a function of the displacement after an entire cycle (distance between the start- and end-position of the cycle). A large area of the trace is a measure of the plastic nature of that particle during a compression cycle, whereas the displacement after a cycle is a measure of the irreversibility of the cycle. The blue points (each belonging to a single particle in that cycle), are taken during the first compression cycle during the experiment, although the particles have been oscillated 5–10 times before data collection started. During this cycle, we see that most particles have both a large encompassed area and large displacement after a cycle, indicating that most particles are irreversibly plastically rearranging. Comparing this to the orange point-cloud, for which each of the points corresponds to a single particle in the last (10th) cycle, we found that both the area encompassed and the displacement after the cycle decreased by approximately an order of magnitude. The displacements are relatively narrowly distributed around  $\sim 2\mu\text{m}$ , for the last cycle. Since this is  $\sim 1\%$  of the particle diameter, we believe most particle trajectories are reversible. The encompassed area is more broadly distributed, spanning from

$10\mu\text{m}^2$  to almost  $1000\mu\text{m}^2$ . This makes it difficult to distinguish the reversible plastic from the reversible elastic regime, like Galloway et al. [53] were able to observe. We're aware that the Surveyor's algorithm works less well for self-intersecting polygons, as it will give certain subsections a negative area. A potential improvement would be to use the area calculation algorithm developed by [53].

## 4.4 Conclusion

In this chapter, we have shown a microscopic investigation of the compaction of soft particles under cyclic compression inside a microfluidic channel. The sub-pixel accuracy of our tracking algorithm, combined with the careful determination of the particle radii, allowed us to study the evolution of the particle-particle interactions during compaction.

We found that the strain on the particle level was not identical to the strain of the packing level, but scales as  $\langle \varepsilon_l \rangle \propto \varepsilon_g / 3.4$ . The creation of new contacts during compression was well described by the square root of the strain, as has been observed before in many disordered systems, from numerical glasses to experimental emulsions. The distribution of the inter-particle forces was well described by a Gaussian-distribution.

Furthermore, we were able to calculate the microscopic stress tensor from the particle-particle interactions. Since both the local and the global strain were calculated from the particle positions, they showed no hysteresis during the compression cycles. Similar to the observed strain as function of imposed pressure discussed in the previous chapter (Chapter 3, Figure 3.9), the microscopic stress and global strain of particles with different softnesses collapsed by non-dimensionalizing the pressure with the Young's modulus of the particles. Moreover, they showed the same soft onset of the compression, followed by a linear increase of the pressure with strain, which could reasonably be described by the micromechanical model developed by Cárdenas-Barrantes et al. [18]

Also, we studied the traces of the particles during compression. We found that the paths were not perfectly elastic, and that most particles were reversibly plastic, i.e. the path during decompression was different from the path during compression, yet the position of the particle over a cycle was negligible. We attempted to link this reversible plasticity to the soft onset of compression and the time-independent hysteresis during compression, described in chapter 3. However, no clear trend has been found yet.

Lastly, it was striking that no hysteresis was observed on a microscopic level. The compression cycles were very reproducible, showing no drift over the 7 cycles studied. We thought the poro-viscoelastic properties of the hydrogel particles would also influence the response on a microscopic level, but that was not the case. Only when quantities derived from the particle positions were compared with the imposed pressure, a phase shift could be observed. This is a very interesting observation, as one could thus describe the response of an ensemble of viscoelastic by applying a viscoelastic phase shift, which can be obtained by performing rheological tests on a single particle, to the typical response of a granular media of elastic particles.

## 4.5 References

- [1] Valentin L. Popov. *Contact Mechanics and Friction*. Springer, Berlin Heidelberg, 2017. 58, 61

- 
- [2] M. Van Hecke. Jamming of soft particles: Geometry, mechanics, scaling and isostaticity. *Journal of Physics Condensed Matter*, 22(3), 2010. 59, 62
- [3] Xia Hong, Meghan Kohne, Mia Morrell, Haoran Wang, and Eric R. Weeks. Clogging of soft particles in two-dimensional hoppers. *Physical Review E*, 96(6), 12 2017. 59
- [4] Rok Simič, Joydeb Mandal, Kaihuan Zhang, and Nicholas D. Spencer. Oxygen inhibition of free-radical polymerization is the dominant mechanism behind the “mold effect” on hydrogels. *Soft Matter*, 17(26):6394–6403, 7 2021.
- [5] Jian Ping Gong, T. Kurokawa, T. Narita, G. Kagata, Y. Osada, G. Nishimura, and M. Kinjo. Synthesis of hydrogels with extremely low surface friction [4]. *Journal of the American Chemical Society*, 123(23):5582–5583, 2001. 59
- [6] J. H. Irving and John G. Kirkwood. The statistical mechanical theory of transport processes. IV. The equations of hydrodynamics. *The Journal of Chemical Physics*, 18(6): 817–829, 1950. 59, 60
- [7] S Ogawa. Multitemperature theory of granular materials. In *Proc. of the US-Japan Seminar on Continuum Mechanical and Statistical Approaches in the Mechanics of Granular Materials, 1978*, pages 208–217, 1978. 60
- [8] Charles S Campbell. RAPID GRANULAR FLOWS. Technical report, Department of Mechanical Engineering, University of Southern California, 1990.
- [9] Isaac Goldhirsch. Introduction to granular temperature. *Powder Technology*, 182(2): 130–136, 2 2008. 60
- [10] L Rothenburg and R J Bathurst. Analytical study of induced anisotropy in idealized granular materials. Technical Report 4, University of Waterloo, Ontario, 1989. 61
- [11] Saeid Nezamabadi, Farhang Radjai, Serge Mora, Jean-Yves Delenne, and Mojtaba Ghadiri. Rheology of soft granular materials: uniaxial compression. *EPJ Web of Conferences*, 249:05008, 2021. 61, 62
- [12] David Cantor, Manuel Cárdenas-Barrantes, Itthichai Preechawuttipong, Mathieu Renouf, and Emilien Azéma. Compaction Model for Highly Deformable Particle Assemblies. *Physical Review Letters*, 124(20), 5 2020. 61, 62
- [13] Manuel Cárdenas-Barrantes, David Cantor, Jonathan Barés, Mathieu Renouf, and Emilien Azéma. Three-dimensional compaction of soft granular packings. *Soft Matter*, 18(2):312–321, 2022. 61, 65, 66, 68, 73
- [14] Manuel Cárdenas-Barrantes, David Cantor, Jonathan Barés, Mathieu Renouf, and Emilien Azéma. Micromechanical description of the compaction of soft pentagon assemblies. *Physical Review E*, 103(6):1–10, 2021. 61, 68
- [15] Ivana Agnolin and Jean Noël Roux. Internal states of model isotropic granular packings. I. Assembling process, geometry, and contact networks. *Physical Review E - Statistical, Nonlinear, and Soft Matter Physics*, 76(6), 12 2007. 61, 64

- [16] Ivana Agnolin and Jean Noël Roux. Internal states of model isotropic granular packings. II. Compression and pressure cycles. *Physical Review E - Statistical, Nonlinear, and Soft Matter Physics*, 76(6), 12 2007.
- [17] Ivana Agnolin and Jean Noël Roux. Internal states of model isotropic granular packings. III. Elastic properties. *Physical Review E - Statistical, Nonlinear, and Soft Matter Physics*, 76(6), 12 2007. 61
- [18] Manuel Cárdenas-Barrantes, David Cantor, Jonathan Barés, Mathieu Renouf, and Emilien Azéma. Compaction of mixtures of rigid and highly deformable particles: a micro-mechanical model. 5 2020. 61, 76
- [19] Manuel Cárdenas-Barrantes, Jonathan Barés, Mathieu Renouf, and Émilien Azéma. Experimental validation of a micromechanically based compaction law for mixtures of soft and hard grains. *Physical Review E*, 106(2):1–6, 2022. 61
- [20] Corey S. O’Hern, Leonardo E. Silbert, Andrea J. Liu, and Sidney R. Nagel. Jamming at zero temperature and zero applied stress: The epitome of disorder. *Physical Review E - Statistical Physics, Plasmas, Fluids, and Related Interdisciplinary Topics*, 68(1):19, 2003. 62, 63, 70
- [21] Alexei V. Tkachenko and Thomas A. Witten. Stress propagation through frictionless granular material. *Physical Review E - Statistical Physics, Plasmas, Fluids, and Related Interdisciplinary Topics*, 60(1):687–696, 1999. 62
- [22] H. P. Zhang and H. A. Makse. Jamming transition in emulsions and granular materials. *Physical Review E - Statistical, Nonlinear, and Soft Matter Physics*, 72(1):1–12, 2005.
- [23] Kostya Shundyak, Martin Van Hecke, and Wim Van Saarloos. Force mobilization and generalized isostaticity in jammed packings of frictional grains. *Physical Review E - Statistical, Nonlinear, and Soft Matter Physics*, 75(1):1–4, 2007. 62
- [24] Leonardo E. Silbert, Andrea J. Liu, and Sidney R. Nagel. Structural signatures of the unjamming transition at zero temperature. *Physical Review E - Statistical, Nonlinear, and Soft Matter Physics*, 73(4), 2006. 63, 64
- [25] D J Durian. Bubble-scale model of foam mechanics: Melting, nonlinear behavior, and avalanches. 55(2):1–13, 1997. 64
- [26] Corey S. O’Hern, Stephen A. Langer, Andrea J. Liu, and Sidney R. Nagel. Random Packings of Frictionless Particles. *Physical Review Letters*, 88(7):4, 2002. 63
- [27] D. J. Durian. Foam mechanics at the bubble scale. *Physical Review Letters*, 75(26): 4780–4783, 1995. 63
- [28] Patrick Charbonneau, Jorge Kurchan, Giorgio Parisi, Pierfrancesco Urbani, and Francesco Zamponi. Fractal free energy landscapes in structural glasses. *Nature Communications*, 5, 4 2014. 63, 65
- [29] Patrick Charbonneau, Jorge Kurchan, Giorgio Parisi, Pierfrancesco Urbani, and Francesco Zamponi. Exact theory of dense amorphous hard spheres in high dimension. III. the full replica symmetry breaking solution. *Journal of Statistical Mechanics: Theory and Experiment*, 2014(10), 2014. 63, 73

- 
- [30] Yinqiao Wang, Jin Shang, Yuliang Jin, and Jie Zhang. Experimental observations of marginal criticality in granular materials. *Proceedings of the National Academy of Sciences of the United States of America*, 119(22), 2022. 63, 64, 65, 73
- [31] P Claudin, J.-P Bouchaud, M E Cates, and J P Wittmer. Models of stress fluctuations in granular media. Technical report, 1998. 65
- [32] Hernán A Makse, David L Johnson, and Lawrence M Schwartz. Packing of Compressible Granular Materials. Technical report, 2000. 65
- [33] Jasna Brujić, Sam F. Edwards, Dmitri V. Grinev, Ian Hopkinson, Djordje Brujić, and Hernán A. Makse. 3D bulk measurements of the force distribution in a compressed emulsion system. *Faraday Discussions*, 123(1):207–220, 2003. 65
- [34] Heinrich M. Jaeger, Sidney R. Nagel, and Robert P. Behringer. Granular solids, liquids, and gases. *Reviews of Modern Physics*, 68(4):1259–1273, 1996. 65
- [35] Farhang Radjai, Dietrich E. Wolf, Michel Jean, and Jean Jacques Moreau. Bimodal character of stress transmission in granular packings. *Physical Review Letters*, 80(1):61–64, 1998. 72
- [36] J. F. Peters, M. Muthuswamy, J. Wibowo, and A. Tordesillas. Characterization of force chains in granular material. *Physical Review E - Statistical, Nonlinear, and Soft Matter Physics*, 72(4):1–8, 2005. 65
- [37] Jacco H. Snoeijer, Thijs J.H. Vlugt, Martin van Hecke, and Wim van Saarloos. Force Network Ensemble: A New Approach to Static Granular Matter. *Physical Review Letters*, 92(5):4, 2004. 65
- [38] Brian P. Tighe, Jacco H. Snoeijer, Thijs J.H. Vlugt, and Martin Van Hecke. The force network ensemble for granular packings. *Soft Matter*, 6(13):2908–2917, 2010. 65, 72
- [39] Patrick Charbonneau, Eric I. Corwin, Lin Fu, Georgios Tsekenis, and Michael Van Der Naald. Glassy, Gardner-like phenomenology in minimally polydisperse crystalline systems. *Physical Review E*, 99(2), 2 2019. 65
- [40] Lars Kool, Patrick Charbonneau, and Karen E. Daniels. Gardner-like crossover from variable to persistent force contacts in granular crystals. *Physical Review E*, 106(5):1–6, 5 2022. 65, 72
- [41] Jonathan E. Kollmer and Karen E. Daniels. An experimental investigation of the force network ensemble. *EPJ Web of Conferences*, 140:1–4, 2017. 65
- [42] Colin Thornton. On the relationship between the modulus of particulate media and the surface energy of the constituent particles. *Journal of Physics D: Applied Physics*, 26(10):1587–1591, 1993. 65
- [43] Farhang Radjai, Michel Jean, Jean-Jacques Moreau, and Stéphane Roux. Force Distributions in Dense Two-Dimensional Granular Systems. Technical report, Université de Montpellier II, 1996. 65

- [44] C-h Liu, S R Nagel, D A Schecter, S N Coppersmith, S Majumdar, T A Witten, S R Nagel D A Schecter, T A Wtten, and James Franck. Force Fluctuations in Bead Packs. *Science*, 269(5223):513–515, 1995.
- [45] Corey S. O’Hern, Stephen A. Langer, Andrea J. Liu, and Sidney R. Nagel. Force distributions near jamming and glass transitions. *Physical Review Letters*, 86(1):111–114, 1 2001. 65
- [46] Farhang Radjai, H Troadec, and Stéphane Roux. Micro-statistical features of cohesionless granular media. *Italian Geotechnical Review-Revista Italiana de Geotecnica*, 3:39, 2003. 72
- [47] Bruno Andreotti, Yoël Forterre, and Olivier Pouliquen. *Granular media: between fluid and solid*. Cambridge University Press, 2013. 72
- [48] Patrick Charbonneau, Jorge Kurchan, Giorgio Parisi, Pierfrancesco Urbani, and Francesco Zamponi. Glass and Jamming Transitions: From Exact Results to Finite-Dimensional Descriptions, 3 2017. 73
- [49] Karen E. Daniels, Jonathan E. Kollmer, and James G. Puckett. Photoelastic force measurements in granular materials. *Review of Scientific Instruments*, 88(5), 2017. 73
- [50] Nathan C. Keim, Joseph D. Paulsen, Zorana Zeravcic, Srikanth Sastry, and Sidney R. Nagel. Memory formation in matter. *Reviews of Modern Physics*, 91(3):35002, 2019. 74
- [51] Monoj Adhikari and Srikanth Sastry. Memory formation in cyclically deformed amorphous solids and sphere assemblies. *European Physical Journal E*, 41(9), 9 2018.
- [52] Nidhi Pashine, Daniel Hexner, Andrea J Liu, and Sidney R Nagel. Directed aging, memory, and nature’s greed. Technical report, 2019. 74
- [53] K. Lawrence Galloway, Douglas J. Jerolmack, and Paulo E. Arratia. Quantification of plasticity: Via particle dynamics above and below yield in a 2D jammed suspension. *Soft Matter*, 16(18):4373–4382, 2020. 74, 76
- [54] Jasna Brujić, Ping Wang, Chaoming Song, David L. Johnson, Olivier Sindt, and Hernán A. Makse. Granular dynamics in compaction and stress relaxation. *Physical Review Letters*, 95(12), 9 2005. 74
- [55] Bart Braden. The Surveyor’s Area Formula. *The College Mathematics Journal*, 17(4): 326–337, 1986. 75

## Chapter 5

# Discharge of soft particles through a microfluidic hopper

In the previous chapters, we have studied the compaction of packings of viscoelastic particles from a rheological and micro-mechanical point of view. In this chapter we will study an industry-relevant case, hopper flow, i.e., the discharge of viscoelastic particles through a narrow orifice.

This chapter starts by highlighting the historical relevance of hopper flow. This followed by the description of a constitutive law relating the size of the particles and the orifice to the discharge rate. Next, we will describe the formation of clogs during hopper flow. Then, we will give a brief overview of other soft particle systems that have been used to study hopper flow.

Next we will show that it is difficult to obtain a dense suspension in a microfluidic hopper, and describe our newly developed microfluidic hopper that allows us to study hoppers with any orifice size. We then use this microfluidic hopper to study the evolution of the discharge rate over time during a discharge for both pressure and flow rate driven discharges. We will then try to find the scaling laws of the microfluidic hopper with the applied pressure or flow rate, and the dependency of the discharge on the orifice size. Lastly, we will make some qualitative statements on the effects of particle softness on the discharge and clogging.



## 5.1 Introduction

One of the unique properties of granular materials is that they cannot only behave as a solid when confined, as has been extensively discussed in Chapter 3 and 4, but also flow like a liquid in the absence of such confinement. This property is used ubiquitously in industry, as granular materials can be easily displaced using augers and dispensed using a hopper. While hoppers have most likely been used for much longer, the earliest examples of granular hoppers date back to the 14th century. For example, an hourglass can be seen in Ambrogio Lorenzetti fresco “Allegory of Good Government” painted in 1338.

Interestingly, the earliest examples of liquid filled hoppers for timekeeping have been around for much longer. Working examples of water-clocks (clepsydra) dating back to the 5th century BC are displayed in the Ancient Agora Museum in Athens. The question arises, why were the water-clocks replaced with sand-based hourglasses? Firstly, there are some small practical reasons. Water evaporates, meaning that each time the clock is used it needs to be refilled to the correct level. Also, a completely sealed water-clock doesn’t work, as surface tension prevents water from flowing into the air-filled lower compartment and air in the water-filled upper compartment. Instead, a riser-tube would be needed, which complicates the design and fabrication of the device, whereas the voids in a granular material are percolating, allowing the air to flow between the grains, removing the need for a riser-tube.

Furthermore, the hydrostatic pressure at the bottom of a container filled with liquid depends linearly on the fill-height

$$P(h) = \rho gh \quad (5.1)$$

with  $P(h)$  the fill-height dependent pressure,  $\rho$  the density of the liquid,  $g$  the gravitational acceleration and  $h$  the fill-height. In the limit of negligible viscous friction, all potential energy is converted into kinetic energy, resulting in the volumetric flow rate  $\dot{V}$  being proportional to  $\sqrt{h}$  (Torricelli’s law). Whereas in the viscous limit, most energy is lost via viscous dissipation, resulting in  $\dot{V} \propto h$ . This means that the flow-rate is not only dependent on the fill-height, but the scaling also depends on other parameters, such as the orifice size and viscosity. In the viscous limit, a constant decrease of the fill-height  $\dot{h} = \text{const}$  can be achieved if the ratio between the flow rate and the cross-sectional area at the fill-height is constant

$$\dot{h} = \frac{\dot{V}}{A} \propto \frac{h}{\pi r^2} \rightarrow r \propto \sqrt{h} \quad (5.2)$$

This also means that the time to discharge a volume  $V$  scales as  $t \propto V^{2/3}$ . This makes it difficult to tune the water-clock to an arbitrary time.

### 5.1.1 Hopper discharge

It turns out that this scaling doesn’t hold for granular materials. Huber-Burnand [4] found that the discharge rate for granular materials was constant over time, and thus didn’t depend on the fill-height or even external pressure applied on the packing. This was further investigated by Hagen [1], who argued that the pressure exerted on a disk at the bottom of a cylindrical container (red area in Figure 5.1A) is equal to the weight of the material above the disk (green area) minus the frictional force exerted by the surrounding sand (orange area)  $\pi r^2 \rho H - 2\pi r \rho \mu H^2$ , with  $r$  the radius of the disk,  $\rho$  the specific weight of the granular material,  $H$  the fill-height. This leads to an initial linear increase of the pressure on the disk with increasing fill-height, followed by a quadratic decrease. Hagen argued that the increase

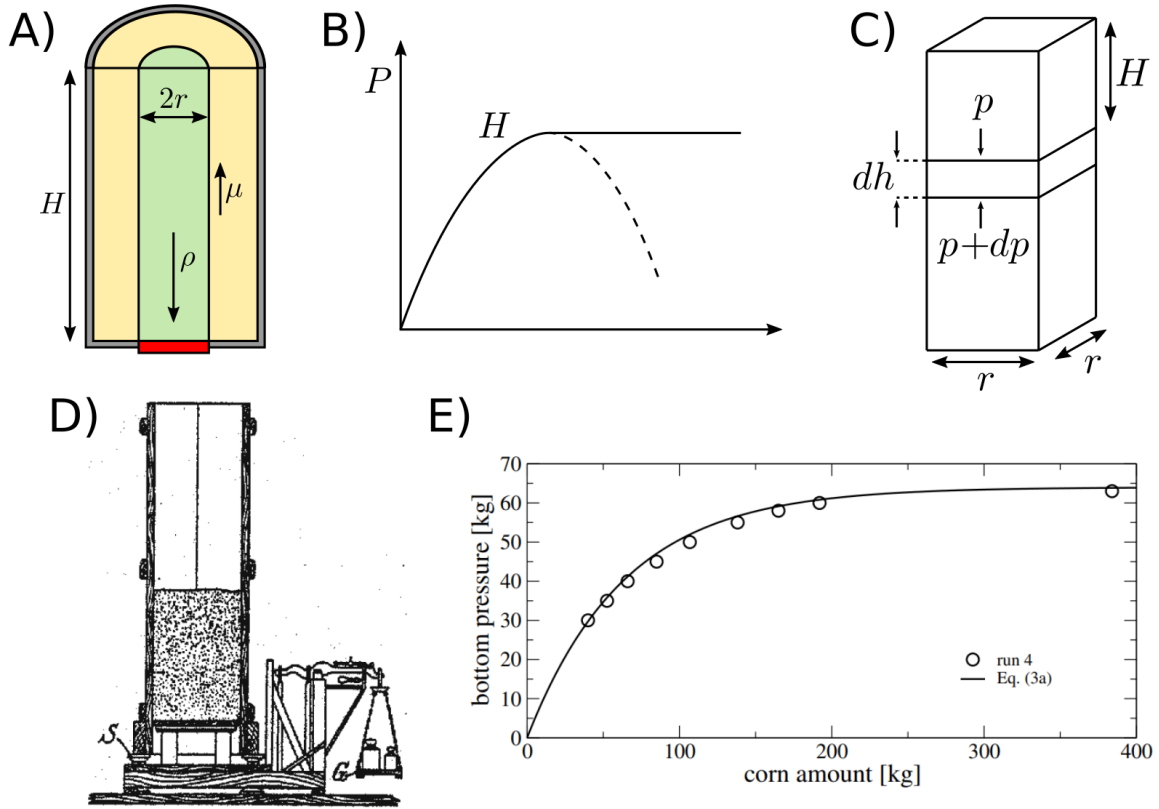


Figure 5.1: A) Schematic representation of a silo of height  $H$ , and an opening with radius  $r$  (indicated in red). Hagen [1] argued that the pressure on the red plate should be equal to the weight of the column above the plate (green), minus the friction with the particles surrounding the column (yellow). B) Pressure at the orifice as function of the fill-height, according to Hagen [1]. C) Schematic representation of the model Janssen [2] used to determine the pressure in a granular packing as function of the position in the packing. D) Drawing of the experimental setup of Janssen [2] to determine the pressure at the orifice as function of the fill-height of the hopper. Figure taken from [3] E) Data point obtained with the setup in D), line is the fit with the model described by C). Figure taken from [3]

in friction force involved with extending the column by adding particles can never be higher than the increase in gravitational force of the added particles, as the particles are not rigidly connected. Hence, the pressure would remain constant after it has reached its maximum at  $H = \frac{4r}{\mu}$ , rather than decreasing (Figure 5.1B) [1, 5].

This idea was further refined by Janssen [2], Sperl [3], who considered the force balance on a thin slice of thickness  $dh$  of a square container with length and width  $r$  as function of the height of the packing above the slice,  $H$ :

$$dp = \rho dh - \frac{Kpu}{A} dh \quad (5.3)$$

where  $\rho$  is the specific weight,  $K$  the radial pressure multiplied by the friction coefficient over the axial pressure,  $u$  the circumference and  $A$  the cross-sectional area. Rearranging eq. 5.3 gives

$$\frac{dp}{\rho \left(1 - \frac{Kpu}{A\rho}\right)} = dx$$

Integration of both sides yields

$$-A \ln \left( 1 - \frac{ku}{A\rho} p \right) = Ku(x - x_0)$$

Given that the pressure on the top layer is zero,  $H = 0$ ;  $p = 0$  the solution becomes

$$\ln \left( 1 - \frac{ku}{A\rho} p \right) = \frac{Kux}{A}$$

After rearranging one finds the pressure as function of the packing height

$$p = \frac{A\rho}{Ku} \left( 1 - e^{-\frac{Ku}{F}x} \right) \quad (5.4)$$

Rather than a quadratic approach followed by a plateau (as was found by Hagen), Janssen found that the pressure exponentially approached a limit, which agreed very well with the experiments he performed on a corn filled silo (Figure 5.1DE) [2, 3]. Hence, this phenomenon is commonly known as the Janssen-effect.

The height-independence of the pressure at the bottom is commonly given as the reason for the constant discharge rate of granular materials [6–11]. This makes for convenient time-keeping pieces, as the discharge time scales linearly with the fill-height, allowing for easy graduation of the container, interpolation of the time, and the weight of sand is directly proportional to the time needed for discharge. It is also very important in industry, as this proves that most of the load is carried by the walls of the silo, not the bottom. Improper reinforcement of the sides of silos commonly leads to their collapse.

### 5.1.2 Hagen-Beverloo law

One can assume that the discharge of grains is governed by dissipation, given the frictional nature of granular media. This means that the discharge rate, would be governed by the orifice size. In his seminal paper, Hagen [1] initially proposed a cubic scaling of the discharge rate with the orifice size, but found that the scaling underestimated the discharge rate slightly for small orifices and overestimated the discharge rate at large orifices (Figure 5.2A). Instead, he proposed that the mass discharge rate ( $W$ ) should scale with the area of the orifice, and the velocity of the particles passing through the orifice, which he approximated by the velocity after a free-fall of height  $h$

$$W = 2\pi\rho r^2 \sqrt{gh} \quad (5.5)$$

Hagen found, however, that a small correction ( $x$ ), in the order of a grain diameter, needed to be applied to the radius for the fit to work, with the justification that particles touching the edge of the orifice slow down, and impede the flow of neighboring particles [1, 5]. Combining this with the suggestion by Brown and Richards [13] that the particles start their free-fall when they pass through an arch with a radius equal to the radius of the orifice (Figure 5.2), results into

$$W \propto \rho(D - x)^{2.5} \quad (5.6)$$

The effect of orifice size and shape and particle size was further studied by Beverloo et al. [12]. They found that, for various seeds, the correction factor scaled with the seed size, and the prefactor is constant if the specific weight of the granular medium is taken into account, yielding the well known Hagen-Beverloo equation:

$$W = C\rho\sqrt{g}(D - kd)^{2.5} \quad (5.7)$$

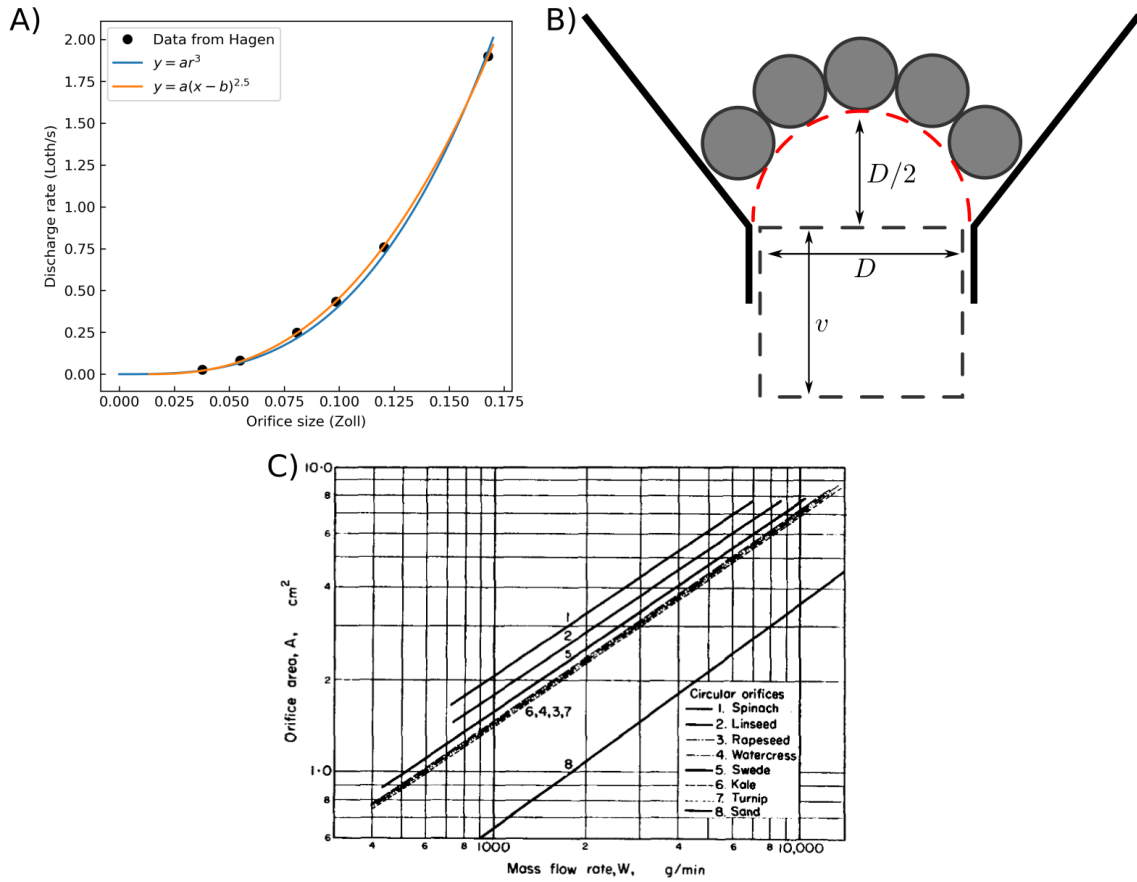


Figure 5.2: A) Discharge rate as function of the orifice size, data taken from [1]. The line indicate two fits, the blue was deemed incorrect by Hagen [1], who proposed a new model  $y = a(x - b)^{2.5}$ , which is indicated by the orange line. B) Schematic representation of the model proposed by Beverloo et al. [12] to explain the orifice size dependence of the discharge rate. C) Discharge rates as function of orifice size for a wide collection of seeds, all following the same scaling, as described by Hagen and Beverloo. Figure taken from Beverloo et al. [12]

with  $C$  a proportionality constant (35 for the experiments done by Beverloo et al. [12]),  $\rho$  the specific weight,  $g$  the gravitational constant,  $D$  the diameter of the orifice,  $k$  the correction factor for the orifice size (typically 1.4 [12]), and  $d$  the particle diameter.

Further research has shown that this scaling is very robust, as it works for non-spherical particles [1, 5] and a wide variety of materials (such as grains, plastics, metals, and glass) [11, 12, 14–16]. Advances in the understanding of the discharge of granular materials have not halted.

Recently, Janda et al. [17] showed that the velocity-profiles near the orifice are self-similar. They found a model for the velocity profile, which confirms the scaling of the discharge rate with the square root of the orifice radius,  $W \propto \sqrt{R}$ , indicating that the empty-annulus concept coined by Brown and Richards [13] doesn't justify the “ $k$ ” coefficient in eq. 5.7. Dorbolo et al. [18] experimentally confirmed the scaling of the discharge rate with the square root of the gravitational acceleration,  $W \propto \sqrt{g}$ , by placing a granular hopper in a large centrifuge. Rubio-Largo et al. [19] showed both experimentally and numerically that the “free-fall arch” does not exist. They did not find discontinuities in the contact forces, but rather a linear decrease

as the particles get closer to the orifice. Rubio-Largo et al. [19] also found that there is a singular region above the orifice where the velocity profile is decided. However, this region is parabolic, rather than circular, and extends much deeper into the hopper. However, despite the flaws in the reasoning behind the Hagen-Beverloo law, the scaling still holds.

### 5.1.3 Clogging

The Hagen-Beverloo model for the discharge of hoppers only works when the particles can flow freely. When the orifice size is less than  $\sim 5$  particle diameters, the flow of particles can be (temporarily) impeded due to the formation of clogs, invalidating the Hagen-Beverloo model [20–22]. Dressaire and Sauret [23] defined 3 mechanisms of clog formation in microfluidic systems: 1) Sieving, the orifice is smaller than one or more of the particles, preventing them from leaving the hopper. 2) Bridging, multiple particles can form an arch, blocking the orifice [24, 25]. 3) Aggregation, attractive forces can cause particles to aggregate near the orifice, blocking it [26, 27].

Focussing on the formation of arches, Clément et al. [28] were the first to observe that the probability of finding an avalanche of size  $M$  decreased exponentially with the size  $M$ . Zuriguel et al. [29] explained this trend by assuming each particle has the probability  $P_{flow}$  to not clog the hopper, regardless of the environment around the orifice. The probability of  $N$  particles flowing out, followed by a clog is:

$$P(N) = P_{flow}^N (1 - P_{flow}) \quad (5.8)$$

Taking the log on both sides gives  $\ln(P(N)) = N \ln(P_{flow}) + \ln(1 - P_{flow})$ . Hence, the logarithm of the probability of finding an avalanche of  $N$  grains scales linearly with the avalanche size. The exponential decay has been observed in a wide variety of systems 2D and 3D flat-bottom silos [29], tilted hoppers [30], with obstacles present [31], and in fluid driven systems [25, 32–34]

### 5.1.4 Soft particles

The time-independent discharge rate and Hagen-Beverloo scaling of the discharge rate with the orifice size have proven to be quite robust. However, simulations and experiments on soft and or frictionless particles have shown that they don't always hold. Several numerical simulations reported a decrease in discharge rate as the hopper discharged for low frictional damping or friction coefficient [37–39].

Recently, emulsions and hydrogel particles have been used to study the effect of friction and softness on the discharge of granular materials in a hopper. Koivisto et al. [40] and Desmond et al. [41] found that the fill-height independence of the pressure (Janssen-effect) doesn't hold for their frictionless experimental systems (immersed glass particles and both oil-droplets in water and hydrogel particles, respectively). Following this, Ashour et al. [42] and Pongó et al. [35] showed that for soft frictionless spheres, the discharge rate decreases as the hopper empties, which Hong et al. [43] postulated, but did not measure. Wang et al. [44] showed that the addition of only a small amount of frictional particles ( $\sim 10\%$  v) completely removes the height dependent discharge rate, as well as reducing the overall discharge rate. Also, more qualitative differences between the discharge of frictional and frictionless particles have been found. Where hoppers filled with hard particles showed stagnant zones, the hoppers filled with soft frictionless particles completely discharged [36, 42, 44]. Furthermore, soft frictionless particles were found to be much less prone to clogging [35, 36, 42–45],

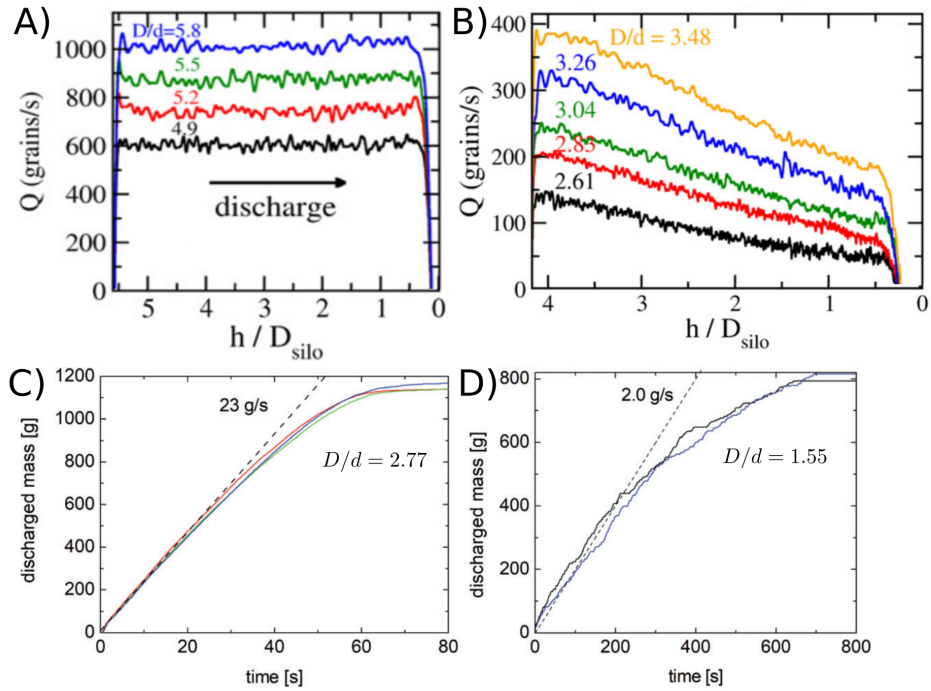


Figure 5.3: A) Discharge rate of a granular hopper with hard frictional particles as function of the fill-height of the hopper. Figure taken from [35] B) Discharge rate of a granular hopper with soft frictionless particles as function of the fill-height of the hopper. Figure taken from [35] C) Cumulative discharge of soft frictionless particles over time. Figure taken from [36] D) Cumulative discharge of soft frictionless particles through a very narrow orifice over time. Figure taken from [36]

and if a clog formed it typically dissolved naturally, i.e., without external interference [36, 43]. In hard-particle systems, the clogs typically dissolve only upon external perturbation, such as vibrations of the hopper, thermal fluctuations or activity of the “particles” themselves [46–48].

It turns out, however, that it can be difficult to decouple the effects of particle softness from inter-particle friction in experiments, as the soft particle systems discussed above turn out to be frictionless, and the hard particle systems frictional. In this chapter, we will discuss the discharge of frictionless particles fabricated with the in-situ lithography technique, which allows us to change the particle softness without affecting any of the other particle properties.

## 5.2 Materials and Methods

### 5.2.1 Hopper channels

Our first attempts at studying the discharge of particles with varying softness involved channels with a constriction, as can be seen in Figure 5.4AB. We put the bottom wall of the hopper at an angle, as to prevent air from getting trapped in the corners during the filling process, which should not influence the discharge rate of the hoppers if the angle is kept below  $\sim 45^\circ$  [49, 50]. The small openings in the bottom plate of the hopper were to maintain a homogeneous flow field across the hopper.

However, these channels did not work. During the fabrication process, we are not able to create a jammed packing, as printing the particles too close to each other causes them to fuse together. As a result, our initial condition has a packing fraction of  $\sim 0.4$  (Figure 5.4AB). This

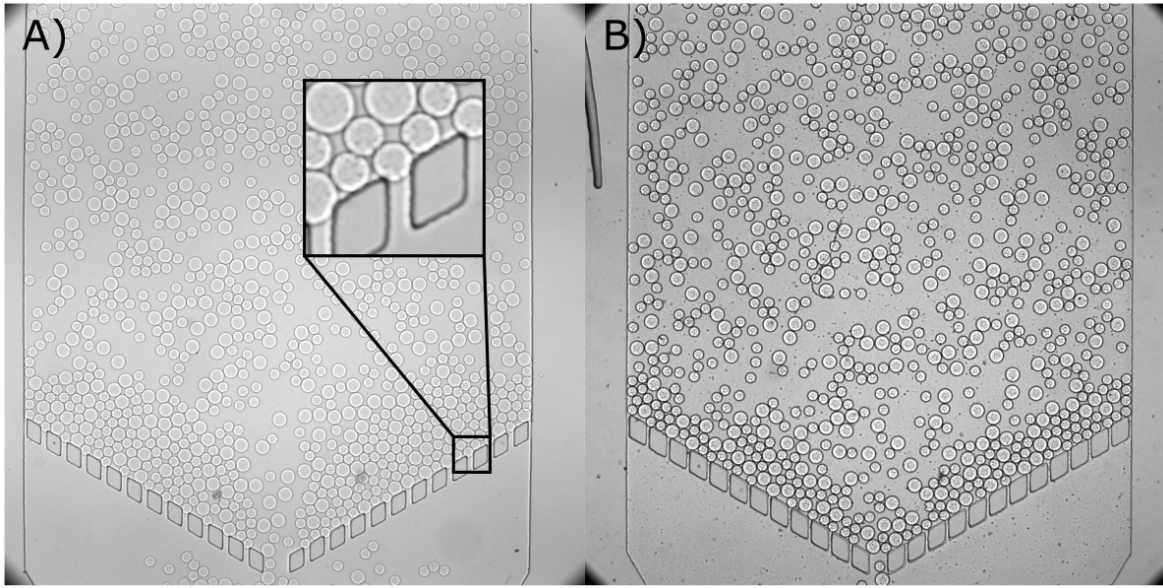


Figure 5.4: A) Settling of a mixture of 160 and 120  $\mu\text{m}$  particles in a microfluidic hopper with an orifice of 250  $\mu\text{m}$ . Inset: Zoom of particles lodging themselves between the PDMS blocks. B) Settling of a mixture of 160 and 120  $\mu\text{m}$  particles in a microfluidic hopper with an orifice of 180  $\mu\text{m}$ .

meant that we relied on the formation of an arch for the particles to collect near the orifice. We found that if the orifice size was slightly too large,  $D/d \gtrsim 1.7$ , no clog would form and all the fabricated particles would pass through the orifice unimpeded (Figure 5.4A). While if the orifice was slightly too small,  $D/d \lesssim 1.5$ , arches would be so stable that they would not break and after external perturbation would reform quickly, limiting the avalanches to only several particles (Figure 5.4B). It thus became obvious that the orifice size cannot be varied independently of the particle size in this setup.

We also noticed particles tended to stick to the bottom wall. We attribute this to the mechanical interlocking of the soft particles with the gaps (Figure 5.4A), as well as the attraction of the particles to the gap due to hydrodynamic drag being oriented towards the gaps. We, therefore, omitted them in future designs, and accepting the focusing of the flow of the suspending fluid towards the orifice.

We needed a more robust way to collect the particles near the orifice, which should also work for larger orifice sizes. An intuitive solution is to embed a movable object in the channel to act as a valve. While this will probably work, this method has some drawbacks. Firstly, if this object extends through the side of the channel, to be able to manipulate it externally, it tends to introduce leaks, which might affect the flow in the channel. Embedding a small metal object and using a magnet to displace, would also cause problems. During the channel fabrication, the PDMS is not yet fully cured (and thus sticky) when the channel is sealed, which would cause the metal object to bind to the PDMS and not move at all. We, therefore, discarded this idea and moved to a different design.

### 5.2.2 Fabrication of Quake valves

The solution to this problem came from the field of microfluidic large scale integration, i.e., a microfluidic analog to a computer array and memory storage, in the form of Quake valves.

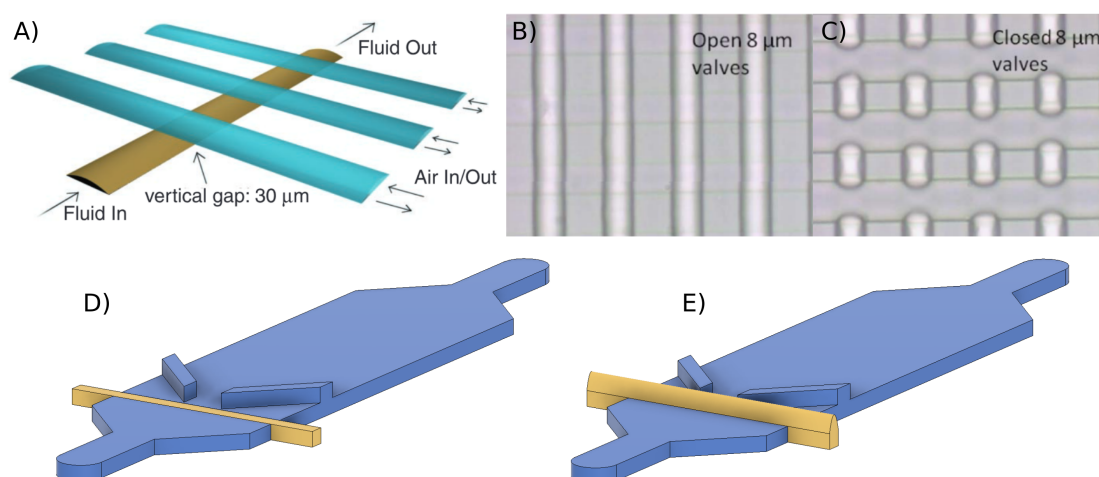


Figure 5.5: A) Schematic representation of a fluid channel (yellow) and three pneumatic valve channels (blue). Images taken from [51] B) Microscopy image of four vertical channels filled with fluid and three horizontal valve channels. The valve has been filled with an index matched fluid, hence they are nearly invisible. Image taken from [52]. C) Same four vertical channels and 3 horizontal valve channels as in B, but now with the valves closed. D) Schematic representation of our hopper channel with open valve. E) Schematic representation of our hopper channel with closed valve.

A Quake valve works by having two channels orthogonal to each other, separated by a thin membrane (Figure 5.5A). By applying a pressure to one of the channels, either pneumatic or hydraulic, the membrane is deformed, blocking the other channel (Figure 5.5BC) [51–53].

Figure 5.5D shows a schematic representation of our microfluidic hopper. When the pressure in the hopper channel (blue) and valve channel (yellow) is roughly equal, the membrane is deflated, and the orifice is open. Upon increasing the pressure in the valve channel, the membrane deforms, blocking the orifice (Figure 5.5E). We tuned the height of the valve by changing the pressure applied to the valve channel, so that the particles are retained, but a gap remains, allowing the fluid to pass [54].

The fabrication of the hoppers with integrated Quake valves was not straight-forward. Figure 5.6A shows the standard channel fabrication (as discussed in chapter 2), where a cured piece of PDMS with a negative of the channel is pressed onto a semi-cured layer of PDMS spin-coated on a glass slide. The Quake valve is made by placing a thin layer of PDMS containing the valve channel between the hopper channel, and the spin-coated glass slide (Figure 5.6B). This thin layer is made by spin-coating a silicon wafer with the design pattern of the valve channel with PDMS. Removing the  $\sim 50\mu\text{m}$  layer of PDMS from the silicon mold is nearly impossible, as it can easily break/tear, as well as stick to itself. Therefore, the Quake valve was first bonded to the hopper channel, before taking it off the silicon mold. This thick layer of PDMS gave support to the thin membrane, allowing it to come off the silicon mold undamaged. After the hopper channel and the valve channel were properly bonded, we tried placing them on the PDMS coated glass. However, the membrane tended to stick to the hopper channel. The hopper channel is very wide (5 mm), hence the thin and flexible membrane is easily able to bridge the  $100\mu\text{m}$  height of the hopper channel and stick itself to the hopper channel. This caused air to get trapped under the channel, rendering the channel unusable (Figure 5.6B red dashed line, and D discontinuous horizontal channel, as well as air bubble in the top part of the channel).



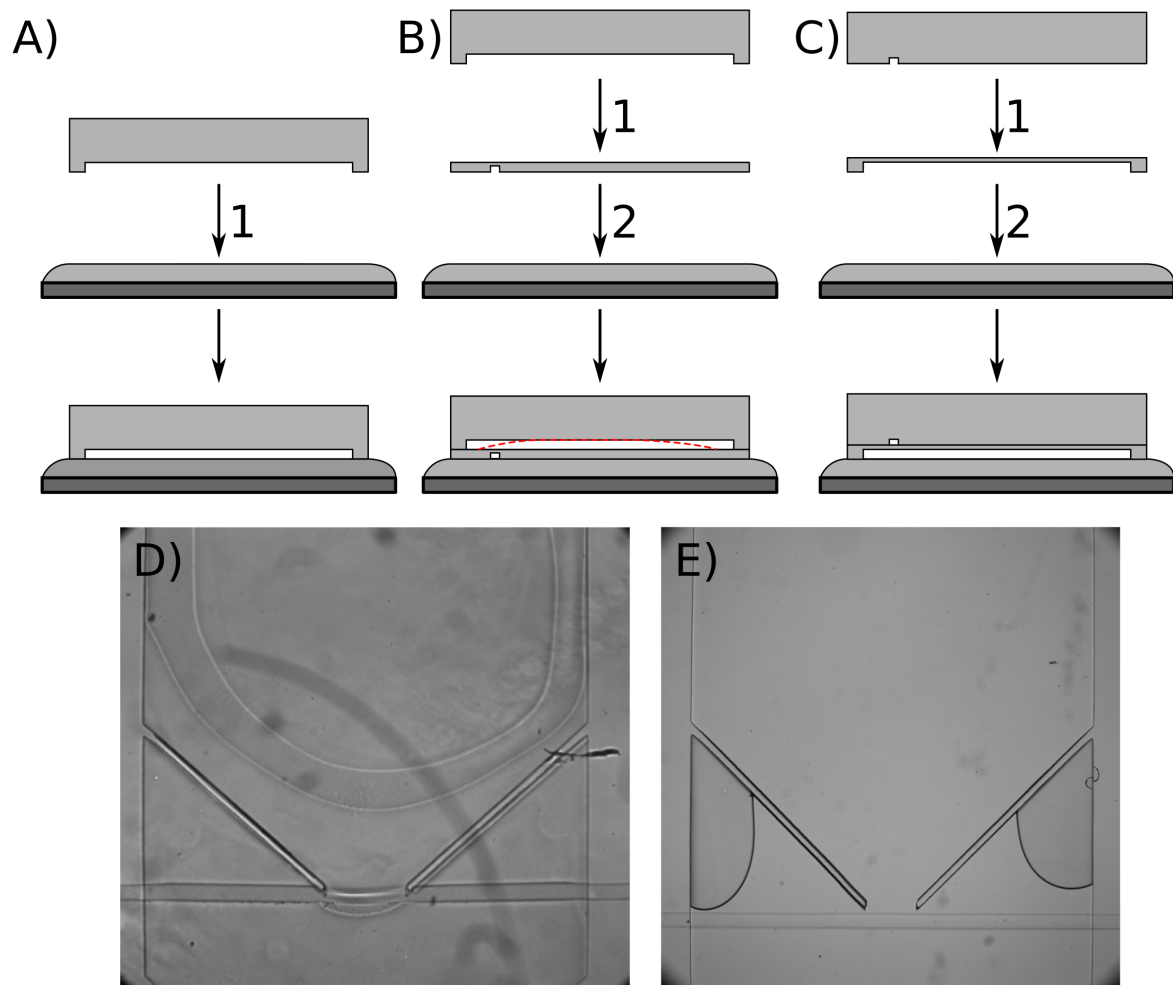


Figure 5.6: A) Typical fabrication of a PDMS microfluidic channel. A thick ( $\sim 5$  mm) PDMS layer is bonded to a PDMS coated glass slide. B) Typical procedure to fabricate a Quake-style valve. The first step is to bond a thick layer of PDMS (similar to A) to the spin-coated valve channel, while the valve channel is still attached to the silicon mold. After bonding together, they were removed from the silicon mold, and bonded to the PDMS coated glass slide, in the second step. This, however, caused air to get trapped (red dashed line). C) “Inverted” Quake valve. Here, the valve channel cast in a thick layer of PDMS, and then bonded to the PDMS spin-coated hopper channel. The second step is to bond the combined valve and hopper channel to the PDMS coated glass slide. Any air would be trapped inside the hopper channel, which is filled with air anyway. D) Quake-style channel fabricated using method B). A big air bubble is trapped between the membrane and the spin-coated PDMS (ovals in the center of the image), rendering the channel inoperable. E) Hopper channel fabricated using method C). The hopper is mostly filled with a PEG/PEGDA solution, apart from two air bubbles, which are sufficiently out of the way of the orifice to not impede the flow.

This problem was fixed by creating an “inverted” Quake-style valve, by embedding the hopper channel in the thin PDMS layer, and casting the valve channel in a thick layer of PDMS to give stability to the channel. Then, the thick PDMS layer was first bonded to the membrane, to stabilize it, and then to the PDMS coated glass slide (Figure 5.6C). The membrane was not able to bridge the  $200 \mu\text{m}$  wide valve channel, resulting in a working Quake-style valve (Figure 5.6E). The typical actuation pressure of this channel ( $P_Q$ ) was

determined to be 170-180 kPa, by trial and error. During the filling process, the fluid cannot push all the air out of the channel. Due to a design error, some air will get trapped in the corners under the bottom walls of the hopper (dark regions in on the left- and right-hand side of Figure 5.6E). Since the flow is nearly stagnant in this zone, this doesn't influence this flow rate of the fluid.

### 5.2.3 Initialization of microfluidic hoppers

Once the channel has been fabricated, the experiments are started, similar to the compression experiments. First, the channel is filled with the PEGDA solution corresponding to the desired softness. Then the inlet is blocked to limit the drift of the particles during the fabrication process. Since the outlets of the hopper channels are much wider than the typical inlet/outlets (5 mm compared to 1 mm), it is not possible to block the outlet. In other experiments, the inlet and outlet were blocked using a metal plug. However, removing the plug would displace  $\pi * 0.25^2 * 0.5 \approx 0.2mL$  of volume, whereas the channel only contains  $0.5 * 2 * 0.1 = 0.1mL$  of PEGDA solution. The pressures involved with manually removing the plug would "suck" most particles past the valve, leaving only a few particles to do experiments on. Hence, we decided to leave the outlet open.

Blocking the outlet with just the valve was, however, not enough to limit drift over the extended period of time ( $\sim 30$  min) to print all particles for a bidisperse mixture. We, therefore, only worked with monodisperse particles. These could be printed in a triangular lattice from left-to-right. This heavily reduces the impact of the drift, as particles in close proximity were also printed shortly after each other, which was not necessarily true for the randomized bidisperse packing.

Once the channel is properly blocked and aligned (as described in chapter 2), the particles were printed. The number of particles was adjusted such that the total volume of particles at the start of each discharge was constant. Then the orifice was closed by applying pressure to the Quake channel. Typical pressures required to close the channel sufficiently to retain the particles, while still letting the fluid pass, were 1600-2000 mbar. The required pressure depended mostly on the particle softness, where a higher pressure was needed to block the softer particles, as they tended to deform and squeeze over the valve.

Once the valve was closed, a  $\Delta P$  of 60-70 mbar was applied to deposit the particles on the growing pile near the orifice. The time needed for all particles to collect near the orifice depended on the softness of the particles, where it took  $\sim 5$  min for the 12 MPa particles and  $\sim 10$  min for the 0.4 MPa particles. It took longer for the soft particles, as they would deform when squeezed against the valve, and almost hermetically seal the channel, whereas the seal with the harder particles was less complete leading to a higher flow-rate (since our experiments were pressure driven), hence a higher rate of deposition. Applying a higher pressure to speed up this process was not possible, as this would push particles over the valve (especially the softer particles). Compensating this by increasing the pressure of the Quake channel was not possible, as the maximum pressure of the pressure controller was 2000 mbar, and the PDMS layers can delaminate at pressures over 2000 mbar. A potential improvement could be to increase the width of the Quake channel, or decrease the thickness of the membrane. We have, however, not tested this.

As soon as the particles have collected near the orifice, the camera was started,  $\Delta P$  was changed to the desired value and pressure of the Quake channel  $P_Q$  was set to  $\Delta P$ . This is quite important, when  $P_Q > \Delta P$  the membrane will protrude into the hopper channel and impede the flow, as intended. However, if  $P_Q < \Delta P$ , the membrane will "sink" into the Quake

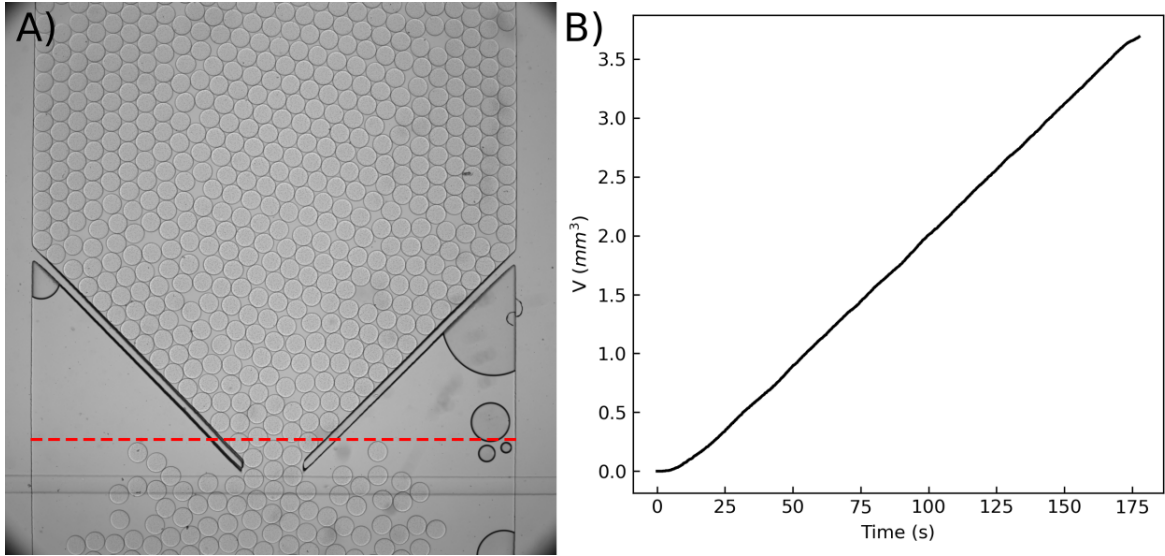


Figure 5.7: A) Typical image of the microfluidic hopper filled with particles during discharge. The red dashed line indicates the threshold defining whether a particle has been discharged or not. B) Typical cumulative discharge of a microfluidic hopper.

channel creating a trough which can also impede the flow of the particles.

## 5.3 Results and Discussion

### 5.3.1 Discharge rate

Once the Quake valve is opened, particles start to flow through the orifice. Typically, the discharge rate of hoppers is given as the mass discharge rate, as this can be easily measured using an electronic balance. This is, however, not possible for our experiments, as the total mass (carrier fluid and particles combined) flowing out of the channel is not necessarily proportional to the amount of particles discharged. Therefore, we will only deal with volumetric discharge. We define the cumulative volumetric discharge as the sum of the particle volumes that have crossed a certain threshold (red dashed line, Figure 5.7A)

$$V(t) = \sum_i^{N_p} \pi R_i^2 L_i \mathcal{H}(y - r_{i,y}(t)) \quad (5.9)$$

with  $N_p$  the total number of particles,  $R_i$  and  $L_i$  the radius and length, respectively, of particle  $i$ , and  $\mathcal{H}$  the Heaviside function such that  $\mathcal{H}(y - r_{i,y}) = 1$  if particle  $i$  has crossed the threshold value  $y$  and 0 if it hasn't

$$\mathcal{H}(y - r_{i,y}) = \begin{cases} 0 & \text{if } y \leq r_{i,y} \\ 1 & \text{if } y > r_{i,y} \end{cases} \quad (5.10)$$

This threshold was not placed exactly at the orifice, but slightly above the orifice. We found that placing the threshold exactly at the orifice sometimes lead to a slight under-detection of the total number of particles discharged. First, the particle velocity is the highest at the orifice. This would sometimes lead to motion blur, causing our particle finding algorithm to not identify a particle. Furthermore, particles would sometimes move more than a

particle radius, especially small particles, which could cause mislabelling of the particles by the tracking algorithm. Lastly, the dark lines of the Quake-channel sometimes interfered with the detection of the particles near the orifice. To avoid all these problems, we decided to place the slightly above the orifice to improve the stability and robustness of our data-analysis.

### 5.3.A First observation

Figure 5.7B shows the cumulative volumetric discharge of 200  $\mu\text{m}$  particles through a 600  $\mu\text{m}$  orifice at an imposed pressure drop of 1.5 kPa. Here  $t = 0$  is the moment the camera starts recording. At this point, the Quake valve is still closed. After 5–10 seconds (indicated by the dashed vertical line), the valve is opened and particles started to flow out. We found that the cumulative discharge increases linearly with time, meaning that the discharge rate,  $\dot{V}_d$ , is independent of time, similar to the discharge of dry granular particles in a gravity driven hopper. This is quite surprising, as there is no reason to expect the discharge of submerged frictionless grains to behave similarly to dry frictional grains. We will now investigate its origin.

### 5.3.B Addition of surfactant

First, we should note that the constant discharge rate was not always observed at first. Figure 5.8A shows the total volume of particles discharged over time. Approximately 10 seconds after the start of the experiment, the valve is opened, and the particles are able to flow out. However, unlike with gravity driven hoppers and the previously shown discharge, it takes a significant amount of time for the hopper to start flowing. We noticed that at the start of the experiment, when the valve was still closed, the system is densely packed (Figure 5.8B). As soon as the valve opens, the particles at the orifice start to move, but the majority of the bulk particles hardly move. So, a “cavity” is formed, like in Figure 5.8C. After a while (the exact time fluctuates heavily, but appears to decrease with increasing applied pressure), this cavity collapses, and the hopper quickly enters a constant discharge rate regime (Figure 5.8D). This ability to sustain a load indicates that there is a slight adhesion between particles [55]. This adhesion was not enough to affect the compaction (chapter 3 and 4), due to the much higher pressures involved (20 kPa, compared to 0.5–3 kPa for the hopper flow). A small amount of surfactant (0.1 % v/v of tween-80) was added to the solution to limit adhesive effect. Furthermore, before the valve was opened, the particles were manually agitated by pushing on the channel near the outlet. These measures prevented the slow onset of the discharge.

### 5.3.C Fluid velocity during discharge

We will now discuss the origin of the constant particle discharge rate. First, the particles contribute to the hydraulic resistance of the channel. One could expect the hydraulic resistance of the channel to drop as particles are discharged, this would result in an increase in the carrier fluid velocity, and therefore an increase in the hydrodynamic drag exerted on the particles, increasing the discharge rate as the hopper empties. We’ve studied the carrier fluid velocity during discharge by means of Particle Image Velocimetry (PIV, section 2.5). The fluid velocity was measured in a region without particles, along the center-line of the channel.

Figure 5.9 shows the average carrier fluid velocity over time during a discharge. Each data point corresponds to a set of 10 images (so 9 correlations) taken 20 ms apart. Each

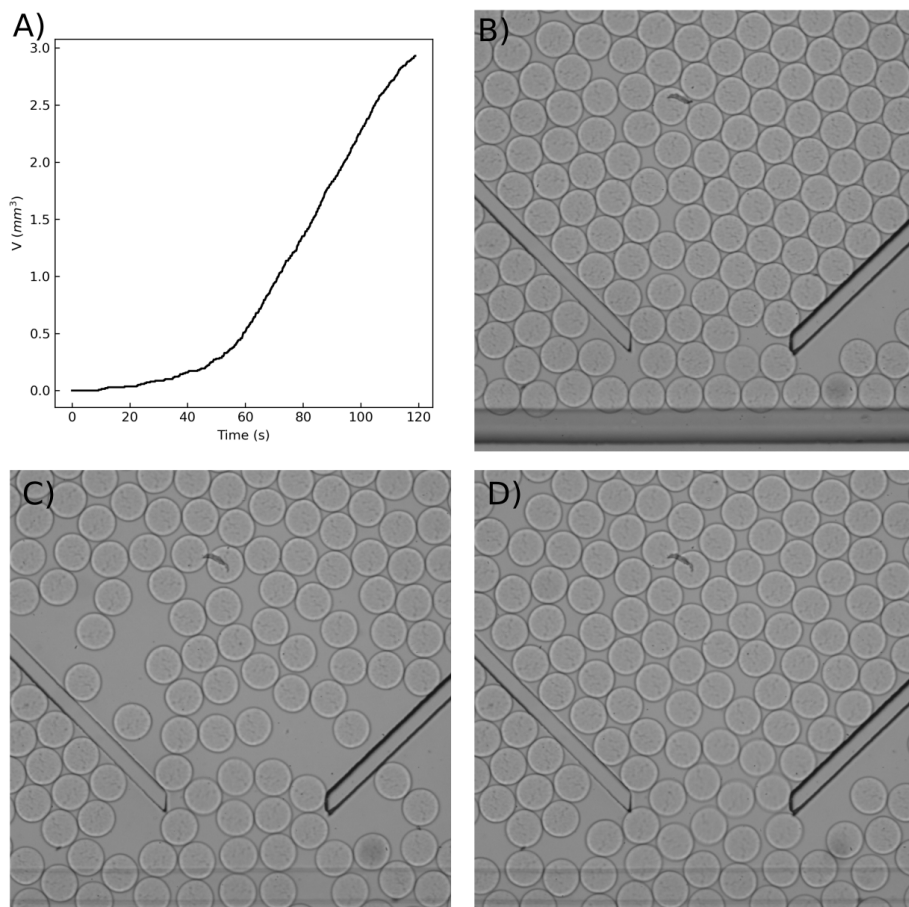


Figure 5.8: A) Cumulative discharge of  $150 \mu\text{m}$  particles that were not agitated manually and didn't have surfactant added through a  $600 \mu\text{m}$  orifice. B) Hopper filled with the particles before the Quake valve is opened, as can be seen from the dark valve below the particles ( $t=0$  s in Fig A). C) "Cavity" formed once the valve is opened. The open valve is almost transparent ( $t=30$  s in Fig A). D) Particles near the orifice during the constant discharge rate regime ( $t=70$  s in Fig A).

image was divided into a  $9 \times 9$  grid. The velocity of the fluid was determined in each of the grids. The average fluid velocity in that set of images was then taken as the average of the velocity in all grids of that set ( $9 \times 9 \times 9 = 729$  grids). The error bars in Figure 5.9 indicate the standard deviation of the fluid velocities. The broad distribution is most likely due to the height of the channel and large working distance of the objective used. The velocity gradient is in the Z-direction for a Hele-Shaw cell, so the velocity of the tracer particles depends on the Z-position of the tracer. We used a normal inverted fluorescence microscope, with which we observe the entire Z-range at once, albeit that tracer above/below the selected focal plane are slightly out of focus. The fact that we can see all particles, irrespective of their position along the Z-direction in the channel (and thus their velocity), gives rise to spatial (and temporal) fluctuations. This is further confirmed by the fact that the standard deviation scales linearly with the measured velocity. A better measure of the accuracy are thus the fluctuations in the average velocity when the channel is empty (plateau in Figure 5.9,  $\sim 6 * 10^{-6}$ ), which are much smaller than the standard deviation ( $\sim 2 * 10^{-5}$ ). This error could also be reduced by using a confocal microscope. A confocal microscope blocks all out of focus light, and one can

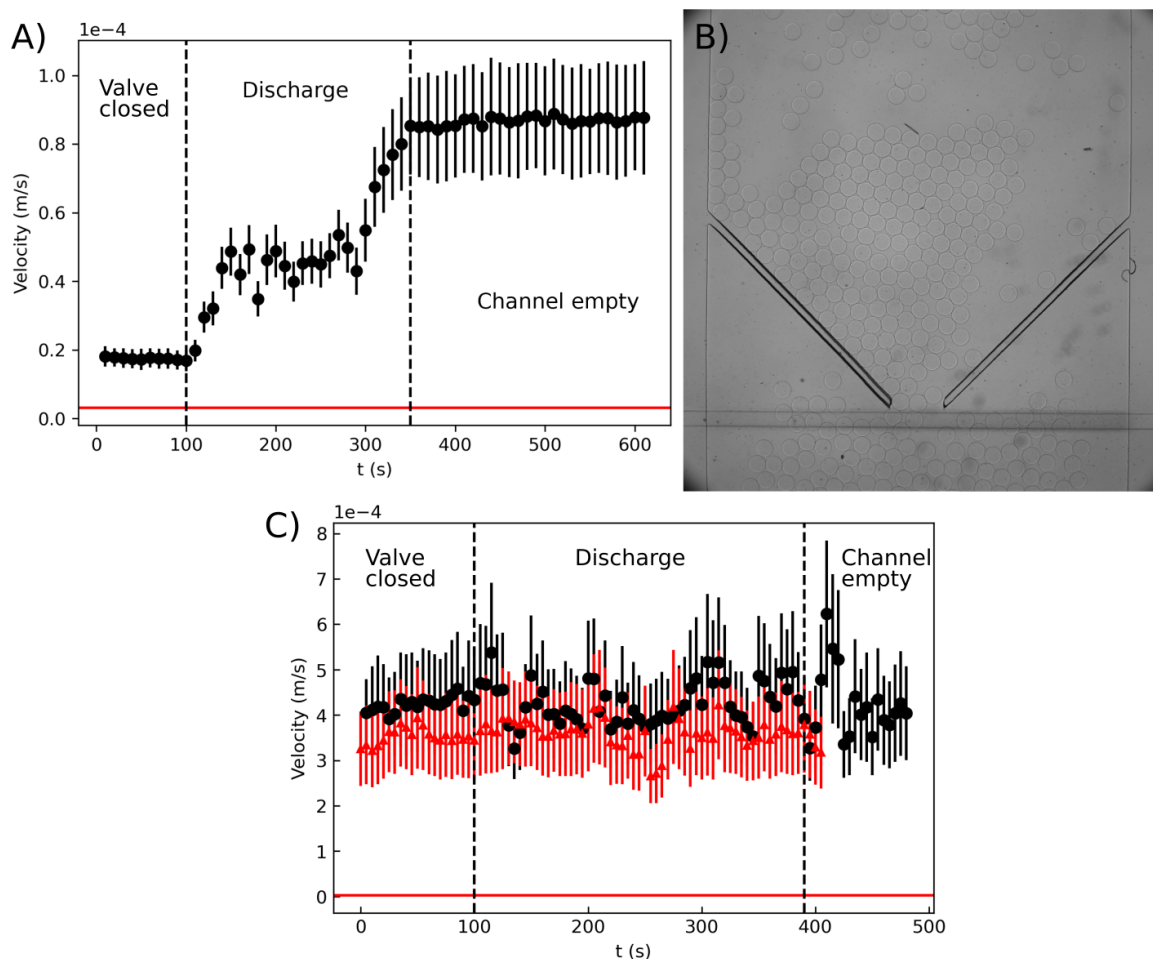


Figure 5.9: A) The velocity of the fluid during the pressure driven discharge of hoppers shows three phases: an initial phase with constant fluid velocity, while the valve is still closed (it is manually opened at 100 s). A second phase during which the discharge takes place, where the fluid velocity fluctuates around a constant mean. Lastly, the third phase, where the fluid velocity is constant again. The red line indicates the limit of detection of the PIV with the settings used. B) Occasion where the packing is no longer percolating at when the hopper is almost fully discharged. The fluid is able to pass through the hopper on the right side, without having to flow over the particles. C) The velocity of the fluid during the flow rate driven discharge of hoppers. The black circles and red triangles are experiments, both taken at 20 nL/s. The red line indicates the limit of detection of the PIV with the settings used.

therefore only observe tracers in a specific Z-plane, which should all have the same velocity.

The main drawback is that the PIV is done with fluorescent beads, observed far away from the PEGDA particles so that the fluid flow is undisturbed. The PEGDA particles are not fluorescent, meaning that it is only possible to measure the PEGDA particle discharge with bright-field microscopy, or measure the fluid velocity with fluorescence microscopy, not both.

We found that the carrier fluid velocity is low then the valve is closed, as expected, as it is indented to impede the flow (Figure 5.9A, left of first dotted line). When the valve is opened, the carrier fluid velocity increases, as the valve no longer impedes the flow. We found that

there is a transient period of 30–40 seconds where the fluid velocity increases, until it reaches a constant, but fluctuating, velocity during the discharge. After the particles have discharged, the carrier fluid velocity increases over 40–50 seconds to reach a plateau corresponding well to the fluid velocity in an empty channel. We believe that the first transient is due to the slow startup that is sometimes observed, especially when no surfactant was added (see Figure 5.8) as was also the case in this experiment.

The plateau during discharge (after opening the valve and before the channel is empty) indicates that the carrier fluid velocity, and therefore the hydrodynamic drag exerted on the particles, is roughly constant during the discharge. This is surprising, as the length of the packing decreases during the experiment. We believe that the hydraulic resistance of the channel is mainly governed by the presence of particles in a small region around the orifice. The packing fraction in this region fluctuates around an average, resulting in a fluctuating flow rate. It is, however, currently not possible to correlate the packing fraction around the orifice with the carrier fluid velocity. A method to simultaneously observe the carrier fluid velocity and the particles would be needed. Future efforts could focus on measuring the fluid velocity using an external flow sensor, or observe the fluorescent beads and the hydrogel particles at the same time, to correlate the local packing fraction and the fluid velocity.

The second rise in fluid velocity occurs when the hopper is nearly empty. It can happen that the packing is no longer percolating (no longer a single row of touching particles spanning the channel from left to right), like in Figure 5.9B. A small path of lower hydraulic resistance is formed, increasing the fluid velocity. This path widens as the last particles are discharged, reducing the hydraulic resistance of the channel, and increasing the fluid velocity even further, until all particles are discharged. After the particles are discharged, the fluid velocity matches the fluid velocity in an empty channel at that pressure.

These combined observations leads us to believe that the constant discharge rate of the particles is mainly caused by the constant carrier fluid velocity.

### 5.3.D Flow rate controlled discharge

To further confirm that the constant carrier fluid velocity causes the constant discharge rate, we forced the fluid velocity to be constant by imposing a volumetric flow rate, rather than a pressure drop over the channel. The fluid velocity during the flow rate driven these discharges was also checked, and found to be constant over time (Figure 5.9C). This can most likely be attributed to the inconsistent flow rates produced by a syringe pumps, especially at these low flow rates [56]. Similarly to the pressure driven discharge, we find that the discharge rate for a flow rate driven discharge is also constant over time (Figure 5.10CD).

This is a clear indication that indeed the constant discharge rate is caused by a constant carrier fluid velocity in the channel during the discharge. For flow rate driven discharges, this is very intuitive. However, for pressure driven discharges this was surprising, and must entail that the hydraulic resistance during the discharge remains constant, despite the decreasing number of particles in the hopper. This leads us to conclude that the hydraulic resistance of a microfluidic hopper is mainly governed by the particles close to the orifice.

From Figure 5.10AC, it becomes apparent that the discharge rate is not perfectly constant throughout the discharge. There are moments where the discharge rate drops to zero, the hopper clogs (cumulative discharge constant over time). However, when the clogged periods are removed from the cumulative discharge, we do obtain a constant discharge rate over time (Figure 5.10BD).

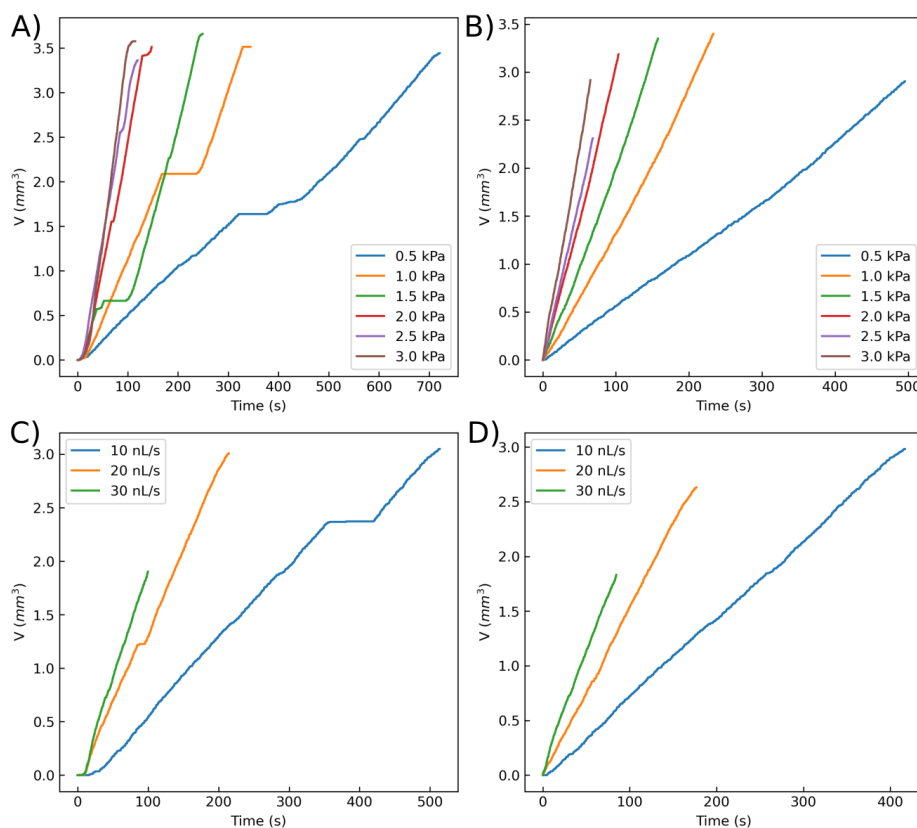


Figure 5.10: A) Cumulative discharge of 250  $\mu\text{m}$  particles with a Young's modulus of 12 MPa through a 600  $\mu\text{m}$  orifice for different applied pressures. B) Same cumulative discharge as in A, but with the clogged periods removed. C) Cumulative discharge of 250  $\mu\text{m}$  particles with a Young's modulus of 12 MPa through a 600  $\mu\text{m}$  orifice for different applied flow rates. D) Same cumulative discharge as in A, but with the clogged periods removed

### 5.3.E Discharged particles

During the discharge, we also noticed that particles were accumulating after the orifice, as can be seen in Figure 5.7A and 5.9. This is caused by the widening of the channel by 5-10x after the orifice, this causes the suspending fluid to slow down by an equal factor, resulting in the particles also slowing down, and thus accumulating after the orifice.

This is reminiscent of the experiments done in the lab of Zuriguel and Maza (Universidad de Navarra) [57, 58], where they have a conveyor belt below the hopper. The conveyor belt has a maximum volumetric transport rate, and as long as the free-flowing discharge rate of the hopper is more than the maximum volumetric transport rate, the discharge is limited by the conveyor belt.

One could make the analogy that there is a maximum transport rate of particles below the orifice, which is lower than the transport rate in the hopper, as fluid is able to flow around the particles, thereby exerting only a negligibly hydrodynamic drag on the particles. There is, however, an important distinction between the two systems. The forces in the conveyor belt case are all elastic, the particles are in the end all supported by the conveyor belt, and increasing the load on the conveyor belt doesn't make it move faster. Whereas in the case of microfluidic hoppers, the resistance is of viscous origin. Applying a higher load on the already



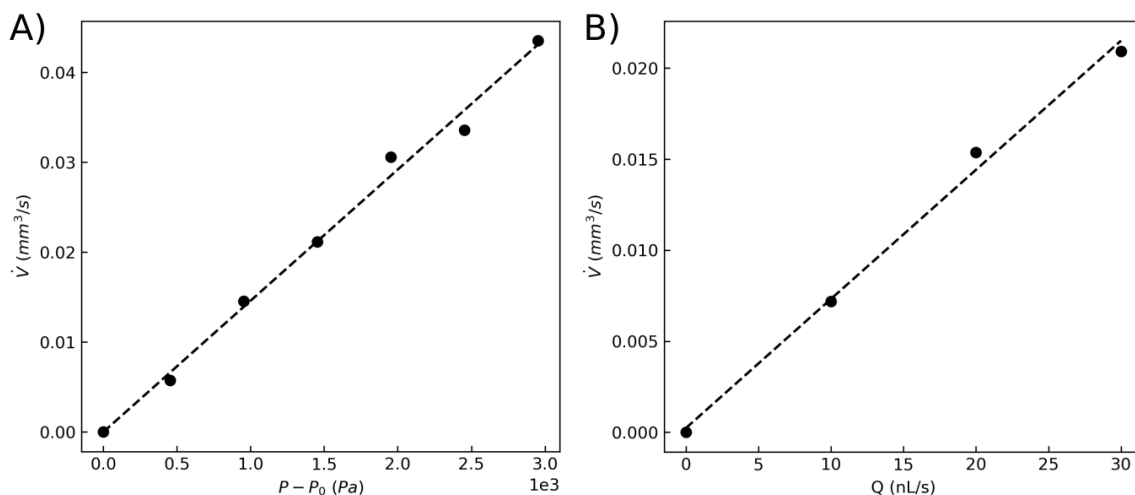


Figure 5.11: A) Discharge rate as function of the applied pressure for the discharge of 250  $\mu\text{m}$  particles with a Young's modulus of 12 MPa through a 600  $\mu\text{m}$  orifice. The black dashed line highlights a linear fit. B) Discharge rate as function of the imposed flow rate for the discharge of 250  $\mu\text{m}$  particles with a Young's modulus of 12 MPa through a 600  $\mu\text{m}$  orifice. The black dashed line highlights a linear fit.

discharged particles will make them move faster.

So, at a first glance, one would expect the discharge rate to decrease during the flow rate driven discharge, as the discharge is impeded by a growing collection of particles. However, due to the viscous nature of the resistance caused by the particles (they cannot sustain a finite load), and our observation that the discharge is constant over time (Figure 5.10), we believe that the particles accumulating below the orifice don't impede the discharge.

### 5.3.2 Scaling laws of microfluidic hopper discharge

#### 5.3.A Driving force

Now we have established that the discharge rate is constant during the discharge, we can look at the scaling laws of microfluidic hoppers. First, how does the discharge rate scale with the driving force? Most dry granular hoppers are gravity driven, and as discussed in section 5.1.2 Beverloo et al. [12] showed a square root dependence on the gravitational acceleration  $\dot{V} \propto \sqrt{g}$ . Where gravitational acceleration acts as a body force on the grains in a dry granular hopper which scales with the volume of the grains, the hydrodynamic drag on the particles acts as a surface force on the particles which scales with the surface area of the base of the cylindrical particles. Hence, we might expect that  $\dot{V} \propto \sqrt{\Delta P}$  or  $\dot{V} \propto \sqrt{U}$ , depending on the mode of driving.

Figures 5.10A and C show the cumulative discharge of 12 MPa particles with a diameter of 250  $\mu\text{m}$  through a 600  $\mu\text{m}$  orifice over time for different imposed pressures and for different imposed flow rates, respectively. The Hagen-Beverloo law describes the free flow of granular materials. Hence, the discharge rates were determined from the cumulative discharges where the clogged periods were taken out (Figure 5.10BD).

Figure 5.11 A and B show the discharge rates as function of the imposed pressure and flow rate, respectively. Unlike dry granular hoppers, the discharge rate scales linearly with the driving force,  $\dot{V} \propto \Delta P$ .

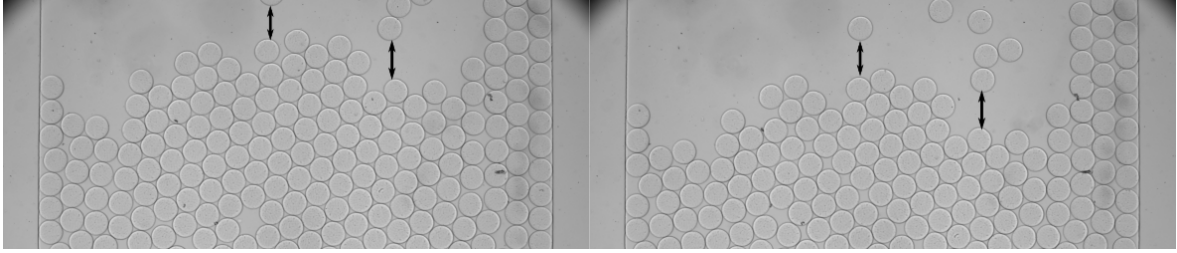


Figure 5.12: Two snapshots, A and B, taken 10 seconds apart during the discharge of  $250 \mu\text{m}$  particles. The length of the arrows is kept constant between the two snapshots.

As described in section 5.1.2, the square root scaling of the discharge rate with the driving force stems from the assumption that particles are in a free fall when passing through the orifice. This is, however, not the case in our experiments. When the particles are free to flow i.e., they are within the “free-fall arch” as described in the Hagen-Beverloo model, they quickly reach a constant velocity proportional to the carrier fluid velocity as the flow is dominated by viscous forces,  $Re = 10^{-4} - 10^{-5}$ . This means that  $v = \sqrt{g}$  becomes  $v = v_t(\Delta P) \propto \Delta P$  or  $v = v_t(Q)$ , where  $v_t(\cdot)$  is the terminal velocity of the particle under the imposed driving force.

A similar scaling has been observed by De-Song et al. [59] and Aguirre et al. [60] who studied the discharge of a horizontal hopper, where the particles were driven by sliding friction of a conveyor belt passing under the particles. They found, like us, a linear dependency of the discharge rate on the belt speed, up to a critical belt speed. Below a critical belt speed, all particles moved with the same velocity as the belt, and rearrangements were quick enough to not impede the flow. At belt speeds above a critical belt speed, De-Song et al. [59] found that the discharge rate fluctuates strongly, but remains roughly constant. Aguirre et al. [60] attributed this to the timescale involved with rearrangements. If rearrangements happen faster than the time needed for a particle to escape the orifice region, the system flows, and the flow is impeded if the rearrangements are slower than the escape time. This bears some similarity to the shear jamming of granular materials, where the viscosity of a granular material below jamming, such as a suspension, increases sharply when driven fast [61–63]. There are, however, key differences between the conveyor belt experiments and our microfluidic experiments, most notably the increase in the fluid velocity due to the constriction. This causes a slight elongational flow, which will most likely prevent shear-jamming, as it pulls particles apart right where the shear-rate is highest.

Perhaps a more comparable system was used by Wilson et al. [64] and Koivisto et al. [40]. They studied the discharge of particles of different sizes and densities in a fully submerged hopper. They found that the discharge rate scaled linearly with the terminal velocity obtained from balancing the Stokes drag and gravitational force, suggesting that indeed the viscous dissipation governs the discharge.

This viscous scaling is further confirmed near the end of the discharge. During the preparation of the hopper, not all particles settle on the packing in time. There are always a few particles freely floating. The freely floating particles move at terminal velocity, since nothing is preventing them from moving faster. The height of the particle packing decreases with the same speed, as can be observed in the two snapshots in Figure 5.12, meaning that the particles in the packing also move at terminal velocity. Note that the terminal velocity is not constant throughout the channel. At the point where the channel becomes more narrow,

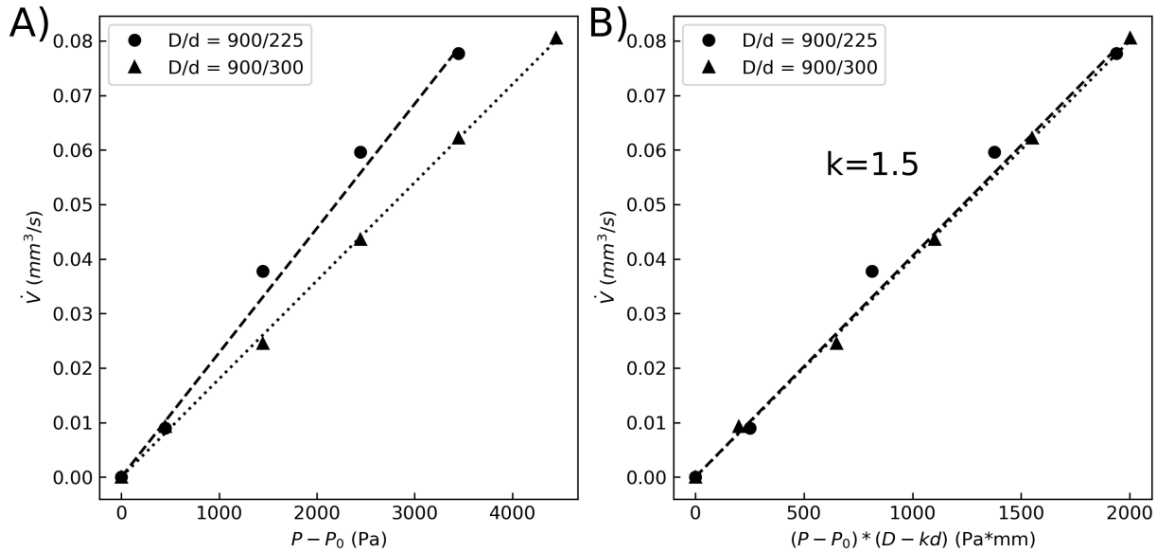


Figure 5.13: A) Discharge rate as function of the applied pressure for two different particle sizes 225 and 300  $\mu\text{m}$ , both flowing through a 900  $\mu\text{m}$  orifice. The dashed and dotted lines are linear fits. B) Discharge rate as function of the applied pressure, corrected for the particle to orifice size ratio.

conservation of mass and the incompressibility of fluids give that the fluid velocity increases, and since we're in the viscous regime, the terminal velocity of the particles increases linearly with the fluid velocity.

### 5.3.B Orifice size

The viscous scaling of the velocity at the orifice doesn't only affect the scaling with the driving force. It also affects the scaling with the orifice size, as for dry granular hoppers  $v \propto \sqrt{g(D - kd)} \rightarrow \dot{V} \propto (D - kd)^{3/2}$ . In our experiments, the terminal velocity is independent of the orifice size, hence we expect  $\dot{V} \propto D$ . Figure 5.13A shows the discharge rate as function of the pressure applied, for two different particle sizes (225 and 300  $\mu\text{m}$ , corresponding to the  $\bullet$  and  $\blacktriangle$ , respectively) flowing through an orifice of the same size (900  $\mu\text{m}$ ). The curves were collapsed by correcting the applied pressure with  $D - kd$ , where  $k$  was a fitting parameter (Figure 5.13B). We found that  $k \approx 1.5$ , which is in good agreement with other hopper experiments [12].

The validity of the  $\dot{V} \propto D - kd$  scaling was further investigated by discharging particles of different sizes, ranging from 175  $\mu\text{m}$  to 300  $\mu\text{m}$ , through a 600  $\mu\text{m}$  orifice. Figure 5.14 shows the discharge rate as function of  $D - kd$ , non-dimensionalized by the orifice size, where we took  $k=1.5$ , as determined in the previous experiment. We see that, indeed, the discharge rate appears to depend linearly on orifice size non-dimensionalized with the particle diameter and corrected by the  $k$ -factor.

### 5.3.C Particle softness

The story becomes a lot more complicated for particles with a Young's modulus of 0.4 MPa (previous experiments were performed on particles with a Young's modulus of 12 MPa). We found that the discharges of soft particles were not very reproducible (Figure 5.15, lines with

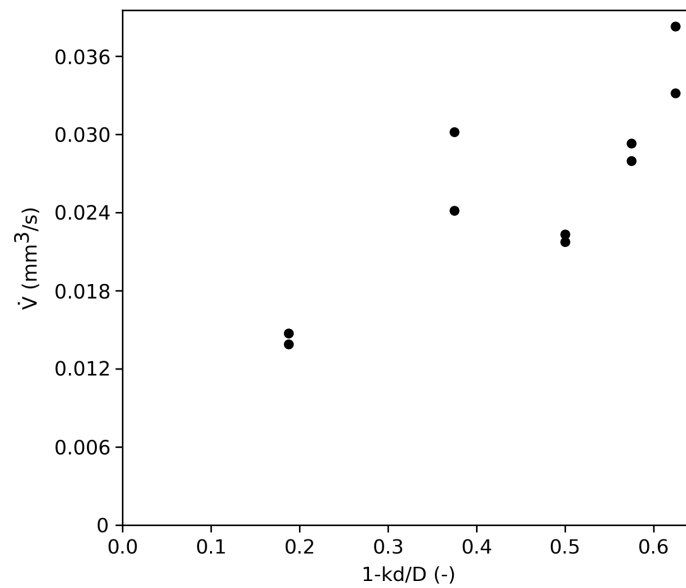


Figure 5.14: Discharge rate as function of the orifice size non-dimensionalized with the particle diameter, where  $k=1.5$

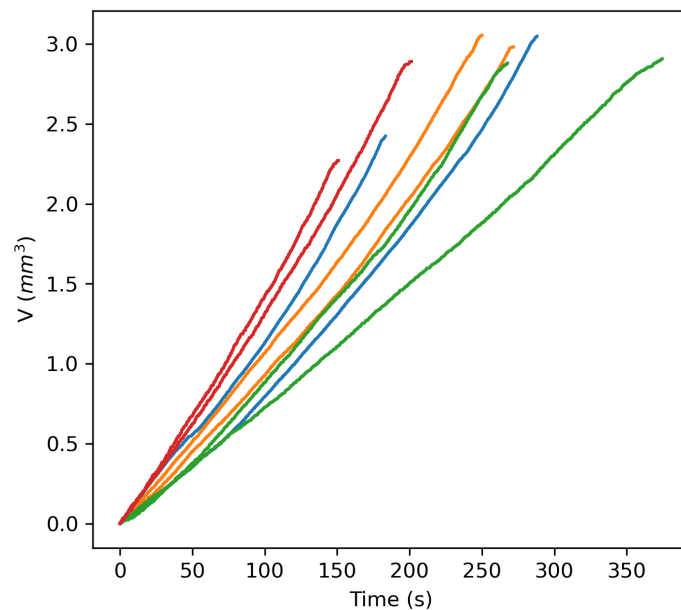


Figure 5.15: Cumulative discharge over time of 0.4 MPa particles of different sizes (blue 300  $\mu m$ , orange 250  $\mu m$ , green 200  $\mu m$ , and red 175  $\mu m$ ) through a 600  $\mu m$  orifice.

identical color are repeats). Furthermore, the discharge rate seemed to increase slightly during the discharge, as we initially expected for the pressure driven discharge. Both effects combined also made it impossible to conclude anything on the effect of particle size on the discharge rate of soft particles. We are not sure what caused this, and future efforts should focus on a more systematic study of the effect of particle softness.

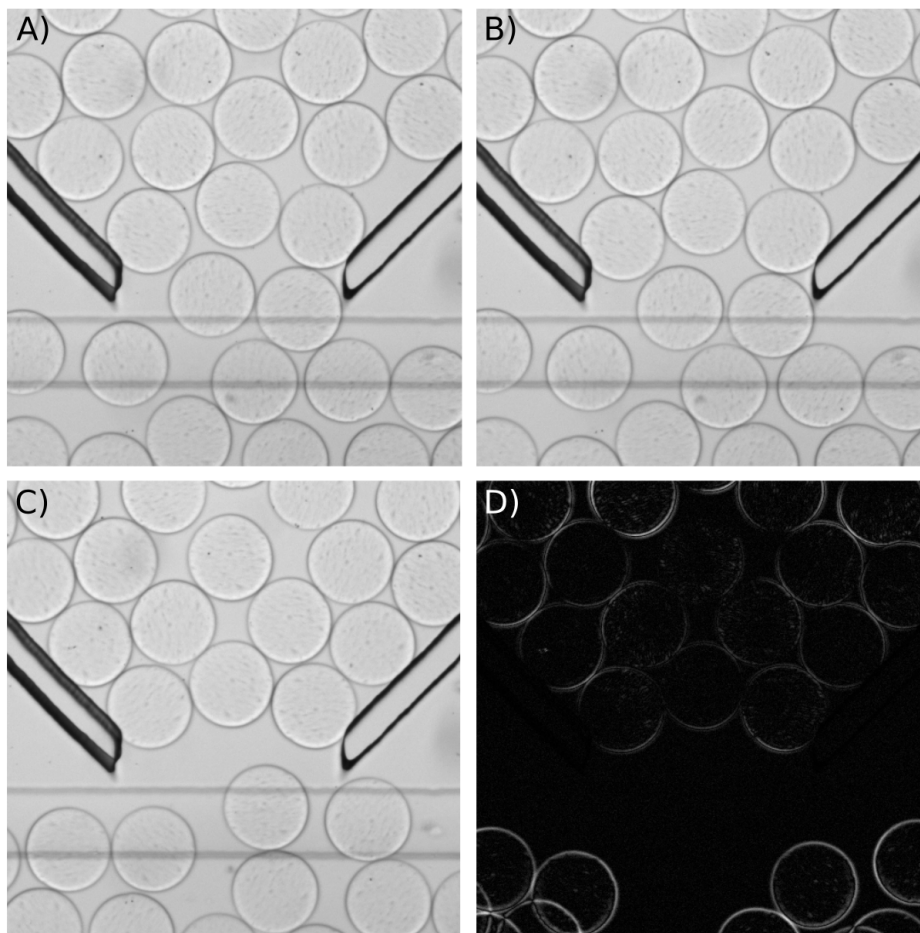


Figure 5.16: A) Zoom of particles near the orifice 1 frame before a clog. One can see that the left and center particle are not yet touching. B) Zoom of the same particles as in A) near the orifice, but 1 frame later. As you can see, the three particles blocking the orifice are now all touching. Hence, the system is clogged. C) Zoom of the same clog, but 30 seconds later. The three particles forming the arch have not moved. D) Difference between the image in C and the image taken another 30 seconds later.

### 5.3.3 Clogging of microfluidic hoppers

As mentioned before, the discharge of hoppers was sporadically interrupted by clogs. We define a clog as a concave arch of touching particles spanning from one side of the hopper to the other, which persists for a period of at least 5 frames ( $\sim 1$  second) and impedes the flow of other particles. This would mean that Figure 5.16A is not yet clogged, as the left and center particle near the orifice are not yet touching, whereas Figure 5.16B is clogged, as the particles in the blocking the orifice are all touching. We found two types of clogs: persistent clogs and transient clogs. We defined clogs to be persistent if no particles in the arch displaced for 30 seconds. Figure 5.16B and C are two images taken of the same clog, approximately 30 seconds apart. There is no visible difference in the particle sin the between the two images, however, particles further away have rearranged slightly. Figure 5.16D is the difference in magnitude of Figure 5.16 C and a picture taken another 30 seconds later. The particles near the orifice are hardly visible, indicating that the pixel intensities have not changed over 30

seconds. This arch was therefore classified as 'permanent'. All transient arches collapsed, most within seconds, several took much longer.

We were not able to gather enough statistics in these preliminary experiments to study the clogging probability as function of particle softness. But we were able to suggest some trends. First, we found that for an orifice to particle size ratio more than 3, we did not observe any clogs. For a ratio of  $\sim 2.5$ , we did observe some clogs. Furthermore, an increase in pressure or flow rate reduced the chance of clogging (Figure 5.10AC). Lastly, the soft particles did not appear to form any clogs at all.

## 5.4 Conclusions

In this chapter, we showed a novel microfluidic hopper that can be opened and closed by a Quake-style valve. This allows for the collection of particles near the orifice, and therefore the study of the flow of dense suspensions through a narrow orifice.

With these microfluidic hoppers, we showed that the discharge rate is independent of the remaining amount of particles in the channel, for both pressure and flow rate driven experiments. We observed with PIV that the flow rate of the carrier fluid during a pressure driven discharge was constant during the discharge. This indicates that the hydraulic resistance of the channel was independent of the remaining number of particles, and that therefore the hydraulic resistance of the channel is mostly dependent on the number of particles close to the orifice.

Furthermore, we showed that the discharge rate of our microfluidic hopper did not follow the Hagen-Beverloo scaling, and instead scaled linearly with the applied pressure or the applied flow rate. This scaling was due to the large amount of viscous dissipation, which is ignored in the Hagen-Beverloo scaling.

We also tested the discharge of soft particles in microfluidic hoppers. We found that the discharge rate was no longer independent of the remaining number of particles. We were, however, not able to determine the origin of this behavior. We suspect that the hydraulic resistance of the channel is no longer independent of the remaining number of particles in the channel. This can be confirmed by 2 additional experiments. First, one should monitor the flow rate of the carrier fluid over time during the discharge of soft particles. I suspect that the flow rate will slowly increase as the channel empties, causing the flow rate to increase during the discharge. I suspect that the ratio between the discharge rate of the particles and the flow rate of the carrier fluid will remain constant, indicating that the discharge of soft particles is still governed by viscous dissipation. This can be further confirmed by carrying out flow rate controlled experiments, rather than pressure controlled experiments.

Lastly, we observed some (temporary) clogging during our experiments. We noticed that clogging was not observed for orifice size to particle size ratios over 3. We attribute this due to the lack of friction to stabilize potential arches. Interestingly, we did not see any clogs for the soft particles. We were not able to determine the cause, or find out if this is connected to the increase in discharge rate over time. This was, however, mostly due to time constraints and this research has paved the way to investigate the origin (and possible connection) of both phenomena.

## 5.5 References

- [1] G Hagen. Druck und Bewegung des trockenen Sandes. *Bericht über die zur Bekanntmachung geeigneten Verhandlungen der Königlich Preussischen Akademie der Wissenschaften zu Berlin*, pages 35–42, 1852. 82, 83, 84, 85
- [2] H.A. Janssen. Versuche über Getreidedruck in Silozellen. *Zeitschr. d. Vereines deutscher Ingenieure*, 39:1045, 1895. 83, 84
- [3] Matthias Sperl. Experiments on corn pressure in silo cells - Translation and comment of Janssen's paper from 1895. *Granular Matter*, 8(2):59–65, 2006. 83, 84
- [4] Pierre Huber-Burnand. Ueber den Ausfluß und den Druck des Sandes. *Kunst-und Gewerbeblatt des Polytechnischen Vereins für das Königreich Bayern*, 15(51):730–740, 1829. 82
- [5] Brian P. Tighe and Matthias Sperl. Pressure and motion of dry sand: Translation of Hagen's paper from 1852. *Granular Matter*, 9(3-4):141–144, 2007. 83, 84, 85
- [6] Heinrich M. Jaeger and Sidney R. Nagel. Physics of the Granular State. *Science*, 255(5051):1523–1531, 1992. 84
- [7] Heinrich M. Jaeger, Sidney R. Nagel, and Robert P. Behringer. Granular solids, liquids, and gases. *Reviews of Modern Physics*, 68(4):1259–1273, 1996.
- [8] James Kakalios. Resource Letter GP-1: Granular physics or nonlinear dynamics in a sandbox. *American Journal of Physics*, 73(1):8–22, 2005.
- [9] J. E. Hilton and P. W. Cleary. Granular flow during hopper discharge. *Physical Review E - Statistical, Nonlinear, and Soft Matter Physics*, 84(1), 7 2011.
- [10] Charles S. Campbell. Granular material flows - An overview. *Powder Technology*, 162(3):208–229, 2006.
- [11] C. Mankoc, A. Janda, R. Arévalo, J. M. Pastor, I. Zuriguel, A. Garcimartín, and D. Maza. The flow rate of granular materials through an orifice. *Granular Matter*, 9(6):407–414, 2007. 84, 85
- [12] W A Beverloo, H A Leniger, and J Van De Velde. The flow of granular solids through orifices. *Chemical Engineering Science*, 15:260–286, 1961. 84, 85, 98, 100
- [13] R L Brown and J C Richards. Profile of flow of granules through apertures. *Trans Instn Chem Engrs*, 38:243, 1960. 84, 85
- [14] Juha Koivisto and Douglas J. Durian. The sands of time run faster near the end. *Nature Communications*, 8:1–6, 2017. 85
- [15] Hojin Ahn, Zafer Başaranoglu, Mustafa Yilmaz, Abdulcelil Buğutekin, and M. Zafer Gül. Experimental investigation of granular flow through an orifice. *Powder Technology*, 186(1):65–71, 2008.
- [16] Hector Pacheco-Martinez, Henk Jan van Gerner, and J. C. Ruiz-Suárez. Storage and discharge of a granular fluid. *Physical Review E*, 77(2):1–6, 2008. 85

- 
- [17] Alvaro Janda, Iker Zuriguel, and Diego Maza. Flow rate of particles through apertures obtained from self-similar density and velocity profiles. *Physical Review Letters*, 108(24):1–5, 2012. 85
- [18] S. Dorbolo, L. Maquet, M. Brandenbourger, F. Ludewig, G. Lumay, H. Caps, N. Vandewalle, S. Rondia, M. Mélard, J. Van Loon, A. Dowson, and S. Vincent-Bonnieu. Influence of the gravity on the discharge of a silo. *Granular Matter*, 15(3):263–273, 2013. 85
- [19] S. M. Rubio-Largo, A. Janda, D. Maza, I. Zuriguel, and R. C. Hidalgo. Disentangling the Free-Fall Arch Paradox in Silo Discharge. *Physical Review Letters*, 114(23):1–5, 2015. 85, 86
- [20] M. D. Haw. Jamming, two-fluid behavior, and "self-filtration" in concentrated particulate suspensions. *Physical Review Letters*, 92(18), 5 2004. 86
- [21] Damiano Genovese and Joris Sprakel. Crystallization and intermittent dynamics in constricted microfluidic flows of dense suspensions. *Soft Matter*, 7(8):3889–3896, 4 2011.
- [22] Iker Zuriguel, Angel Garcimartín, Diego Maza, Luis A. Pugnaloni, and J. M. Pastor. Jamming during the discharge of granular matter from a silo. *Physical Review E - Statistical, Nonlinear, and Soft Matter Physics*, 71(5):1–9, 2005. 86
- [23] Emilie Dressaire and Alban Sauret. Clogging of microfluidic systems. *Soft Matter*, 13(1):37–48, 2017. 86
- [24] K. V. Sharp and R. J. Adrian. On flow-blocking particle structures in microtubes. *Microfluidics and Nanofluidics*, 1(4):376–380, 2005. 86
- [25] Mathieu Souzy and Alvaro Marin. Role of liquid driving on the clogging of constricted particle suspensions. *Journal of Fluid Mechanics*, 953:1–19, 2022. 86
- [26] Benjamin Dersoir, Matthieu Robert de Saint Vincent, Manouk Abkarian, and Hervé Tabuteau. Clogging of a single pore by colloidal particles. *Microfluidics and Nanofluidics*, 19(4):953–961, 2015. 86
- [27] Matthieu Robert De Saint Vincent, Manouk Abkarian, and Hervé Tabuteau. Dynamics of colloid accumulation under flow over porous obstacles. *Soft Matter*, 12(4):1041–1050, 2016. 86
- [28] E Clément, G Reydellet, F Rioual, B Parise, V Fanguet, J Lanuza, and E Kolb. Jamming Patterns and Blockade Statistics in Model Granular Flows. In Dirk Helbing, Hans J Herrmann, Michael Schreckenberg, and Dietrich E Wolf, editors, *Traffic and Granular Flow '99*, pages 457–468, Berlin, Heidelberg, 2000. Springer Berlin Heidelberg. 86
- [29] Iker Zuriguel, Luis A. Pugnaloni, Angel Garcimartín, and Diego Maza. Jamming during the discharge of grains from a silo described as a percolating transition. *Physical Review E - Statistical Physics, Plasmas, Fluids, and Related Interdisciplinary Topics*, 68(3):4, 2003. 86
- [30] C. E. Thomas and D. E. Durian. Fraction of Clogging Configurations Sampled by Granular Hopper Flow. *Physical Review Letters*, 114(17), 4 2015. 86



- [31] Iker Zuriguel, Alvaro Janda, Angel Garcimartín, Celia Lozano, Roberto Arévalo, and Diego Maza. Silo clogging reduction by the presence of an obstacle. *Physical Review Letters*, 107(27):1–5, 2011. 86
- [32] Mathieu Souzy, Iker Zuriguel, and Alvaro Marin. Transition from clogging to continuous flow in constricted particle suspensions. *Physical Review E*, 101(6):1–6, 2020. 86
- [33] Patrick G. Lafond, Matthew W. Gilmer, Carolyn A. Koh, E. Dendy Sloan, David T. Wu, and Amadeu K. Sum. Orifice jamming of fluid-driven granular flow. *Physical Review E - Statistical, Nonlinear, and Soft Matter Physics*, 87(4):1–8, 2013.
- [34] Alfredo Guariguata, Masika A. Pascall, Matthew W. Gilmer, Amadeu K. Sum, E. Dendy Sloan, Carolyn A. Koh, and David T. Wu. Jamming of particles in a two-dimensional fluid-driven flow. *Physical Review E - Statistical, Nonlinear, and Soft Matter Physics*, 86(6):1–10, 2012. 86
- [35] Tivadar Pongó, Viktória Stiga, János Török, Sára Lévy, Balázs Szabó, Ralf Stannarius, Raúl Cruz Hidalgo, and Tamás Börzsönyi. Flow in an hourglass: Particle friction and stiffness matter. *New Journal of Physics*, 23(2), 2021. 86, 87
- [36] Kirsten Harth, Jing Wang, Tamás Börzsönyi, and Ralf Stannarius. Intermittent flow and transient congestions of soft spheres passing narrow orifices. *Soft Matter*, 16(34):8013–8023, 9 2020. 86, 87
- [37] D. Hirshfeld, Y. Radzyner, and D. C. Rapaport. Molecular dynamics studies of granular flow through an aperture. *Physical Review E - Statistical Physics, Plasmas, Fluids, and Related Interdisciplinary Topics*, 56(4):4404–4415, 1997. 86
- [38] D. Hirshfeld and D. C. Rapaport. Granular flow from a silo: Discrete-particle simulations in three dimensions. *European Physical Journal E*, 4(2):193–199, 2001.
- [39] R. Balevičius, R. Kačianauskas, Z. Mróz, and I. Sielamowicz. Microscopic and macroscopic analysis of granular material behaviour in 3D flat-bottomed hopper by the discrete element method. *Archives of Mechanics*, 59(3):231–257, 2007. 86
- [40] Juha Koivisto, Marko Korhonen, Mikko Alava, Carlos P. Ortiz, Douglas J. Durian, and Antti Puisto. Friction controls even submerged granular flows. *Soft Matter*, 13(41):7657–7664, 2017. 86, 99
- [41] Kenneth W. Desmond, Pearl J. Young, Dandan Chen, and Eric R. Weeks. Experimental study of forces between quasi-two-dimensional emulsion droplets near jamming. *Soft Matter*, 9(12):3424–3436, 2013. 86
- [42] Ahmed Ashour, Torsten Trittel, Tamás Börzsönyi, and Ralf Stannarius. Silo outflow of soft frictionless spheres. *Physical Review Fluids*, 2(12):1–9, 2017. 86
- [43] Xia Hong, Meghan Kohne, Mia Morrell, Haoran Wang, and Eric R. Weeks. Clogging of soft particles in two-dimensional hoppers. *Physical Review E*, 96(6), 12 2017. 86, 87
- [44] Jing Wang, Bo Fan, Tivadar Pongó, Kirsten Harth, Torsten Trittel, Ralf Stannarius, Maja Illig, Tamás Börzsönyi, and Raúl Cruz Hidalgo. Silo discharge of mixtures of soft and rigid grains. *Soft Matter*, 17(16):4282–4295, 4 2021. 86

- [45] Ran Tao, Madelyn Wilson, and Eric R. Weeks. Soft particle clogging in two-dimensional hoppers. *Physical Review E*, 104(044909), 10 2021. 86
- [46] B. V. Guerrero, L. A. Pugnaroni, C. Lozano, I. Zuriguel, and A. Garcimartín. Slow relaxation dynamics of clogs in a vibrated granular silo. *Physical Review E*, 97(4):1–8, 2018. 87
- [47] B. V. Guerrero, B. Chakraborty, I. Zuriguel, and A. Garcimartín. Nonergodicity in silo unclogging: Broken and unbroken arches. *Physical Review E*, 100(3):32901, 2019.
- [48] Iñaki Echeverría-Huarte, Zhigang Shi, Angel Garcimartín, and Iker Zuriguel. Pedestrian bottleneck flow when keeping a prescribed physical distance. *Physical Review E*, 106(7): 1–7, 2022. 87
- [49] David Méndez, Raúl Cruz Hidalgo, and Diego Maza. The role of the hopper angle in silos: experimental and CFD analysis. *Granular Matter*, 23(2), 5 2021. 87
- [50] Saeed Albaraki and S. Joseph Antony. How does internal angle of hoppers affect granular flow? Experimental studies using digital particle image velocimetry. *Powder Technology*, 268(1):253–260, 12 2014. 87
- [51] Marc A. Unger, Hou Pu Chou, Todd Thorsen, Axel Scherer, and Stephen R. Quake. Monolithic microfabricated valves and pumps by multilayer soft lithography. *Science*, 288(5463):113–116, 2000. 89
- [52] Ismail Emre Araci and Stephen R. Quake. Microfluidic very large scale integration (mVLSI) with integrated micromechanical valves. *Lab on a Chip*, 12(16):2803–2806, 2012. 89
- [53] Todd Thorsen, Sebastian J Maerkl, and Stephen R Quake. Microfluidic Large-Scale Integration. 298(October):580–585, 2002. 89
- [54] Vincent Studer, Gao Hang, Anna Pandolfi, Michael Ortiz, W. French Anderson, and Stephen R. Quake. Scaling properties of a low-actuation pressure microfluidic valve. *Journal of Applied Physics*, 95(1):393–398, 1 2004. 89
- [55] Antonio Perazzo, Janine K. Nunes, Stefano Guido, and Howard A. Stone. Flow-induced gelation of microfiber suspensions. *Proceedings of the National Academy of Sciences of the United States of America*, 114(41):E8557–E8564, 2017. 93
- [56] Zida Li, Sze Yi Mak, Alban Sauret, and Ho Cheung Shum. Syringe-pump-induced fluctuation in all-aqueous microfluidic system implications for flow rate accuracy. *Lab on a Chip*, 14(4):744–749, 2014. 96
- [57] Diego Gella, Diego Maza, and Iker Zuriguel. Granular flow in a silo discharged with a conveyor belt. *Powder Technology*, 360:104–111, 1 2020. 97
- [58] D. Gella, D. Maza, and I. Zuriguel. Granular internal dynamics in a silo discharged with a conveyor belt. *Journal of Fluid Mechanics*, 925, 2021. 97
- [59] Bao De-Song, Zhang Xun-Sheng, X. Guang-Lei, Pan Zheng-Quan, Tang Xiao-Wei, and L. Kun-Quan. Critical phenomenon of granular flow on a conveyor belt. *Physical Review E*, 67(6):3, 2003. 99

- 
- [60] M. A. Aguirre, J. G. Grande, A. Calvo, L. A. Pugnaloni, and J. C. Géminard. Pressure independence of granular flow through an aperture. *Physical Review Letters*, 104(23): 1–4, 2010. 99
- [61] M E Cates, J P Wittmer, J.-P Bouchaud, and P Claudin. Jamming, Force Chains, and Fragile Matter. *Physical Review Letters*, 81(9):1841–1844, 1998. 99
- [62] Robert P. Behringer and Bulbul Chakraborty. The physics of jamming for granular materials: A review, 1 2019.
- [63] Jeffrey F. Morris. Shear Thickening of Concentrated Suspensions: Recent Developments and Relation to Other Phenomena. *Annual Review of Fluid Mechanics*, 52:121–144, 2020. 99
- [64] T. J. Wilson, C. R. Pfeifer, N. Meysingier, and D. J. Durian. Granular discharge rate for submerged hoppers. *Papers in Physics*, 6, 2 2014. 99

## Chapter 6

# Conclusion and Perspectives

In this thesis, we have studied a model system for granular materials, a pseudo-2D packing of cylinders in microfluidic channels. We have developed an experimental setup to systematically study the effect of softness on the behavior of granular materials in two model experiments, compaction, and hopper discharge. These experiments correspond to two industry relevant processes, and we hope that these and future experiments will help the further understanding of the mechanics and dynamics of granular materials, and especially the role of particle softness. The results obtained may have many applications, in and outside the field of granular materials, such as understanding the mechanics of cell clusters from the mechanics of single cells or clog prevention in biomedical devices.

### 6.1 Conclusions

We used a microfluidic system to fabricate hydrogel particles inside the microchannel used for the experiments, and we developed a system that is able to fabricate particles of different sizes in predefined locations. To define random initial positions, we used numerical simulations in which we “dropped” the desired amount of particles in a box and recorded their position. We could control the softness of the particles by adjusting the ratio between a cross-linkable polymer and a chemically similar but inert polymer. We were able to drive the particles by imposing a flow of the uncured UV-sensitive solution in the channel by either controlling the pressure drop over the channel with a pressure controller, or controlling the flow rate with a syringe pump. The percolating nature of the particle packing allowed us to approximate the relative contributions of the force due to the pressure difference across the packing, and the force caused by the hydrodynamic drag of the fluid passing over/under the particles. We developed a fully parallelized convolution-based algorithm to determine the locations of  $\sim 2000$  particles in the field of view of the camera with sub-pixel accuracy.

We, then, experimentally studied the compaction of the 2D packing of particles by imposing a flow of uncured solution over and under the particles, causing them to be compressed against a membrane. We could determine the strain upon an imposed pressure by tracking the displacement of the particle centers with respect to their unstressed position in the channel. First, we studied the creep and relaxation of the packing of hydrogel particles upon a step-wise increase in the applied stress. We modelled the strain response with a generalized Kelvin-Voigt model, which typically describes the response of a viscoelastic solid well. We found that one timescale was not enough to capture the complex creep/relaxation of the

hydrogel packing. Adding a second timescale, however, proved much more successful. This provided a full viscoelastic description of the hydrogel packing. We tried to link one of the timescales to the poro-elastic relaxation timescale of the hydrogel particles, however, future efforts will be needed to measure the poro-elastic relaxation in independent experiments. We, then, used the relaxation timescales to study the strain response of the hydrogel packing upon an oscillating imposed pressure. We found that the imposed stress and strain response were out of phase. A model for the expected lag time was derived from the storage and loss compliance of a Kelvin-Voigt model. The model correctly predicted that the lag time was only weakly dependent on the softness of the particles. Furthermore, it described the decrease of the lag time with increasing oscillation period well, except for the existence of a limit value. We expected that this lag time would approach zero for high periods. This, however, seemed not to be the case, even at very long periods, the stress and strain were out of phase. We investigated this further by performing a step-wise oscillation of the pressure, where the packing was allowed to reach equilibrium at each step. Here, we also found that, despite the packing reaching equilibrium at each step, the strain was not uniquely defined for each imposed stress. We suspect that this time-independent hysteresis is caused by changes in the micro-structure. However, conclusive evidence has yet to be found.

Then, we studied the same oscillatory compaction, but from a completely different point of view. Previously, we studied the global response of the packing under compaction from a complex fluid rheology point-of-view. This approach ignores the vast amount of microscopic information that can be extracted from the same data. Using the sub-pixel accuracy of the particle finding algorithm, combined with the careful determination of the particle radii, we were able to determine the strain on a particle level, and compare this to the strain on the packing scale. We found that these strains were not identical, as we initially expected, but proportional. Furthermore, we studied the heterogeneous nature of the microstructure of granular materials. From the local strains, we could follow the spatial distribution of the forces and reconstruct the force network over time. We also found that the magnitude of the inter-particle forces showed a Gaussian distribution, where the distribution became more homogeneous (narrower) at higher compression. We found that the more homogeneous distribution was accompanied by an increase in the average number of contacts per particle. From all this information, we were able to construct a microscopic stress tensor, using the Kirkwood-Irving equation. Similar to the imposed stress, the microscopic stress increased slowly and non-linearly with increasing strain, the cause of which remains to be found. The onset regime was followed by a linear increase of the pressure with strain. We found that the scaling of the microscopic stress non-dimensionalized with the Young's modulus and the strain of the packing, was well described by the compaction model derived from the Kirkwood-Irving equation, by assuming that the inter-particle forces are randomly distributed, the interaction forces can be approximated by the Hertz contact model for cylinders with parallel axes, and the polydispersity is minimal. Lastly, we investigated the traces of the particles. We found particles that followed the same path during compression as during decompression, behaving reversibly elastic. We also particles that did not follow the same path during compression and decompression, but ended up in the same spot over a compression-decompression cycle, behaving reversibly plastic. We attempted to cluster the reversibly plastic particles by investigating the encompassed area during a compression cycle, and the displacement over a cycle. However, no clear distinction between the reversibly elastic and reversibly plastic particles could be found.

Lastly, we investigated the discharge of hydrogel particles through a microfluidic hopper. Initially, we relied on the formation of a clog to collect the particles near the orifice. However, this limited the range of parameters severely. If the ratio of the orifice size to the particle diameter was slightly too big, no arch would form and the semi-dilute suspension would flow through the orifice without any particle-particle interactions. Conversely, if the orifice was slightly too small, a stable arch would form immediately, and clogging would be so frequent that it was impossible to study the discharge. We solved this problem by integrating a low-displacement, soft, microfluidic valve right after the orifice. The opening and closing of the valve could be tuned to let the carrier fluid through, but retain the particles. This allowed us to study any orifice size and particle size. We then studied the discharge over time as function of the applied pressure. We expected that the discharge rate would increase as the hopper emptied, as the hydraulic resistance of the channel would decrease as the remaining number of particles decreased, resulting in an increase in the flow of carrier fluid, and thus an increase in discharge rate. However, we found that the discharge rate was independent of the number of remaining particles in the channel, indicating that the velocity of the carrier fluid was independent of the remaining number of particles. We investigated this further by measuring the fluid velocity with PIV during the discharge. This, indeed, confirmed that the fluid velocity was constant during the discharge. As a final check, we imposed a constant flow rate, rather than a pressure drop over the channel, which also resulted in a constant discharge rate over time. Therefore, we can conclude that the hydraulic resistance of the channel is governed by the number of particles close to the orifice, which fluctuates around an average during the discharge. This could also explain the fluctuations observed in the carrier fluid velocity we observed during the pressure driven discharge. We followed this up by investigating the discharge rate as a function of the imposed pressure or flow rate, and found that the discharge rate scaled linearly with both the pressure and flow rate, and not with the square root of the driving force as is predicted by the Hagen-Beverloo scaling, which is commonly observed for the discharge of granular materials. This is due to the dominant viscous dissipation. Particles quickly reach their terminal velocity, which scales linearly with the applied pressure or flow rate. Lastly, we found that at small orifices, the particle would form an arch above the orifice, impeding the discharge of particles. Like in other soft particle systems, the arched collapsed without external perturbation.

## 6.2 Perspectives

It is quite common in research to end with more questions than you started. This was definitely the case during this project. In this section, I will discuss some of the ideas we had, but were not (or only partially) able to investigate, and that definitely deserve further investigation.

### 6.2.1 Relaxation of single particles and particle packings

We have suggested the intuitive link between the poro-viscoelastic relaxation of the particles, and at least one of the relaxation timescales observed in the compaction of the packing. If such connection can be found, it would be possible to disentangle the packing and particle contributions. One could then perform rheological experiments, like step-stress and oscillatory compression, on small particles inside microfluidic channels. These experiments are typically difficult to perform on such small particles, as indicated in section 3.3.B, and often require expensive, specialized equipment. Performing these experiments in-situ matches the

experimental conditions more closely, and could therefore provide a better estimation of the properties of the particles. One could, for instance, deposit a small layer (in the order of the size of a particle) on a solid substrate such as a glass slide. I expect that the size dependent relaxation time depends on the smallest length-scale, which for a thin film is the height. This eliminates the difficulty of finding the particle, as you can probe anywhere on the substrate.

To clearly establish a link between the packing and particle relaxation, it might be beneficial to observe this in a system that is easier to characterize. One could for instance buy commercial hydrogel beads ( $\sim 1$  cm when hydrated) and study their relaxation time by compressing them between two plates. Either by applying a step strain and observing the stress relaxation with a load cell, or by applying a weight on top and observing the deformation of the hydrogels. One could then perform the exact same experiment on a packing of these particles, both in a thin cell to mimic a 2D system, and in a larger container to measure the relaxation time of a 3D system. The information gained could help design future microscopic experiments. Possible experiments could be tested include nanoindentation and AFM measurements.

We have done some initial tests with  $\sim 2$  cm hydrogel beads with Chandan Shakya, in the lab of Joshua Dijkstra at Wageningen University/University of Amsterdam. We found that the stress relaxation of a packing of hydrogel upon a step-increase in strain is well described by a generalized Kelvin-Voigt model with 2 elements. The stress relaxation of a single hydrogel particle upon a step-increase in strain was described quite well by a single Kelvin-Voigt element, with only minor deviations at very short timescales. This is the first proof that indeed the relaxation of single particles can be recovered when compressing a packing. Similar to our microfluidic experiments, we found that the cyclic compression of a packing is hysteretic, even in the step-wise compression experiments where the response is extrapolated to the equilibrium limit. Whereas, we found that the cyclic compression of a single particle was not hysteretic in the extrapolated quasi-static limit. These experiments have proven very insightful and progressed quickly

### 6.2.2 Reversible plasticity

During compression, we also noticed a oscillation period independent time lag between the imposed stress and observed strain. We suggested that this might be due to microscopic rearrangements, and we have performed some initial investigations. So far, it was not possible to conclude if rearrangements play a role in the hysteresis. Microscopic data is very rich, and we might not have chosen the right analytics to confirm or deny this hypothesis yet. A very interesting next step would be to investigate the microstructure in more detail. We have several ideas that we did not manage to investigate. An interesting topic would be to look for hysteresis in the formation of shear bands. There are multiple metrics that can be used to investigate shear bands. One could check the evolution of the cumulative number of T1 rearrangements [1]. Another would be to find a metric for the local non-affine displacement ( $D_{min}^2$ ) [2, 3], and investigation how this evolves during a compression cycle. One could also study the microstructural information hidden in the  $g(r)$  of the packing, for instance by means of excess entropy [4-6]. I believe this is a promising area to study, where the main challenge is finding the proper metric to report the spatial and/or temporal evolution of the microstructure.

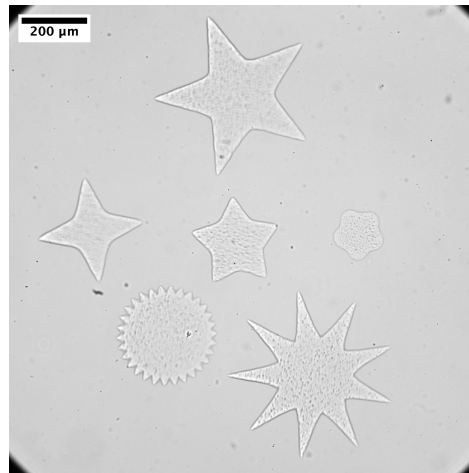


Figure 6.1: Image of various different star shaped particles. Image taken by Jules Tampier

### 6.2.3 Clogging of soft particles in microfluidic channels

Souzy and Marin [7] suggested that the driving method, pressure driven or flow rate driven, influences the formation and stability of arches in microfluidic constrictions. They argue that during the formation of an arch, the hydraulic resistance of the channel increases. In a pressure driven system, this is accompanied by a decrease in flow rate, resulting in a constant pressure at the orifice. In a flow rate driven hopper, however, the increase in resistance caused an increase in pressure, stabilizing the arches. Therefore, driving the suspension slower, was actually faster, due to lower stability of the arches. They were not able to integrate pressure sensors in their microfluidic devices. Furthermore, the 3D nature of their setup, combined with hard particles, did not allow them to build-up of stress near the orifice during a flow rate driven discharge. The experimental system described in this thesis could shed light on this mechanism. Implementing the techniques developed in chapter 4 with the hopper developed in chapter 5, would allow us to not only measure the stability of the arches by measuring the average persistence time of the arches, but also the increase in stress around the orifice, and the stability of the formed force network. A note, care has to be taken with converting the deformation into stresses. The microscopic analysis performed in chapter 4 assumed that the oscillation was quasi-static, and that thus the deformation was independent of the duration of the oscillation cycle. This will not be the case in the formation of arches. The viscoelastic nature of the particles will cause them to deform over time, even at constant stress.

Furthermore, it would be interesting to see how the clogging is affected by the imposed pressure. The slower is faster approach has been observed for hard particles. I suspect that this idea will break down at higher stresses, where the particles deform so much that they will squeeze through the orifice. The experimental setup described throughout this thesis would allow us to study this systematically.

We also did not take a look at the statistics of clogging of soft particles due to time constraints. There are two interesting studies, that can be done simultaneously. First, one can investigate the influence of the particle softness on the probability of clogging. We found that the soft particles did not clog at all, whereas rare clogging events were observed for hard particles. The precise relationship between particle softness and clogging remains to be



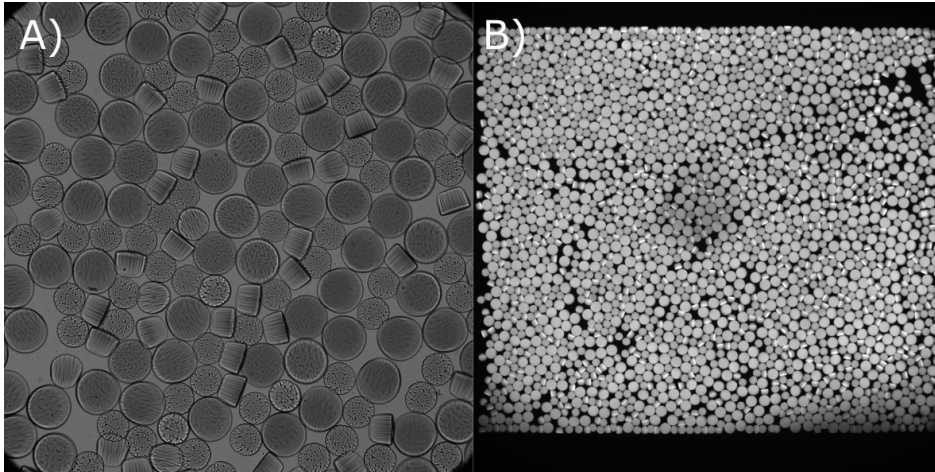


Figure 6.2: A) Bright field image of PEGDA particles with spiropyran incorporated in the network. B) Fluorescence of the spiropyran.

understood.

One can also study the average persistence time of the clogs. Intuitively, we would expect the duration of the clog to scale with the relaxation time of the hydrogels. As soon as the particles form an arch, they are put under a constant stress, and will thus deform slowly over time, which destabilizes the arch. Local destabilization effects, like the deformation of a particle in the arch, are typically well described by an exponential decay, i.e., the probability of finding an arch of duration  $t$  scales with the time  $t$  as  $P(t) \propto e^{-t/\tau}$ , where  $\tau$  is the typical relaxation time of the particles. However, this is not what has been reported. Harth et al. [8] found a power-law scaling of the probability of finding an arch with a certain persistence time. Power-law scalings are commonly observed in experiments with a system-wide self organized criticality. Experiments performed on particles with known relaxation times might provide more insight in this process.

In this thesis, we have limited ourselves to cylindrical particles. The in-situ lithography is, however, not limited to circular masks. Recently, we have performed some initial tests with non-cylindrical particles together with my intern, Jules Tampier. It is, for instance, possible to make star- or gear-shaped particles (Figure 6.1). This would allow us to systematically study the effect of particle roughness on the discharge granular materials. We believe that mechanical interlocking will act as an effective friction coefficient. Experiments that allow for the systematic investigation of not only the particle softness, but also the inter-particle friction could further disentangle the contributions of both properties on the behavior of granular packings.

#### 6.2.4 Visualize force chains

The fabricated hydrogels in this thesis were purely cross-linked PEGDA. However, this does not have to be the case. Dendukuri et al. [9] were also able to incorporate fluorescent molecules in the network, making the network fluorescent. There are also molecules that become fluorescent when put under tension, examples include spiropyrans [10]. As a side project, we have incorporated spiropyrans in the polymer network in collaboration with the group of Costantino Creton (SIMM-ESPCI). We found, however, that the added spiropyran absorbed

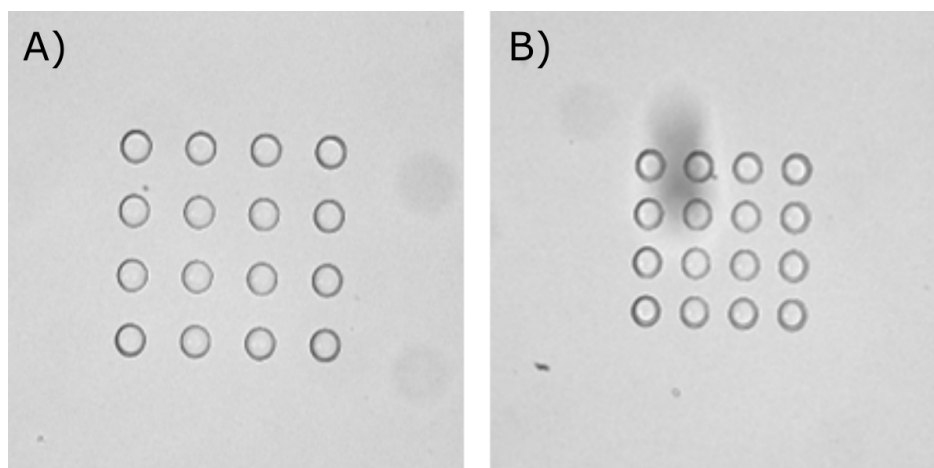


Figure 6.3: Images of an array of  $72\ \mu\text{m}$  pillars separated by A)  $75\ \mu\text{m}$  and B)  $35\ \mu\text{m}$

too much of the UV-light during fabrication, so the particles were malformed and could not be used for further experiments (Figure 6.2AB). We were not able to find the time to optimize this system, e.g., lower the spiropyran concentration, increase the exposure time. When properly tuned, it could be possible to visualize the force network from the particle fluorescence, where a more fluorescent particle is more stressed, and compare this to the forces extracted from the microstructure. This might become a viable alternative to photo-elasticity.

### 6.2.5 Pillar fabrication

The methods developed to fabricate particles in predefined positions can also be used for completely different applications. There has been a great interest in our group to study the transport of flexible filaments and bacteria in porous media. The traditional photolithographic techniques to fabricate microfluidic channels has a low turnover rate, and require a high amount of manual labor. It typically takes several days to design the mask, ask for a quote and get it printed. It then requires 2–3 hours to fabricate the silicon master, and another 2–3 hours of labor to fabricate the microfluidic chips. This makes it very slow to iterate through new designs. Together with two other PhD students in our lab, Peixin Zhang and Zhibo Li, we adapted the method to create solid objects inside a microfluidic channel. This works by replacing the top and bottom of the micro-channel with glass slides (rather than PDMS), which removes the oxygen inhibition layer. The PEGDA did not stick strongly to the glass. We therefore used NOA61, a UV-curable optical adhesive. Curing this inside a microfluidic channel resulted in stable pillars of  $72\ \mu\text{m}$  or bigger (Figure 6.3). Rinsing the channel with acetone and ethanol will remove the leftover NOA61, after which the channel can be filled with the solvent of choice.

This method makes it possible to fabricate a large amount of blank channels, without any features, and fabricate the pillars in the desired positions. It takes approximately 5 seconds to fabricate each pillar. So, a large design of 1000 pillars can be made within 2 hours, during which the researcher doesn't have to be present! This means that a prototype can be made within hours, rather than days. Of course, this method cannot compete with the traditional photo-lithography techniques to fabricate channels in bulk, but it could be a big breakthrough in the prototyping of microfluidic channels.

### 6.3 References

- [1] Isabelle Cantat, Sylvie Cohen-Addad, Florence Elias, François Graner, Reinhard Höhler, Olivier Pitois, Florence Rouyer, and Arnaud Saint-Jalmes. *Foams: Structure and Dynamics*, volume 1. Oxford University Press, Oxford, 1 edition, 2013. 112
- [2] M. L. Falk and J. S. Langer. Dynamics of viscoplastic deformation in amorphous solids. *Physical Review E - Statistical Physics, Plasmas, Fluids, and Related Interdisciplinary Topics*, 57(6):7192–7205, 1998. 112
- [3] Nathan C. Keim and Paulo E. Arratia. Yielding and microstructure in a 2D jammed material under shear deformation. *Soft Matter*, 9(27):6222–6225, 7 2013. 112
- [4] Yaakov Rosenfeld. Relation between the transport coefficients and the internal entropy of simple systems. Technical Report 6, 1977. 112
- [5] Jeppe C. Dyre. Perspective: Excess-entropy scaling. *Journal of Chemical Physics*, 149(21), 12 2018.
- [6] K. Lawrence Galloway, Xiaoguang Ma, Nathan C. Keim, Douglas J. Jerolmack, Arjun G. Yodh, and Paulo E. Arratia. Scaling of relaxation and excess entropy in plastically deformed amorphous solids. *Proceedings of the National Academy of Sciences of the United States of America*, 117(22), 6 2020. 112
- [7] Mathieu Souzy and Alvaro Marin. Role of liquid driving on the clogging of constricted particle suspensions. *Journal of Fluid Mechanics*, 953:1–19, 2022. 113
- [8] Kirsten Harth, Jing Wang, Tamás Börzsönyi, and Ralf Stannarius. Intermittent flow and transient congestions of soft spheres passing narrow orifices. *Soft Matter*, 16(34): 8013–8023, 9 2020. 114
- [9] Dhananjay Dendukuri, Daniel C. Pregibon, Jesse Collins, T. Alan Hatton, and Patrick S. Doyle. Continuous-flow lithography for high-throughput microparticle synthesis. *Nature Materials*, 5(5):365–369, 5 2006. 114
- [10] Yinjun Chen, C. Joshua Yeh, Yuan Qi, Rong Long, and Costantino Creton. From force-responsive molecules to quantifying and mapping stresses in soft materials. *Science Advances*, 6(20):1–9, 2020. 114

## Chapter 7

# Résumé substantiel

### 7.1 Introduction

Nous connaissons tous le sable, qu'il nous rappelle les jeux dans le bac à sable ou les voyages en famille à la plage pendant l'été. Si vous regardez de plus près, vous constaterez que les matériaux granulaires (c'est-à-dire les matériaux constitués de nombreux petits grains) sont partout. Dans l'industrie, les matériaux granulaires sont également omniprésents, puisqu'ils constituent la deuxième matière la plus manipulée en termes de poids, seule l'eau étant dépassée [1]. Imaginez que vous marchiez sur la plage. En marchant sur le lit de sable, votre pied déplace un peu de sable, de la même manière que votre pied déplace de l'eau lorsqu'il est plongé dans une piscine. Cependant, après avoir déplacé une petite quantité de sable (plusieurs ordres de grandeur de moins que ce que prévoyait le principe de flottabilité d'Archimède), le sable ne se déplace plus et le lit de sable semble solide. Pendant un pas, vous faites l'expérience du caractère à la fois fluide et solide des matériaux granulaires. De plus, en continuant à marcher vers l'eau, le lit de sable devient soudainement beaucoup plus sombre et ne se déforme pratiquement pas. Il s'avère que le comportement du sable dépend fortement de son environnement. Comme les grains ne remplissent pas parfaitement l'espace, mais laissent des vides, une petite quantité d'eau peut pénétrer dans le lit de sable. L'eau forme des ponts capillaires entre les particules, ce qui les fait "coller" les unes aux autres. [2-4]. En s'approchant de l'eau, les grains sont complètement englobés par l'eau, ce qui donne une suspension qui s'écoule comme un liquide.

Jusqu'à présent, nous avons vu que le comportement des matériaux granulaires changeait radicalement sous différentes conditions externes, telles que la charge appliquée, le milieu environnant et la présence de ponts capillaires. Cependant, les propriétés des grains constituant le milieu granulaire influencent également le comportement de ce dernier. Pendant l'écoulement, les particules allongées sont connues pour s'aligner à un petit angle par rapport à la direction du cisaillement, ce qui réduit la viscosité [5-7]. Comprendre la réorientation des particules allongées le long de la bande de cisaillement pourrait également s'avérer vital pour prédire l'intégrité structurelle et les modes de défaillance des sols [8, 9].

La rugosité de la surface joue également un rôle important dans le comportement des milieux granulaires et des suspensions. La rugosité peut conduire à un frottement effectif entre les grains [10, 11], et a été suggérée comme un paramètre clé déterminant la densité à laquelle le réseau de force est déterminé dans les verres granulaires [12, 13]. En outre, les particules rugueuses sont connues pour provoquer une très forte augmentation de la viscosité d'une suspension à de faibles concentrations, si le cisaillement est suffisamment rapide [14, 15].

d

Les avancées technologiques en matière de microscopie confocale à fluorescence et de fabrication de canaux aux caractéristiques microscopiques (microfluidique) ont été nécessaires pour observer la microstructure plus en détail. Brujić et al. [16] ont été parmi les premiers à reconstruire le réseau de forces 3D d'une émulsion bloquée et à observer la distribution des forces interparticulaires. Généralement, la rigidité (qui dépend de la tension de surface entre la phase dispersée et la phase continue) a été utilisée pour adimensionner la pression appliquée [17], ce qui suggère que la rigidité n'affecte que l'ampleur des déformations, mais pas la dynamique des particules [18].

Plus récemment, l'écoulement de particules molles à travers un rétrécissement a été étudié, soit en pressant des gouttelettes entre deux plaques parallèles, soit en confinant des réseaux de polymères gonflés (hydrogels) entre deux plaques parallèles [19, 20]. Ashour et al. [20] et Hong et al. [19] ont constaté que ces particules molles, presque sans frottement, avaient moins de chances de bloquer l'orifice, et que les bouchons formés se dissiperaient sans nécessiter de perturbation externe, ce qui ne se produit pas avec les particules dures à frottement. [21, 22].

Il s'avère toutefois que l'étude systématique de l'effet de la rigidité des particules est un défi, en particulier sans affecter les autres propriétés des particules telles que le coefficient de frottement et la rugosité, et en maintenant la compatibilité avec le système expérimental. Dans de nombreuses études expérimentales sur l'influence de la rigidité des particules sur le comportement des matériaux granulaires, la dynamique et la mécanique des particules dures (typiquement avec frottement) sont comparées à des particules molles (typiquement sans frottement) faites d'un matériau complètement différent. Il est donc difficile d'attribuer les différences observées à la seule mollesse des particules ou à une combinaison de la mollesse des particules et de l'un des paramètres modifiés involontairement.

Dans cette thèse, nous étudierons systématiquement l'effet de la mollesse des particules sur le comportement des ensembles granulaires. Pour se faire, nous adapterons une technique de microfabrication pour produire des ensembles granulaires 2D de disques à l'intérieur de canaux microfluidiques, ce qui nous permet de régler la rigidité des particules sans modifier aucune des autres propriétés des particules.

## 7.2 Contenu

Cette méthode a été mise au point par le groupe de Patrick Doyle, qui a développé une technique permettant de synthétiser une particule d'hydrogel à l'intérieur de canaux microfluidiques en exposant localement une solution photosensible à la lumière UV [23, 24]. Ils ont pu modifier la forme et la taille des particules en plaçant un masque sur le trajet de la lumière, en bloquant la majeure partie de la lumière et en formant une particule de la forme et de la taille de l'ouverture du masque. Duprat et al. [25] et Cappello et al. [26] ont découvert qu'il était possible de modifier la rigidité de ces particules en réduisant l'exposition à la lumière UV ou en diluant la solution photosensible. Dans cette thèse, à partir de la méthode de fabrication de particules de rigidité variable développée par Cappello et al. [26], nous étudierons l'influence de la rigidité des particules sur le comportement des ensembles granulaires.

Nous étudierons deux situations différentes à l'aide de ce dispositif : premièrement, le compactage progressif et oscillatoire des ensembles granulaires, à la fois d'un point de vue rhéologique (macroscopique) et d'un point de vue microscopique, et deuxièmement, l'écoulement de particules granulaires à travers un rétrécissement. En détail, le premier chapitre de ce manuscrit passe en revue les méthodes expérimentales utilisées et dévelop-

pées, qui sont utilisées tout au long de cette thèse. Tout d'abord, nous expliquons plus en détail la technique susmentionnée pour fabriquer des particules uniques molles. Ensuite, nous présentons comment nous avons réussi à étendre les capacités de cette technique pour fabriquer des ensembles de particules de différentes tailles dans des endroits prédéfinis à l'intérieur des canaux microfluidiques. Nous décrivons et caractérisons ensuite l'écoulement du fluide porteur à l'intérieur du canal microfluidique et la manière dont il exerce une force sur les particules. Enfin, nous expliquerons comment nous avons extrait les emplacements de  $\sim 2000$  particules (de différentes tailles) dans le champ de vision avec une précision inférieure au pixel.

Le deuxième chapitre est consacré au compactage des ensembles de particules molles à l'intérieur de canaux microfluidiques, que nous étudions d'un point de vue rhéologique. Tout d'abord, nous développons un canal microfluidique qui nous permet de comprimer les particules contre une membrane. Nous utilisons ensuite ce canal pour réaliser des expériences de contrainte par paliers, afin de caractériser le comportement viscoélastique des ensembles de particules. Nous avons constaté qu'un modèle de Kelvin-Voigt généralisé pour les solides viscoélastiques avec deux échelles de temps de relaxation était suffisant pour capturer la réponse complexe d'un ensemble de particules viscoélastiques. Nous avons utilisé ce modèle pour étudier la réponse à la déformation d'ensemble dans la limite quasi-statique, en augmentant la contrainte par étapes et en utilisant le modèle pour déterminer la déformation limite à cette contrainte. Nous avons constaté que la déformation limite pendant la compression n'était pas identique à la déformation limite à la même pression durant la décompression. Pourtant, sur l'ensemble d'un cycle, le système est revenu à son état de non-déformation. Cela indique qu'il existe des mécanismes qui introduisent l'hystérésis, en plus de la relaxation des particules. Cet effet a été étudié plus en détail en utilisant le compactage oscillatoire dynamique. Nous montrons que le décalage de phase entre la contrainte et la déformation diminue avec la période d'oscillation, comme le prévoit le modèle de Kelvin-Voigt, à une exception près. Là où le modèle de Kelvin-Voigt prédit que le décalage de phase diminue jusqu'à zéro, nous constatons que le décalage de phase diminue jusqu'à une valeur non nulle identique au décalage de phase trouvé pendant l'oscillation par paliers. Cela pourrait être dû à des réarrangements microscopiques, mais le rôle et l'échelle de temps des réarrangements à l'échelle des particules sur la relaxation ne sont pas encore clairs.

Le troisième chapitre se concentre sur les mêmes expériences que celles décrites dans le chapitre 3, mais maintenant d'un point de vue micromécanique. Tout d'abord, nous décrivons comment nous avons pu obtenir une description presque complète de la microstructure des ensembles au cours de nos expériences, comme on l'obtiendrait à partir de simulations. Nous constatons que la pression microscopique augmente lentement à de faibles déformations et passe à une dépendance linéaire à des déformations plus élevées. La pente du régime linéaire a été bien saisie par le modèle de compactage dérivé par Cárdenas-Barrantes et al. [27]. Nous pensons que le début doux de la compaction, qui n'a pas été prédit par le modèle, est dû à des réarrangements. Nous avons examiné les réarrangements en étudiant les trajectoires des particules au cours d'un cycle de compression et avons constaté que les trajectoires n'étaient pas parfaitement élastiques et que la plupart des particules étaient réversiblement plastiques, c'est-à-dire que la trajectoire au cours de la décompression était différente de la trajectoire au cours de la compression, mais que le déplacement de la particule au cours d'un cycle était négligeable. Nous avons tenté de relier cette plasticité réversible au début doux de la compression et à l'hystérésis indépendante du temps pendant la compression. Cependant, aucune tendance claire n'a encore été trouvée.

Dans le quatrième chapitre, nous étudions l'écoulement de particules molles dans une

trémie microfluidique. Tout d'abord, nous décrivons la difficulté d'obtenir une suspension bloquée à l'intérieur d'une trémie microfluidique, et comment nous avons intégré une valve de type Quake à l'intérieur de notre canal microfluidique pour collecter les particules au niveau de l'orifice. Nous étudions ensuite le taux d'écoulement de particules de différentes tailles pour des flux entraînés par la pression et le débit et nous le comparons à d'autres expériences de trémie dans le régime visqueux. Nous avons constaté que le taux d'écoulement s'échelonne linéairement avec la pression imposée sur le canal. Ce résultat est surprenant, car le nombre de particules dans la trémie diminue pendant l'écoulement, ce qui augmente le débit du fluide porteur. Nous avons vérifié cette observation en étudiant la vitesse du fluide porteur pendant la décharge des particules sous l'effet de la pression et la décharge des particules sous l'effet du débit (où une vitesse constante du fluide est imposée). Ces deux méthodes ont confirmé que le taux d'écoulement est effectivement constant dans le temps. Nous avons également constaté que le facteur de correction proposé par Hagen et Janssen [28, 29] rendait bien compte de l'influence de la taille des particules. Enfin, nous avons étudié l'effet de la mollesse des particules sur la décharge, et nous avons constaté que la mollesse des particules a un effet non seulement sur le taux d'écoulement, mais aussi sur l'évolution du taux d'écoulement dans le temps, et sur le comportement de colmatage.

### 7.3 Conclusion

En conclusion, nous avons conçu un nouveau système modèle pour les matériaux granulaires, un ensemble pseudo-2D de cylindres dans des canaux microfluidiques. Nous avons mis au point un dispositif expérimental pour étudier systématiquement l'effet de la rigidité sur le comportement des matériaux granulaires dans deux expériences modèles, le compactage et l'écoulement de la trémie. Ces expériences correspondent à deux processus industriels pertinents, et nous espérons que ces expériences et celles à venir permettront de mieux comprendre la mécanique et la dynamique des matériaux granulaires. Les résultats obtenus peuvent avoir de nombreuses applications, dans et en dehors du domaine des matériaux granulaires, telles que la compréhension de la mécanique des amas cellulaires à partir de la mécanique des cellules individuelles ou la prévention du colmatage dans les dispositifs biomédicaux.

### 7.4 References

- [1] P. G. de Gennes. Granular Matter: A Tentative View. *Reviews of Modern Physics*, 71(2):629–643, 1999. 117
- [2] Arshad Kudrolli. Sticky sand. *Nature Materials*, 7(3):174–175, 2008. 117
- [3] Etienne Guyon, Jean-Yves Delenne, and Farhang Radjai. *Built on sand*. The MIT Press, Cambridge, 2020.
- [4] S. Herminghaus. Dynamics of wet granular matter. *Advances in Physics*, 54(3):221–261, 2005. 117
- [5] Tamás Börzsönyi, Balázs Szabó, Sandra Wegner, Kirsten Harth, János Török, Ellák Somfai, Tomasz Bien, and Ralf Stannarius. Shear-induced alignment and dynamics of elongated granular particles. *Physical Review E - Statistical, Nonlinear, and Soft Matter Physics*, 86(5):1–8, 2012. 117

- 
- [6] Tamás Börzsönyi, Ellák Somfai, Balázs Szabó, Sandra Wegner, Pascal Mier, Georg Rose, and Ralf Stannarius. Packing, alignment and flow of shape-anisotropic grains in a 3D silo experiment. *New Journal of Physics*, 18(9), 2016.
- [7] Brisa Arenas-Gómez, Cristina Garza, Yun Liu, and Rolando Castillo. Alignment of worm-like micelles at intermediate and high shear rates. *Journal of Colloid and Interface Science*, 560:618–625, 2020. 117
- [8] Gustavo Pinzón, Edward Andò, Alessandro Tengattini, Gioacchino Viggiani, and Jacques Desrues. Contact evolution in granular materials with inherently anisotropic fabric. *EPJ Web of Conferences*, 249:06015, 2021. 117
- [9] Gustavo Pinzón, Edward Andò, Jacques Desrues, and Gioacchino Viggiani. Fabric evolution and strain localisation in inherently anisotropic specimens of anisometric particles (lentils) under triaxial compression. *Granular Matter*, 25(1):1–12, 2023. 117
- [10] Nicholas A. Pohlman, Benjamin L. Severson, Julio M. Ottino, and Richard M. Lueptow. Surface roughness effects in granular matter: Influence on angle of repose and the absence of segregation. *Physical Review E - Statistical, Nonlinear, and Soft Matter Physics*, 73(3):1–9, 2006. 117
- [11] Guilhem Mollon, Adriana Quacquarelli, Edward Andò, and Gioacchino Viggiani. Can friction replace roughness in the numerical simulation of granular materials? *Granular Matter*, 22(2):1–16, 2020. 117
- [12] Lars Kool, Patrick Charbonneau, and Karen E. Daniels. Gardner-like crossover from variable to persistent force contacts in granular crystals. *Physical Review E*, 106(5):1–6, 5 2022. 117
- [13] Patrick Charbonneau, Eric I. Corwin, Lin Fu, Georgios Tsekenis, and Michael Van Der Naald. Glassy, Gardner-like phenomenology in minimally polydisperse crystalline systems. *Physical Review E*, 99(2), 2 2019. 117
- [14] Philippe Bourriane, Vincent Niggel, Gatién Polly, Thibaut Divoux, and Gareth H. McKinley. Tuning the shear thickening of suspensions through surface roughness and physico-chemical interactions. *Physical Review Research*, 4(3):33062, 2022. 117
- [15] Jeffrey F. Morris. Shear Thickening of Concentrated Suspensions: Recent Developments and Relation to Other Phenomena. *Annual Review of Fluid Mechanics*, 52:121–144, 2020. 117
- [16] Jasna Brujić, Sam F. Edwards, Dmitri V. Grinev, Ian Hopkinson, Djordje Brujić, and Hernán A. Makse. 3D bulk measurements of the force distribution in a compressed emulsion system. *Faraday Discussions*, 123(1):207–220, 2003. 118
- [17] H. P. Zhang and H. A. Makse. Jamming transition in emulsions and granular materials. *Physical Review E - Statistical, Nonlinear, and Soft Matter Physics*, 72(1):1–12, 2005. 118
- [18] Ivane Jorjadze, Lea Laetitia Pontani, and Jasna Brujic. Microscopic approach to the nonlinear elasticity of compressed emulsions. *Physical Review Letters*, 110(4):1–5, 2013. 118



- [19] Xia Hong, Meghan Kohne, Mia Morrell, Haoran Wang, and Eric R. Weeks. Clogging of soft particles in two-dimensional hoppers. *Physical Review E*, 96(6), 12 2017. 118
- [20] Ahmed Ashour, Torsten Trittel, Tamás Börzsönyi, and Ralf Stannarius. Silo outflow of soft frictionless spheres. *Physical Review Fluids*, 2(12):1–9, 2017. 118
- [21] Ran Tao, Madelyn Wilson, and Eric R. Weeks. Soft particle clogging in two-dimensional hoppers. *Physical Review E*, 104(044909), 10 2021. 118
- [22] Kirsten Harth, Jing Wang, Tamás Börzsönyi, and Ralf Stannarius. Intermittent flow and transient congestions of soft spheres passing narrow orifices. *Soft Matter*, 16(34):8013–8023, 9 2020. 118
- [23] Dhananjay Dendukuri, Daniel C. Pregibon, Jesse Collins, T. Alan Hatton, and Patrick S. Doyle. Continuous-flow lithography for high-throughput microparticle synthesis. *Nature Materials*, 5(5):365–369, 5 2006. 118
- [24] Dhananjay Dendukuri, Priyadarshi Panda, Ramin Haghgooie, Ju Min Kim, T. Alan Hatton, and Patrick S. Doyle. Modeling of oxygen-inhibited free radical photopolymerization in a PDMS microfluidic device. *Macromolecules*, 41(22):8547–8556, 2008. 118
- [25] Camille Duprat, H el ene Berthet, Jason S. Wexler, Olivia Du Roure, and Anke Lindner. Microfluidic in situ mechanical testing of photopolymerized gels. *Lab on a Chip*, 15(1):244–252, 1 2015. 118
- [26] Jean Cappello, Mathias Bechert, Camille Duprat, Olivia Du Roure, Fran ois Gallaire, and Anke Lindner. Transport of flexible fibers in confined microchannels. *Physical Review Fluids*, 4(3):1–22, 2019. 118
- [27] Manuel C ardenas-Barrantes, David Cantor, Jonathan Bar es, Mathieu Renouf, and Emilien Az ema. Three-dimensional compaction of soft granular packings. *Soft Matter*, 18(2):312–321, 2022. 119
- [28] G Hagen. Druck und Bewegung des trockenen Sandes. *Bericht  uber die zur Bekanntmachung geeigneten Verhandlungen der K oniglich Preu ischen Akademie der Wissenschaften zu Berlin*, pages 35–42, 1852. 120
- [29] H.A. Janssen. Versuche  uber Getreidedruck in Silozellen. *Zeitschr. d. Vereines deutscher Ingenieure*, 39:1045, 1895. 120




# List of Figures

1.1	Granular phenomena on the beach . . . . .	2
1.2	Granular phase diagram and granular phenomena . . . . .	3
1.3	Examples of experiments involving soft particles . . . . .	4
1.4	Hydrogel squares fabricated in the group of Patrick Doyle . . . . .	5
1.5	Particles during the fabrication and after image analysis . . . . .	6
1.6	Packing before and during compression . . . . .	7
1.7	Reconstructed force network . . . . .	7
1.8	Snapshot during hopper discharge . . . . .	8
2.1	Schematic overview of the light path used to fabricate particles . . . . .	14
2.2	Reaction equations of the radical polymerization reaction . . . . .	15
2.3	Schematic overview of the oxygen inhibition layer . . . . .	15
2.4	Schematic overview of the PDMS fabrication method. . . . .	16
2.5	Schematic overview of the particle fabrication method . . . . .	17
2.6	Effect of focus on the fabricated and observed particles . . . . .	18
2.7	Young’s moduli of particles created under different conditions . . . . .	19
2.8	Snapshot taken during the fabrication of a bidisperse packing . . . . .	21
2.9	Schematic overview of the driving forces inside the microfluidic channels . . . . .	24
2.10	Carrier fluid velocity as function of the applied pressure . . . . .	25
2.11	Influence of the position of the observation plane . . . . .	27
2.12	Overview of the image analysis algorithms . . . . .	28
2.13	Determination of the particle radius . . . . .	30
2.14	Overlay of two images used to calculate the fluid velocity with PIV . . . . .	31
3.1	Schematic representation of the deformation of a solid . . . . .	36
3.2	Schematic representation of the (generalized) Kelvin-Voigt model . . . . .	38
3.3	Schematic overview of the compression channel . . . . .	41
3.4	Mesoscopic strain as function of the position of the particle in the channel . . . . .	42
3.5	Step stress experiments on particles with varying softness . . . . .	43
3.6	Compression of a single particle in a microfluidic channel . . . . .	45
3.7	Time response of the pressure controller . . . . .	47
3.8	Oscillatory compaction and decompaction of an ensemble of particles . . . . .	48
3.9	Strain response of packings of particles with varying softness on an oscillating imposed pressure . . . . .	50
3.10	Influence of oscillation period of the imposed pressure on the strain response of particle packings. . . . .	52
3.11	Step-wise oscillation of a particle packing . . . . .	53

4.1	Schematic overview of inter-particle interactions . . . . .	58
4.2	Contact indeterminacy of frictional particles . . . . .	59
4.3	Pressure as function of strain for simulations in literature . . . . .	62
4.4	Evolution of the coordination number during compaction and its relation to $g(r)$ . . . . .	64
4.5	Distribution of the inter-particle forces during compaction . . . . .	65
4.6	Influence of small changes in the nominal particle radius on the coordination number and microscopic pressure . . . . .	67
4.7	Local strain as function of the global strain . . . . .	68
4.8	Microscopic pressure as function of the global strain and imposed pressure . . . . .	69
4.9	Evolution of the coordination number during compaction . . . . .	70
4.10	Distribution of the contact orientations . . . . .	71
4.11	Distribution of contact orientations depending on compaction protocol, as reported in literature . . . . .	72
4.12	Reconstructed force network . . . . .	73
4.13	Distribution of the magnitudes of the inter-particle forces during compaction . . . . .	74
4.14	Trajectories of particles during a compression-decompression cycle . . . . .	75
5.1	Examples of early studies of hopper flow . . . . .	83
5.2	Early studies of hopper discharge rates as function of the orifice size . . . . .	85
5.3	Cumulative discharges and discharge rates for hard and soft particle systems. . . . .	87
5.4	Settling of particles in a microfluidic hopper without a valve . . . . .	88
5.5	Schematic representation of a Quake valve . . . . .	89
5.6	Fabrication procedure of microfluidic hopper with a Quake-style valve . . . . .	90
5.7	Typical hopper discharge . . . . .	92
5.8	Formation of a cavity in packings that were not agitated before discharge . . . . .	94
5.9	Fluid velocity of the carrier fluid during hopper discharge . . . . .	95
5.10	Cumulative discharge over time for different imposed pressure drops . . . . .	97
5.11	Discharge rate as function of the applied pressure drop or flow rate . . . . .	98
5.12	Snapshots of the top of the packing during discharge . . . . .	99
5.13	Influence of particle size on the discharge rate . . . . .	100
5.14	Discharge rate as function of the non-dimensionalized orifice size . . . . .	101
5.15	Cumulative discharge of soft particles over time . . . . .	101
5.16	Defining a clog in a microfluidic hopper . . . . .	102
6.1	Image of various star-shaped particles . . . . .	113
6.2	Images of particles with incorporated mechanophores . . . . .	114
6.3	Fabrication of solid structures inside microfluidic channels . . . . .	115

# List of Tables

3.1	Table of PEGDA-PEG mixtures used and the associated Young's modulus . .	41
4.1	Table of PEGDA-PEG mixtures used, their associated Young's moduli and the correction factor used for the particle radius . . . . .	67

**Gardner-like crossover from variable to persistent force contacts in granular crystals**Lars Kool <sup>1,2</sup>, Patrick Charbonneau <sup>3</sup>, and Karen E. Daniels <sup>2</sup><sup>1</sup>*Laboratoire de Physique et Mécanique des Milieux Hétérogènes, ESPCI, 75005 Paris, France*<sup>2</sup>*Department of Physics, North Carolina State University, Raleigh, North Carolina 27695, USA*<sup>3</sup>*Department of Chemistry and Department of Physics, Duke University, Durham, North Carolina 27708, USA*

(Received 18 May 2022; accepted 29 September 2022; published 15 November 2022)

We report experimental evidence of a Gardner-like crossover from variable to persistent force contacts in a two-dimensional bidisperse granular crystal by analyzing the variability of both particle positions and force networks formed under uniaxial compression. Starting from densities just above the freezing transition and for variable amounts of additional compression, we compare configurations to both their own initial state and to an ensemble of equivalent reinitialized states. This protocol shows that force contacts are largely undetermined when the density is below a Gardner-like crossover, after which they gradually transition to being persistent, being fully so only above the jamming point. We associate the disorder that underlies this effect with the size of the microscopic asperities of the photoelastic disks used, by analogy to other mechanisms that have been previously predicted theoretically.

DOI: [10.1103/PhysRevE.106.054901](https://doi.org/10.1103/PhysRevE.106.054901)**I. INTRODUCTION**

Granular materials differ from elastic solids in their response to external forces: Rather than homogeneously supporting an applied load, the forces are transmitted by a sparse percolating network of particles [1–5]. If inter-particle contacts are allowed to break and the granular material yields, the topology of the force network changes even if no particle-scale rearrangement takes place [6,7]. By contrast, if contacts are preserved, cyclic (un)loading does not affect the structure of the force network. While recent theoretical and numerical studies suggest the preservation of contacts might not coincide with the jamming transition [8,9], it is yet to be experimentally verified whether such a distinction exists.

The distinction between the onset of contact memory and jamming is reminiscent of the critical transition reported for certain amorphous solids and crystals of slightly polydisperse particles [10–16]. The associated Gardner transition is often depicted using an energy landscape roughened by a hierarchy of metastable basins. Outside of the Gardner regime, the energy scales are well separated from the landscape roughness and the system responds elastically [17]. By contrast, within the Gardner regime, the landscape roughness gives rise to easier pathways to escape from marginally stable subbasins and thus to minute structural rearrangements (much smaller than the particle scale) that result in a different spatial distribution of contact forces at jamming [12,18].

This landscape roughness in the Gardner phase also leaves a dynamical signature. Outside the Gardner regime, the long-time mean square displacement (MSD)  $\Delta$  of the constituent particles plateaus at a value that depends on the particle cage size (and thus density or pressure for a hard-sphere system) [8]. By contrast, within the Gardner regime, particles cannot

effectively sample the landscape over accessible timescales, which results in a MSD that does not saturate with time. Its asymptotically long-time value can nevertheless be estimated from the distance  $\Delta_{AB}$  between two system copies *A* and *B* that started from the same reference configuration at a density below the Gardner regime and then evolved along different stochastic trajectories. One can thus define the Gardner regime as the density for which  $\Delta < \Delta_{AB}$  at (sufficiently) long times. This was first shown experimentally in a granular glass former by Seguin and Dauchot [19], who captured a signature of Gardner physics in the dynamics of a vibrated, two-dimensional (2D), disordered packing of granular disks. More recently, Xiao *et al.* [20] found signatures of Gardner physics in quasithermal (air-fluidized) star-shaped particles. However, the corresponding contact force network has not been observed experimentally, nor have the factors that control the distance of the Gardner transition to jamming been assessed [12].

In this article we investigate the crossover from variable to persistent contacts in a granular crystal (see Fig. 1). We find that this transition is strongly analogous to that predicted by Gardner physics, is clearly distinct from the jamming transition, and the distance between the two appear here to be controlled by the scale of the microscopic asperities of the experimental disks.

**II. METHODS**

Despite numerical studies of ultrastable glasses [22] and polydisperse crystals [12] which successfully suppress particle-scale rearrangements to reveal the Gardner regime, it remains an open challenge to translate these numerical protocols for generating ultrastable glasses to experiments. We study instead marginally stable states generated from a

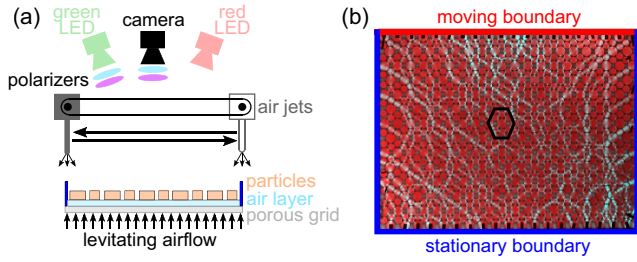


FIG. 1. (a) Schematic of the experimental setup (side view), with the height of the air layer not to scale. (b) Typical image (top view) from which the particle positions (red channel) and force transmission (cyan channel) are extracted. The hexagon marks an H1 unit cell [21].

well-defined 2D crystalline packing to suppress rearrangements via an alternative means. We selected the  $H_1$  crystal symmetry, containing a unit cell of three large and six small disks (see Fig. 1), from among those identified in [21], for having no basis vectors aligned with the compression axis. This choice thereby limits the putative contribution of low-energy local buckling excitations [15,23–25] and focuses the dynamics on the quenched disorder that arises through variability in particle size and surface roughness [12]. We found that this crystal successfully suppresses rearrangements; when one does occur, the system can readily be reinitialized. Although the resulting crystalline axes create an additional coordinate system that is neither orthogonal nor aligned with the natural axes of the apparatus (see Fig. 1), we are able to account for these effects during the data analysis.

We performed our experiments on a single-layer packing of bidisperse photoelastic disks ( $N_S = 507$  small disks with  $R_S = 5.5$  mm and  $N_L = 273$  large disks with  $R_L = 7.7$  mm, Vishay PhotoStress PSM-4) with a reflective back layer levitated on a gentle layer of air forced through a porous grid; this setup was previously described in [26,27]. By reducing basal friction, such that interparticle forces dominate, particles are free to explore their cages and sample available configurations under gentle perturbations. We randomized particle positions *within their cage* by sweeping a turbulent airflow across the upper surface of the packing [see Fig. 1(a)]; time was measured in units of these  $t_r = 20$  s randomization sweeps. We explored cage sizes and separations as a function of density  $\phi$  by uniaxially compressing the system in discrete increments of  $\delta\phi/\phi = 6 \times 10^{-4}$ , moving one boundary with a stepper motor. Each of the four boundaries was laser cut from acrylic sheets. The particles along both the moving boundary and the static boundary opposite were pinned to suppress large-scale crystal rearrangements.

Particle positions and the network of interparticle forces were imaged using a single camera and two light sources: an unpolarized red LED light for the positions and a circularly polarized green LED light for the photoelastic visualization of stresses [see Fig. 1(b)]. We located the centroid of each particle using the convolution of the red channel of the image with a predefined mask matching the particle size [28,29]; this allowed us to determine locations within approximately 0.1 pixel (approximately equal to  $\frac{1}{250}R_L$ ) precision. Because we are studying well-defined crystal configurations, for which

all particle displacements are at least an order of magnitude smaller than the particle size, we were able to bypass traditional particle-tracking algorithms and their caveats. Each particle position was instead determined from the first image, hand checked for completeness, and then used as a reference position for subsequent images. Within these images, the sole particle located within  $R_L$  of the reference particles was attached to its trajectory. To minimize edge effects, particles within  $4R_L$  of the walls were discarded from the data set, leaving  $N_p = 628$  particles for our analysis.

### III. RESULTS

#### A. Gardner crossover

We have adapted the protocol of [19] to identify transitions in the cage dynamics as a function of  $\phi$ , using overhead air jets to randomly promote cage exploration rather than supplying a global vibration of the bottom plate. We determine the cage dynamics at 20 different  $\phi$ , equally spaced between  $\phi_{\min} = 0.8006 \pm 0.0002$  (the limit of mechanical stability of the crystal) and  $\phi_{\max} = 0.8162 \pm 0.0002$  (slightly larger than  $\phi_J$ , guaranteeing that the Gardner regime is traversed but without activating the out-of-plane buckling mode that develops deeper into the jammed phase). From an initial state at  $\phi_{\min}$ , the system is compressed to  $\phi_{\max}$  and then decompressed stepwise and allowed to equilibrate for  $t = 100t_r$  at each intermediate density. Upon reaching  $\phi_{\min}$ , the system is deemed *reinitialized*. We performed a total of ten initializations, shown schematically in Fig. 2(a).

For each  $\phi$ , the cage separation distance  $\Delta_{AB}$  is obtained by comparing particle positions between two different initializations  $A$  and  $B$ , taken at the same  $\phi$ ,

$$\Delta_{AB}(t; \phi) = \frac{1}{N_p} \sum_{i=1}^{N_p} |\mathbf{r}_i^B(t) - \mathbf{r}_i^A(t)|^2, \quad (1)$$

where  $\mathbf{r}_i^\alpha(t)$  is the position of particle  $i$  at time  $t$  in initialization  $\alpha$ . The cage size  $\Delta$  (within a single initialization  $A$ ) at a given  $\phi$  is obtained from particle displacements after a long experimental time of  $100t_r$ , according to

$$\Delta(t; \phi) = \frac{D}{N_p} \sum_{i=1}^{N_p} |\mathbf{r}_{i,y}^A(t) - \mathbf{r}_{i,y}^A(0)|^2. \quad (2)$$

In both cases, the average at each  $\phi$  over all runs is then calculated, denoted by  $\langle \cdot \rangle$ . The corrections  $D$  and  $\mathbf{r}'$  in Eq. (2) ensure that  $\langle \Delta \rangle = \langle \Delta_{AB} \rangle$  in the vicinity of  $\phi_{\min}$ ; they are experimentally motivated as follows. First, even at  $\phi_{\min}$  the MSD of a caged particle plateaus at longer times than are experimentally accessible; we measured this time to be approximately equal to  $1000t_r$ , while our experiments can only reach  $100t_r$ . Because we expect the relative ratio of these length scales to be constant at low  $\phi$ , we have rescaled our measurement of  $\Delta$  by the ratio  $D = 1.2$ , our estimate of this ratio [30]. Second, we observed that for  $\phi > \phi_G$ , histograms of the  $(x, y)$  displacements displayed multiple distinct peaks, each aligned with the direction of one of the lattice vectors of the unit cell, rather than being azimuthally symmetric around zero, as observed for  $\phi < \phi_G$ . To correct for the biased motions introduced by the crystalline axes that give rise to these peaks, we applied a linear transformation to orthogonalize the

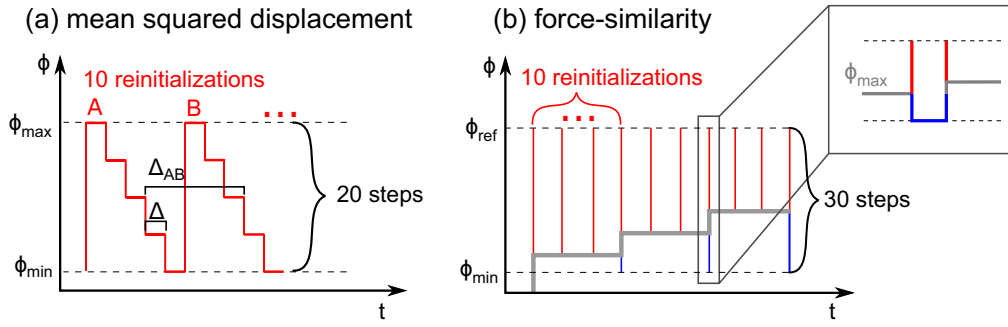


FIG. 2. (a) Schematic representation of the protocol used to determine the cage size  $\Delta$  and the mean cage separation  $\Delta_{AB}$  via the MSD. (b) Schematic representation of the protocol used to determine the persistence of interparticle contacts via the force-similarity analysis.

system. Equation (2) therefore defines  $\Delta$  as the MSD of the Gaussian part of the displacement (along the  $y'$  axis) in the orthogonalized system  $r'_y$  and ignores the displacements along the more-complicated ( $x'$ ) axis [30].

Figure 3 presents the histograms of  $\Delta$  and  $\Delta_{AB}$  measured at various  $\phi$ . At low  $\phi$ , the statistical distributions of  $\Delta$  and  $\Delta_{AB}$  are nearly identical, which is characteristic of a normal solid. In contrast, for  $\phi \gtrsim 0.807$  we observe that  $\langle \Delta \rangle < \langle \Delta_{AB} \rangle$ , indicating the onset of a Gardner-like regime at  $\phi_G = 0.807 \pm 0.0005$ . As  $\phi$  further increases, force chains emerge, thus identifying the jamming point  $\phi_J = 0.8100 \pm 0.0005$  [Fig. 4(c)]; this value is determined by measuring the average proportional change of the pixel intensity  $I_g$  of the photoelastic (green) channel above the minimum observed value [30]. Note that, although we expect  $\Delta = 0$  in the jammed phase, a finite value is measured; this captures the noise floor of our system and analysis.

### B. Interparticle forces

Having identified a Gardner-like crossover using the particle displacement data, we now separately consider the evolution of interparticle forces within each (marginally stable) state at different  $\phi$ . We observe changes in the persistence of the photoelastic fringes [as proxy for interparticle forces;

see Figs. 4(a) and 4(b)], of a given state by compressing the system to a jammed reference density  $\phi_{\text{ref}} = 0.8147 \pm 0.0002$ , which is slightly above  $\phi_{\text{max}} = 0.8127 \pm 0.0002$ , at which a better imaging is obtained. All values of  $\phi$  were measured during *a posteriori* image analysis and thus do not necessarily match between the two types of experiments. The lowest densities for MSD measurements,  $\phi_{\text{min}} = 0.8006$  and for force-similarity measurements  $\phi_{\text{min}} = 0.8002$ , are nevertheless identical within measurement error, but the densest system for MSD measurements,  $\phi_{\text{max}} = 0.8162$ , was significantly denser than for force-similarity measurements,  $\phi_{\text{max}} = 0.8127$ . This difference arises from the observation that deep in the jammed phase, forces become more homogeneous, thus making it harder to detect changes. Choosing  $\phi_{\text{max}}$  for force-similarity measurements closer to  $\phi_J$  therefore makes changes in the fringes more apparent. In both experiments,  $\phi_{\text{max}}$  is nevertheless above the determined jamming density  $\phi_J = 0.8100$ . In this context, because the system is arrested above  $\phi_J$  and the contact network is fully formed, the difference in  $\phi_{\text{max}}$  is not deemed significant. For systems with few interparticle contacts, the correlation between fringes is dominated by noise, whereas in well-jammed systems the force network is completely percolated (due to the crystalline nature of the system), thus making changes to the force network insignificant compared to the average interparticle force.

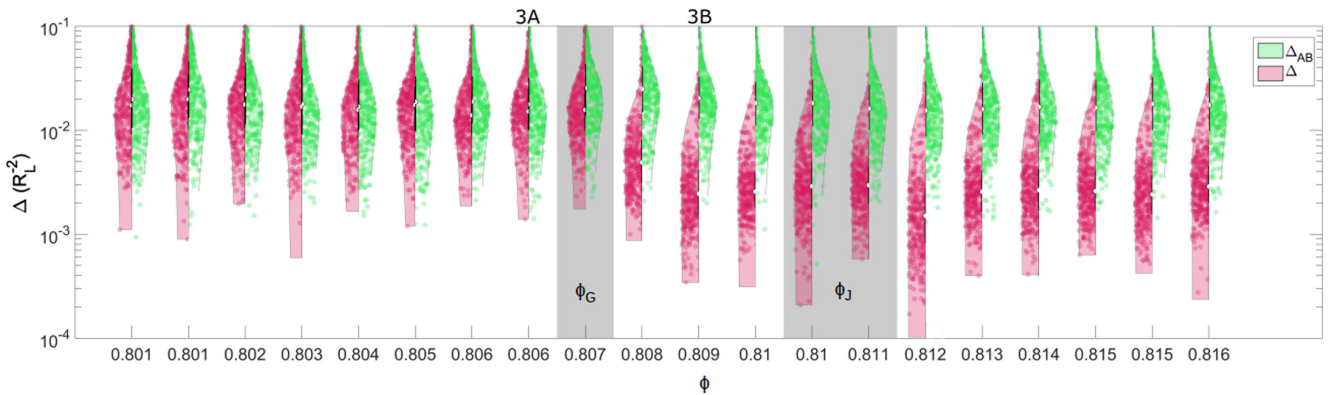


FIG. 3. Side-by-side histograms of the probability density functions of  $\Delta$  (magenta, left) and  $\Delta_{AB}$  (green, right) measured at each density  $\phi$ . Both  $\Delta$  and  $\Delta_{AB}$  are nondimensionalized using the radius of the large particle  $R_L$ . At  $\phi < \phi_G$  (crossover denoted by a gray rectangle), the histograms of  $\Delta$  and  $\Delta_{AB}$  agree (in both the mean and width of the distribution), whereas for  $\phi > \phi_G$ , we see that  $\Delta < \Delta_{AB}$ . Above the jamming point  $\phi_J$  (transition denoted by a gray rectangle), the histograms of  $\Delta$  and  $\Delta_{AB}$  differ markedly. Histograms 3A and 3B correspond to the two snapshots presented in Fig. 4.

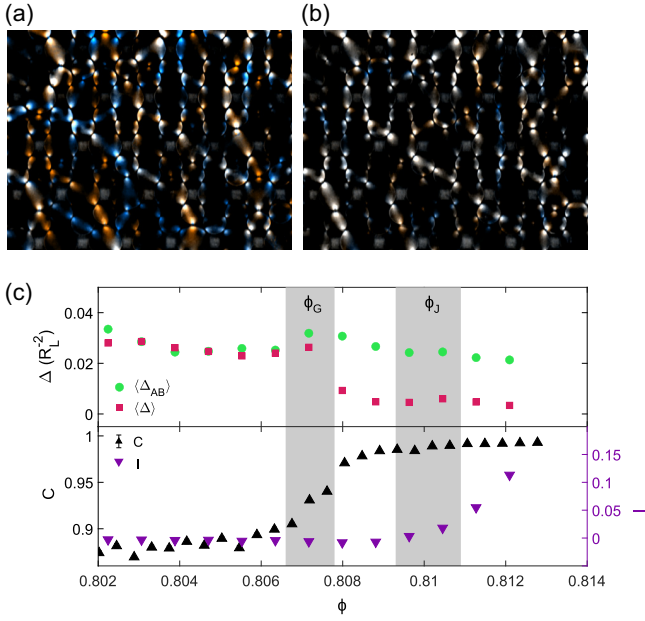


FIG. 4. Overlay of two marginally stable states (red and blue) and their overlap (white) for (a)  $\phi < \phi_G$  ( $\phi = 0.8068$ ) and (b)  $\phi > \phi_G$  ( $\phi = 0.8089$ ). The two states have little overlap for  $\phi < \phi_G$ , whereas for  $\phi > \phi_G$  the two states have a large overlap between their force network. A movie of overlays with increasing density makes this point even more saliently [30]. (c) Overlay of  $\langle \Delta \rangle$  (magenta  $\blacksquare$ ) and  $\langle \Delta_{AB} \rangle$  (green  $\bullet$ ) as a function of  $\phi$  on the top axis and force correlation  $C$  (black  $\blacktriangle$ ) and fringe intensity  $I$  (purple  $\blacktriangledown$ ) on the bottom axis, both as functions of  $\phi$ . Both  $\Delta$  and  $\Delta_{AB}$  are nondimensionalized using the radius of the large particle  $R_L$ .

Changes in the photoelastic fringes at  $\phi_{\text{ref}}$  are determined as follows. We first image the photoelastic fringes of the initial state  $\mathcal{I}$ . The system is then decompressed to  $\phi_{\text{min}} < \phi < \phi_{\text{max}}$  and evolved for  $10t_r$  (sufficient for the force network to randomize) before recompressing to  $\phi_{\text{ref}}$  and to image the photoelastic fringes of this final state  $\mathcal{F}$ . We repeat this protocol for 30 equidistant densities within the interval  $[\phi_{\text{min}}, \phi_{\text{max}}]$ . In all cases, the system is decompressed to  $\phi_{\text{min}}$  before moving to the next  $\phi$  to erase any memory of the previous experiment. The protocol is schematically represented in Fig. 2(b). We quantify the degree of similarity between the  $\mathcal{I}$  and  $\mathcal{F}$  states for a given  $\phi$  using a normalized cross correlation of the photoelastic fringes, taken  $10t_r$  apart,

$$C(\phi) = \left\langle \frac{\sum_{x,y} [\mathcal{I}_i(x,y) - \bar{\mathcal{I}}_i] [\mathcal{F}_i(x,y) - \bar{\mathcal{F}}_i]}{\sqrt{\sum_{x,y} [\mathcal{I}_i(x,y) - \bar{\mathcal{I}}_i]^2 \sum_{x,y} [\mathcal{F}_i(x,y) - \bar{\mathcal{F}}_i]^2}} \right\rangle, \quad (3)$$

with  $\mathcal{I}_i(x,y)$  the pixel intensity of pixel  $(x,y)$  of particle  $i$ ,  $\bar{\mathcal{I}}_i$  the average pixel intensity of particle  $i$  in state  $\mathcal{I}$ , and the average  $\langle \cdot \rangle$  running over all particles in all pairs  $\mathcal{I}$  and  $\mathcal{F}$  of states at a given  $\phi$ .

Figure 4 shows two superimposed images of force chains:  $\mathcal{I}$  (blue) obtained before the air-jet sweeps and  $\mathcal{F}$  (red) after, such that white denotes regions where force chains did not change, while red and blue denote force chains present in only one of the two images. For  $\phi < \phi_G$  [Fig. 4(a)] the rare force chain overlaps (white) indicate that interparticle contacts

remain variable at low  $\phi$ . In contrast, for  $\phi > \phi_G$  [Fig. 4(b)] white regions dominate, indicating that interparticle contacts persist. Similar images obtained over the full density range further reveal that force-chain rearrangements are long range, even though the particle rearrangements are not [30].

Figure 4(c) compares these perspectives, showing  $\langle \Delta \rangle$  and  $\langle \Delta_{AB} \rangle$ , the measure for interparticle forces  $\langle I_g \rangle$ , and the normalized cross correlation  $C$ , all as a function of  $\phi$ . Note that we chose the average green channel intensity  $\langle I_g \rangle$  as a measure for the interparticle forces because standard force detection algorithms do not work well on the minute contact forces present at the onset of jamming. This choice is further motivated by noting that  $\langle I_g \rangle$  scales linearly with the applied load at low loads [30,31]. This plot therefore shows that the onset of the Gardner-like regime (for which  $\langle \Delta \rangle < \langle \Delta_{AB} \rangle$ ) coincides with the onset of the conservation of interparticle contacts (given by the sharp rise in  $C$ ) and is distinct from  $\phi_J$  (defined in the onset of the rise of  $\langle I_g \rangle$ ), suggesting that the force network gets increasingly determined as soon as  $\phi > \phi_G$ .

By analogy to what has been reported for numerical simulations of size-polydisperse particles in otherwise crystalline systems [12], we expect the distance to jamming to be controlled by particle disorder. Given that all particles were cut from flat sheets with the same fixed-radius metal cutter [29], disorder is here expected to be dominated by irregularities along the disk edges (see Fig. 5). Generalizing the polydispersity argument of [12] to this case, we expect the onset of the Gardner regime to be set by the particles' dimensionless deviation from a constant radius

$$\sqrt{\phi_J - \phi_G} \propto 1 - \frac{r}{R}. \quad (4)$$

Two key features emerge from the image analysis: asphericity of approximately 1%, superimposed with a surface roughness of approximately 0.3%. Both quantities are of the same order of magnitude as the relative distance between the Gardner-like crossover in and the jamming point for our system,  $s = \sqrt{0.810 - 0.807} \approx 1\%$ . Because our particles were all cut using the same fixed-radius metal cutter, they have similar irregularities along the disk edges. A systematic investigation of particle roughness is therefore not possible for this system and is left for future consideration.

#### IV. CONCLUSION

We have shown that small particle irregularities, always present in experiments but often neglected, in an otherwise crystalline system exhibit Gardner-physics-like features near jamming. Although 2D systems are expected not to exhibit proper Gardner criticality [13], the finite size of our system suppresses the long-wavelength fluctuations that would normally occlude this effect in the thermodynamic limit, thus preserving some of its physical features. This choice of system further allowed us to study changes in the force network of one specific configuration, where we found experimental evidence correlating the onset of that regime to the determination of force contacts near jamming. For the particles we used, the distance from jamming of the Gardner crossover was similar to the inherent roughness of



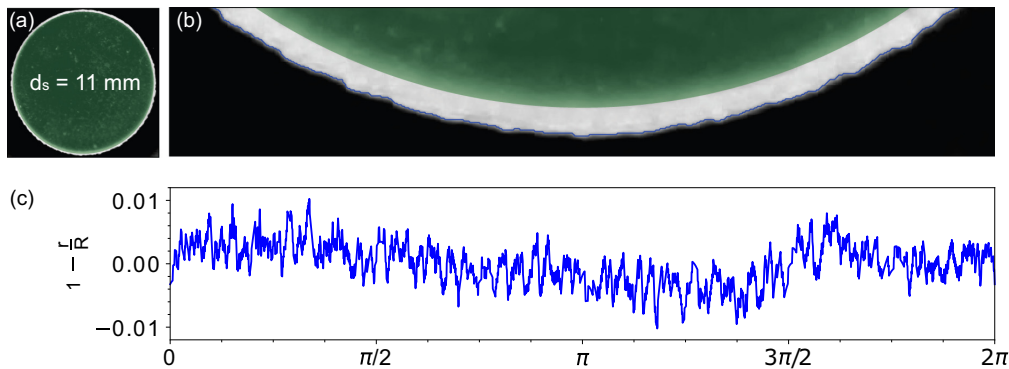


FIG. 5. (a) Micrograph of a single photoelastic particle that is (b) enlarged so as to illustrate the edge detection (blue); the green circle traces a perfect circle for reference. (c) Fractional deviation of the particle edge  $r$  from the average radius  $R$  along the circumference.

the particles, a finding consistent with the study of size polydispersity by Charbonneau *et al.* [12].

Future work should measure the role of irregularities directly, perhaps through the printing of particles with systematically controlled roughness. This work motivates delving further into the influence of particle roughness on a micro-mechanical level. Whereas surface roughness has been investigated on a macroscopic level, such as for relating surface roughness and friction in glass spheres (e.g., [32]), we showed that roughness could also influence interactions on a microscopic level. This finding raises questions about what signatures of frictional jamming found for smooth particles [33] match those needed to describe, more realistic, rough particles [34]. In this context, including geometrical asperities [35] in numerical simulations could provide particularly invaluable insight.

Data associated with this work are available from Dryad [36].

#### ACKNOWLEDGMENTS

We thank Sho Yaida, Jonathan Kollmer, and Eric Corwin for motivating discussions, Joshua Dijkstra for help with image processing, and Jonathan Kollmer, Clayton Kirberger, and Josh Miller for technical assistance. P.C. acknowledges support from the Simons Foundation, Grant No. 454937. K.E.D. acknowledges support from NSF Grant No. DMR-0644743 (apparatus) and support from Grant No. DMR-2104986. L.K. acknowledges support from the European Union's Horizon 2020 research and innovation program Caliper, Marie Skłodowska Curie Grant No. 812638.

- 
- [1] P. Dantu, *Géotechnique* **18**, 50 (1968).
  - [2] H. M. Jaeger, S. R. Nagel, and R. P. Behringer, *Rev. Mod. Phys.* **68**, 1259 (1996).
  - [3] F. Radjai, D. E. Wolf, M. Jean, and J.-J. Moreau, *Phys. Rev. Lett.* **80**, 61 (1998).
  - [4] D. Howell, R. P. Behringer, and C. Veje, *Phys. Rev. Lett.* **82**, 5241 (1999).
  - [5] J. F. Peters, M. Muthuswamy, J. Wibowo, and A. Tordesillas, *Phys. Rev. E* **72**, 041307 (2005).
  - [6] B. P. Tighe, J. H. Snoeijer, T. J. Vlugt, and M. van Hecke, *Soft Matter* **6**, 2908 (2010).
  - [7] J. E. Kollmer and K. E. Daniels, *Soft Matter* **15**, 1793 (2019).
  - [8] P. Charbonneau, J. Kurchan, G. Parisi, P. Urbani, and F. Zamponi, *Annu. Rev. Condens. Matter Phys.* **8**, 265 (2017).
  - [9] P. Charbonneau and P. K. Morse, *Phys. Rev. Lett.* **126**, 088001 (2021).
  - [10] E. Gardner, *Nucl. Phys. B* **257**, 747 (1985).
  - [11] J. Kurchan, G. Parisi, P. Urbani, and F. Zamponi, *J. Phys. Chem. B* **117**, 12979 (2013).
  - [12] P. Charbonneau, E. I. Corwin, L. Fu, G. Tsekenis, and M. van der Naald, *Phys. Rev. E* **99**, 020901 (2019).
  - [13] L. Berthier, G. Biroli, P. Charbonneau, E. I. Corwin, S. Franz, and F. Zamponi, *J. Chem. Phys.* **151**, 010901 (2019).
  - [14] P. Charbonneau, J. Kurchan, G. Parisi, P. Urbani, and F. Zamponi, *Nat. Commun.* **5**, 3725 (2014).
  - [15] G. Tsekenis, *Europhys. Lett.* **135**, 36001 (2021).
  - [16] A. P. Hammond and E. I. Corwin, *Proc. Natl. Acad. Sci. USA* **117**, 5714 (2020).
  - [17] G. Biroli and P. Urbani, *Nat. Phys.* **12**, 1130 (2016).
  - [18] Y. Jin and H. Yoshino, *Nat. Commun.* **8**, 14935 (2017).
  - [19] A. Seguin and O. Dauchot, *Phys. Rev. Lett.* **117**, 228001 (2016).
  - [20] H. Xiao, A. J. Liu, and D. J. Durian, *Phys. Rev. Lett.* **128**, 248001 (2022).
  - [21] C. Likos and C. Henley, *Philos. Mag. B* **68**, 85 (1993).
  - [22] L. Berthier, P. Charbonneau, Y. Jin, G. Parisi, B. Seoane, and F. Zamponi, *Proc. Natl. Acad. Sci. USA* **113**, 8397 (2016).
  - [23] E. Lerner, G. Düring, and M. Wyart, *Soft Matter* **9**, 8252 (2013).
  - [24] P. Charbonneau, Y. Jin, G. Parisi, C. Rainone, B. Seoane, and F. Zamponi, *Phys. Rev. E* **92**, 012316 (2015).
  - [25] P. Charbonneau, E. I. Corwin, G. Parisi, and F. Zamponi, *Phys. Rev. Lett.* **114**, 125504 (2015).
  - [26] J. G. Puckett and K. E. Daniels, *Phys. Rev. Lett.* **110**, 058001 (2013).

- [27] E. S. Bililign, J. E. Kollmer, and K. E. Daniels, *Phys. Rev. Lett.* **122**, 038001 (2019).
- [28] J. Kollmer, Photo-elastic grain solver, <https://github.com/jekollmer/PEGS>.
- [29] K. E. Daniels, J. E. Kollmer, and J. G. Puckett, *Rev. Sci. Instrum.* **88**, 051808 (2017).
- [30] See Supplemental Material at <http://link.aps.org/supplemental/10.1103/PhysRevE.106.054901> for a schematic overview of the protocols, details about the MSD correction and orthogonalization schemes, the jamming point determination, and a movie of force contact overlaps.
- [31] A. A. Zadeh *et al.*, *Granular Matter* **21**, 83 (2019).
- [32] S. Utermann, P. Aurin, M. Benderoth, C. Fischer, and M. Schröter, *Phys. Rev. E* **84**, 031306 (2011).
- [33] L. E. Silbert, D. Ertaş, G. S. Grest, T. C. Halsey, and D. Levine, *Phys. Rev. E* **65**, 031304 (2002).
- [34] S. Pradeep, M. Nabizadeh, A. R. Jacob, S. Jamali, and L. C. Hsiao, *Phys. Rev. Lett.* **127**, 158002 (2021).
- [35] S. Papanikolaou, C. S. O'Hern, and M. D. Shattuck, *Phys. Rev. Lett.* **110**, 198002 (2013).
- [36] L. Kool, P. Charbonneau, and K. E. Daniels, Data from: Gardner-like crossover from variable to persistent force contacts in granular crystals (Dryad, 2022), doi: [10.5061/dryad.kd51c5b97](https://doi.org/10.5061/dryad.kd51c5b97).

# Gardner-like crossover from variable to persistent force contacts in granular crystals

## SUPPLEMENTARY INFORMATION

Lars Kool,<sup>1,2</sup> Patrick Charbonneau,<sup>3</sup> and Karen E. Daniels<sup>2</sup>

<sup>1</sup>*Laboratoire de Physique et Mécanique des Milieux Hétérogènes, ESPCI, Paris, France*

<sup>2</sup>*Department of Physics, North Carolina State University, Raleigh, North Carolina 27695, USA*

<sup>3</sup>*Departments of Chemistry & Physics, Duke University, Durham, North Carolina 27708, USA*

### 1. Description of Movie

The movie (available online) provides a fuller display of the crossover from Fig. 4A to B. Each frame overlays two experimental snapshots: one taken before (blue) and one taken after (red) a single airjet sweep, obtained for gradually increasing  $\phi$ . The overlap between the two images appears as white. For  $\phi < 0.807$ , sparse overlaps (lack of white) of the force chains is clear; far above  $\phi_G > 0.807$ , the overlap drastically increases (white becomes dominant). The quantification of the crossover from variable to persistent force contacts is reported in Fig. 4C.

### 2. Determining the jamming transition

We measure the jamming transition  $\phi_J$  using the photoelastic stresses, visualized using circularly polarized green light. At the onset of jamming, fringes start to develop, while other contributions to the green signal in the image are minimal and constant (*e.g.*, scattering of green light off the porous grid under the particles). We therefore normalize the average green light intensity  $I_g$  according to

$$I(\phi) = \frac{\langle I_g(\phi) \rangle}{\langle I_g(\phi_{\min}) \rangle}$$

where  $\langle I_g(\phi_{\min}) \rangle$  is the background green intensity, measured at the lowest  $\phi$  and  $\langle \cdot \rangle$  denotes the average taken over all pixels at least  $4R_L$  from the boundaries and all images taken at that  $\phi$ .

At low  $\phi$ , there are no photoelastic fringes present in the image ( $I_g$  stays within 0.5% of  $I_g(\phi_{\min})$ ), indicating that the system is not yet jammed. For  $\phi > 0.8096$ ,  $I_g$  lies above the background level, but remains within the noise floor of 0.5%; only at  $\phi = 0.8105$  (greyed region in Fig. 4C), does  $I$  deviate significantly (1.8%), thus indicating that the system has entered the jammed phase. We therefore identify the jamming transition as  $\phi_J = 0.8100 \pm 0.0005$ .

### 3. Mean squared displacement correction

In our experiments, we compare the mean cage size,  $\Delta$ , with the mean cage separation,  $\Delta_{AB}$ . However, due

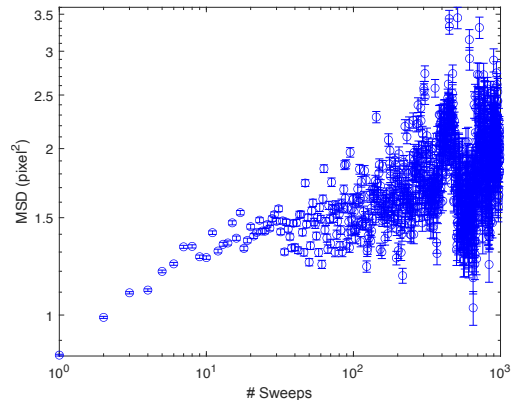


FIG. A.6. Time evolution of the MSD, showing plateau above a few hundred sweep cycles ( $t_r$ ).

to the slow nature of the airjet sweeps used to randomize particle positions within their cage, the true long-time limit of MSD is not experimentally attainable. The full extent of our data collection, out to  $1000t_r$ , is shown in Fig. A.6.

We therefore determined the ratio between the long-time MSD (at  $1000t_r$ ) and an attainable timescale,  $100t_r$ , and corrected all reported  $\Delta$  values accordingly through a constant rescaling factor,

$$D = \frac{\text{MSD}(950)}{\text{MSD}(100)} = 1.2$$

with  $\text{MSD}(950)$  the average MSD between  $900t_r$  and  $1000t_r$ , and  $\text{MSD}(100)$  the average MSD between  $95t_r$  and  $105t_r$ . We average over a range of MSD values, due to the difficulty of obtaining stochastically independent trajectories at longer timescales.

### 4. Orthogonalizing lattice vectors

Recall that the H1 unit cell has lattice vectors which are both non-orthogonal to each other, and not perpendicular to the axes of the experiment, as shown in Fig. A.7A. We observed that within the Gardner phase ( $\phi \gtrsim 0.807$ ), the displacement components were no longer Gaussian and azimuthally symmetric around  $v_x = v_y = 0$  (the mean however, was still at  $v_x = v_y = 0$ ), as shown

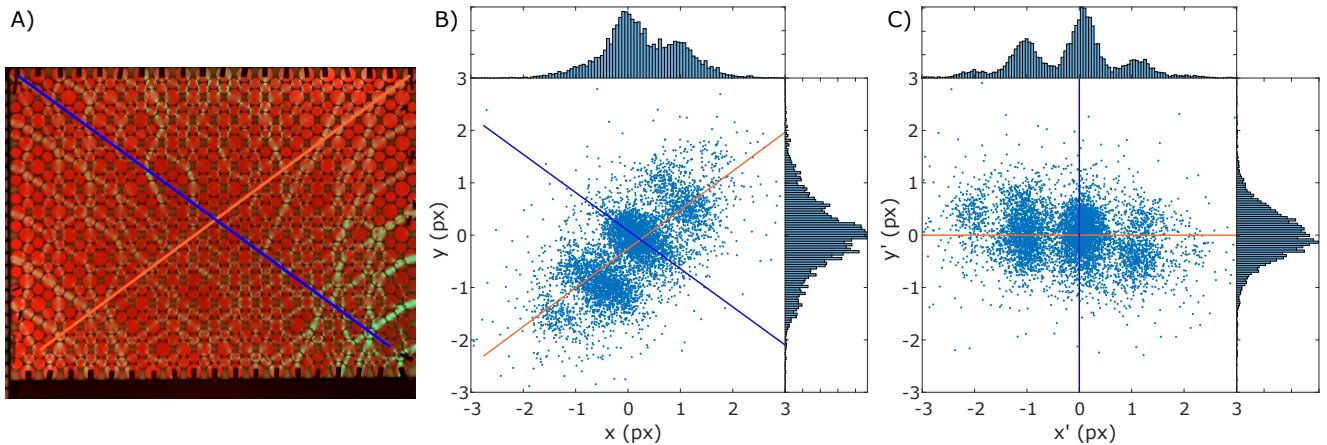


FIG. A.7. A) Typical image obtained during experiments, where the blue and orange lines indicate the lattice vectors of the crystal. B) Displacement components of  $\Delta$  in the Gardner phase, with the blue and orange line indicating the lattice vectors of the crystal. The probability density functions in the  $x$  and  $y$  directions are given along their respective axis. C) Displacement components of  $\Delta$  in the Gardner phase after linear transformation to orthogonalize the system, with the blue and orange line showing the lattice vectors of the orthogonalized system. The probability density functions in the  $x'$  and  $y'$  directions of the orthogonalized system are given along their respective axis.

in Fig. A.7B. Instead, the displacement components split up into distinct bands, aligned with the lattice vectors of the crystal.

Therefore, we applied a linear transformation to the data such that the lattice vectors became orthogonal; this resulted in two different probability density functions for the displacement components, shown in Fig. A.7C. The PDF in the  $y'$ -direction (blue axis) is now Gaussian, whereas the distribution in the  $x'$ -direction is more

complicated, and metrics like mean displacement, mean squared displacement, or standard deviation do not reflect the nature of the distribution, nor were they very reproducible. These features likely reflected an anisotropy in our experimental setup, that affected the configurational sampling of our system. We therefore chose to use the distribution in the  $x'$ -axis to calculate  $\Delta$ , which showed no such artefact.